Exotic Gravitational Microlensing Effects as a Probe of Stellar and Galactic Structure

Andrew Cameron Becker

A dissertation submitted in partial fulfillment
of the requirements for the degree of

Doctor of Philosophy

University of Washington

2000

Program Authorized to Offer Degree: Astronomy

University of Washington

Graduate School

This is to certify that I have examined this copy of a doctoral dissertation by

Andrew Cameron Becker

and have found that it is complete and satisfactory in all respects,
and that any and all revisions required by the final
examining committee have been made.

Chair of Supervisory Committee:

_____

Christopher W. Stubbs

Reading Committee:

_____

Craig Hogan

_____

Tom R. Quinn

Date: _____

In presenting this dissertation in partial fulfillment of the requirements for the Doctoral degree at the University of Washington, I agree that the Library shall make its copies freely available for inspection. I further agree that extensive copying of this dissertation is allowable only for scholarly purposes, consistent with "fair use" as prescribed in the U.S. Copyright Law. Requests for copying or reproduction of this dissertation may be referred to Bell and Howell Information and Learning, 300 North Zeeb Road, Ann Arbor, MI 48106-1346, or to the author.

Signature_____

Date_____

University of Washington

Abstract

Exotic Gravitational Microlensing Effects as a Probe of Stellar and Galactic Structure

by Andrew Cameron Becker

Chair of Supervisory Committee:

Professor Christopher W. Stubbs
Departments of Astronomy and Physics

The nature of the "dark matter" which comprises the majority of the mass of our Universe is one of the most elusive, yet fundamental, cosmological properties. Its presence has been inferred on a variety of scales by indirect observational measurements. It remains to be seen whether or not this dark matter is composed of discrete units (Machos – Massive Compact Halo Objects) or is a sea of fundamental particles (WIMPs – Weakly Interacting Massive Particles).

The MACHO project was founded to test for Machos orbiting in the halo of our Milky Way Galaxy. The experiment makes use of the one property we know about dark matter – it exerts a gravitational force on its surroundings. Einstein's theory of general relativity implies the region of influence sensitive to dark matter includes the fundamental fabric of space–time itself. A bizarre consequence of this is that matter may warp space, splitting the light from a background source into multiple images on the sky, hence acting as a gravitational lens.

Millions of source stars in the Large and Small Magellanic Clouds have been observed for signatures of intervening, lensing dark matter. Approximately 20 events have been discovered. Several hundred additional events have been seen towards our Galactic bulge. Given the dearth of lensing events, the focus of the gravitational microlensing field has

evolved from passive surveys to an aggressive pursuit of lightcurve fine structure. Embedded in each microlensing lightcurve are clues to the nature of the lensing system. Recognizing these features in real–time requires frequent sampling and high precision measurements.

This dissertation includes the development and maintenance of the MACHO Alert System, which recognized these rare events in real–time. This Alert System required daily vigilance between its inception in 1995 and the completion of the MACHO Survey in 1999. However, the focus of this dissertation was the Global Microlensing Alert Network (GMAN). This system comprises telescopes in Australia, Chile, Israel, and New Zealand. These resources were reallocated in real–time to provide maximum sensitivity to lightcurve fine–structure. The nightly scheduling of targets, real–time reduction of tens of thousands of astronomical images, and final analysis of the ensemble of events are the focus of this dissertation.

TABLE OF CONTENTS

LIST OF FIGURES

LIST OF TABLES

ACKNOWLEDGMENTS

Life would be meaningless without family and friends. There are dozens of people I have encountered in the course of my life who have left significant impressions, provided unexpected moments of clarity, and generally made my life a true adventure. And since I can do it, I'm going to make this long and fun!

Those people who assisted me in my earliest learning experiences should be credited, as well as those who refined my critical thought processes, which allowed me to understand the scientific principles contained within this dissertation. In particular, **Marjorie Johnson**, who was the first (and likely only) person to call me profound, for letting me know that I actually had such a thing in me. **Ted Hope**, for letting the our High School percussion section get away with ridiculous escapades and for truly solidifying my appreciation and love for music. **Mark West**, for introducing me to the subject of physics in the most stimulating atmosphere I encountered in high school. Dr. **James Gaidos**, who took a chance in hiring a mohawked undergraduate, for introducing me to the intricacies of astrophysics. Dr. **John P. Finley**, who provided a fraternal work atmosphere as a hip, car–antenna wielding advisor. And finally, to the professor most responsible for the science contained herein, I would like to compliment my advisor **Chris Stubbs** for finally shaving his beard.

For my first really close–knit group of friends, who represented a variety of interests but taught me what it was like to really enjoy life : Tim Adams, Shawn Berg, Dave and Chris Boyle, Chris Grigman, Sean Martin, Chris McMahan, Dan Petrizzo, Mike Roberts, Sonny Selko, and of course the lovely Rebecca Campo.

For my friends from Purdue University, who dabbled in the absurd on a daily basis and provided everything a collage experience should be : Tim Adams, Paul Amico, Jon Briner, Carrie Crawford, Dan Johnson, Krista Lane, Nate Letsinger, Catherine Marlow,

Jason Meyers, Anthony Roach, Joy Wimberg, and what the hell, Chris Schenk.

It seems each bunch of friends gets more and more diverse the further along I move in life, and its refreshing to realize its probably more a function of myself than anything else. But life in grad school was actually extremely fun, and I shared all sorts of cool experiences which made the whole experience worthwhile, including : enduring the hell which is a graduate school physics course with Rebecca Hoffenberg, Chuck Duba, and Karsten Heeger; the other sort of challenge entirely which was the entire astronomy program with classmates Joachim Stadel (also the consummate – meaning fearlessly psychotic – outdoorsman) and Ted Wyder; frequent trips to the Pub with old–schoolers Mark **Hammer**gren, Luis Mendoza, Dara Norman, and Knut "rooty toot toot tooty" Olsen (and I even took a final exam there!); snowboarding trips up to Whistler, Canada with folks including Jason "the cruiser" Alexander, Bernie Beck, Eric Deutsch, and Jeff Gardner; ultimate frisbee on the poop–soaked fields of the IMA with all sorts of people including Rory Barnes, Heidi Iverson, Dave Reiss, and "the rookies"; nights of high stakes poker with Vandana Desai and Darren Reed; squish fests with Vjeran Punkrockovic; watching the Seattle Supersonics sag under the weight of Vin Baker with Frank van den Bosch, Armin Rest, and Derek Richardson; a really nice thing with Beth Willman; watching Bernadette Rodgers have not just one (hi Joshua!) but *two* kids; and all sorts of people and things I missed out on because I gotta turn this thing in soon! And finally to the constituents of the Slag Heap, Astronomy's most rocking band, who went down in a blaze of glory on Oct 4, 2000. This includes Chris "the Craw" Laws, Ben (ny–ha–ha) Williams, the lovely Lelia, Jon Briner the Big Train, and the furnace which smelted our slag, Tammy Craw.

On a more serious note, much of the science contained in this dissertation could not have been accomplished without man (and woman)–years of work done by members of the MACHO Collaboration. These include Charles Alcock, Robyn Allsman, David Alves, Tim Axelrod, David Bennett, Kem Cook, Andrew Drake, Ken Freeman, Marla Geha, Kim Griest, Matt Lehner, Stuart Marshall, Dante Minniti, Cailin Nelson, Bruce Peterson, Piotr Popowski, Mark Pratt, Peter Quinn, Alex Rodgers, Chris Stubbs, Will Sutherland, Austin

Tomaney, Thor Vandehei, and Doug Welch.

Finally, several individuals were of the utmost assistance in making the GMAN effort happen, including Bob Schommer (CTIO), Dan Maoz (WISE), Brian Crook (MSO30/RAPT), Phil Yock (MJUO/MOA), and Boyd Duffee and Bob Garrison (UTSO).

DEDICATION

To my parents, Philip Cameron Becker and Joan Dale Becker, for whom I've worked so hard to impress. And if this doesn't do it, then maybe I'll just become that musician...

Chapter 1

THE UNIVERSE

1.1 General Relativity

Albert Einstein's geometrodynamic field equations, which may be used to predict and describe the physics appropriate to the evolution of the Universe after the Big Bang, the relativity of the persistence of time, and such trivialities as the bending of starlight by gravity, may be written down in the simple form

$$G_{\mu\nu} = 8\pi T_{\mu\nu} - \Lambda_{\mu\nu}. \tag{1.1}$$

Each component of this equation is a tensor, or a (in this case) 4×4 matrix of operators which define the *behavior* of the object it represents, but not necessarily its measurable properties. Indices μ and ν are each meant to be iterated over 1..4, representing the 4–dimensions of the GR theory, corresponding to 3 spatial and 1 temporal dimension. Thus each tensor has 16 components.

In GR, the tensor $G_{\mu\nu}$ is a unique, conserved measure of geometrically curved space–time. In this context, $T_{\mu\nu}$ represents the stress–energy of the matter enclosed in this space–time – the source of the gravitational field causing the curvature. $\Lambda_{\mu\nu}$ represents a vacuum energy density, or virtual quantum excitations of space–time itself. It may also be considered the zero point energy of a yet–to–be–formulated theory of quantum gravity. Equation 1.1 implies geometry tells matter how to move, and the matter tells geometry how to curve through its gravity.

The dominant laws of gravitational physics, indeed the evolution of the entire Universe, can be derived by evolving the covariant conservation equation

$$G^{\mu\nu}{}_{;\nu} \equiv 0 \tag{1.2}$$

so that the derivative of $G^{\mu\nu}$ with respect to each of the 4 space–time components, including the change in geometry as you evolve along the derivative (the parallel transport of your tangent direction), is exactly zero.

As described below, these equations allow a dynamic Universe which evolves in time, something Einstein regarded in 1917 as unrealistic. The $\Lambda_{\mu\nu}$ term, whose presence naturally occurs in the theory, was given a value scaled to *exactly* counter the dynamic nature of the Universe implied by the theory. This resulted in a static, unchanging model Universe. However, in the process of formulating this theory, Einstein had unknowingly predicted one of the most fantastic yet bizarre characteristics of the Universe - the fact that it should be evolving in time. Subsequent observations by Hubble (1929) indicated that external galaxies farther and farther from our own are receding at a faster and faster rate, unmistakable evidence for a dynamic, in fact expanding, Universe. That Einstein was unable to overcome his personal biases and admit such a fantastic prediction of this theory he has considered his "biggest blunder" (Einstein 1970). This prediction is one of the most powerful pieces of evidence that mankind is arriving at a fundamental understanding of the behavior of the Universe.

1.2 Evolution of the Field Equations = a Universe!

The consequences of evolving the field equations (Equation 1.1) are most easily evaluated in a homogeneous and isotropic space–time.

1.2.1 Homogeneity and Isotropy

Observationally, there is evidence for an assumption of isotropy and homogeneity in the Universe. The distribution of galaxies on the sky, and their distribution in distance from us, indicate the Universe contains large gravitationally clustered structures. But when averaged over large enough scales, the Universe does appear appear homogeneous.

The most significant piece of evidence for overall isotropy is the cosmic microwave background (CMB) radiation, the residual radiation from the so–called "Big Bang". The spectrum of this radiation is remarkably consistent with that of a purely theoretical blackbody,

with a residual anisotropy in temperature of $\delta T/T \sim 10^{-5}$ (there is however a larger amplitude dipole term due to our peculiar motion through the Universe). The prior construction of a theoretical model, the blackbody, which accurately derives and predicts the thermodynamic state of the early Universe must also be considered one of the greatest triumphs in man's study of the Universe. In any case, with this assurance of a large degree of isotropy, homogeneity is naturally implied. We will approximate the geometry and composition of the Universe as a "cosmological fluid" in which we can approximate galaxies as mere particles. Gravity's natural tendency is to cluster, in galaxies or in larger–scale filamentary structures, so this approximation will only be accurate on scales larger than the largest observed gravitational structures in the Universe – super–clusters of galaxies around 65 million light–years in size. For comparison, the Universe is thought to be around 13 billion years old.

The isotropic idealization is only valid for an observer who is moving with the cosmological fluid. An observer moving *within* this would experience an anisotropy along the direction of their motion. This coordinate system defines what are referred to as "co–moving coordinates". All random or peculiar motions are identically zero in this coordinate system, in which the fluid is at rest with respect to the spatial coordinates. The overall implication of this assumption is that the Universe has a global curvature which is the same at all regions of a space–like hypersurface (a 3–dimensional slice of our 4–dimensional space–time).

1.2.2 Space–time Metric: $G_{\mu\nu}$

One of the fundamental steps in constructing a theoretical framework for the Universe, beyond developing that you need such a thing, is defining a metric to describe the length of a displacement. A metric allows one to extract a length or distance independent of the coordinate system used – it is more fundamental than coordinates, and allows the determination of an interval of any unspecified displacement dx. In the most generic terms, this distance can be represented as

$$ds^2 = g_{\mu\nu} dx^\mu dx^\nu. \tag{1.3}$$

where the coefficients of $g_{\mu\nu}$ reflect the geometry of the underlying space–time. By deciding on the form of $g_{\mu\nu}$, you determine the curvature coefficients in Equation 1.1. These components $G_{\mu\nu}$ are determined through prodigiously complex combinations of derivatives of the metric coefficients $g_{\mu\nu}$. These calculations are complicated in such a manner that it warrants the historic praise directed towards their creator, Albert Einstein.

Under the assumption of **perfect** homogeneity and isotropy, we can further refine this metric in co–moving coordinates

$$ds^2 = dt^2 - a^2(t)\gamma_{ij}dx^i dx^j. \tag{1.4}$$

The isolation of the proper time parameter t is due to our choice of co–moving coordinates, which evolve with the cosmological fluid. Since the coordinates evolve with space, in time, we arrive at a familiar realization, that time is orthogonal to space. This removes any correlation between the spatial and temporal coordinates in $g_{\mu\nu}$. We therefore separate the terms, leaving for the spatial coordinates a 3×3 sub–matrix of $g_{\mu\nu}$, called γ_{ij}. The shape – but not the size – of the hypersurfaces of our familiar 3–D space are determined by the 3–metric γ_{ij}. The entire geometrical dynamics of the Universe are fully described by the term $a(t)$, denoted the expansion factor.

The conditions of isotropy and homogeneity severely limit the form of the spatial 3–metric – in fact all representations of the 3–metric are equivalent and can be transformed one to another through gymnastics of coordinate transformation. One representation of the geometry of each hypersurface is

$$ds^2 = dt^2 - a^2(t) \times \left(\frac{dr^2}{1 - Kr^2} + r^2(d\theta^2 + \sin^2\theta \; d\phi^2) \right). \tag{1.5}$$

This is a maximally symmetric space–time, described here by the Robertson–Walker metric. The co–moving coordinates in this representation are (t, r, θ, ϕ). Recall $a(t)$ is the scale factor, or "radius", of the Universe (i.e. each hypersurface is a 3–D hypersphere of proper circumference $2\pi a(t)$), and K is the "curvature parameter" which represents the overall topology of the space–time. In the case of it being positive, negative, or zero, the Universe is open, closed, or flat, respectively (for $\Lambda = 0$). This equation yields the

components of $G_{\mu\nu}$.

1.2.3 Cosmological Fluid: $T_{\mu\nu}$

The components of $T_{\mu\nu}$ are derived by addressing the Universe as a thermodynamic system, whose nature is to minimize energy and maximize entropy. This requires knowledge of all non–gravitational fields, such as energy, momentum and stresses. These fields are represented in terms of the enclosed mass–energy ρ and pressure p. The requirements of isotropy (and thus homogeneity) imply that ρ and p are only functions of time, and not of location in space.

$T_{\mu\nu}$ as evaluated in a frame moving with a 4–velocity $\vec{\mathbf{u}}$ may be represented as

$$T_{\mu\nu} = (\rho + p)u_\mu u_\nu + p g_{\mu\nu}. \tag{1.6}$$

As with all tensors, the components of $T_{\mu\nu}$ are independent of the coordinates with which they are described. The classical equations of motion and electromagnetics can be derived from the equation of motion for this stress–energy tensor

$$T^{\mu\nu}{}_{;\nu} \equiv 0. \tag{1.7}$$

For example, Equation 1.7 is reduced to the first law of thermodynamics when projected along the world line of the fluid itself. That is, when evaluated in the normal 3–D space where $\vec{\mathbf{u}} = (\mathrm{c}, \vec{\mathbf{v}})$, and $\vec{\mathbf{v}}$ is a standard velocity vector. The first law reads $dE = -pdV$, there E is the mass–energy and V is the volume of any fluid element. We can represent the mass–energy by $E = \rho V$ (by analogy to $E = mc^2$, and setting $c = 1$). The evolution of the proper volume of a co–moving sphere should scale $V \propto a(t)^3$ (recall $a(t)$ sets the relative size of the Universe). The first law reduces to an equation expressing the evolution of the density of the Universe as a function of the scale factor a and pressure p

$$\frac{d\rho}{da} = -3\frac{(p + \rho)}{a}. \tag{1.8}$$

The parameter ρ comprises the mass–energy of all components in the Universe. The three anticipated components of the Universe are **matter**, **radiation**, and **vacuum energy**,

each of which has a different equation of state relating their pressure to their density. These equations of state allow us to evaluate the evolution of density ρ with scale factor a using Equation 1.8.

Matter is effectively pressureless, $p = 0$, meaning ρ_m evolves with the scale factor as $\frac{d\rho_m}{da} = -3\frac{\rho_m}{a}$, or $\rho_m \propto a^{-3}$. At early times in the Universe, radiation dominated the energy density. However, the expansion of the Universe has caused an internal cooling, diluting the current contribution of ρ_r to the mass–energy density of the Universe. Radiation pressure is equal to 1/3 of the radiation density, so it evolves much faster than ρ_m as $\rho_r \propto a^{-4}$. Finally the vacuum energy density contribution of a Λ term is ρ_Λ = constant, so $\rho_\Lambda = -p_\Lambda$.

1.2.4 Scale Factor: $a(t)$

We are now able to characterize the evolution of the field equation Equation 1.1 for various epochs in the history of the Universe. Describing the expanding Universe requires reducing these equations to a solution for the scale factor a as a function of coordinate t (proper time). The result is a first–order differential equation

$$\left(\frac{\dot{a}}{a}\right)^2 = \frac{8}{3}\pi G\rho - \frac{k}{a^2} + \frac{\Lambda}{3}. \tag{1.9}$$

G is the standard Newtonian gravitational constant, and k represents the overall sign of the curvature parameter K – thus it is limited to values of +1, -1, and 0.

Equation 1.9 may be re–written to express the dependence of $\dot{a}/a$ on each component of the mass–energy density,

$$\left(\frac{\dot{a}}{a}\right)^2 = \frac{8\pi G}{3}\left(\rho_m\left(\frac{a_o}{a}\right)^3 + \rho_r\left(\frac{a_o}{a}\right)^4 + \rho_\Lambda\right) - \frac{k}{a^2}. \tag{1.10}$$

1.3 Simplified Cosmologies

All the components of the General Relativity theory are in place for it to be presented as a mathematically consistent and closed system. The derivation of $a(t)$ in Equation 1.9 allows one to determine the evolution of the density $\rho(t)$ (and pressure $p(t)$) from Equation 1.8, given an equation of state. The components of $T_{\mu\nu}$ are next found from Equation 1.6, which

is equivalent to determining the curvature tensor $G_{\mu\nu}$ (Equation 1.1). Finally, the metric coefficients $g_{\mu\nu}$, of which $a(t)$ is an integral component, are determined from the components of $G_{\mu\nu}$.

This formalism is a unique solution for an isotropic and homogeneous Universe of constant curvature. We next address the primary cosmological parameters which are in principle measurable, and play a leading role in determining the appropriate cosmological model.

1.3.1 Expansion Rate: H

The fractional rate of the increase in distances due to the Universe's expansion (Equation 1.9) is referred to as the "Hubble constant"

$$H \equiv \frac{\dot{a}(t)}{a(t)} \tag{1.11}$$

after astronomer Edwin Hubble. The units of H are inverse time, and the Hubble time H^{-1} is a linearly extrapolated estimate of the age of the Universe. Since this "constant" is actually variable with time, its current value is referred to as H_0. The parameter $h = H_0/(100\,\mathrm{km\,s^{-1}\,Mpc^{-1}})$ is commonly used to scale astronomical measurements such as mass, distance, and luminosity, since its actual value has been the subject of much historical debate within the astronomical community.

The practical use of H_0 is to provide an actual distance D to an astronomical object, given a measurement of the redshift z of light from the object. This technique relies on the location, in wavelength, of specific features in the spectrum of the object which are doppler shifted due to the recession velocity of the galaxy, presumed to be caught up in the expansion of the Universe. Thus the galaxies serve as tracers of the expansion of the cosmological fluid, also called the Hubble flow. The form of this relationship is simply expressed as

$$cz = H_0 D. \tag{1.12}$$

1.3.2 Density Parameter: Ω

Since the Universe evolves under gravity, if we are to understand its past, present, and future history we need to know the total amount of mass–energy causing the gravitational field. This requires an unbiased inventory of $T_{\mu\nu}$, since the components of $G_{\mu\nu}$, as properties of the space–time, are not directly observable.

An illustrative example is an isotropic and homogeneous *flat* Universe, meaning $k = 0$. This implies a total energy density of the Universe ($\rho_{\rm tot} = \rho_m + \rho_r + \Lambda/8\pi G$) equal to a "critical density" to close the Universe

$$\rho_{crit} = \frac{3H_0^2}{8\pi G}. \tag{1.13}$$

This density is equivalent to approximately 1 proton per cubic meter of volume in the Universe. The current density of the Universe is commonly presented as the ratio of the current density to the critical density

$$\Omega \equiv \frac{\rho_{tot}}{\rho_{crit}}. \tag{1.14}$$

Ω determines the future evolution and final state of the Universe. We can divide up Ω into

$$\Omega = \Omega_m + \Omega_r + \Omega_\Lambda, \tag{1.15}$$

corresponding to the components of $\rho_{\rm tot}$. At the current epoch, radiation does not play a significant role. Ω_m encompasses all forms of matter, and Ω_Λ represents the density of the vacuum energy. The 3 possible ranges of Ω each have considerably different implications for cosmology. In the following we assume $\Omega_\Lambda = 0$.

- If $\Omega < 1$, the Universe is does not contain enough matter to halt its current expansion. This is referred to as an "open" Universe, and its ultimate fate is to expand forever until it dies a thermodynamic heat death, and all that remain are slowly evaporating black holes. An infinite range of coordinates are allowed in this space–time.

- $\Omega > 1$ indicates a finite and "closed" Universe which has high enough total density to turn around the current expansion, leading to a future "Big Crunch". There is no actual spatial boundary to this Universe, but the integral value of the energy contained in this space–time is zero.

- $\Omega = 1$ implies a "flat" Universe, where the total energy density is exactly equal to the critical energy density. The total energy of an asymptotically flat space time is greater than zero. However, this is the theoretically preferred condition, since any Universe which starts with $\Omega \neq 1$ is expected to have $\Omega \ll 1$ currently.

This preference for $\Omega = 1$ can be seen below. Begin with $(k/H^2a^2) = \Omega - 1$, and integrate

$$t = \int \frac{da}{\dot{a}} \tag{1.16}$$

over each of the possible 3 equations of state. We can then deduce that, during an epoch dominated by each respective component, a and $(\Omega - 1)$ evolve like

$$\begin{aligned} Matter \quad & a \propto t^{2/3} \quad \rightarrow \quad (\Omega - 1) \propto t^{2/3} \\ Radiation \quad & a \propto t^{1/2} \quad \rightarrow \quad (\Omega - 1) \propto t \\ Vacuum \quad & a \propto e^{Ht} \quad \rightarrow \quad (\Omega - 1) \propto e^{-2Ht} \end{aligned} \tag{1.17}$$

.

We will assume $(\Omega_0 - 1)$ is of order 1, such that Ω_0 is currently close to, but not quite, the critical density. One can then trace this value back through the matter dominated epoch to the epoch of equipartition, where radiation and matter contributed equally to Ω. Assuming the Universe is currently 13 billion years old, we find

$$Equipartition\ epoch \quad t \sim 4000\ yr \quad \rightarrow \quad (\Omega - 1) \lesssim 5 \times 10^{-5} \tag{1.18}$$

Thus Ω must have been much closer to 1, off by only 5 parts in $100,000$. If we further track this back through the radiation–dominated epoch to one of the first major epochs

in the early Universe, where 3 of the 4 known forces were one–and–the–same, the Grand Unification epoch, we find

$$Grand\ Unification\ epoch \qquad t \sim 10^{-35}\ sec \quad \rightarrow \quad (\Omega - 1) \lesssim 10^{-51} \tag{1.19}$$

This indicates that Ω must have been *exceedingly*, if not unreasonably, close to 1 at these early stages of the evolution of the Universe, if it is not in fact exactly 1.

1.4 Not–so–simplified Cosmology

It turns out this is not the only problem with the standardized model of cosmology as described above. The previously mentioned cosmic microwave background (CMB) radiation is similar all across the sky to 1 part in 10,000. This is extremely smooth, and suggests some sort of thermal process which lead to a large degree of homogeneity at the creation of the CMB radiation. However, simple calculations indicate that regions on the sky farther apart than approximately 1 degree were not in causal contact when this radiation began its trip towards us. Thus there is no reason to expect that regions on the sky more than 1 degree apart should have the same temperature to 1 part in 10,000 – they were beyond each other's event horizons.

A more obscure problem lies with the expected creation of cosmological defects in the early Universe. Phase transitions, occurring when the Universe expands and cools, are expected to produce stable energy concentrations if they occur rapidly enough. These can be single or multi–dimensional, and candidates include such objects as magnetic monopoles, cosmic strings, and domain walls. None have as of yet been found.

1.4.1 Inflation

The occurrence of an "inflationary epoch" in the very early Universe, a theory originally assembled by Guth (1981), solves all of the above issues. Addressing this problem by looking at the horizon problem is a useful approach. This involves parameterizing the flow of information in the early Universe. The maximum coordinate displacement of information, i.e. light, can be described as

$$\int \frac{dt}{a(t)} = \int_0^{a_0} \frac{da}{a\dot{a}} \propto \int_0^{a_0} \frac{da}{a^2 \rho^{1/2}}. \tag{1.20}$$

If there is an epoch in the Universe where ρ varies less rapidly than a^{-2}, the integral in equation (1.20) will diverge. This implies that information can travel extended distances, giving causal processes the ability to smooth out any irregularities which would be manifested in CMD anisotropies.

Recall that for a vacuum dominated Universe, ρ_Λ = constant, which does not vary at all with scale factor. This suggests a solution where, in the early Universe, a term which acts like a cosmological constant dominated the energy–density. Scalar fields, called inflatons, have been constructed which reduce to Λ–like fields in the early Universe. This solves the horizon problem by generating causal contact between distant regions on the sky, allowing their environments to thermalize and leading to the homogeneity required to result in the isotropic CMB we see today.

The analogy to a cosmological constant term may be extended to provide solutions to the flatness and relic problems. Equation 1.17 indicates that the scale factor would expand by a factor of $a \propto e^{H\Delta t}$ during a vacuum–dominated epoch of duration Δt. In "slow roll" models of inflation, $H\Delta t$ is much larger than one. Peebles (1993) suggests a value near $H\Delta t \sim 60$. In this case, the Universe expands by a factor of 10^{26} in less than approximately 10^{-34} seconds (although the exact time and duration of the inflationary epoch is unknown). This rapid expansion serves as an effective means to dilute any prior cosmological relics.

Finally, in a similar duration of time, $(\Omega - 1) \propto e^{-2H\Delta t}$ is driven to 0 to very high accuracy, 10^{-53}. Thus inflation drives Ω, no matter what its value before inflation, exponentially close to 1. Since inflation predicts a nearly flat Universe, the implication is that there is "more" Universe beyond our horizon. If we were able to view this region, we would see large–scale fossil pre–inflationary structure.

Chapter 2

DARK MATTER

In the context of Einstein's cosmology, the overall density of the Universe (Ω) determines its ultimate fate. It is therefore of utmost importance to our understanding of the Universe to measure – in most cases merely to estimate – the enclosed mass in a volume of space. However, until very recently, astronomers have been limited to measurements of the astronomical menagerie by looking only at the *light* emitted from individual bodies.

It must be emphasized that the mapping from luminosity to mass is very uncertain. The mass–to–light ratio Υ in fact varies wildly from object to object even in our most local part of the Universe, the solar neighborhood. For example, stars brighter (or heavier) than the sun contribute $\sim 95\%$ of the local luminosity, while contributing only $\sim 25\%$ of the local mass (Mihalas & Binney 1981). The local distribution in mass is actually composed of almost equal components in gases and stars, and a slightly smaller fraction in stellar remnants such as white dwarfs and neutron stars.

Fukugita, Hogan, & Peebles (1998) derive a critical mass–to–light ratio in the B photometric passband, corresponding to an ($\Omega_m = 1,\ \Omega_\Lambda = 0$) Universe, of $\Upsilon_{B,\mathrm{crit}} = (1390 \pm 140) h\, \Upsilon_\odot$. For comparison, Binney & Merrifield (1998) find a local mass–to–light ratio in the same passband of $\Upsilon_{B,\mathrm{local}} = 2.3\, \Upsilon_\odot$. This suggests our local environment is either severely under–massive or over–luminous compared to the rest of the Universe! In actuality, the magnitude of the mass–to–light ratio *is* generally seen to increase when one moves to larger and larger scales. However, the actual value of Υ for any particular class of object, size of object, or color in which one views the object, has confounded astronomers since the discovery by Zwicky (1933) that there appear to be ubiquitous components of the Universe which contain significant amounts of mass but emit very little (if any!) light.

2.1 The "Discovery" of Dark Matter

One of the first efforts to measure the gravitational binding energy of a large–scale structure was undertaken by Zwicky (1933). Radial velocity measurements of (only 8) galaxies contained in the Coma Cluster of galaxies were taken and their dispersion in velocity calculated. He found that the galaxies had much too high of a velocity dispersion to remain as bound components of the observed cluster. That is, the cluster mass inferred from the luminous matter was insufficient to prevent the individual galaxies from being ejected from the cluster. Zwicky concluded it would require $\Upsilon \sim 400$ to explain the dynamics of the Coma system (it should be noted that modern values of the Hubble constant lessen this overdensity to $\Upsilon \sim 50$). A similar measure by Smith (1936) of the Virgo Cluster of galaxies supported Zwicky's conclusions – on cluster sized scales, there is some form of "dark matter" which dominates the gravitational potential. Closer to home, Babcock (1939), and subsequently Roberts & Whitehurst (1975) observed the flat rotation curve of the Andromeda Galaxy out to 30 kpc, inferring $\Upsilon > 200$ at these large distances.

Thus astronomers were faced with an unpleasant situation where they needed to be clever enough to infer the mass contribution of something which could not directly be measured, but can only be inferred by its influence on its surroundings. Only recently have technological advances in computing power and rapid advances in observing resources begun to resolve some of the tricky issues involved in this determination.

2.2 Measurement of H_0

An auxiliary but necessary step in determining the value of Ω is the measurement of the current value of the expansion rate, H_0. One of the primary goals of the Hubble Space Telescope (HST)[1] was to measure this value to within 10%, after decades of thunderous disagreement on the issue. The procedure was to use the HST to measure the apparent brightnesses of Cepheid variable stars, whose intrinsic brightness are known once their period of variability is established. The distance to these objects could then be estimated assuming

[1]The NASA/ESA Hubble Space Telescope is operated by AURA, Inc., under NASA contract NAS5–26555.

a geometric dilution of the detected flux. These were then used to zero-point other methods to determine the distances to galaxies, including the Tully–Fisher relationship (Sakai et al. 2000), Type Ia supernovae (Gibson et al. 2000), surface brightness fluctuation methods (Ferrarese et al. 2000), and the fundamental plane relating the physical parameters of elliptical galaxies (Kelson et al. 2000). This mission was initiated with the study of galaxy M18 (Freedman et al. 1994), and completed with a joint analysis of 25 galaxies, which established an array of distance markers out to 25 Mpc from the Milky Way (Mould et al. 2000).

This final analysis by Mould et al. (2000) yields $H_0 = 71 \pm 6\,\mathrm{km\,s^{-1}\,Mpc^{-1}}$. However, keeping the coals of controversy stoked, it must be noted that the analysis of the lightcurves of ~ 60 supernova (SN) by Phillips et al. (1999) yields a value for the Hubble constant of $H_0 = 63.3 \pm 2.2(\mathrm{internal}) \pm 3.5(\mathrm{external})\,\mathrm{km\,s^{-1}\,Mpc^{-1}}$. An additional analysis by Tonry et al. (2000) of Cepheid data and the statistics of surface brightness fluctuations finds $H_0 = 77 \pm 4(\mathrm{internal}) \pm 7(\mathrm{external})\,\mathrm{km\,s^{-1}\,Mpc^{-1}}$. However, it does seem fair to say that the value of the Hubble constant can be regarded as $H_0 = 70\,\mathrm{km\,s^{-1}\,Mpc^{-1}}$, to within 10%.

2.3 Measurement of Ω_{Baryon}

The first, and at this stage the only absolutely necessary, component of the Universe required in a mass inventory includes the familiar material of which we are made – the baryonic component of the mass density. Baryons are a class of massive particles called hadrons, itself a family of particles which experience the strong force (as opposed to leptons, like the electron, which do not). Baryons are constructed with 3 quarks and have $^1/_2$ integer spins. The most famous of baryons are the protons and neutrons, which make up the majority of the mass of Hydrogen and Helium (and all the remaining elements as well). These two elements in turn make up the extreme majority of the mass of stars, planets, and clouds of gas which we see as components of our and external galaxies. In fact, all measurements of the light content of galaxies are made using light emitted from baryonic components. Thus we have a very strong bias towards baryons when making astronomical measurements.

An global inventory of baryons has been undertaken by Fukugita, Hogan, & Peebles

(1998). They have combined multiple measurements of the mass–to–light ratios for typical components of galaxies. Most galaxies contain a spheroidal component, such as galactic bulges in spiral galaxies or the entirety of elliptical galaxies. These are generally older populations of stars, meaning they have had time to age and dim. Fukugita, Hogan, & Peebles (1998) find $\Upsilon_B \sim 6.5$ in stars and stellar remnants for this spheroidal component. For the disk components of spiral galaxies, which are generally younger and thus more luminous, they find $\Upsilon_B \sim 1.5$. Compared with the $\Upsilon_{B,\rm crit} = 1390h\,\Upsilon_\odot$ we can estimate

$$\begin{aligned} \Omega_{m,Spheroid\ \ stars} &\rightarrow 0.0026 \\ \Omega_{m,Disk\ \ stars} &\rightarrow 0.00086 \end{aligned} \tag{2.1}$$

This is disconcertingly small compared to the expected value of $\Omega = 1$. So the question must be posed : where are the rest of the baryons? It turns out most of the baryons are in fact NOT in stars, but in the form of X–ray detected plasma in groups and clusters of galaxies. This diffuse component is contained in the huge volume of these structures between the individual galaxies, and prevented from collapsing by gravitational heating leading to a hydrostatic equilibrium. A full accounting of the baryons by Fukugita, Hogan, & Peebles (1998) leads to an empirical range of $0.007 \lesssim \Omega_B \lesssim 0.041$, with a best estimate of $\Omega_B = 0.021$ for $h = 0.7$. Stars and remnants account for $\Omega_B = 0.0035$, which is only 17% of the baryon budget. The remainder are in hot, warm, and cold gases, neutral atomic gases, molecular clouds, and stellar remnants.

This appears to be a dire situation, where we can only directly account for 2% of the critical density of the Universe. However, a theory of nucleosynthesis has been developed which predicts the primordial abundances of light elements, which were formed seconds after the big bang. Comparison of this theory of Big Bang Nucleosynthesis (BBN) with the baryon inventory should indicate if there is a dark baryonic component to the Universe, whose presence we cannot directly infer by looking at the light content of Galaxies.

2.3.1 Big Bang Nucleosynthesis

The theory of big bang nucleosynthesis is used to predict the primordial abundances of the light elements Hydrogen (H), Helium (^{3,4}He), Deuterium (D) and Lithium (Li). To a very good approximation, there were the only elements created in the big bang. Important elements like Carbon and Oxygen are subsequently created as natural byproducts of stellar evolution.

The original abundances of all of these elements are functions of one parameter in this model, the baryon–to–photon ratio η. Measuring the primordial abundance of only one of the elements establishes the value of η, and thus reveals the primordial abundance of the others. The photon number is well known from measurements of the CMB, and thus an expected baryon mass density Ω_B can be established. However, it is quite difficult to measure these primordial values, since stellar processes are known to involve these elements, and thus can confound measurements of their initial values.

One method is to look at very metal–poor (old) stars, where the material the star is composed of is thought to have undergone very little processing since the big bang. The fewer heavy metals you find in stars (these metals are created in the same processes which alter the primordial element abundances) the closer the element distribution is to the primordial value. This is the technique used to estimate the primordial abundance of Lithium by Ryan et al. (2000), who look at the composition of very metal–poor stars to determine η, and estimate $\Omega_B = (0.025 - 0.057)h^{-1}$, or $\Omega_B = (0.036 - 0.081)$.

Another method is to look at very distant clouds of gas, which are themselves in a very early primordial state. These are seen at cosmological distances, and serve as a partial screen which absorbs background light. To penetrate this screen, very bright background sources are necessary. Quasars, the bright nuclei of galaxies, are routinely observed at high spectral resolution to determine the amount of absorption by Helium and Deuterium contained in these clouds of gas. A bayesian analysis of observations of Helium absorption by Hogan, Olive, & Scully (1997) yields a constraint on $\Omega_B h^2 \leq 0.013$, or $\Omega_B \lesssim 0.026$. However, the ideal baryometer is thought to be Deuterium, as there are no known astrophysical processes which actually produce Deuterium – it is always destroyed. Thus any measurement of the

Deuterium abundance is a lower bound to its actual, primordial abundance. Combined constraints on several analysis of Deuterium abundance yield $0.01 < \Omega_B < 0.05$ (Olive, Steigman, & Walker 2000).

While this range is very similar to the observed baryon budget of Fukugita, Hogan, & Peebles (1998), $\Omega_B = 0.021$, the upper end of this range does allow room for some sort of "dark" baryonic component. However, it appears unlikely that we are able to close the Universe with baryons. We next explore methods to ascertain less biased measurements of Ω_m.

2.4 Measurements of Ω_m

Various methods have been developed to infer the total amount of mass enclosed in a volume of space, without a baryon bias. This overall Ω_m is most easily measured where the matter has gravitationally clustered, requiring assumptions of varying validity to extrapolate to the average density of the Universe.

2.4.1 Rotation Curves of Spiral Galaxies

The most secure of these methods involves observations of one of the fundamental building blocks of the Universe, the spiral galaxy. The most widely used method involves measuring the rotation velocity as a function of galactocentric radius by using the doppler effect, which shifts the location of spectral features depending upon how fast the spiral disk is rotating. That is, the orbital velocity at each radius can be determined spectroscopically – since the orbits are essentially circular this gives a measure of the depth of the gravitational potential confining the components of the galaxy. If the mass distribution were spherical (in reality its somewhat flattened which only slightly modifies the following function), one can relate the mass enclosed $M(r)$ to the observed circular velocity $V_c(r)$

$$M(r) = \frac{rV_c^2(r)}{G} \tag{2.2}$$

In practice, one observes individual stars in the disk as far as possible, and beyond this various emission lines from gases, like the 21–cm neutral hydrogen line. Beyond the visible

portion of essentially *all* spiral galaxies, large circular velocities are observed for objects which appear to be gravitationally bound to it. There appear to be significant amounts mass beyond the observed stellar distribution supporting these high rotation velocities.

One example is shown in Figure 2.1, indicating the rotation curve of one of the more well studied galaxies, NGC 3198 (e.g. van Albada et al. 1985). The actual rotation curve as measured by Begeman (1989) and Corradi et al. (1991) is indicated with the filled and open circles, respectively. However, the rotation curve able to be supported by the observed stellar component is shown with the *short dashed* line, which is unable to support the rotation curve beyond a galactocentric radius of ~ 4 kpc. A second component must be inferred to support the rapid rotation of the disk at large galactocentric distances, which is indicated with a *long dashed* line. This is the dark matter distribution in the galaxy, which the lower panel indicates begins to dominate the mass of the system beyond ~ 12 kpc. The large amount of this "dark matter" compared to the stellar matter indicates it is unlikely to be all baryonic.

Persic, Salucci, & Stel (1996) have modeled the rotation curves of $\gtrsim 1000$ spiral galaxies with dark and luminous components. They find an empirical relationship indicating one parameter, the total luminosity of the spiral galaxy, may be used to infer the rotation curve V_c at any radius. This Universal Rotation Curve is shown in Figure 2.2 for galaxies of various intrinsic brightnesses, using 2 component models contributing to the rotational velocity. Persic, Salucci, & Stel (1996) find that the luminous matter is unable to support the rotation curve beyond R_{opt} (the radius encompassing 83% of the integrated light). Within R_{opt}, the dark matter comprises between 15% and 85% of the total mass of the brightest and faintest models, respectively. Beyond R_{opt}, the dark to visible density ratio is 15–30 times the ratio at R_{opt}. The minimum total mass fraction of the dark matter ranges between 50% and 95%. Thus dark matter is seen to dominate nearly all spiral galaxies, usually modeled as an elliptical component extending far beyond the visible edge of the spiral disk. This suggests dark matter is a fundamental component of the Universe, and not just an occasional accounting error.

2.4.2 Clusters of Galaxies

A more legitimate extrapolation is to extend the mass–energy density measured on $1h^{-1}Mpc$ scales to the overall density of the Universe. Clusters of galaxies are hundreds of times more massive and hundreds of times more voluminous than individual galaxies. The hope is that the range of dark matter contributions discovered in individual galaxies averages out on these large scales, and a global average can be ascertained. One difficulty in examining larger and larger scale structures is that the ensemble of measurements used to estimate the enclosed mass are generally evaluated in a statistical context. These analyses require a state of dynamical equilibrium which is invalid if the entire system is not virialized or relaxed. The largest structures are thought to be the youngest and still collapsing gravitationally. They are only now beginning the dissipative processes which bring the entire system into equilibrium. However, galaxy clusters are thought to a large degree to be virialized, and several techniques are employed to estimate their overall mass–energy density.

X-ray Observations

Within many galaxy clusters there resides a hot, X–ray emitting gas composed of fully ionized H and He. This gas undergoes hydrostatic heating by predominantly thermal pressure, and effectively is heated by the gravitational potential of the cluster. The surface brightness profile in X–rays allows a measurement of the heating gravitational potential required to support both the gas and galaxy distribution. This technique requires that the gas is in hydrostatic equilibrium.

As an example, Nevalainen, Markevitch, & Forman (2000) are able to constrain the gas fraction of the relaxed galaxy cluster A3571 to be $f_{gas} = 0.19^{+0.06}_{-0.03}h_{50}^{-3/2}$, with the majority of the rest of the cluster in an unseen dark component. They estimate an upper limit to the overall cosmological matter density $\Omega_m < 0.4$. Similar limits have been established using a collection of 36 X–ray clusters by Ettori & Fabian (1999).

Cluster Velocity Dispersions

The techniques of Zwicky have been continued into modern astronomy, and studies of cluster velocity dispersions now use hundreds of galaxies to trace the cluster potential. The virial mass of large galaxy clusters may be determined by the velocity dispersion of the galaxy components, in a manner similar to the study of Zwicky (1933). A study by Carlberg et al. (1996) of the velocity dispersion of thousands of individual galaxies contained in 16 galaxy clusters yields an average mass–to–light ratio in the K photometric passband of $295 \pm 53h\ \Upsilon_\odot$. For comparison, the local K–band mass–to–light ratio is ~ 1 (Binney & Merrifield 1998). Assuming that clusters of galaxies trace the mass of the Universe, Carlberg et al. (1996) find this indicates $\Omega_m = 0.24 \pm 0.05 \pm 0.09$ (random and systematic errors).

Large Scale Velocity Flows

The mass–energy density field on large scales can also be derived by modeling departures from the Hubble flow. Assuming clusters of galaxies are clustered no more than galaxies are clustered, this serves as a way to measure how different the clustering of light is (in galaxies) compared to the true clustering of mass. Tonry et al. (2000) have modeled the infall velocity departures from the Hubble flow due to the Virgo cluster of galaxies and the so–called Great Attractor. The GA, while much farther away than Virgo, is approximately 10 times heavier ($\sim 10^{16} \mathrm{M}_\odot$), and provides a non–negligible contribution to the velocity field. The model results in measurements of the masses of these clusters in terms of the overdensities of the enclosed masses with respect to the background δ. Tonry et al. (2000) find $\Omega_{m,Virgo} = 0.19\ \delta^{1.5}$ and $\Omega_{m,GA} = 0.14\ \delta^{1.5}$. Comparing the peculiar velocities in this survey with the distribution of galaxies in the IRAS flux–limited redshift survey, and making the explicit assumption that the IRAS survey is an unbiased tracer of the mass distribution, Blakeslee et al. (1999) find $\Omega_m = 0.24 \pm 0.05$.

2.4.3 Implications of Cluster Abundances

Finally, the evolution of cluster abundance as a function of redshift allows joint estimates of Ω_m and the amplitude of mass fluctuations leading to gravitational clustering σ_8, which are

degenerate when measuring the observed present–day abundance of rich clusters of galaxies. In high density ($\Omega_m = 1$) models, very few clusters ($\sim 10^{-5}$) are expected to be found at $z > 0.5$ because the evolution is so strong. Bahcall & Fan (1998) examine the abundance of massive clusters ($M \gtrsim 5 \times 10^{14} h^{-1} \mathrm{M}_\odot$) of galaxies at redshift $z > 0.5$ detected in X–ray surveys. They find even the existence of the single most distant cluster is a strong constraint. They exclude at high confidence $\Omega_m = 1$, and conclude $\Omega_m = 0.2^{+0.3}_{-0.1}$.

2.4.4 Super–clusters

The next structures larger than galaxy clusters are super–clusters, which contain $\gtrsim 1000$ times the volume of galaxy clusters. However, these structures are so large that they are not in equilibrium. Small et al. (1998) examined the Corona Borealis Supercluster – given its linear dimensions of $\sim 20 h^{-1} Mpc$, it is not known if the structure has yet begun to collapse. However, Small et al. (1998) estimate a total mass of this supercluster of $3 \times 10^{16} h^{-1} \mathrm{M}_\odot$, yielding a $\mathrm{B_{AB}}$–band mass–to–light ratio of $\Upsilon_B = 564 h\, \Upsilon_\odot$. A background supercluster was also detected, with $\Upsilon_B = 726 h\, \Upsilon_\odot$. The joint analysis of these 2 super–clusters yields $\Omega_m > 0.4$.

2.4.5 Strong Lensing

One of the least biased estimates of the mass in an enclosed region comes from the gravitational lensing technique. This takes advantage of a chance alignment of a background galaxy with a foreground mass distribution which may act as a lens, splitting the background galaxy into multiple images on the sky. The separation of pairs of images on the sky allows an estimate of the mass of the lens, although any lens asymmetry substantially complicates the modeling process.

The statistics of gravitational lens number counts is also important for cosmology. Since it takes both source and lens galaxies to form a lensing system, the number of expected chance superpositions can be calculated for different cosmologies. As an example, in a flat Universe with $\Omega_\Lambda = 0$, an order of magnitude fewer lensing configurations are expected compared to $\Omega_\Lambda = 1$.

Colley, Tyson, & Turner (1996) observed a system of images around the high redshift ($z = 0.39$) cluster 0024+1654, where detail in several of the images could be resolved. This allows an accurate reconstruction of the mass distribution. The most recent analysis of these data by Tyson, Kochanski, & dell'Antonio (1998) yields 8 resolved sub–images of the background galaxy. They are able to construct a high–resolution mass map of the lens out to $107h^{-1}$ kpc radius, and find a rest–frame V–passband $\Upsilon = 276 \pm 40h\,\Upsilon_\odot$. For comparison, $\Upsilon_{V,local} = 0.67\,\Upsilon_\odot$ (Binney & Merrifield 1998).

2.4.6 Weak Lensing

A mass concentration can also act as a weak gravitational lensing agent when the source is substantially mis–aligned with the lens. This lens induces a slight ellipticity in the source, but does not create multiple observable images. By looking at a collection of thousands of galaxies around the perimeter of galaxy clusters, one may be able to resolve this signature of weak lensing. However, there are imposing systematic errors associated with measuring the expected signal. Included in this are equipment–induced ellipticites, difficulties distinguishing between foreground stars and background galaxies, and uncertainty about the distance of the background galaxies which are being lensed.

The amplitude of this cosmic shear has recently been measured by Wittman et al. (2000) and Van Waerbeke et al. (2000), who observed blank fields on the sky to avoid known mass concentrations. Both groups find a weak lensing signal, although neither group is able to suggest a preferred cosmological solution. This method has also been used to measure the weak lensing contribution of a known X–ray cluster of galaxies, MS 1054–03 at a redshift of $z = 0.83$ (Luppino & Kaiser 1997). Within a $0.5h^{-1}$ Mpc aperture, Luppino & Kaiser (1997) find a the mass–to–light ratio is $\Upsilon_V > 350h\,\Upsilon_\odot$, or $\Upsilon_V = 580h\,\Upsilon_\odot$ if the mean redshift of the sheared galaxies is $z = 1.5$.

2.4.7 The Case for Non–baryonic Dark Matter

The ensemble of measurements above seem to suggest that the mass density of the Universe Ω_m is considerably less than 1, and at high confidence. Most measurements seem to suggest

a mass density of $\Omega_m \sim 0.3$, which while smaller than 1 is larger than $\Omega_B \sim 0.02$. This latter discrepancy is the crux of the dark matter problem. It appears baryonic material contributes only 10% of the mass of the Universe, meaning gravitational structures and galaxies are dominated by a form of matter we are not familiar with. However, the picture is not complete until we can measure the overall curvature of the Universe.

2.5 Measurements of Global Curvature $\Omega_m + \Omega_\Lambda$

Recall that the flat Universe $\Omega = 1$ is the theoretically preferred condition. It appears that the overall mass density is insufficient to close the Universe, so we must take seriously the possibility of a cosmological constant if we have any confidence in our ability to correctly model and understand the Universe (Equation 1.15 suggests radiation as a possible solution, but we can directly measure the temperature of the CMB in all directions, and it currently only accounts for an additional 10^{-5} to Ω). Since we have no means to directly measure the contribution of a dark energy Ω_Λ component, we must attempt to measure the overall curvature of the Universe, and infer the value of this component from the overall curvature.

The observables which are most sensitive to the overall curvature of the Universe are the angular scale of the fluctuations in the CMB. Any small perturbations in the very early energy density of the Universe are thought to have grown, from gravitational instability, into the large–scale structures we observe in the current Universe. These perturbations should be seen as peaks and dips (anisotropies) in the CMB, the residual radiation from that early epoch. The angular power spectrum of these anisotropies, measured in spherical harmonic amplitudes, provides a very sensitive measure of the initial conditions in the Universe. Acoustic oscillations in the early Universe lead to a wealth of structure encoded in the power spectrum which depends upon $\Omega_m + \Omega_\Lambda$.

A complimentary study of these parameters may be undertaken by not just measuring the expansion velocity of the Universe, but its acceleration or deceleration. This may be done with observations of very distant supernova, whose brightness may be seen across cosmological distances. The intrinsic brightness of the SN event is thought to be known, and its distance can be inferred by observing its redshift using Equation 1.12. The most distant

SN can be used to measure the linearity of Equation 1.12 – any systematic apparent dimming (or brightening) of these objects about their expected brightnesses yields a measure of the acceleration (or deceleration) of the Universe. The deceleration parameter is represented as a function of $\Omega_m - \Omega_\Lambda$. Thus the CMB and SN experiments constrain both bases in the $(\Omega_m, \Omega_\Lambda)$ plane, and provide a powerful constraint on cosmological parameters when taken together (Eisenstein, Hu, & Tegmark 1999).

Multiple teams have begun the study of SN lightcurves to constrain the deceleration parameter by observing high redshift SN. This includes the Supernova Cosmology Project (Perlmutter et al. 1999) and the High–z Supernova Search Team (Garnavich et al. 1998). Both groups find that the Universe is not decelerating in its expansion, which would be expected if Ω_m dominated the Universe given gravity's inherent attractive nature, but is in fact accelerating! This was a completely unexpected result, and indicates some sort of vacuum energy driving the expansion, analogous to inflation but with a lower amplitude. Garnavich et al. (1998) find evidence for a spatially flat Universe, $\Omega = \Omega_m + \Omega_\Lambda = 0.94 \pm 0.26$. The data of Perlmutter et al. (1999) are strongly inconsistent with a $\Lambda = 0$ flat cosmology. Their confidence limits for a flat cosmology indicate $\Omega_m = 0.28^{+0.09}_{-0.08}(internal)^{+0.05}_{-0.04}(external)$, or $\Omega_\Lambda \sim 0.7$. Figure 2.3 illustrates the constraints on $(\Omega_m + \Omega_\Lambda)$ from Perlmutter et al. (1999). Note the confidence contours are oriented perpendicular to the diagonal line indicating a flat Universe.

Measurements of the CMB have recently entered the small angular scale regime where interesting information about the global curvature resides. The early large–scale experiments, such as COBE (Bennett et al. 1996a), and the recent experiments such BOOMERanG (de Bernardis et al. 2000) and MAXIMA–I (Hanany et al. 2000), may be combined to yield the power spectrum out to several hundred Legendre multipoles. The combined analysis of these data by Jaffe et al. (2000) yields impressive (95% confidence limits) constraints on the overall density of the Universe $\Omega_m + \Omega_\Lambda = 1.11^{+0.13}_{-0.12}$, as well as the baryon density $\Omega_B = 0.032^{+0.005}_{-0.004}$. Figure 2.4 shows the results from the combined analysis of COBE, BOOMERanG, and MAXIMA–I, expressed in the $(\Omega_m, \Omega_\Lambda)$ plane. The shaded regions parallel to $\Omega = 1$ are the confidence contours using CMB data alone, and the SN data are also plotted to illustrate their complimentary nature. The bold regions represent a joint analysis

of the CMB+SN data, and are suggestive of a closed Universe.

2.5.1 The Case for Dark Energy

Not only is there thought to be significant amounts of dark matter, represented in the difference between $\Omega_m \sim 0.3$ and $\Omega_B \sim 0.02$, but it also appears likely that we live in a flat Universe with $\Omega = 1$. This indicates a dominant component of the Universe in a form which behaves like a cosmological constant, $\Omega_\Lambda \sim 0.7$.

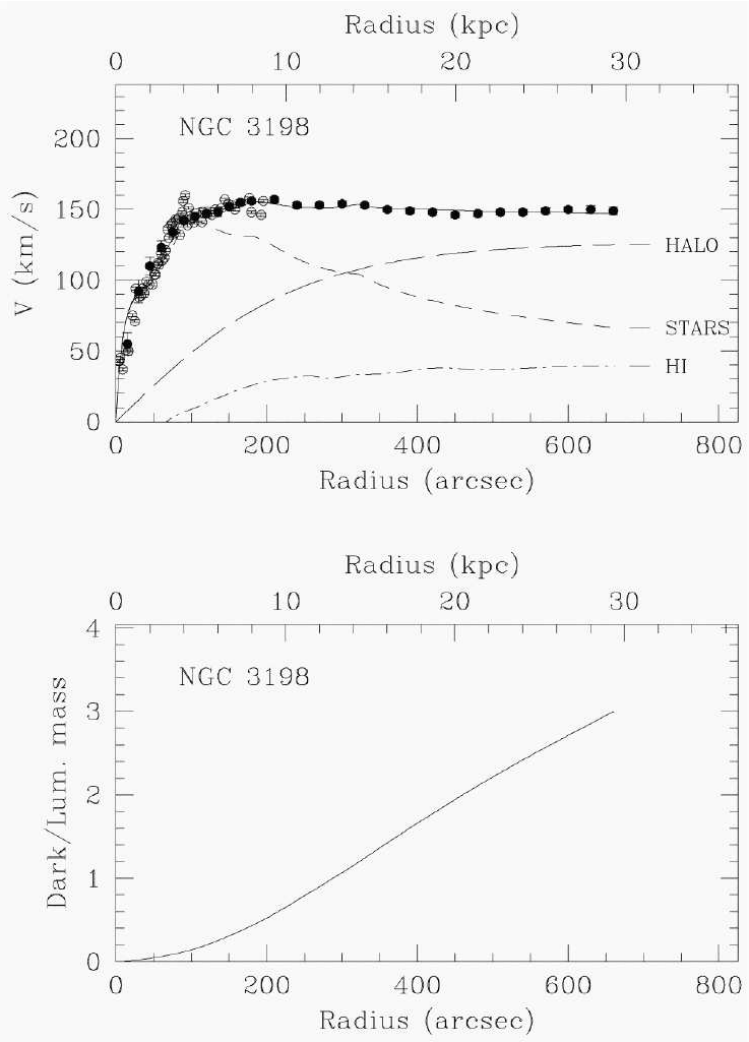

Figure 2.1:
The rotation curve of galaxy NGC 3198 is plotted in the top panel, as a function of galactocentric radius. The *short dashed* line labeled "Stars" represents $M(r)$ extrapolated from the light distribution in the galaxy, and translated into $V(r)$ from Equation 2.2. This is the expected rotation curve supported by the mass in luminous matter. The *solid* line represents $V(r)$ measured directly from spectroscopic doppler shifts of H I (filled circles) (Begeman 1989) and H α (open circles) (Corradi et al. 1991) lines. The *long dashed* line represents the extra "dark" mass, over and above the known luminous mass, needed to support the observed rotation curve. This is modeled as a spherical halo component, which quickly dominates the overall mass of the galaxy, as seen in the lower panel. Figure from Blais-Ouellette et al. (1999)

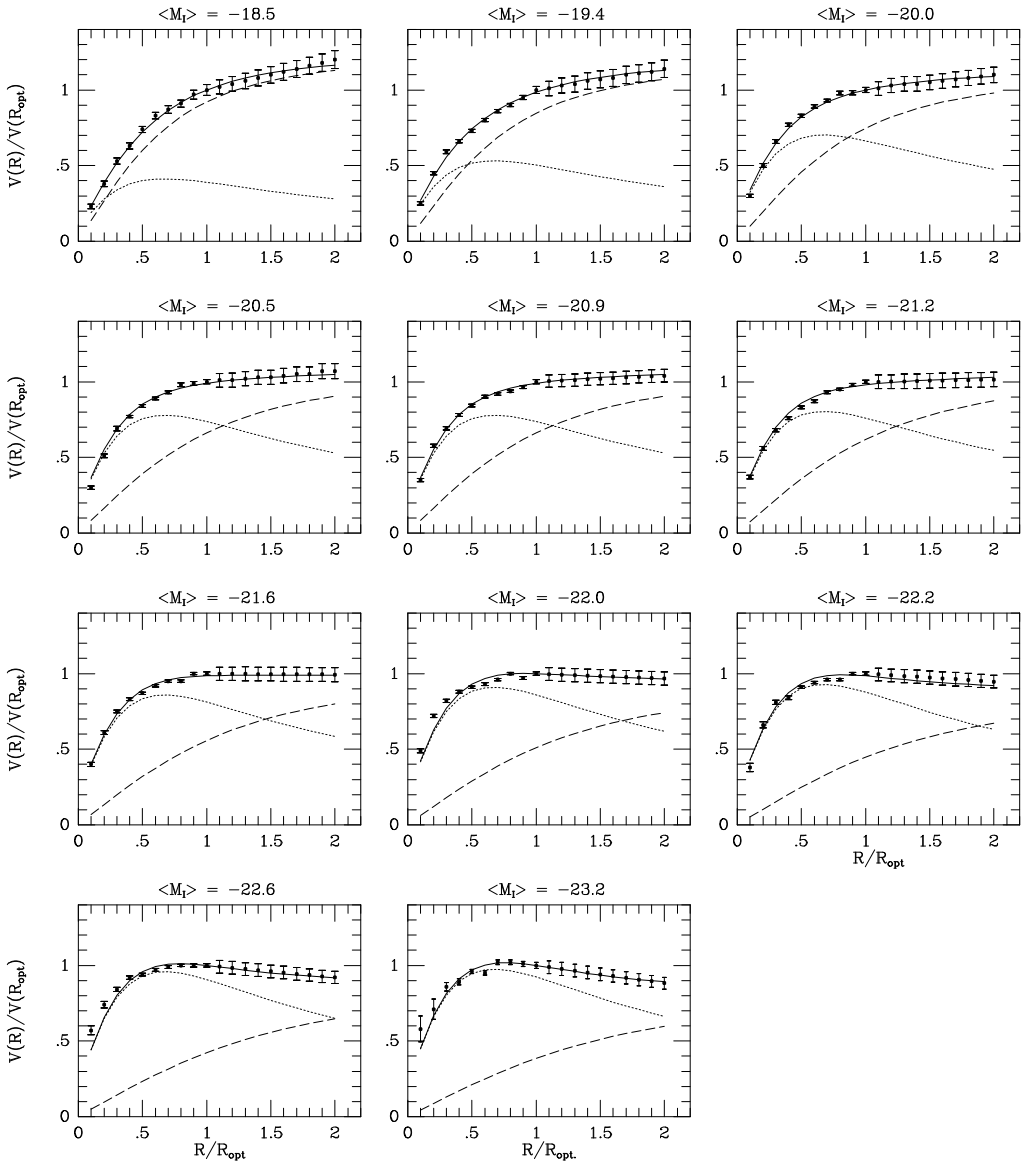

Figure 2.2:
Each panel represents a slice of the Universal Rotation Curve (URC) of Persic, Salucci, & Stel (1996) for a given host galaxy intrinsic brightness $< M_I >$. The data points represent averages of hundreds of rotation curves for each $< M_I >$. The *solid* line represents the URC slice. The *dotted* line is the typical contribution from known (luminous) matter, such as stars and gases, while the *dashed* line illustrates the contribution from the "dark" component needed to reconcile the observed rotation curve with the expected *dotted* line. In all cases, dark matter dominates the dynamics of the system beyond a certain galactocentric radius. Figure from Persic, Salucci, & Stel (1996).

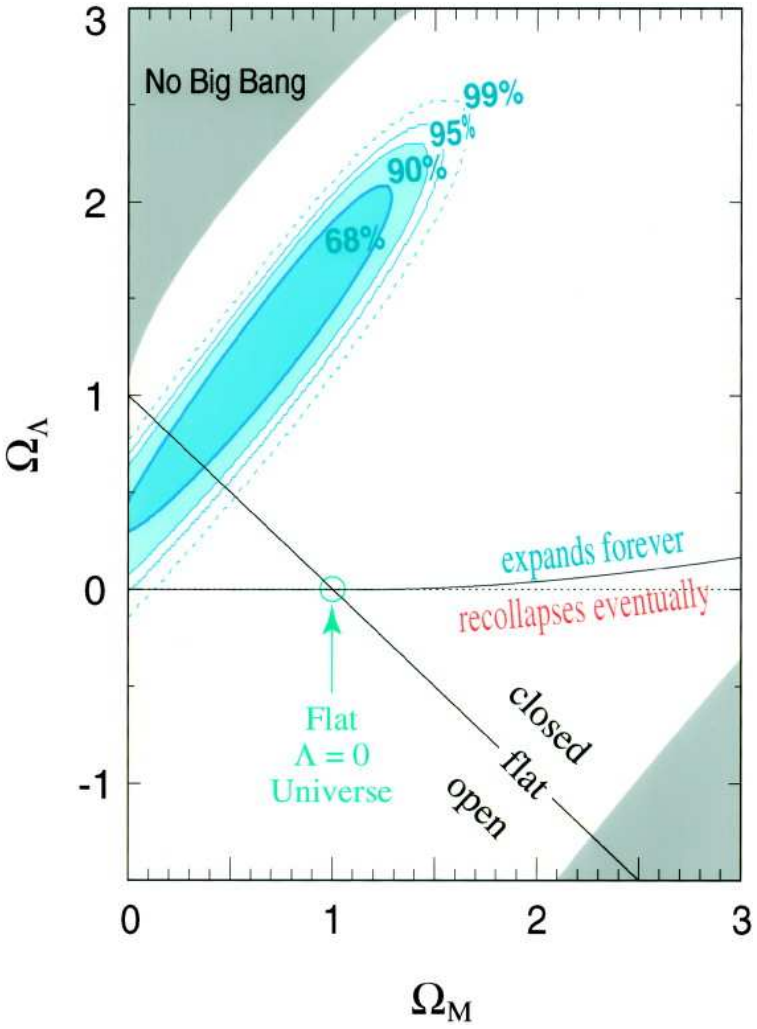

Figure 2.3:
The elliptical regions define the best–fit confidence regions in the (Ω_m, Ω_Λ) plane from the analysis of 42 type Ia supernova by Perlmutter et al. (1999). The ellipses contain 68%, 90%, 95%, and 99% of the likelihood of the current cosmological parameters. These ellipses are orthogonal to the line $(\Omega_m + \Omega_\Lambda) = 1$, indicating they more strongly constrain the orthogonal basis $(\Omega_m - \Omega_\Lambda)$. Note the Universe is expected to expand forever, but the overall topology is not yet determined. These ellipses are consistent with a flat Universe where $\Omega_m = 0.28^{+0.09}_{-0.08}$. The theoretically preferred model ($\Omega_\Lambda = 0$, $\Omega_m = 1$) is excluded at high confidence. Figure from Perlmutter et al. (1999).

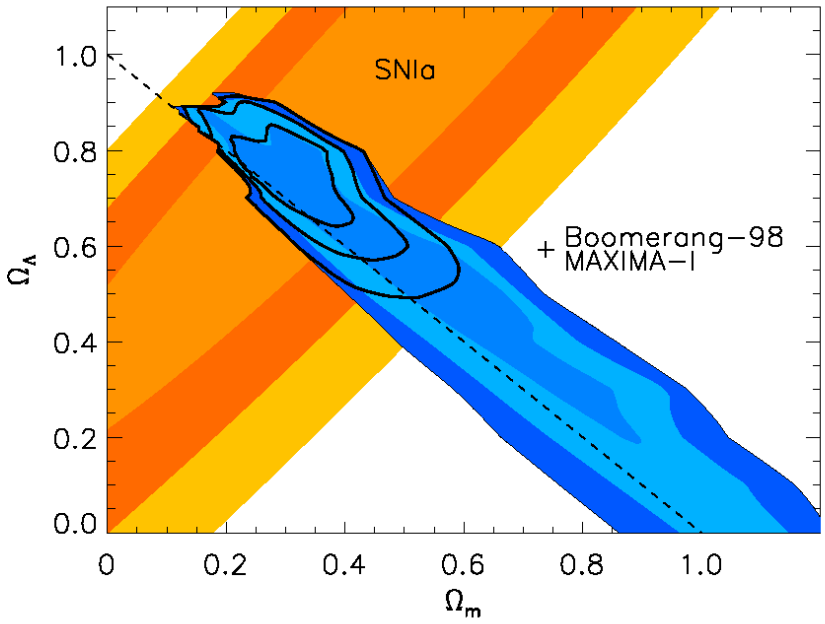

Figure 2.4:
Cosmic microwave background (CMB) constraints on the cosmological parameters Ω_m and Ω_Λ. Power spectra from the COBE–DMR (Bennett et al. 1996a), BOOMERanG–B98 (de Bernardis et al. 2000), and MAXIMA–I (Hanany et al. 2000) experiments were jointly analyzed to ascertain the angular scale of early density perturbations as seen on the sky, a measurement of the global topology of the Universe. The sensitivity of these measurements to the overall curvature may be seen by noting the elongation of the confidence limits along the $(\Omega_m + \Omega_\Lambda) = 1$ direction. The shaded regions define $1, 2$, and $3 - \sigma$ confidence limits, and the orthogonal regions are SN Ia constraints, similar to Figure 2.3. The bold contours arise from a joint analysis of the SN and CMB data. Figure from Jaffe et al. (2000).

Chapter 3

GRAVITATIONAL MICROLENSING

3.1 The Gravitational Lensing Effect

The study of the gravitational lensing effect uses astronomical sources to backlight a foreground mass distribution. If this mass distribution contains a dark matter component in the form of compact objects – collectively known as Machos, or Massive Compact Halo Objects – gravitational lensing events may occur. Lensing occurs due to the bending of light rays by gravity, and observable effects are very well described by the weak field, small angle limit of the gravitational scattering of photons.

Figure 3.1 demonstrates a typical lensing system. Since lensing deflection angles are generally extremely small, we can represent each circle by its tangent plane for our approximation. In Figure 3.1, the original source location on the sky is represented by the angle β from the observer–lens optical axis. In the presence of the lens, an image is seen at angle θ. Equivalently, evaluated in the source plane the source is originally at location $\vec{\eta}$ from the optical axis, and the resulting image would be at position $\vec{\eta} + \vec{\delta\eta}$. However, the lensing system is traditionally evaluated in the lens plane. Here the source is originally at $\vec{s}$ from the optical axis, and the image is seen at $\vec{i}$, which represents the impact parameter of the light that is deflected towards the observer.

Given the assumptions of a point–mass lens and a point source, the microlensing system is fully described by the lens equation (e.g. Refsdal 1964; Schneider, Ehlers, & Falco 1992)

$$\begin{aligned} \vec{s} &= \vec{i} - D_s\, x(1-x)\, \hat{\alpha}(\vec{i}) \\ \vec{s} &= \vec{i} - R_{\rm E}^2 \frac{\vec{i} - \vec{l}}{(\vec{i} - \vec{l})^2}\ , \end{aligned} \tag{3.1}$$

where $\vec{s}$, $\vec{i}$, and $\vec{l}$ are the positions of the source, image, and lens, projected along the line

of sight into the lens plane. D_s and D_l are the distances between observer and source, and observer and lens, and the fractional distance to the lens $x \equiv D_l/D_s$. The lensing deflection angle is given by

$$\hat{\alpha} \quad = \quad \frac{4GM_l}{c^2}\frac{\vec{i}-\vec{l}}{(\vec{i}-\vec{l})^2}\,. \tag{3.2}$$

Here M_l is the mass of the lensing object, and G is the Newtonian gravitational constant. Since gravity is known to act on massive bodies, and photons are massless, the only way to deflect photons is to distort the medium in which they are traveling. This is the favored interpretation of gravity – that it is a measurable consequence of the distortion of space–time by a massive body.

Finally, $R_{\rm E}$ refers to the "Einstein ring radius" given by

$$R_{\rm E}^2 \equiv \frac{4GM}{c^2}D_s x(1-x) \tag{3.3}$$

which is a natural distance scale in the lens plane.

If we define the origin of the lens plane as the position of the lens ($\vec{l}=0$), then Equation 3.1 indicates $\vec{i} \,||\, \vec{s}$. This symmetry allows two images during a lensing event. There is actually a third image of negligible magnification that can be found if we give the lens a finite extent, or if we depart from the weak field approximation. In the case of a non–zero $\vec{s}$, solving the lens equation for $\vec{i}$ yields two images whose positions in the lens plane are

$$\left(\frac{\vec{i}}{R_{\rm E}}\right)_{\pm} = \frac{\vec{u}}{2}\left(1 \pm \sqrt{1+\frac{4}{u^2}}\right). \tag{3.4}$$

Here, $\vec{u} = \vec{s}/R_{\rm E}$ is the source location in the lens plane, in units of $R_{\rm E}$. This also represents the lens impact parameter. A lens with impact parameter $\vec{s} = \vec{u} = 0$ will not distort the source into 2 images, but instead an "Einstein ring" of radius $R_{\rm E}$.

The action of the lens is to map the coordinates of the source onto 2 locations on the sky. Figure 3.2 illustrates the action of this mapping on an arbitrary–sized region. The lens object is located at coordinates (0,0). $R_{\rm E}$ is indicated, and sets the scale for the lensing effect. The original "Source" region is, under the influence of lensing object, mapped to two

locations, labeled "Image$_+$" and "Image$_-$". The major image is located outside $R_{\rm E}$, and a minor image is inside $R_{\rm E}$.

3.1.1 Source Magnification

If the source is an astronomical object, its apparent brightness is proportional to its surface area on the sky. Since this coordinate mapping is seen to distort the shape of the lensed object, seen in Figure 3.2, the brightnesses of the images are expected to be different than the source brightness. The lensing effect conserves surface brightness, hence the magnification[2] of the source is determined by diving the surface area of the image by the original surface area of the source region. This area ratio is equivalent to a flux ratio for an object with constant surface brightness.

The magnification of each image (the area distortion caused by the mapping) can be found through the determinant of the Jacobian of the coordinate mapping $\vec{i} \rightarrow \vec{s}$. Explicitly,

$$A_{\pm} = \left| \frac{\delta \vec{s}}{\delta \vec{i}} \right|^{-1} . \tag{3.5}$$

The magnification of the primary image alone is always greater than 1, and as the lens moves away from the source, this image returns to the natural source position and dimensions. The secondary image is associated with the lensing object, and as the lens moves away from the source the surface area of this image converges to zero size, and the location converges to the position of the lens. Hence the intervention of the lens adds a second image, and distorts the original source. The overall magnification of the source is always greater than 1. It is interesting to note that every source on the sky is lensed to some degree by every lens on the sky.

One may note that if this determinant in Equation 3.5 disappears, the magnification factor (the inverse of this determinant) formally diverges. The regions in the source plane for which this occurs are known as "caustics" – in the lens plane they are known as "critical curves". For a point lens, a point caustic occurs at the projected location of the lens – that

[2]The term "magnification" is preferred over the term "amplification" even though the traditional symbol for the brightening is "A". The former implies something acting upon the source, itself a passive participant in such a spectacular demonstration of gravitational physics.

is, when the lens passes directly over the source, the source is mapped into an Einstein ring with (formally) infinite magnification. This magnification factor only diverges for a pure point source, which serves as a common assumption in modeling microlensing lightcurves. A realistic extended source limits the maximum magnification factor. For a binary lens, the caustics are extended, closed curves.

3.1.2 Microlensing Limit

It is useful to estimate the typical separation of the images by estimating the angular size of the Einstein ring on the sky. For sources located in the Galactic bulge at 8 kpc, lensed by a Galactic disk lens at half the source distance, typical $R_{\rm E}$ and image separation values are

$$\begin{aligned} R_{\rm E} &\sim 4\left(\frac{M}{M_\odot}\right)^{1/2}\left(\frac{D_l}{4\,{\rm kpc}}\right)^{1/2}{\rm AU} \\ \theta_{\rm E} &\sim 1\times 10^{-3}\left(\frac{M}{M_\odot}\right)^{1/2}{\rm arcsec.} \end{aligned} \tag{3.6}$$

For a source in the LMC, at 50 kpc, a typical lens would be located about 10 kpc along the line of sight, and

$$\begin{aligned} R_{\rm E} &\sim 8\left(\frac{M}{M_\odot}\right)^{1/2}\left(\frac{D_l}{10\,{\rm kpc}}\right)^{1/2}{\rm AU} \\ \theta_{\rm E} &\sim 0.8\times 10^{-3}\left(\frac{M}{M_\odot}\right)^{1/2}{\rm arcsec.} \end{aligned} \tag{3.7}$$

The estimate that the images are separated by only milli–arcseconds means that we are currently not able to resolve these images from the ground. The images are smeared together into a single object by the turbulent motions of the Earth's atmosphere, and we are only able to observe the overall brightening of the source due to the combination of image brightnesses. The term "microlensing" applies to this limit of the strong lensing effect where the image separation is *milli* to *micro* arcseconds.

For an object to act as a lens and not as an occulting body, it should have a physical size less than $R_{\rm E}$. Thus a Galactic disk lens weighing $1\,M_\odot$ should have a linear size less than

$\sim$ 4 AU. This is reasonable for a typical stellar object – for instance our Sun has a radius of only 0.005 AU. It is also worth mentioning the validity of a point source assumption in microlensing lightcurves. The angular radius of the lensed source star should be considerably smaller than the angular radius of the Einstein ring to prove an appropriate assumption. A quick check of the angular radius of the Sun at Galactic bulge and LMC distances (0.6 and 0.09 *micro* arcseconds) indicates this is indeed generally a valid assumption.

3.2 Modeling of the Microlensing System

The orbital motion of the sources, lenses, and observer(s?) in the Galactic potential implies that the lensing system is constantly in motion. The brightening of the source due to the intervening lens is therefore a function of time. We define the microlensing model below as a function of 3 lensing parameters, and 1 practical consideration.

3.2.1 $u_{\rm min}$: Minimum Impact Parameter

The observed magnification of the source is purely a function of the lens impact parameter, represented by u. The sum of the brightnesses of the two images, evaluating Equation 3.5, is

$$A = \frac{u^2 + 2}{u\sqrt{u^2 + 4}}. \tag{3.8}$$

When the source passes within the lens' Einstein radius ($u = 1$), it is magnified by a factor of $A = 1.34$. The lens' circularly symmetric isomagnification contours are unevenly spaced in u, rising rapidly like $A \propto 1/u$ near the location of the lens. All values of the minimum impact parameter $u_{\rm min}$ are equally likely, implying high–magnification events are less likely than low magnification events. Isomagnification contours are represented by the *dotted* circles in Figure 3.3. Note, this parameter does not contain any useful information about the properties of the lens itself.

3.2.2 t_0: Time of Maximum Magnification

This represents the time at which the event is at maximum magnification, or minimum impact parameter $u = u_{\rm min}$. This parameter should be distributed randomly in time, and also does not contain information about the lensing system.

3.2.3 $\widehat{t}$: Event Timescale

Parameter $\widehat{t}$ represents the time it takes the lens to move a distance equal to its own Einstein diameter ($2R_{\rm E}$). This may be put in terms of the lens' transverse velocity $v_\perp$, so that $\widehat{t} = 2R_{\rm E}/v_\perp$ (note this can also be put in terms of the lens proper motion $\widehat{t} = 2\ \theta_{\rm E}/\mu$). Since $R_{\rm E}$ is itself a function of lens parameters M_l and D_l, we find that $\widehat{t}$ is a degenerate combination of all properties we would like to know about the lensing system (mass M_l, distance D_l, and transverse velocity $v_\perp$). Without additional information, it is impossible to uniquely characterize any particular microlensing object. This indicates a continuum of lens parameters which can conspire to produce similar duration microlensing events.

3.2.4 f: Blending

The effective index of refraction of the gravitational lensing potential is not a function of wavelength, meaning a lensed object should be magnified by the same amount in all colors. However, since most microlensing observations are made in crowded fields, it is highly likely that within a typical atmospheric seeing disk ($\sim 1''$) there are multiple sources. Note, one lens is generally unable to simultaneously lens multiple objects in a seeing disk, since the lensing scale is $\sim 0.001''$. The observed magnification of an object must therefore be practically modeled as having a fraction f of the light lensed and the remainder in unlensed light. This unlensed light may be from neighboring sources, or from the lens itself in cases where the lens is not completely dark. Equation 3.8 must be modified to

$$A_{observed} = f \times \frac{u^2+2}{u\sqrt{u^2+4}} + (1-f). \tag{3.9}$$

3.2.5 Microlensing Lightcurve

The motion of the lensing object past the source is assumed to be rectilinear, ignoring non–inertial terms such as the Earth's orbit around the Sun. The distance traversed by the lens in the time t, scaled by $R_{\rm E}$, can be represented as $u_{motion} = t\ v_\perp / R_{\rm E}$. We wish to add in quadrature this scaled distance due to the lens motion to the minimum impact parameter, to determine the actual impact parameter of the lens as a function of time. Since $u = u_{\rm min}$ when $t = t_0$, we find for the lens impact parameter

$$u(t) = \sqrt{u_{min}^2 + (v_\perp (t - t_0)/R_{\rm E})^2}; \qquad u(t) = \sqrt{u_{min}^2 + (2(t - t_0)/\widehat{t})^2}. \tag{3.10}$$

Brightening profiles of the source star, $A\left(u(t, \widehat{t}, t_0, u_{\rm min})\right)$, are shown in Figure 3.3 for various minimum impact parameters. The top schematic represents the linear trajectories of the source through the lens' isomagnification contours, which are represented by the *dotted* circles. The outer *dashed* isomagnification contour corresponds to $A = 1.34$, or $u = R_{\rm E}$. The resulting microlensing lightcurves are shown below. Note the maximum magnification is larger the closer the lens' approach to the source. The maximum magnification is formally divergent for the *dotted–dashed* trajectory, which has $u_{\rm min} = 0$. Note the source passes within $R_{\rm E}$ ($u = 1$) at the time $t = t_0 - \widehat{t}/2$ and leaves at time $t = t_0 + \widehat{t}/2$.

3.3 Microlensing Optical Depth

The fraction of the sky along a line–of–sight covered by microlenses, called the optical depth τ, can be calculated in a straightforward manner. The optical depth can also be considered the expected number of lenses within one Einstein radius of a line–of–sight.

A microlensing event is defined as when a lens comes within $R_{\rm E}$ of a source, so the total area on the sky covered by a particular microlens is $\pi R_{\rm E}^2$. This value should be integrated over lens distances dD_l, or $D_s dx$, weighted by the density of lenses n. The optical depth is then

$$\tau = \int_0^{D_s} \pi R_{\rm E}^2\ n(D_l)\ dD_l. \tag{3.11}$$

Since $R_{\rm E}^2 \propto M$ and $n = \rho/M$, the product $R_{\rm E}^2 \times n$ is independent of the mass spectrum of the lenses, depending only on the density profile. Therefore, τ can be calculated as

$$\tau = \frac{4\pi G}{c^2} D_s^2 \int_0^1 \rho(x) x(1-x) dx. \tag{3.12}$$

Given a particular model of the Galaxy, one can evaluate the expected optical depth through the density distribution. A model of the Galactic–LMC system (Griest 1991) yields $\tau_{LMC} \sim 4.3 \times 10^{-7}$, meaning less than one star in a million will be magnified by $A > 1.34$ at any given moment. Microlensing surveys must then monitor literally millions of stars on a nightly basis to provide reasonable sensitivity to this effect. This also implies that for any given star the likelihood of being lensed is τ, or a likelihood of τ^2 for it to be lensed twice. Thus the gravitational microlensing signature must be a unique feature in the source's lightcurve.

Reviews of the state of the field of gravitational microlensing are presented in Gould (1996) and Paczynski (1996).

3.4 Constraining the Lens Proper Motion μ

In certain instances, it is possible to resolve deviations from the point source, point lens, inertial motion lightcurve presented in Figure 3.3. These deviations are present to some degree in each microlensing lightcurve, but are for the most part present at levels below the precision of astronomical measurements, and therefore undetectable. These involve the violation, to some degree, of various assumptions made above in the formulation of the generic microlensing lightcurve.

These "exotic" microlensing events allow more stringent constraints on the lens parameters. Characterization of these secondary effects involves an additional parameter in the representation of the source magnification, which enters as a fraction of $R_{\rm E}$, and is in principle a measurable quantity. Examples include the angular radius of a source star (extended source effects, explained in detail in Chapter 6 and also important in certain cases of binary microlensing, Chapter 7), the angular size of the semi–major axis of a binary source system (Chapter 8), and the angular size of the Earth's semi–major axis (parallax effects,

Chapter 5).

Each of these yields a measurement of the lens proper motion μ, once the physical system characterizing the additional fit parameter is known. The two constraints (μ and $\widehat{t}$) on the three lens parameters allows one a one–to–one relationship between the lens mass and distance. With a plausible model of the galaxy, one may extract a most likely lens mass and distance, given this measurement of the lens proper motion.

3.4.1 Measurement of $\widehat{v}$

In the case of extended source and binary source effects, the additional measured quantity is the velocity of the lens projected back to the source plane $\widehat{v}$. This is represented as $\widehat{v} \equiv \mu\ D_s = v_\perp / x$, and with the substitution of $R_{\rm E} = \widehat{v}\ x\ \widehat{t}/2$ into Equation 3.3 we find

$$M(x) = \frac{\widehat{v}^2\ \widehat{t}^2\ c^2}{16\, G D_s} \frac{x}{1-x}. \tag{3.13}$$

We may obtain additional constraints on x by using a model for the distributions of sources and lenses, since the likelihood of obtaining the observed value of $\widehat{v}$ is also a function of x.

For given lens mass, the rate of microlensing is proportional to

$$d\Gamma \propto \sqrt{x(1-x)}\, \rho_L(x)\, v_\perp f_S(\mathbf{v}_S)\, f_L(\mathbf{v}_L)\, dx\, d\mathbf{v}_S\, d\mathbf{v}_L. \tag{3.14}$$

where ρ_L is the density of lenses at distance x, $f_L(\mathbf{v}_L)$ and $f_S(\mathbf{v}_S)$ are the lens and source velocity distribution functions (normalized to unity) in the plane perpendicular to the line of sight. The source and lens velocities $\mathbf{v}_S, \mathbf{v}_L$ are related to $\widehat{\mathbf{v}}$ by $\mathbf{v}_L = (1-x)\mathbf{v}_\odot + x(\mathbf{v}_S + \widehat{\mathbf{v}})$, where $\widehat{\mathbf{v}} = (\widehat{v}\cos\phi, \widehat{v}\sin\phi)$ and ϕ is the (unknown) direction of the relative proper motion.

Given a model for ρ_L, f_S, f_L, we may integrate Equation 3.14 and thus obtain joint probability distributions for any of the variables. Since we have measured $\widehat{v}$, and the lens mass depends on only one unknown (x), we need to consider the joint probability distribution of events in the $(x, \widehat{v})$ plane, and then marginalize to get a probability distribution of x given the observed value of $\widehat{v}$.

Thus, we change variables from $d\mathbf{v}_L$ to $d\widehat{v}\,d\phi$, giving

$$d\Gamma \propto \sqrt{x(1-x)}\,\rho_L(x)\,v_\perp f_S(\mathbf{v}_S)\,f_L(\mathbf{v}_L)\,dx\,d\mathbf{v}_S\left|\frac{\partial \mathbf{v}_L}{\partial(\widehat{v},\phi)}\right| d\widehat{v}\,d\phi. \tag{3.15}$$

We then substitute for $\mathbf{v}_L$ and $v_\perp$ and integrate over the unknowns $\mathbf{v}_S$ and ϕ, giving a likelihood as a function of distance for a given $\widehat{v}$,

$$\mathcal{L}(x;\widehat{v}) = \left.\frac{d\Gamma}{dx d\widehat{v}}\right|_{\widehat{v}} \propto \sqrt{x(1-x)}\,\rho_L(x)\,\widehat{v}^2\,x^3 \times \int\int f_S(\mathbf{v}_S)\,f_L\left((1-x)\mathbf{v}_\odot + x(\mathbf{v}_S+\widehat{\mathbf{v}})\right)\,d\mathbf{v}_S\,d\phi. \tag{3.16}$$

This result may be understood as follows: the integrals are over all combinations of source and lens velocity which give rise to the observed $\widehat{v}$. The $\sqrt{x(1-x)}$ and ρ_L terms arise from the x–dependence of the Einstein radius and density of lenses, respectively. There is a factor of $v_\perp = \widehat{v}x$ because a given lens contributes a lensing rate $\propto v_\perp$, and a factor of $x^2\widehat{v}$ from the Jacobian $\det(\partial\mathbf{v}_L/\partial(\widehat{v},\phi))$.

To evaluate Equation 3.16, we must adopt models of the LMC and Milky Way Galaxy.

- For microlensing events towards the Galactic bulge, we assume a disk velocity dispersion of 30 km s^{-1} in each direction, with a flat rotation curve of 220 km s^{-1}. We adopt a bulge velocity dispersion of 80 km s^{-1} in each direction, and no bulge rotation. For the density profiles, we use a standard double–exponential disk, and a barred bulge as in Han & Gould (1995). We assume the source is a member of the bulge, so we take f_S to be the above velocity distribution function of bulge stars, and then we evaluate Equation 3.16 separately for ρ_L, f_L appropriate for lenses either in the disk or the bulge.

- For events towards the LMC, the Galactic halo is represented by Model S of Alcock et al. (1997a), where assume ρ_L is a 'standard' isothermal sphere with core radius 5 kpc. Distribution f_L is a Gaussian with zero mean, and velocity dispersion 155 km s^{-1} in each component. The LMC is represented by the preferred model of Gyuk, Dalal, & Griest (2000), with a scale–height of 300 pc, tilt of 30 deg from face–on, central surface density of 190 $M_\odot$/pc^2, and the source is assumed to be 1 scale height behind the midplane. The Solar velocity in Galactic X, Y, Z is $(9, 231, 16)$ km s^{-1}, while the

LMC velocity is (53, –160, 162) $\mathrm{km\,s^{-1}}$, with isotropic random velocities of 22 $\mathrm{km\,s^{-1}}$ (e.g., Graff et al. 2000) in each direction. For a LMC halo component, we assume a similar profile to the Galactic halo, with a central density of $0.0223\mathrm{M}_{\odot}$, core radius of 2 kpc, and velocity dispersion of $50\,\mathrm{km\,s^{-1}}$. We truncate this halo at 11 kpc.

- For events towards the SMC, we use the same Galactic model as above. Distribution f_S is a Gaussian with velocity dispersion of $30\,\mathrm{km\,s^{-1}}$ in each component, centered on the SMC mean velocity, which is taken as the projection of $(U, V, W) = (40, -185, 171)\,\mathrm{km\,s^{-1}}$ onto the plane normal to the line of sight (Gardiner & Noguchi 1996).

3.4.2 Measurement of $\tilde{v}$

Measurement of the parallax effect involves a projection of the lens' Einstein ring to the solar position, leading to a measurement of the lens velocity projected to the solar system $\tilde{v}$. Its representation is similar to $\widehat{v}$: $\tilde{v} \equiv \mu D_l/(1-x) = v_\perp/(1-x)$. The mass–distance relationship involving the measurement of $\tilde{v}$ is

$$M(x) = \frac{\tilde{v}^2\ \widehat{t}^2\ c^2}{16\,GD_s}\frac{1-x}{x}. \tag{3.17}$$

Note, Equation 3.17 is very similar to Equation 3.13, with $\widehat{v} \leftrightarrow \tilde{v}$ and $x \leftrightarrow 1-x$.The likelihood function to evaluate is of the form

$$\mathcal{L}(x;\tilde{v}) \propto \sqrt{x(1-x)}\,\rho_L(x)\,\tilde{v}(1-x)^3 \times \int f_S(\mathbf{v}_S)\, f_L\left((1-x)(\mathbf{v}_\odot + \tilde{\mathbf{v}}) + x\mathbf{v}_S\right) d\mathbf{v}_S. \tag{3.18}$$

Note there is no integration over ϕ in this case. This is an additional parameter in the parallax microlensing fit.

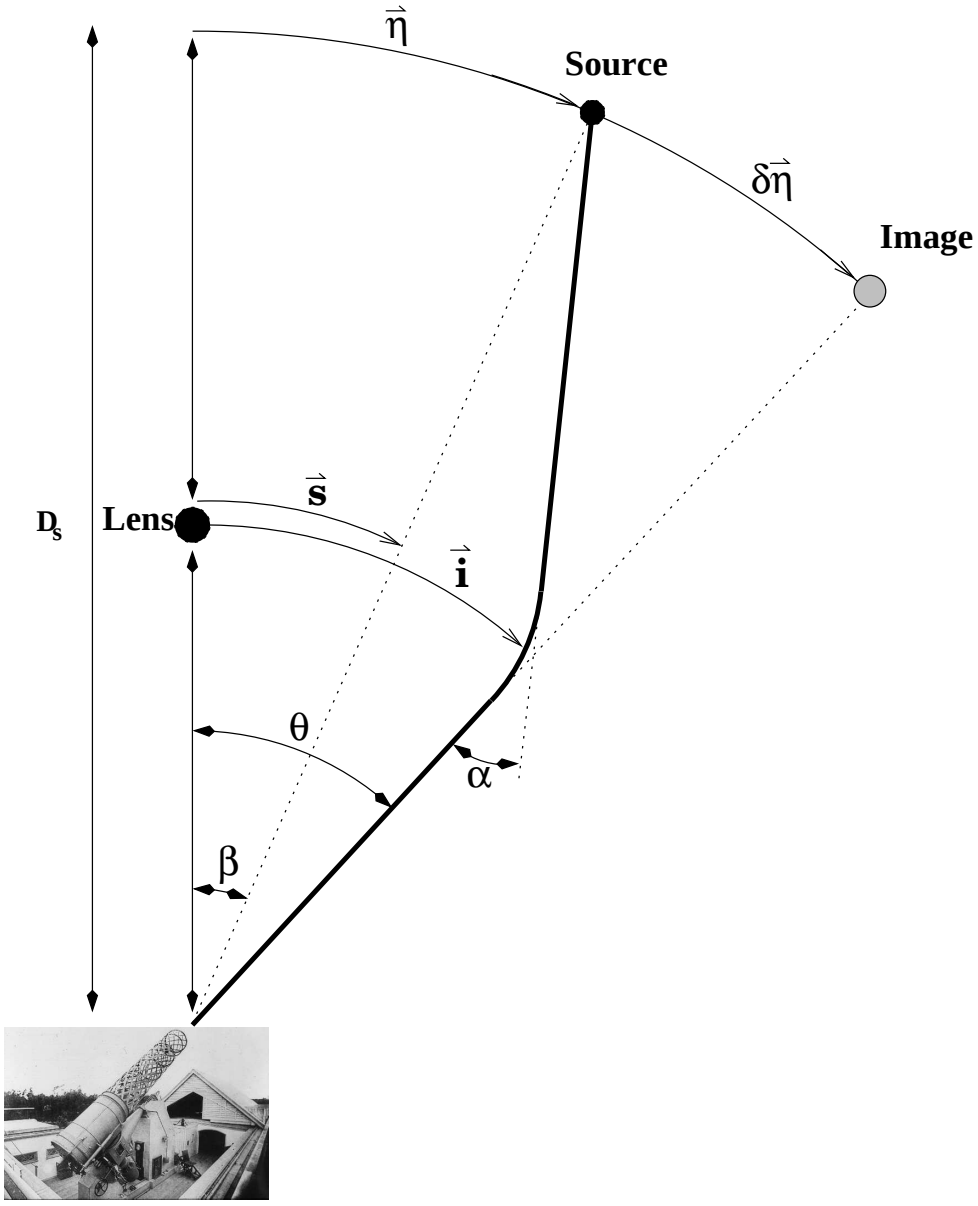

Figure 3.1:
Geometry of a lensing system. The lens passes near the source along the line of sight. Light rays which pass within $\vec{i}$ of the lens are deflected to us, the observer, by the action of the lens. The deflection angle is α. An image of the source (originally at $\vec{s}$ from our line of sight to the lens), is now seen at $\vec{i}$. The mapping takes $(\vec{\eta}, \vec{s}, \beta)$ into $(\vec{\eta} + \delta\vec{\eta}, \vec{i}, \theta)$. By symmetry, there is another image on the other side of the lens.

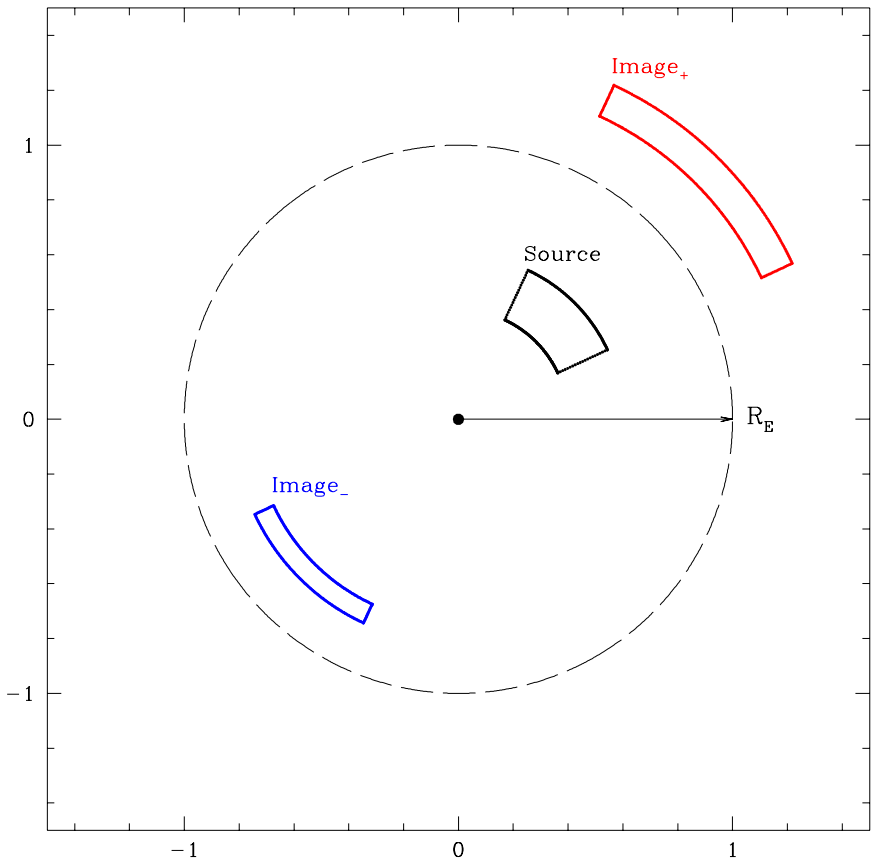

Figure 3.2:
The lensing effect is demonstrated on an arbitrary shape to illustrate the properties of the coordinate mapping. The source coordinates are mapped to 2 locations, each in a line connecting the source coordinate and lens position. Note the images are distorted with respect to the source. If the source represents an astronomical body, such as a star, its brightness is proportional to its surface area. Each image may therefore be magnified or de–magnified with respect to the source, depending on how the area changes under the coordinate mapping.

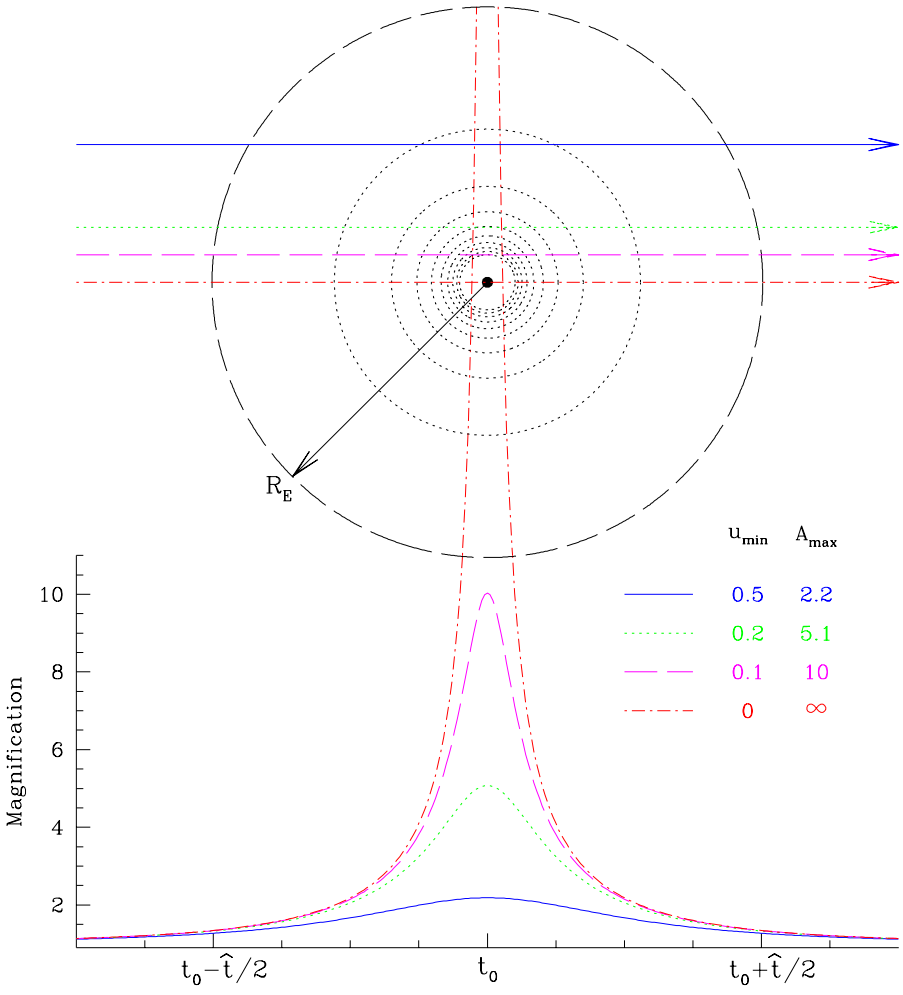

Figure 3.3:
The relationship between the source's transit through the lensing region and the observable lightcurve is shown for different minimum impact parameters. The upper panel shows a series of isomagnification contours due to the lensing object, located in the center. The outer isomagnification contour corresponds to $u = R_{\rm E}, A = 1.34$. The inner ones correspond to $A = 2, 3, 4, 5, 6, 7, 8, 9, 10$. Note the rapid rise in magnification as you get closer to the lens. The 4 source trajectories through the lensing region are shown for: $u_{\rm min} = 0.5, A_{\rm max} = 2.2$ (*solid* line); $u_{\rm min} = 0.2, A_{\rm max} = 5.1$ (*dotted* line); $u_{\rm min} = 0.1, A_{\rm max} = 10$ (*dashed* line); $u_{\rm min} = 0, A_{\rm max} = \infty$ (*dotted–dashed* line). The corresponding lightcurves, representing the brightening of the source over time, are shown in the bottom panel. The microlensing event lasts from time $t = t_0 - \widehat{t}/2$ to $t = t_0 + \widehat{t}/2$, centered on $t = t_0$. This corresponds to u evolving as $u = (1, u_{\rm min}, 1)$.

Chapter 4

MACHO SURVEY PROJECT AND GMAN

The MACHO Survey system was designed to undertake a massive survey of stellar variability to detect the rare instances of stellar brightening caused by intervening microlenses (Machos). The core science of the program involved monitoring source stars in the LMC and SMC. The line of sight to these sources passes through our dark Galactic halo, and thus this technique would probe directly if the Galactic dark matter in is a compact form. Such a program was originally suggested by Paczyński (1986).

A control experiment was also undertaken towards the Galactic bulge, where the expected rate was approximately 10 times higher than towards the LMC (Paczyński 1991). There are known populations of candidate microlenses along this line of sight, such as normal dim stars in the Galactic disk. The sample of events collected towards the Galactic bulge would be used to define a empirically derived set of microlensing cuts to apply to the LMC and SMC candidates.

The survey mode of the MACHO Project required an observation strategy optimized to *detect* microlensing events in millions of time–series of stellar brightness measurements, each thousands of observations in length. This necessitated the nightly sampling of large fields, and rapid (hence imprecise) photometry to match the rate of data flow. However, many of the secondary effects which lead to the measurement of $\widehat{v}$ and $\tilde{v}$ occur on short time–scales, or at low amplitudes, requiring precise photometry. A more agile project was required to provide sensitivity to these exotic effects. The Global Microlensing Alert Network (GMAN) was developed as a complimentary project to the MACHO Survey. Its purpose was to *characterize* events detected by MACHO, and look for (or limit) exotic effects which might provide information about the nature of the lensing object.

In the following Chapter, the procedures implemented by the MACHO Collaboration to allow real–time dissemination of microlensing data and the operations of the GMAN project

are described.

4.1 MACHO Survey Project

The MACHO collaboration is undertaking an extensive search for gravitational microlensing by objects in the Galactic halo, bulge, and disk. Nightly observations of millions of stars in the Large Magellanic Cloud (LMC) and Galactic bulge have yielded a total of 13–17 LMC (Alcock et al. 2000a) and some 500 bulge events (Alcock et al. 1995b; Alcock et al. 1997d; MACHO Alert system). The observations towards the LMC and SMC can be used to ascertain whether compact astrophysical objects constitute the dark matter halo of the Milky Way (Roulet & Mollerach 1997; Paczynski 1996).

Statistical analysis of an ensemble of microlensing events provides a useful discriminant between Galactic structure models. For example, 5.7 years of observations towards the LMC yield a microlensing optical depth representing approximately 20% of a "standard" Galactic halo comprised entirely of massive compact halo objects (Alcock et al. 2000a). The nature of this lensing population is unknown. A similar style analysis of Galactic bulge data, as reported by MACHO and OGLE (Udalski et al. 1994; Alcock et al. 1997d; Alcock et al. 2000b), indicate an optical depth a factor of ~ 3 larger than predicted by contemporary Galactic models (e.g. Griest et al. 1991; Paczyński 1991). Consistent Galactic models have been constructed which include a Galactic bar viewed nearly end–on (Kiraga & Paczynski 1994; Zhao, Rich, & Spergel 1996; Binney, Gerhard, & Spergel 1997). However, it is difficult to identify clearly a lensing population because the mass, velocity, and distance of each lens are not uniquely determined in the standard microlensing solution (see Chapter 3.1.2).

Are the excess LMC microlensing events due to Galactic dark matter in the form of Machos? The key to resolving this issue lies in determining the location of the lensing objects. If the excess microlensing optical depth seen towards the Magellanic Clouds is due to lensing by objects in the Magellanic Clouds (Sahu 1994), then the microlensing surveys will have ruled out Machos in the mass range $10^{-7} \rightarrow 1 M_{\odot}$ as significant contributors to the mass of the Galaxy's dark halo (Alcock et al. 1997a; Renault et al. 1997; Alcock et al. 1998).

The system and data collection of the MACHO experiment are described in Alcock et al. (1997a). The data are obtained simultaneously in two specially designed wide–pass filters with effective wavelengths of approximately 5150 Å and 6900 Å. This allows tests for achromaticity during stellar brightening events. However, the blending effect does contribute a non–negligible amount of chromaticity to most events. Transformations from the MACHO instrumental photometry system to the standard V and R_{KC} system have been derived by comparisons with several thousand tertiary standard stars calibrated in the LMC (Alcock et al. 1999c). Checks of the photometry with published photometry in Baade's Window confirm a zero point uncertainty of less than 0.1 mag in V and R, where this uncertainty is a conservative estimate of small zero point differences between fields monitored by MACHO in the bulge.

The MACHO Collaboration is only one of several projects undertaking a gravitational microlensing survey. In addition to MACHO, the following collaborations have engaged in microlensing surveys.

- The EROS Collaboration is observing the LMC with 3 reported candidates (Lasserre et al. 2000); the SMC with 1 reported event (Afonso et al. 1999); the Galactic bulge with 10s of candidate events (EROS Alert Page); and spiral arms of the Galaxy (Derue et al. 1999) with 3 detected events. Lasserre et al. (2000) exclude Machos as the primary component of the Galactic halo, a similar analysis to Alcock et al. (2000a). EROS has also recently obtained real–time microlensing alert capability.

- The OGLE Collaboration is observing the LMC, reporting 2 events (OGLE Early Warning System); the SMC; the Galactic bulge with more than 200 events (Udalski et al. 2000); and the spiral arms of the Galaxy (Mao 1999). OGLE have done an excellent job of making their database available to astronomers at large, leading to dozens of publications regarding stellar variability, reddening, and distance determinations.

- The MOA Collaboration is observing the Galactic center (Yock et al. 2000), and has recently evolved from a follow–up program into a survey team, releasing alerts in real–time.

- The DUO Collaboration has observed the Galactic center, with 2 reported events (Alard & Guibert 1997).

- AGAPE are observing unresolved stars in the neighboring galaxy M31 (Ansari et al. 1997), with at least 1 possible event (Ansari et al. 1999).

- A similar study is being undertaken by the VATT/Columbia microlensing group, with 6 reported events (Crotts & Tomaney 1996).

Many of these collaborations provide information on current microlensing on the World Wide Web[3].

4.1.1 Observing Strategy and Data Reduction

The MACHO Project has made full–time use of the 1.27 meter telescope at Mount Stromlo Observatory, Australia, since July 1992. Details of the telescope system are given in Hart et al. (1996), and the camera system is described in Stubbs et al. (1993) and Marshall et al. (1994). A wide field of view (42×42 arcmin^2) is afforded by corrective optics, and fields are imaged by eight 2048^2 pixel CCD detectors, simultaneously in two colors. Over 6 TBytes of raw image data were collected in the course of the survey. About 55% of this is of the LMC, 10% of the SMC, and the remainder of the Galactic bulge. Observations are obtained during all clear nights and partial nights, except for occasional gaps for telescope maintenance. The default exposure times are 300 seconds for LMC images, 600 seconds for the SMC, and 150 seconds for the bulge, and over 60 exposures are taken per clear night.

The LMC observations favor the central $5^\circ \times 3^\circ$ of the LMC disk – these fields are overlayed on an image of the LMC in Figure 4.1. The highest priority fields are often observed twice per night, with an average of 4 hours between exposures. The Galactic bulge also serves as a convenient target from an observational standpoint, as it is visible when the Magellanic Clouds are too low in the sky to observe, $\lesssim 25^\circ$ above the horizon.

---

[3] EROS **http://www-dapnia.cea.fr/Spp/Experiences/EROS/alertes.html**
MACHO **http://darkstar.astro.washington.edu**
MOA **http://www.phys.canterbury.ac.nz/~physib/alert/alert.html**
OGLE **http://www.astrouw.edu.pl/~ftp/ogle/ogle2/ews/ews.html**

The sampling varies quite substantially among the Galactic bulge fields, since the observing strategy was changed several times in order to balance the desire of more sensitivity to short events with the addition of fields. For instance, 1993 observations focused on 10 fields. In 1994, observations concentrated on high Galactic latitude fields with 4 low latitude fields observed at the beginning and end of the sequence. And in 1999, 4 fields were chosen to be observed several times per night, to gain sensitivity to $0.2 - 4$ day events.

The desire to keep up with the incoming data necessitated a rapid system to provide the millions of photometric measurements per night. The photometry code chosen, SoDoPhot (son of DoPhot) was derived from DoPhot (Schechter, Mateo, & Saha 1993), and optimized for speed at the expense of some accuracy. The photometry requires a prior good–quality template image, which is used to define the list of stellar positions and magnitudes for that field. All subsequent observations are registered to this image, and photometry is recorded in the database for these objects **only**, to avoid time–consuming object detection each time an image is entered into the pipeline. This fixed–position photometry leads to systematic errors when an object which does not appear in the catalogue appears out of the background, and this flux is picked up by a neighboring object. Henceforth, a distinction will be drawn between the photometered object, which only serves as a receptacle for the lensed flux, and the lensed source, which is the actual source acted upon by the lens. This situation is an extreme case of the blending effect, and a serious consideration when calculating microlensing detection efficiencies (Alcock et al. 2000c).

The cost of reducing these data in real–time is a loss in both precision and accuracy, and therefore less sensitivity to the fine–structure of a stars' brightness history. This includes loss of sensitivity to detailed microlensing features. However, the rapid increase in available computing power in the late 1990s allows today the real–time use of difference imaging techniques (Alard 2000), which can probe variability in square degree fields in real–time, and at the statistical Poisson noise limit of precision. Thus, any next–generation microlensing surveys would surely make use of this technique (Stubbs 1999).

The upshot of keeping up with the observations in real–time is knowledge of the current state of any on–going microlensing event. This information can than be disseminated to the microlensing community, and allows complimentary follow–up programs which can focus

resources on individual microlensing events. These follow–up collaborations are able to better characterize the nature of a microlensing deviation, and detect or set limits on exotic microlensing features.

4.1.2 MACHO Alert System

The MACHO Alert System was designed to interact, in real–time, with the evolving photometry database. This includes the generation of alerts on individual measurements showing high quality anomalies, as well as daily summary reports. The first step in generating a microlensing alert involves looking at recently photometered data.

Automated Variability Trigger

After the photometry for each observation is completed, an automated script is run which extracts information on stars which pass basic variability cuts in both MACHO passbands, and on source star color. If too many stars in any observation trigger this script (500), the observation is rejected as bogus. The basic variability trigger requires a brightening of 0.5 mag above the brightness in the template observation, with a reported photometric error less than 1/7 the amplitude of the variability (0.07 magnitudes at the trigger threshold). A cut on the redness of the star is also applied – in MACHO magnitudes, $(V-R)_{\rm Bulge} > 3.0$ and $(V-R)_{\rm LMC,SMC} > 1.1$ are likely intrinsically variable stars.

This can only be done when a field has been tagged for alerting. This involves the identification of a large fraction of the known intrinsically variable stars, which may be tagged and excluded from overwhelming the alert system. If a field has not been added to the Alert pipeline, all triggers found at this stage are written to a holding directory to facilitate the future cataloging of variable stars, and thus entry of the field into the Alert System.

An individual star may be tagged for "Minimal Cuts", meaning any sort of variability is reported, or "Always Ignore", meaning any variability is ignored. This classification happens on the user–end. For each event which passes the above criteria, the software will then cache its lightcurve and pass it through a filter which looks for evidence of active microlensing.

This includes a uniqueness criterion, multi–color information, shape parameters, and the amount of cumulative signal in any deviation. High quality events are tagged as especially interesting. Information on all triggers is immediately e–mailed to interested members of the collaboration. This process is begun immediately after the image is reduced, and no more than a couple of hours after the image was observed (depending upon the photometry backlog). This true real–time alert recognition was achieved in Dec, 1997.

On the user–end, priority is given to those triggers which are tagged as especially interesting. The user may immediately request the most recent data (generally 2 to 3 years worth) for interactive visualization in the SuperMongo environment. Any MACHO team member may view these alerts, and have access to the MACHO database, from their host institution. The database software was specially designed to take such advantage of the evolving World Wide Web capabilities. While reviewing these triggers, a user may register the star in the MACHO database with the following variability flags :

1] Generic variable	6] Pseudo – microlensing
2] Egregious variable	7] Supernova echo
3] Long – period variable	8] Eclipsing binary
4] Eruptive variable	9] Cepheid
5] Microlensing	10] RR Lyrae

Examples of each of the backgrounds to microlensing can been seen in Figure 4.2. These are actual lightcurves which passed the basic variability cuts, were passed on to the alert system manager, and tagged as intrinsically variable upon visual inspection. While these may be astrophysically interesting of their own accord, they are merely background in the search for microlensing.

However, one class of variability deserves special mention, and these are category 7 above. A certain class of pseudo–microlensing triggers had shown up frequently in the alerts, all occurring in a certain region of the LMC. The lightcurve shapes were all similar (see Figure 4.2(g)), and exhibited a slight dip before a generally symmetric brightening and dimming occurred. Their clustering on the sky indicated they were likely a stellar

background to microlensing, unless they were caused by a grouping of Machos, such as suggested by Moore & Silk (1995). By plotting the location of these alerts on the sky, as in Figure 4.4, we were able to discern they appeared in a circular pattern, generally on stars superimposed over nebulosity. The center of this pattern was associated with the location of Supernova 1987a, at RA 05:35:27.98, DEC -69:16:11.31 (J2000). It appears these are light echoes of the supernova explosion, reflecting off dust grains in the interstellar medium of the LMC. This region of the sky has since been excluded from the microlensing alert system.

In most cases, it is obvious whether or not an alert is legitimate. Many triggers are single deviant high points, possibly due to an asteroid passing near the object, a satellite track, or photometry error. These types of alerts are ignored. Intrinsically variable stars are generally easy to identify, by looking at the multi–year time–series at hand. These stars are classified with one of the variability tags above, and marked as "Always Ignore". A final possibility is that this trigger signifies the most recent in a cumulative series of brightening data points which looks like microlensing. A set of legitimate microlensing triggers, captured at the time of their alert, are presented in Figure 4.3.

Possible Microlensing Event

For each legitimate microlensing trigger, finding charts are extracted from the MACHO database from the template observation. If available, the image from the observation which triggered the alert is also extracted – however, these are only available for several hours before being written to a spinning disk store. The actual images prove a useful and rapid discriminant against bad photometry (due to poor seeing, edge–of–chip effects) or defective images. The region surrounding the alert star is also examined for possible contamination by nearby variable stars, or evidence for a background galaxy (which would suggest a supernova interpretation).

Having passed these visual tests, the 2–color MACHO lightcurve of the event is fitted for microlensing with a seven parameter fit – the three standard microlensing parameters and two baseline parameters (lensed and blended flux) for each passband. The quality of

the microlensing portion of the event is compared statistically to the quality of the baseline history of the object. A fit χ^2 parameter is calculated for the region before and during the possible event. This can help to discern whether a bad fit to the microlensing portion of the lightcurve is significant in the context of the baseline time–series. Bad fits to a smooth baseline may indicate a history of systematic photometric errors, and thus one would expect worse than normal fits to the microlensing portion of the curve. In many cases, fits to these developing lightcurves lead to unphysical parameters, such as divergent peak magnifications.

The color of any blended (unlensed) light is also examined. If the event gets brighter in the red passband than in blue, this indicates any unlensed object blended with the source is bluer, an unlikely situation. The population of dim stars, which generally provide the flux constituting any blend and **also** serve as candidates for the lens itself, are intrinsically red. Thus for a true blended lensing event, we would expect $f_B > f_R$. If the early fits indicate $f_B \ll f_R$, an alert is not issued unless evolution of the lightcurve shape presents compelling evidence. This is also reasonable in the context of the stellar variability background to microlensing. Many of these types of variability involve the expansion of the star's photosphere, which leads to redder colors as the surface temperature of the expanding star decreases.

Microlensing Alert!

Objects meeting the above criteria are considered legitimate microlensing candidates. The event is named according to the year it was discovered (e.g. "99–"), the line of sight to the source star ("BLG–", "LMC–", "SMC–"), and enumerated based upon the number of events discovered previously along the line of sight that calendar year. An entry is added on the MACHO Alert page (http://darkstar.astro.washington.edu), including current event parameters, the expected peak magnification and date, coordinates, magnitudes, finding charts, and in 1999 the actual data from the MACHO database. A sample entry from the MACHO Alert page reads

Event	Field.Tile.Seq	RA	Dec	V	R	Comments	
99-BLG-7	403.47491.770	17:54:38.7	-29:33:13	17.9	16.7	Peak of A $\sim$ 2.4 on 19 Mar duration 47 $\pm$ 1 days	
99-BLG-8	403.47849.756	17:56:25.2	-29:40:31	15.8	14.5	A $\sim$ 3.8 and rising on 16 Jul duration 211 $\pm$ 9 days. Likely PARALLAX event.	

where **99–BLG–7** and **99–BLG–8** represent hyper–links to an ftp site where finding charts and lightcurve data are stored. These entries are updated on a daily basis, to reflect the on–going status of each event, including evidence of any exotic effects.

As the final step, an e–mail containing similar information is sent to the microlensing community via an e–mail forwarding alias. The full process takes approximately 30 minutes, and can be initiated immediately upon receipt of the internal e–mail signifying an interesting event. This process was repeated on a daily basis for 5 years, as long as there was a clear night in Australia and the equipment was functional. Bad weather, the bane of many an astronomer, was occasionally a blessing.

4.2 Global Microlensing Alert Network (GMAN)

The preceding information allows the general microlensing community real–time access to all on–going microlensing events. Several follow–up efforts were undertaken to take advantage of the advent of the MACHO and OGLE (and subsequently the EROS and MOA) alert systems. This includes the Probing Lensing Anomalies NETwork (PLANET), and the Global Microlensing Alert Network (GMAN), both of which began successful operations in the summer of 1995. Later collaborations include the Microlensing Planet Search (MPS) Collaboration, which began observations in 1997. The goal of these collaborations was to provide the temporal and photometric resolution necessary to distinguish light–curve "fine structure". These collaborations provide updated information on current microlensing events on the World Wide Web[4].

---

[4]MPS **http://bustard.phys.nd.edu/MPS/**
PLANET **http://www.astro.rug.nl/~planet/index.html**

Table 4.1: Summary of observatories participating in GMAN follow–up observations.

Observatory	Latitude, Longitude	Aperture	Detector	″/pixel
MACHO	149 ° 00.5 ′ E , 35 ° 19.2 ′ S	1.27 m	8 x 2048 x 2048 Loral	0.63
CTIO	70 ° 48.9 ′ W , 30 ° 30.9 ′ S	0.9 m	1024 x 1024 Tektronics	0.40
MJUO	170 ° 27.9 ′ E , 43 ° 59.2 ′ S	0.61 m	1536 x 1024 KAF1600	0.23
MSO30	149 ° 00.5 ′ E , 35 ° 19.2 ′ S	0.76 m	1024 x 1024 Site TK1024AB	0.36
MSO74	149 ° 00.5 ′ E , 35 ° 19.2 ′ S	1.9 m	2048 x 4096 SI–002AB	0.37
UTSO	70 ° 42.0 ′ W , 29 ° 00.5 ′ S	0.61 m	512 x 512 Photometrics	0.45
WISE	34 ° 45.8 ′ E , 30 ° 35.8 ′ N	1.0 m	1024 x 1024 Tektronics	0.70

The GMAN follow–up project was designed from its inception to seamlessly merge with the MACHO survey project. The GMAN team comprised members of the MACHO collaboration, affiliate astronomers who volunteered time and effort, as well as service observers. The success of this effort hinged upon the interaction between the evolving MACHO database, and the dynamic allocation of the GMAN resources. The crux of this dissertation involved developing and taking advantage of the interplay between these collaborations.

The ultimate goal of the GMAN follow–up effort was to sample light–curves with an accuracy and frequency not permitted by the MACHO survey system. The smaller scale of this effort allowed re–allocation of resources to better sample known events, without the collateral damage in sensitivity which might be incurred if this were to happen with the survey system on a regular basis. The photometry was to be performed in a more careful manner, allowing measurements in many cases at the 1% level.

4.2.1 Resources

GMAN consisted of the observing resources listed in Table 4.1, located around the globe, for various intervals of its operational lifetime 1995–1999.

The GMAN resources were utilized in the following way:

- MACHO (Mount Stromlo Observatory, Canberra, Australia): The MACHO telescope was used to detect new microlensing events by establishing a prior baseline lacking variability, and noting real–time excursions from this baseline. The MACHO data

were used to trigger observations by other GMAN resources. The MACHO survey was *very* rarely rescheduled to observe exotic events. One notable exception involves observations of the second caustic crossing of event MACHO 98–SMC–1 (Chapter 7.2).

- CTIO (Cerro Tololo Inter–American Observatory, Cerro Tololo, Chile): Nightly observations on the CTIO 0.9m telescope 1995–1999 amounted to generally 1 hour of sky time per night. However, the staff were extremely flexible in scheduling, and we were able to re–allocate CTIO resources and extend observing time on a real–time basis on many occasions. This was considered the workhorse of the GMAN effort, and followed most of the events GMAN focused on, generally in the R passband. The observing strategy was optimized in 1997 to target LMC/SMC events at highest priority (and paid off with the real–time detection of binary event MACHO 98–SMC–1, Becker, Rhie, & Bennett 1998), and thus the frequency of observations of our bulge events decreases.

- MJUO (Mount John University Observatory, Lake Tekapo, New Zealand): The Microlensing Observations in Astrophysics (MOA – Yock et al. 2000) team contributed dense observations of several on–going exotic events from 1995–1999 from Mount John's University Observatory (MJUO) in New Zealand. These were generally taken in the R passband.

- MSO30: (Mount Stromlo Observatory, Canberra, Australia): Starting in 1997, we arranged microlensing follow–up observations at the Mount Stromlo Observatory 30" (MSO30) telescope in Canberra, Australia, with the Reynolds Amateur Photometry Team (RAPT). This group of amateur astronomers staffed the telescope nightly, on a volunteer basis. The data–taking system proved to be somewhat unreliable, since it was not supported by the technical staff at high priority. We received observations of select events for several intervals of time in the R passband.

- MSO74 (Mount Stromlo Observatory, Canberra, Australia): The Microlensing Planet Search (MPS) team began its pilot season of observations in 1997, and has contributed

data from the MSO 74" (MSO74) telescope to the GMAN effort. MPS undertakes rapid, precise monitoring of dozens of on–going Galactic bulge events to look for the short–timescale signature of planets around the lensing object. Observations were taken in the R passband until the 2000 bulge season, when MPS switched to the I passband. MPS used an independent software package to reduce their data. Software controlling the real–time flow and reduction of these data was also designed during this dissertation work, but is considered here an auxiliary effort.

- UTSO (University of Toronto Southern Observatory, Las Campanas, Chile): For the observing seasons 1995–1996, we were allotted approximately 50% of the bulge time at the University of Toronto Southern Observatory (UTSO) 0.6m telescope at Las Campanas, Chile for microlensing follow–up. Here we focused on a sub–set of the on–going events with high frequency sampling in multiple passbands.

- WISE (Wise Observatory, Mitzpe Ramon, Israel): Wise Observatory provided co-ordinated observations on the 1.0m telescope at Mitzpe Ramon, Israel from 1995 to 1999. These were auxiliary observation, and occurred at the permission of the observer scheduled for telescope time. We generally received an observation or 2 a night. These observations were requested for a subset of the bulge alert events which had begun to show unusual features. The sparse coverage was also ideal to cover long–time scale events to limit or detect parallax effects. Observations were taken in the R passband.

4.2.2 Strategy

When a new alert was issued by MACHO, a GMAN site (or sites) for observations was chosen to observe this event, depending upon the event's current state. Long timescale events were scheduled to be observed approximately once per night, usually at two of the GMAN locations spaced in latitude. Short timescale events, or events which showed promise for yielding exotic effects (such as possible high magnification events and events which were not fit well by the point source, point lens model), were observed at least twice per night at multiple locations. Target lists for each site were manually constructed, and events were assigned priority, based upon the status of all on–going microlensing events. These

were updated approximately daily, and copied to the GMAN site for consultation by the observers.

The better seeing conditions, and the requirement that we keep up real–time photometry on merely hundreds, instead of millions, of stars indicates that the GMAN program should be able to achieve better overall lightcurves than the MACHO survey system, and thus be more sensitive to small amplitude deviations.

4.2.3 Photometry

Images taken by the GMAN telescopes were automatically processed on site [5]. The data taken at the primary GMAN sites (CTIO, UTSO, MSO30, MSO74) sites were reduced in real–time by automated PERL scripts. However, the reduction package differed slightly for the MSO74 effort. Data from MJUO were independently reduced as part of the MOA microlensing program (Yock et al. 2000). Star lists for each field were automatically extracted from the MACHO database, to assist in automating the GMAN photometry and normalizing the resulting lightcurves.

Pre–photometry Preparations

Templates were extracted from the MACHO database to allow registration of images and identification of the target star. Lists of stars used to create the MACHO point spread function (PSF) were also extracted in this region. These are isolated stars which provide a good starting point for iterating the GMAN PSF construction process in these crowded fields. Finally, the MACHO lightcurves of all stars within $1.5'$ of the target star are analyzed to ascertain their variability. This allows the construction of a list of "normal" stars which are used to create a local relative zero–point to measure the variability of the target star. After being generated, these files are automatically copied to the GMAN site and stored locally.

---

[5] WISE data were originally reduced on–site and in real–time, but the available computing resources were too slow, the forms of the data received too variable, and the network connection inadequate to retrieve the data in real–time. Instead the images were sent via data tape, after the event.

Real–time Photometry Package

The actual photometry package includes a series of PERL scripts which iteratively call the photometry programs DaoPhot and Allstar (Stetson 1994) to model each image's point spread function (PSF) and perform crowded field photometry. The scripts also manage the data flow and notify the user on the status of the reductions.

The script is invoked by the observer on–site on the UNIX command line, and subsequently proceeds on its own, cleaning up when it determines there are no more images to reduce. This script will initially search through the directory for images. If any calibration images (such as flat or bias sets) are found in the directory, it will first combine these using system calls to the IRAF data reduction environment. It will archive these combined calibration images for future use. Next, this script will identify object images existing in the directory. All object images are automatically reduced (trimmed, flat–fielded and bias corrected). The script requires each image to have the internal MACHO ID of the alert star in the image header, so that the script may identify which field to register the frame to. The frame is then registered to the MACHO template, using the output from a DaoPhot FIND command on the GMAN image. If the image fails in the registration process, a PSF is constructed, and the user is notified of this failure. These images are examined manually in the final data analysis.

PSF stars are identified in the image, and DaoPhot chooses enough additional stars so that 100 total stars are used in the first construction of the PSF. This is initially constructed without a lookup table, with the analytic model automatically chosen by the DaoPhot program to minimize the overall profile error χ. Stars which are significant outliers (determined from the profile errors output from the DaoPhot task PSF) are rejected, and the analytic model is reconstructed. The rejection algorithm compares each star's χ to a multiple of χ_{median}, as determined from the ensemble of PSF stars. The acceptable multiplier tightens on each iteration through the rejection algorithm. A maximum of 3 of the following iterations occur: calls to Allstar to subtract off neighbors to the PSF stars; DaoPhot construction of an improved model PSF with a look–up table; and 3 internal iterations of rejecting bad PSF stars. Once this maximum of 9 iterations has been reached, a maximum of 70 stars

have been rejected, or the PSF model converges such that all stars have $\chi/\chi_{median} < 1.3$, the PSF is considered complete.

Next, a $1.5' \times 1.5'$ postage stamp is carved out of the full image, centered on the target star. All stars identified in the MACHO template are subtracted off using Allstar, and two rounds of dim object detection are undertaken. All stars are fit jointly in a final Allstar run, leading to the final photometry output of that observation. Note, only a fraction of the image is fully photometered. Information on each star is written to an ascii file identified by the observation number, which is constructed from the Julian Date of the observation. If the star was originally found in the MACHO template, it is identified by MACHO's internal ID number. If it was found in a round of dim star detection, it is assigned an arbitrary number determined from one of the photometry runs. Thus for each alert and at each GMAN site, the scripts build a time–series of observations, with independent photometry files for each observation but a common list of stars derived from the MACHO template.

The final data products per observation are the image's PSF, the $1.5'' \times 1.5''$ postage stamp in FITS file format, and ascii photometry file. Team members have immediate network access to GMAN data, which is subsequently used for real–time scheduling during on–going events.

Final–stage Photometry Package

Given the full time–series of data on a completed event, all GMAN light–curves are reanalyzed *en masse* using the Allframe package (Stetson 1994). This after–the–fact reduction allows manual interaction with the images to correct, for instance, images which did not register, or PSFs which did not converge. Massaging this final 10% of the data did in fact consume 90% of the time spent in this final stage.

The starlists from all observations of each event, taken at all sites, are compared against one another to define a common starlist and to register all images to a common system. A good seeing image is chosen as the "master image". The Allframe package is run on all the images with the joint starlist. This software performs a joint fit to the global positions of all the stars, using the full time–series as constraints. Once a star's location converges, photometry is performed on each star, in each image, at the same location. This allows good

quality images to define the positions of stars in the poorer quality images, which are then able to be photometered accurately. These stars are subtracted off each image. After the Allframe run, star–subtracted images are co–added to look for very dim stars which were not detected in any particular image, but may show up as a collective signal of undetected residuals. Any new stars are added to the master starlist, and the procedure is repeated. This yields the high–quality GMAN lightcurves presented in this dissertation.

4.2.4 Constructing a Lightcurve

Normalization is performed on–the–fly using the list of normal reference stars obtained from the MACHO data set. The most recent data set of any star may be retrieved by executing a network query, which uses the Unix RPC library. This query first gathers all of the ascii photometry files for the object requested, on a site by site basis. These are sorted by date, and further sorted by stars common to each ascii file – the MACHO template stars. Only "normal" MACHO stars which have passed a non–variability test are included in this matrix. Each query initiates a matrix inversion which results in a normalized lightcurve. The procedure returns a binary–format lightcurve which is stored next to the locally cached MACHO lightcurve, as well as GMAN lightcurves from other sites.

Normalization

The normalization problem is addressed using N constant reference stars from the MACHO database, observed in T GMAN observations. The N stars are indexed with variable j, and the T observations with variable i.

We first assume each of the N stars has a "constant" magnitude M_j. For each observation there is a first order image zero–point offset D_i affecting each star, which is mainly a function of exposure time and transparency of the atmosphere. Second order color effects may become large for stars of extreme color, or high airmass observations where refraction is important. If a star brightens significantly, it is possible the majority of the stars of comparable apparent brightness will be red giant stars. To avoid any overall color bias, each observation may have an additional color term E_i to apply to each star of known color C_j.

The observed magnitude m_{ij} of each star in each observation carries an associated error of σ_{ij}. We can then predict that

$$m_{ij} = M_j + D_i + C_j E_i \pm \sigma_{ij}. \tag{4.1}$$

To determine M_j, D_i, and E_i using the information from all stars in all observations, we require a χ^2 function to minimize. This is defined as

$$\chi^2 = \sum_{i=1}^{T} \sum_{j=1}^{N} \left(\frac{m_{ij} - M_j - D_i - C_j E_i}{\sigma_{ij}} \right)^2. \tag{4.2}$$

A global minimum of this function may be found by requiring the derivatives of χ^2 with respect to M_j, D_i, and E_i be zero. This leads to three sets of equations

$$M_j = \frac{P_j}{S_j} - \frac{1}{S_j} \sum_{i=1}^{T} \frac{D_i + C_j E_i}{\sigma_{ij}^2}, \tag{4.3}$$

$$D_i = \frac{P_i}{S_i} - \frac{1}{S_i} \sum_{j=1}^{N} \frac{M_j + C_j E_i}{\sigma_{ij}^2} \tag{4.4}$$

and

$$E_i = \frac{K_i}{L_i} - \frac{1}{L_i} \sum_{j=1}^{N} \frac{C_j M_j + C_j D_i}{\sigma_{ij}^2}. \tag{4.5}$$

Here we have used

$$\begin{aligned} S_i &= \textstyle\sum_{j=1}^{N} \frac{1}{\sigma_{ij}^2}, \quad P_i = \sum_{j=1}^{N} \frac{m_{ij}}{\sigma_{ij}^2}, \qquad K_i = \sum_{j=1}^{N} \frac{m_{ij} C_j}{\sigma_{ij}^2} \\ S_j &= \textstyle\sum_{i=1}^{T} \frac{1}{\sigma_{ij}^2}, \quad P_j = \sum_{i=1}^{T} \frac{m_{ij}}{\sigma_{ij}^2}, \quad \text{and} \quad L_i = \sum_{j=1}^{N} \frac{C_j^2}{\sigma_{ij}^2}, \end{aligned}$$

to represent sums of known quantities. Substituting equation 4.3 into equations 4.4 and 4.5, we arrive at 2 sets of linear equations for D_i and E_i :

$$\begin{aligned} D_k \left(\frac{1}{S_i} \sum_{j=1}^{N} \frac{1}{S_j \sigma_{ij}^2 \sigma_{kj}^2} - \delta_{ik} \right) = \\ \frac{E_k}{S_i} \left(\delta_{ik} \sum_{j=1}^{N} \frac{C_j}{\sigma_{ij}^2} - \sum_{j=1}^{N} \frac{C_j}{S_j \sigma_{ij}^2 \sigma_{kj}^2} \right) + \frac{1}{S_i} \left(\sum_{j=1}^{N} \frac{P_j}{S_j \sigma_{ij}^2} - P_i \right) \end{aligned} \tag{4.6}$$

and

$$E_k \left(\frac{1}{L_i} \sum_{j=1}^{N} \frac{C_j^2}{S_j \sigma_{ij}^2 \sigma_{kj}^2} - \delta_{ik} \right) = \frac{D_k}{L_i} \left(\delta_{ik} \sum_{j=1}^{N} \frac{C_j}{\sigma_{ij}^2} - \sum_{j=1}^{N} \frac{C_j}{S_j \sigma_{ij}^2 \sigma_{kj}^2} \right) + \frac{1}{L_i} \left(\sum_{j=1}^{N} \frac{C_j P_j}{S_j \sigma_{ij}^2} - K_i \right) . \quad (4.7)$$

To completely constrain this system, we impose an additional condition on a particular observation t (this is selected as the observation with the lowest average reported error), such that $D_t = E_t = 0$.

This problem is addressed in matrix form, inserting Equation. 4.7 into Equation. 4.6, solving for D_i with matrix inversion and Gauss–Jordan elimination, and using this solution to uniquely determine E_i. Stars which are significant outliers from the derived solution are removed, and the normalization is repeated. For the standard GMAN observations, all color terms (E_i) are equal to zero. This full expression is only used for normalizing photometry required for the MPS project.

4.3 Integrating MACHO and GMAN

The MACHO database software was designed in the C++ programming language, and the locally–stored (portable) MACHO and GMAN photometry files were written in a format which allowed them to be merged for analysis. Methods were designed to transform data extracted from the MACHO database, as well as data extracted from the GMAN sites, into "common light–curves". These are single–passband light–curves cleaned of data failing basic quality cuts on photometry flags, and stored in a basic time series of date, flux, error, and observation ID. A "light–curve set" is then constructed with all available common light–curves, resulting in a multi–passband representation of the event. The light–curve set generally contains the 2 MACHO passbands and at least 1 GMAN passband.

These data are then jointly fit for microlensing, using global parameters $\widehat{t}$, t_0, and $u_{\min}$, and separate baseline parameters for each passband. This results in $2\ n+3$ parameters in the global microlensing fit, where n is the number of passbands which makes up the light–curve set. The data of on–going events were jointly fitted daily, after automated scripts updated the local cached versions of the data. The fitting process occurred in an environment which

interacted directly with the locally stored binary files. The lightcurve function is globally minimized with respect to the data, using the Levenberg–Marquardt method for a nonlinear least–squares fit (Press et al. 1992). Additional fits were also performed in the MINUIT environment (James 1994).

4.4 Comparison of MACHO and GMAN

The GMAN project realized several advantages over MACHO, which are described below.

4.4.1 Sampling Frequency

Figure 4.5 shows a histogram of MACHO's sampling frequency for all microlensing alerts also followed by GMAN. This represents the interval between subsequent observations of a particular event, summed over all events. The *solid line* shows all observations excluding the 1999 season, since the MACHO observing strategy was changed for the final bulge season (1999) to provide sensitivity to ~ 0.2 day events. The *dotted line* includes this 1999 season, and the fractional contribution of the 1999 season near 0.01 days is significantly larger than over the rest of the timescales. The primary peak near 1 day is due to MACHO's nightly sampling pattern. A second peak near 100 days represents the interval between Galactic bulge seasons.

The sampling frequency for these same events obtained in the course of the GMAN project is shown in Figure 4.6. This distribution is taken from observations of alert events at CTIO, MSO30, UTSO, and WISE sites. It is apparent that a larger fraction of GMAN's observations of a particular object were taken less than 1 day apart. There is a sharp peak at approximately 5 minutes, which is a typical exposure time for bulge observations. Many of the observations taken longer than 100 days apart are for the purpose of constraining the baseline brightness of the object after the event is over. This is extremely important, since once needs to characterize the blending fraction of an event to extract the correct event parameters. This requires knowledge of the baseline brightness of the source, as well as global shape of the variability.

The comparison between the MACHO and GMAN sampling rates is more easily seen in Figure 4.7. This shows the cumulative fraction of observations taken below a certain

sampling frequency. More than half of the observations taken in the course of the GMAN follow–up effort were taken within 1 hour of the previous observation. For comparison, only 7.5% of MACHO's observations were taken with this intensity of coverage.

4.4.2 Seeing Conditions

Another improvement GMAN can take advantage of is better seeing conditions at the observing sites. A histogram of seeing conditions from MACHO's site, Mount Stromlo, Australia, is shown in Figure 4.8, which indicates that the median seeing is near $2''$, a poor situation in any astronomer's book. The *solid line* represents MACHO's red passband, and the *dashed line* MACHO's blue passband, which receives slightly better seeing. The distribution of seeing conditions taken from GMAN observations is seen in Figure 4.9, which indicates the median GMAN seeing is close to 1.1 arcseconds. The distribution of seeing conditions is also narrower than MACHO's.

Finally, we compare the distribution of seeing conditions for MACHO and GMAN in Figure 4.10. This cumulative distribution is presented in a format similar to Figure 4.7. Note, the majority of GMAN's observations are taken in less than $1.5''$ seeing. Less than 8% of MACHO's observations are in seeing this good. The MACHO data average between 2.1 and $2.2''$.

4.4.3 Photometry

The final GMAN time–series provided by the Allframe package yielded considerably better photometry than was realized by the SoDoPhot software. Figure 4.11 indicates that GMAN obtained better than 10% photometry out to $R \gtrsim 21$, whereas the minimum error envelope for MACHO reaches 10% at $R \sim 19.5$. This translates directly into more sensitivity to exotic microlensing effects, which are described in detail in the following chapters.

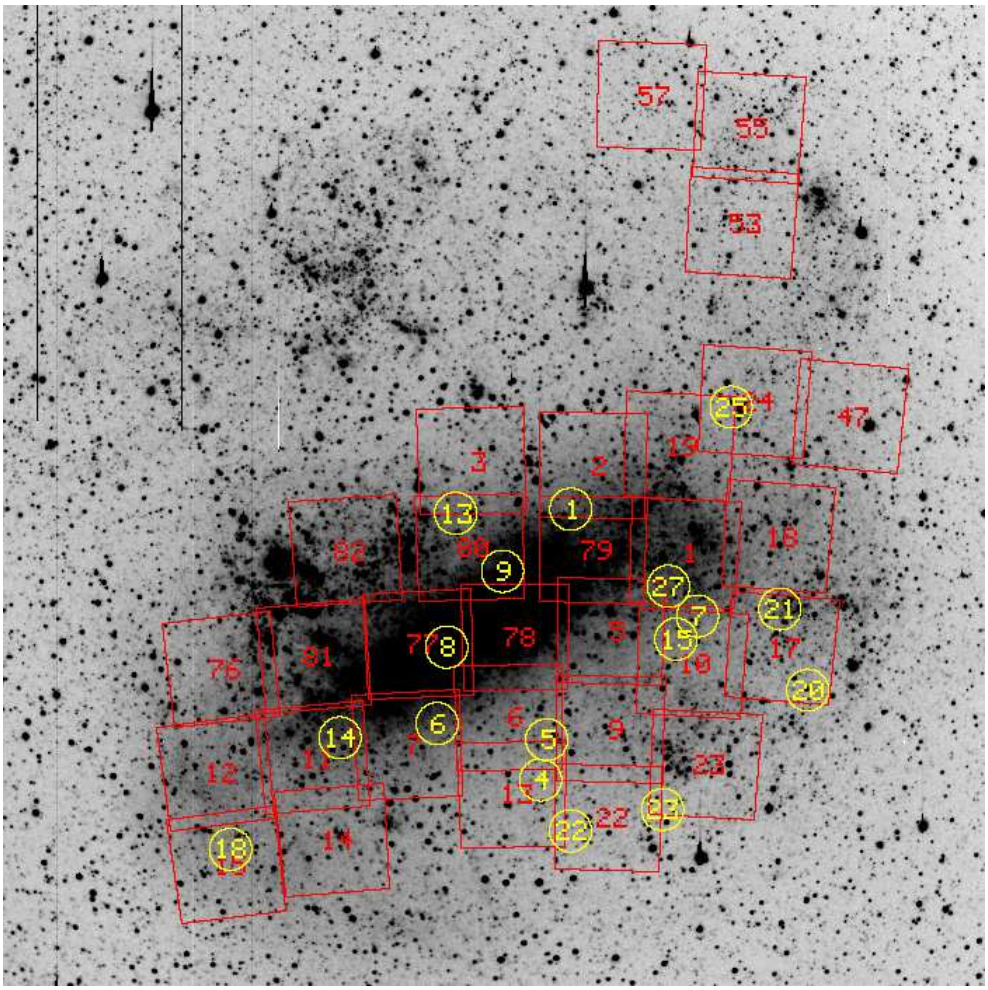

Figure 4.1:
An R–band image of the LMC, 8.2 degrees on a side (G. Bothun, private communication), showing the locations of 30 fields observed by MACHO. Also shown as circles are the locations of the 17 microlensing candidates discussed in Alcock et al. (2000a).

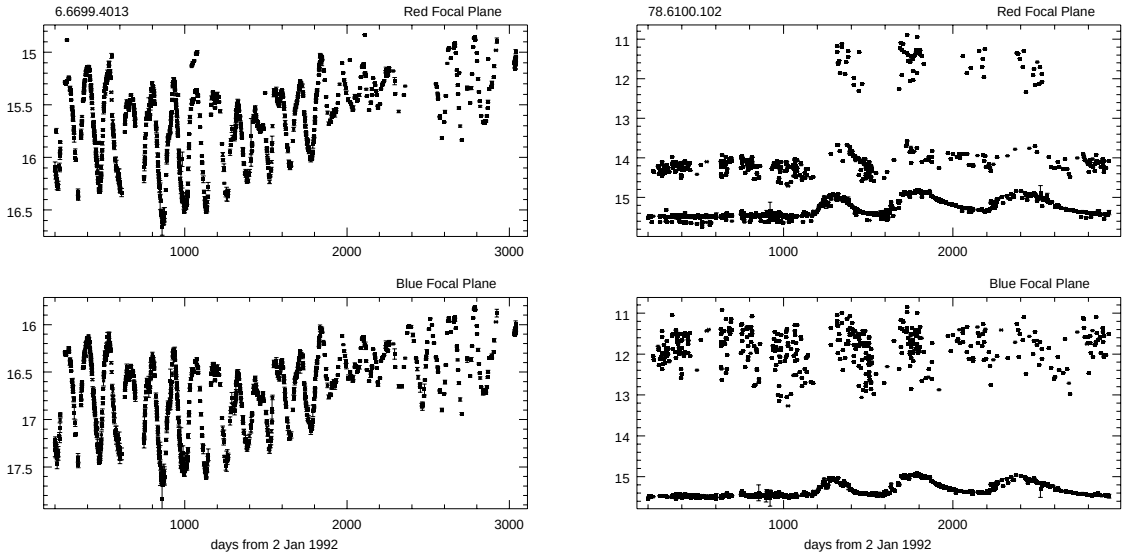

(a) Generic Variable

(b) Egregious Variable

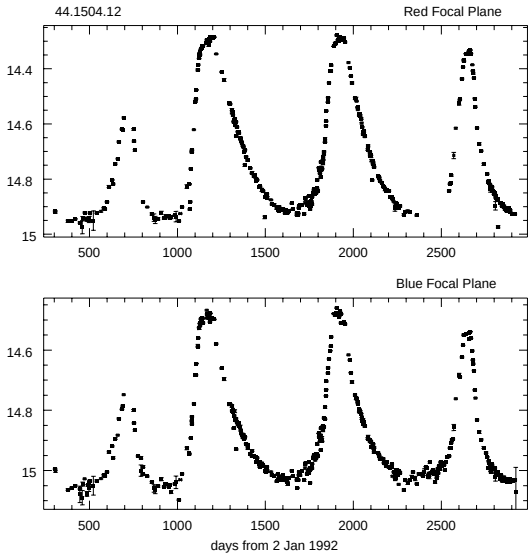

(c) Long-period Variable

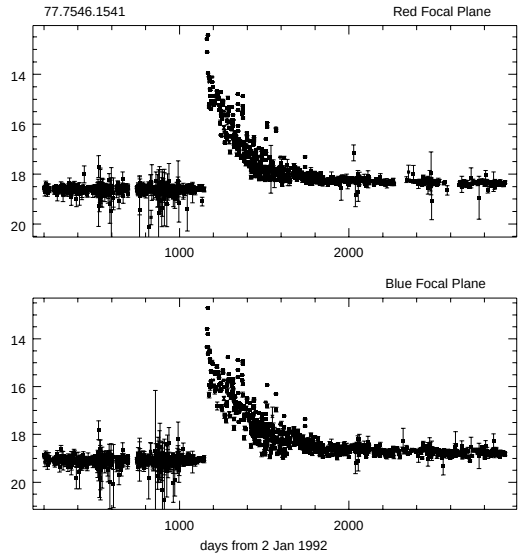

(d) Eruptive Variable (Nova)

Figure 4.2:
Each panel represents a photometric time–series which passed the MACHO Alert System variability trigger. In each of these cases, team members received an e–mail alerting them to a possible microlensing event in progress, and were directed to view the lightcurves presented here. Each was categorized as intrinsically variable, and excluded from future alerts.

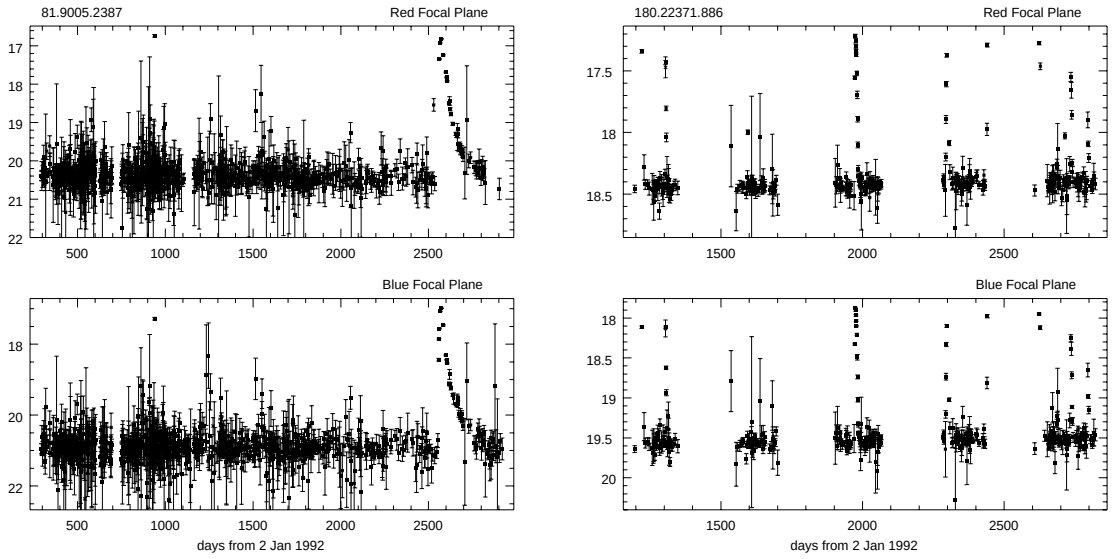

(e) Eruptive Variable (Supernova)

(f) Pseudo-microlensing

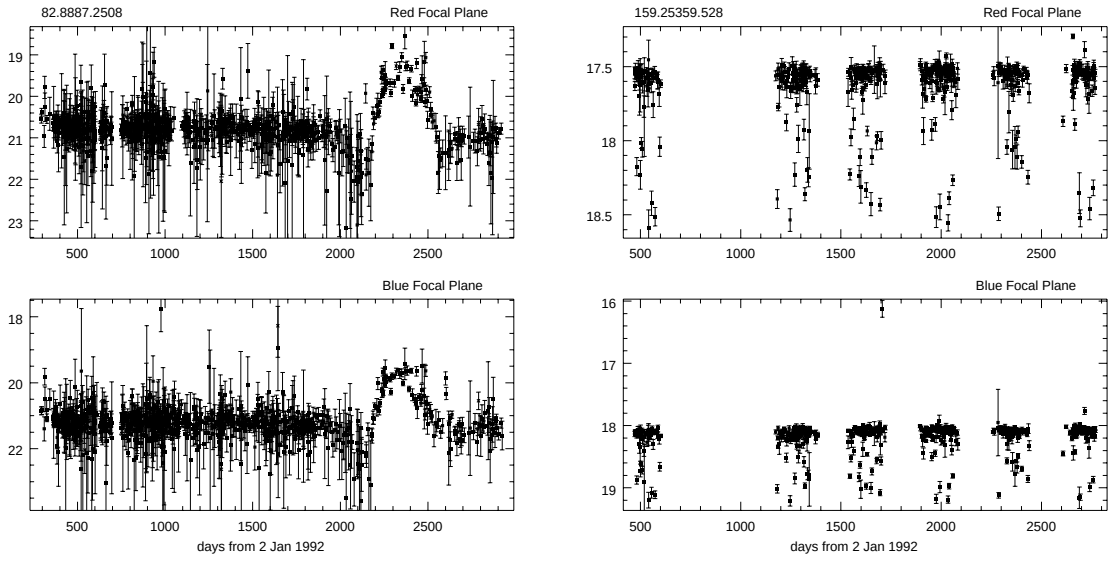

(g) Supernova 1987a Echo

(h) Eclipsing Binary

Figure 4.2: (continued)

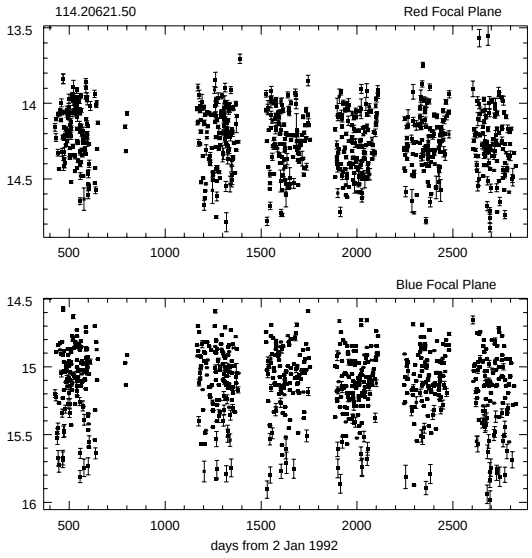

(i) Cepheid

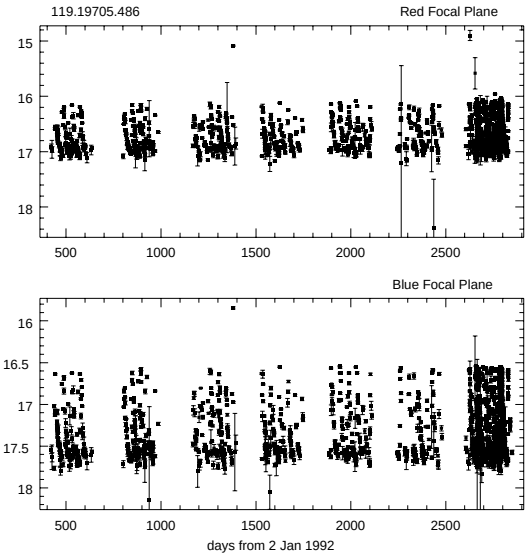

(j) RR Lyrae

Figure 4.2: (continued)

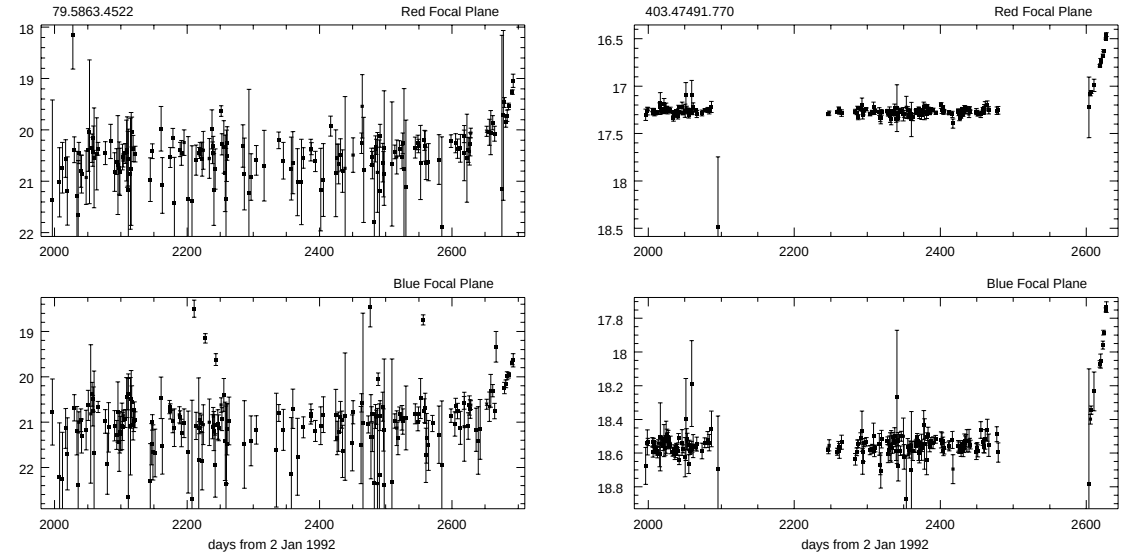

(a) 99–LMC–2

(b) 99–BLG–7

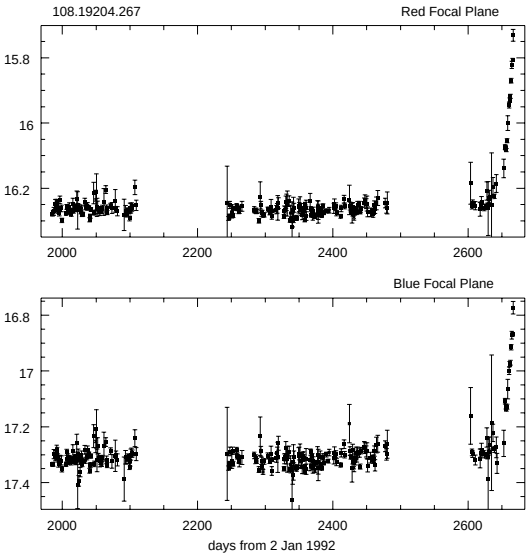

(c) 99-BLG-18

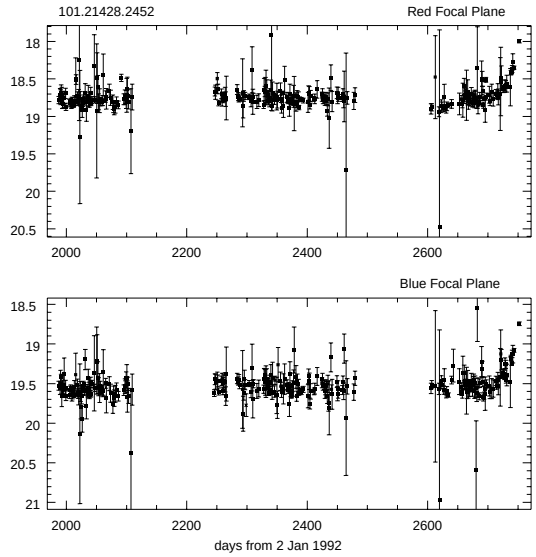

(d) 99–BLG–42

Figure 4.3:
Each panel represents a photometric time–series which passed the variability trigger in the MACHO Alert system. Each figure includes all of the data up to the observation which triggered the alert system. Alerts were immediately issued for each of these events, which all appear to be due to microlensing.

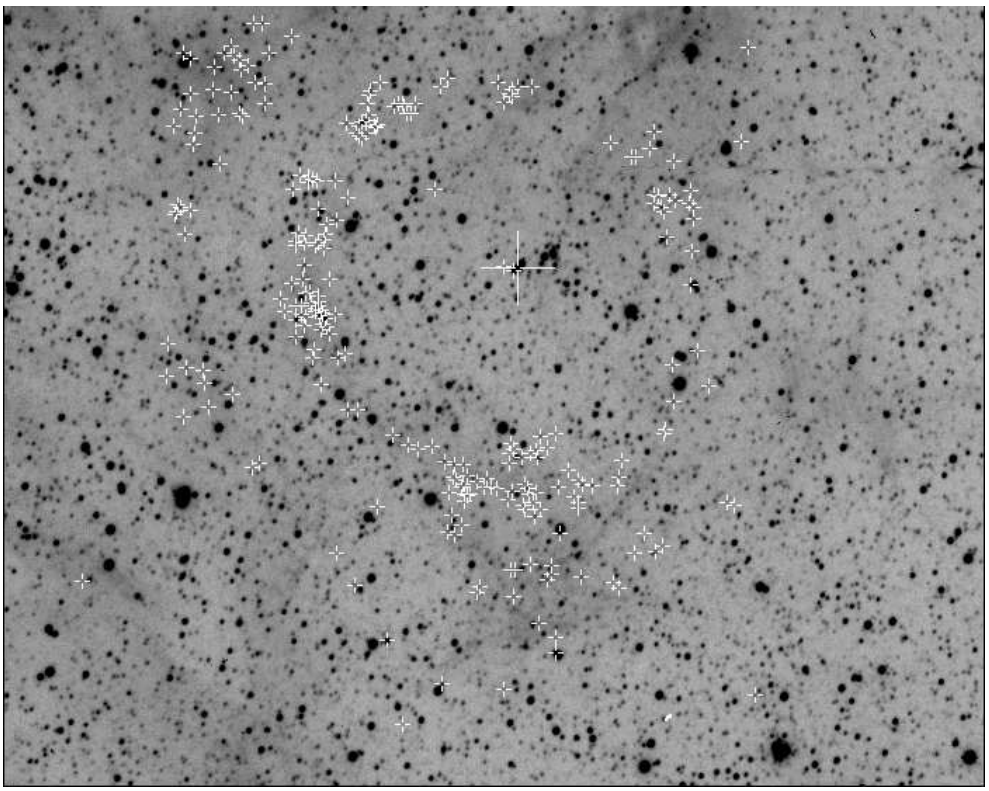

Figure 4.4:
The finding chart shows a region of MACHO's LMC field surrounding Supernova 1987a, indicated with the large cross. Pseudo–microlensing triggers are represented by the smaller crosses, and seem to trace nebulosity surrounding 1987a in 2 concentric circles. The triggers were eventually established as resulting from echos of the light from the SN explosion reflecting off the interstellar medium in the LMC. These reflections were superimposed on the brightness of LMC stars, triggering the Alert system. Stars in this region were henceforth excluded from microlensing alerts.

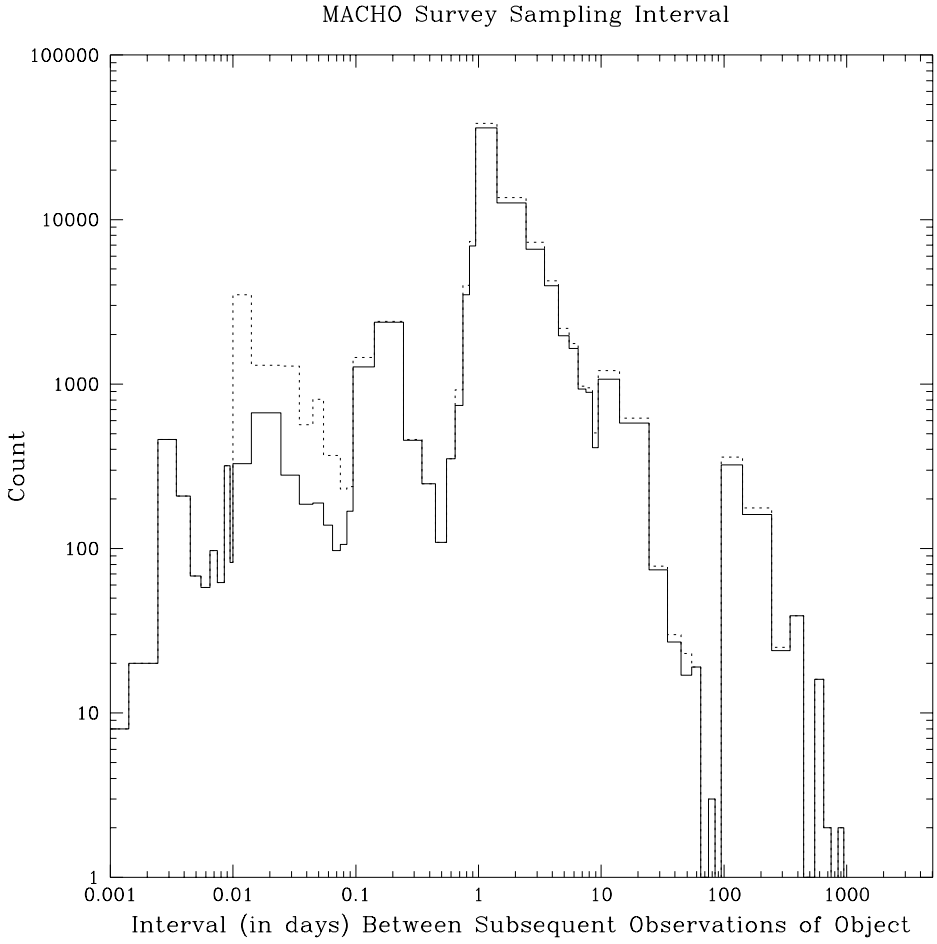

Figure 4.5:
The sampling frequency of the MACHO Survey is shown, representing the duration between subsequent observations of a particular star, summed over all stars also followed by the GMAN project. The most prominent feature at 1 day represents the approximately nightly sampling MACHO was able to achieve over its lifetime. The secondary peak at ~ 100 days represents the interval between observations at the end of one bulge season and the start of the next, when the Galactic bulge is behind the Sun. Secondary peaks are also seen at half–night and half–hour intervals, representing variation in observing strategy. The contribution of the 1999 bulge season is indicated with the *dashed* histogram, since the observing strategy was drastically altered to observe 4 fields at high frequency and gain sensitivity to ~ 0.2 day events.

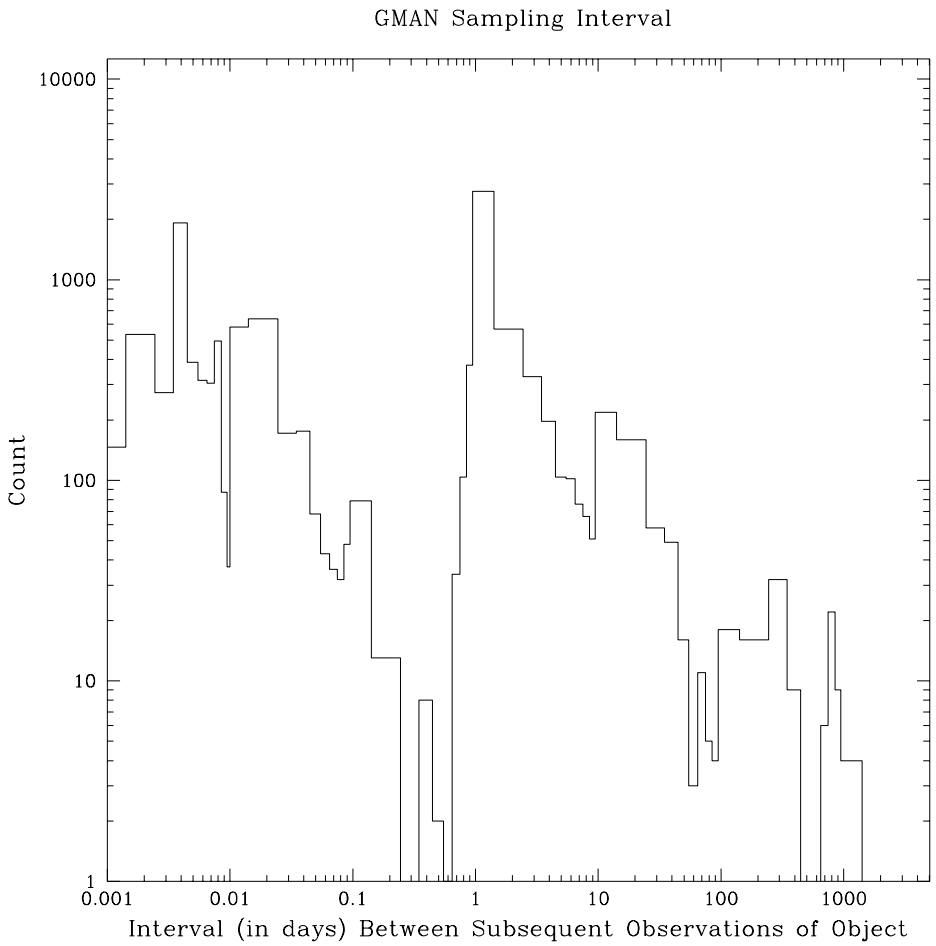

Figure 4.6:
The sampling frequency of the GMAN project is shown with the same objects used to make Figure 4.5. The short frequency regime contributes more significantly to the overall distribution here compared to MACHO's, due to GMAN's ability to focus resources on particularly interesting events. Significant peaks are seen at half–night, half–hour, and 5–minute intervals, where the latter is a typical exposure time. GMAN also required $\sim$ 1000 day interval observations to constrain source baseline brightnesses, since the lightcurves lacked MACHO's several year prior baseline.

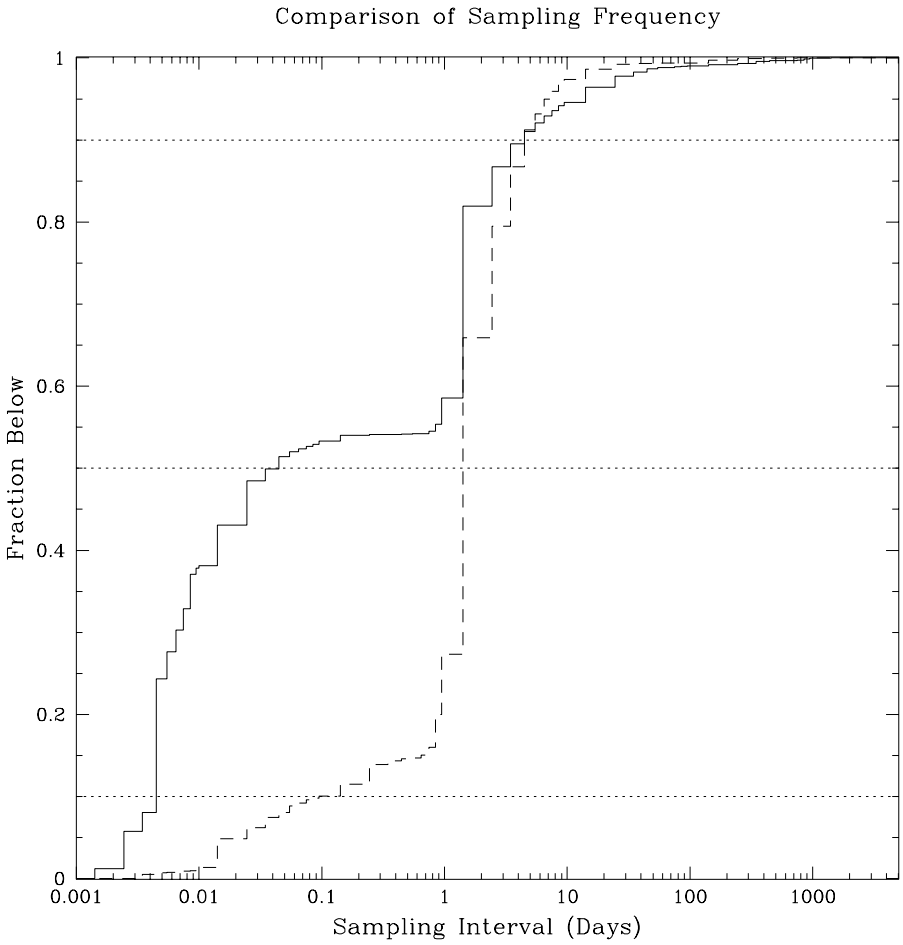

Figure 4.7:
A comparison of the distribution of MACHO's and GMAN's sampling frequencies is presented, showing the cumulative fraction below a given sampling frequency. The *solid* line indicates GMAN's cumulative distribution, the *dashed* line MACHO's. Horizontal lines represent 10%, 50%, and 90% of the distribution. More than half of the observations taken by GMAN were taken within 1 hour of the previous observation of the same object. The large jump in the GMAN distribution near 0.004 days is due to large numbers of observations taken 5 minutes apart, where 5 minutes is a typical exposure time. Both distributions show a similar feature at 1 day sampling. Note only 7.5% of MACHO's observations were taken with better than 1 hour sampling.

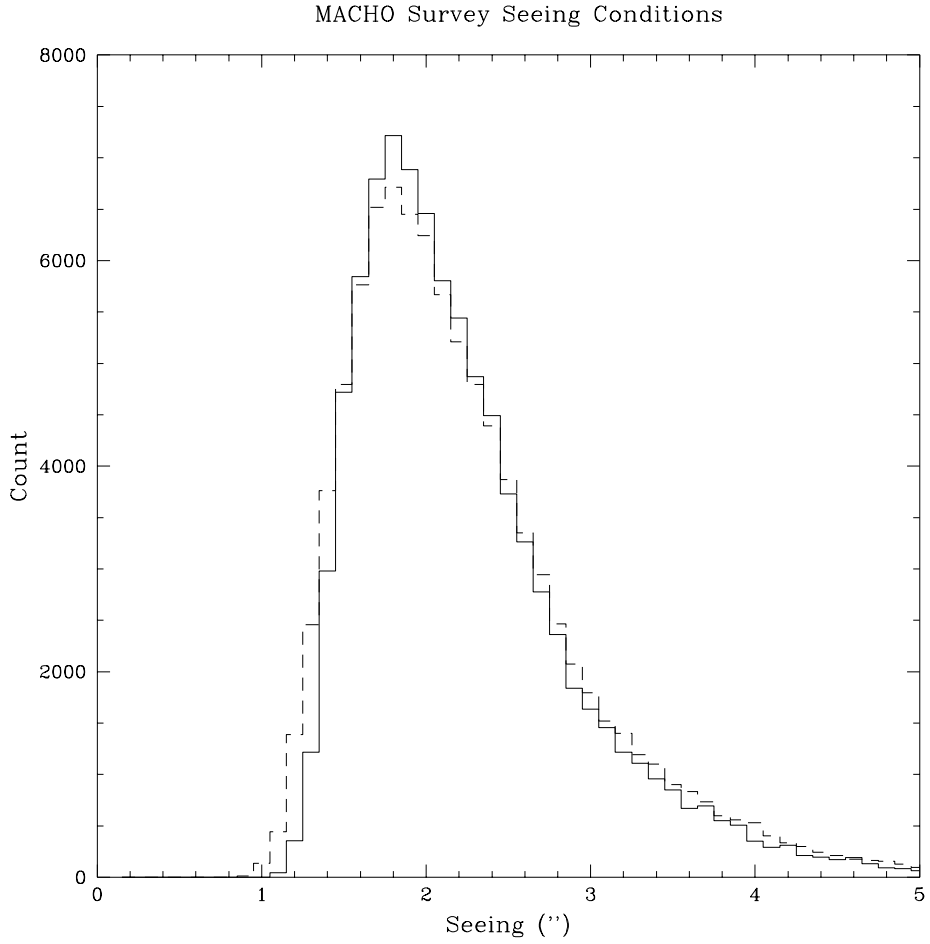

Figure 4.8: The distribution of seeing conditions for MACHO's observations of alerted events also followed by GMAN. The MACHO–Red passband is represented by the *solid* line, and the MACHO–Blue passband (which received slightly better seeing) the *dashed* line.

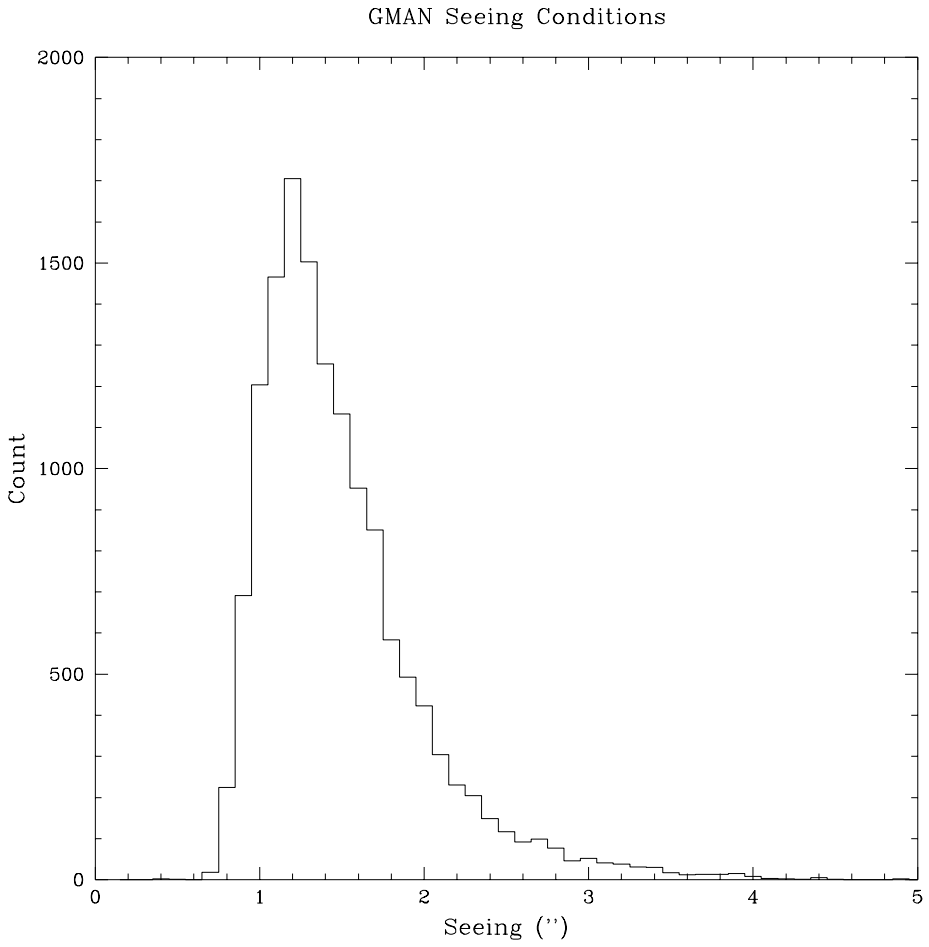

Figure 4.9: The distribution of GMAN's seeing conditions for the same set of alerts used to make Figure 4.8.

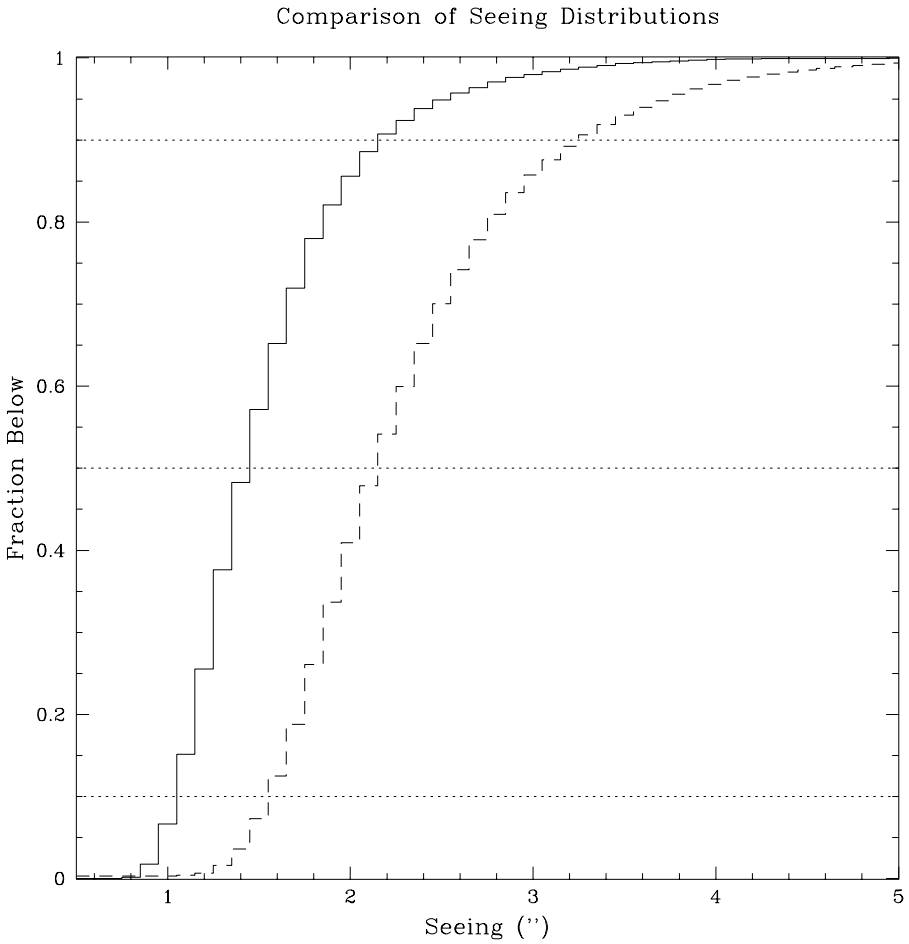

Figure 4.10:
The cumulative distributions of seeing conditions, presented as a fraction below a given seeing value. The *solid* line is the GMAN distribution, the *dashed* line is MACHO's. Horizontal lines represent 10%, 50%, and 90% of the distribution. The majority of GMAN's observations were taken in better than 1.5″ seeing, while less than 8% of MACHO's observations were of similar quality.

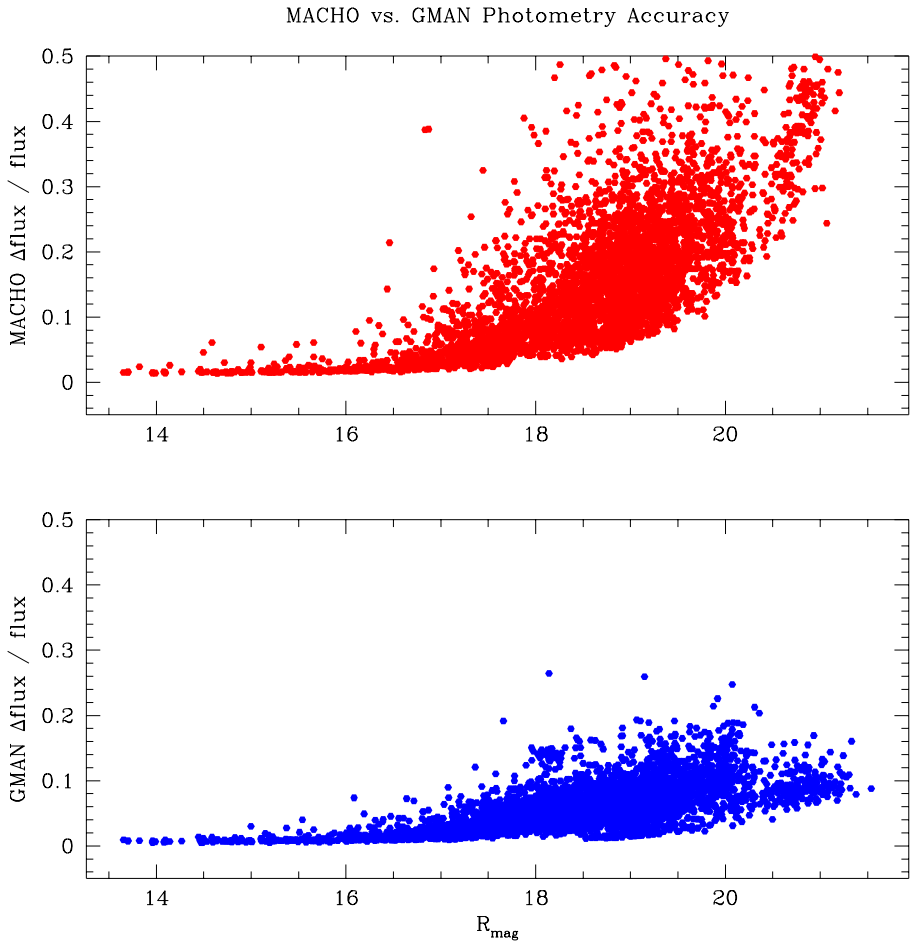

Figure 4.11:
Each panel indicates the average photometric errors in the lightcurves of $\sim$ 4500 stars, observed by both MACHO and the GMAN follow–up program. The minimum–error envelope for MACHO reaches 10% near $R \sim 19.5$, while GMAN is able to achieve similar accuracy photometry out past $R \gtrsim 21$.

Chapter 5

EXOTIC MICROLENSING: PARALLAX EVENTS

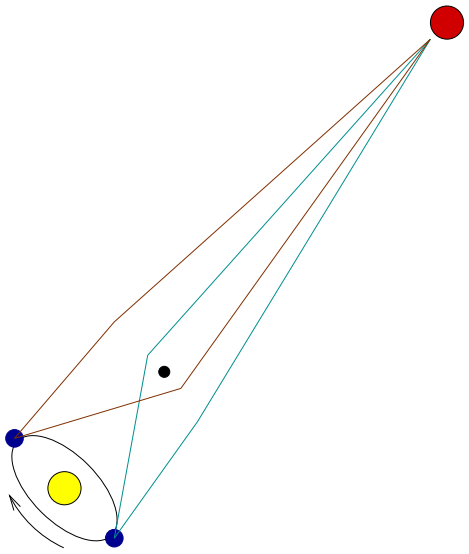

5.1 Parallax Theory

During very long timescale microlensing events ($\widehat{t} \gtrsim 100$ days), the Earth's annual motion around the Sun may introduce a significant deviation from the (assumed linear) motion of the source through the lens isomagnification contours. In this case, it is more appropriate regard the motion of the lens impact parameter (Equation 3.10) as linear with respect to the Solar position. To project this value to the Earth requires incorporating the Earth's orbital dynamics into the motion of the line–of–sight through the lensing system. This involves changing the form of the lens impact parameter $u(t)$ – the full representation may be found in Dominik (1998b). To first order in the Earth's eccentricity ϵ, this may be put in the form (Alcock et al. 1995a)

(5.1)

$$
\begin{aligned}
u^2(t) &= u_{\rm min}^2 + (2(t-t_0)/\widehat{t})^2 \\
&+ \alpha^2 \sin^2[\Omega(t-t_c)] \\
&+ \alpha^2 \sin^2\beta \cos^2[\Omega(t-t_c)] \\
&+ 2\alpha \sin[\Omega(t-t_c)]\,[(2(t-t_0)/\widehat{t})\sin\phi + u_{\rm min}\cos\phi] \\
&+ 2\alpha \sin\beta \cos[\Omega(t-t_c)][(2(t-t_0)/\widehat{t})\cos\phi - u_{\rm min}\sin\phi],
\end{aligned}
$$

where

$$\Omega(t-t_c) = \Omega_0(t-t_c) + 2\epsilon\sin[\Omega_0(t-t_p)] \tag{5.2}$$

and

$$\alpha = \frac{2{\rm R}_\oplus}{\tilde{v}\ \widehat{t}}\,(1-\epsilon\cos[\Omega_0(t-t_p)])\,. \tag{5.3}$$

The additional known parameters which enter into this equation are

- β: ecliptic latitude of the source star ,
- t_p: the time of perihelion in Earth's orbit, defined here as JD 2448989.813 ,
- t_c: the time when the Earth is closest to the Sun-source axis ,
- ϵ: ellipticity of the Earth's orbit (0.0167) ,
- ${\rm R}_\oplus$: semi–major axis of the Earth's orbit (1 Astronomical Unit) ,
- Ω_0: $2\pi\,{\rm yr}^{-1}$.

For a parallax event, there are 2 additional parameters which are fit for. These are:

- $\tilde{v}$: transverse speed of the lens projected to the solar position, $\tilde{v} \equiv v_\perp/(1-x)$,
- ϕ: angle between $\mathbf{v}_\perp$ and the North ecliptic axis. This indicates we are able to extract the proper motion **direction** of the lensing object – the motion of the Earth establishes the lightcurve shape in the absence of lens motion.

Note that $u_{\rm min}$ is no longer the minimum distance between the lens and the observer–source axis, but is the minimum distance between the lens and the Sun–source axis. The measurement of $\tilde{v}$ can be turned into a lens proper motion by

$$\mu \equiv \frac{v_\perp}{D_l} = \frac{\tilde{v}(1-x)}{D_l}. \tag{5.4}$$

Equation 3.17 may be used to determine a one–to–one relationship between the lens mass and distance. The likelihood analysis in parallax events is more secure than in exotic events where $\widehat{v}$ is determined, since Equation 3.18 does not involve an integration over ϕ.

The amplitude of the parallax contribution to $u(t)$ may be presented as $\delta u = (1-x)\mathrm{R}_\oplus/R_{\rm E}$, and thus represents a projection of $\mathrm{R}_\oplus$ into the lens plane. The physical situations which are likely to lead to parallax detections involve events where the lens is relatively close to the Earth, such that the projection of $\mathrm{R}_\oplus$ into the lens plane is not significantly smaller than $R_{\rm E}$. Also, the event is required to be long, such that the Earth's motion is not negligible for the duration of the event. This is generally true for slowly moving lenses, or lenses which are extremely massive. Gould (1992) suggests parallax allows sensitivity out to $M_l \sim 10^6 \mathrm{M}_\odot$.

5.2 Parallax Detections

The cumulative parallax signal accumulates slowly over time, thus an efficient observing strategy is to observe long events sparsely (once per night) at a particular site for the duration of the event. Many of the parallax candidates spanned multiple observing seasons, thus there are regions of time where the fit is not constrained. However, the GMAN program was able to schedule observations beyond the normal end of the Galactic bulge season, observing very early in the evening as the bulge was setting. For several of these events (96–BLG–5 and 96–BLG–12 in particular), GMAN provided significant lightcurve coverage which fully quantified the parallax signal. Properties of the microlensing events which show significant parallax are listed in Table 5.1. Included in this table are estimates of the apparent magnitude and color of the source object identified by MACHO, using the calibrations of Alcock et al. (1999c). However, since this object is likely to be a blend of

multiple stars, we also present the brightness of the lensed source, which is obtained from the blending parameters in the overall parallax fit.

The best microlensing fit parameters are presented in Table 5.2, and the blend fractions are presented in Table 5.3. For each fit, the MACHO data alone were fit with standard and parallax microlensing, labeled as fits "M:S" and "M:P" in Tables 5.2 & 5.3. A χ^2 improvement for the parallax fit was calculated. If GMAN data were also available for the event, it was refit using the full dataset, leading to fits "M+G:S" and "M+G:P". An empirical threshold of $\Delta\chi^2 = 25$ was established to signify a parallax detection. This was determined by looking at the distribution of $\Delta\chi^2$ for short (20 – 30 day) events, which should not show significant improvement when fit with parallax, and thus present a false signal. For each event in Table 5.1, the lightcurve, including the best standard and parallax fits, is presented in the odd numbered Figures 5.1–5.34.

For each event, the parallax $\hat{t}$ and $\tilde{v}$ are used to evaluate Equation 3.18 and Equation 3.17. This results in likelihood profiles for Galactic disk and bulge lens populations, seen as *dashed* and *dotted* lines in the even numbered Figures 5.2–5.34. The mass–distance Equation 3.17 is also plotted with the *solid* line as a function of x. We define a median distance $x_{\rm med}$ such that half of the integrated likelihood arises from $x < x_{\rm med}$. Similarly, we define a $1-\sigma$ confidence interval (x_1, x_2) such that 16% of the integrated likelihood arises from each of $x < x_1$ and $x > x_2$. These confidence limits on mass and distance are listed in Table 5.4. Given a significant number of parallax events, or another observer constraining these events (such as a parallax satellite), the mass spectrum of these Galactic disk lenses could be firmly established (Han & Gould 1995).

5.2.1 Conclusions

The exceptional parallax events are considered the following: 104–C (Figure 5.5), also the first reported parallax event (Alcock et al. 1995a); 96–BLG–5 (Figure 5.11) whose parallax behavior was predicted and subsequently detected; 96–BLG–12 (Figure 5.13) which is the best candidate, with $\Delta\chi^2 = 5713$; 99–BLG–1 (Figure 5.27) which shows clear deviations from the standard microlensing fit; and 99–BLG–8 (Figure 5.29) which is covered by GMAN for a substantial portion of its lightcurve. It is interesting that each of these events implies

a lens mass substantially heavier than a typical Galactic disk lens mass of $0.3 M_\odot$ – in all cases except 99–BLG–1, $M_l > 1\ M_\odot$. While it is expected that parallax events are likely to reveal the heavier end of the lens mass distribution, the most important result of this ensemble of parallax events is the extent of the mass distribution in objects heavier than a solar mass.

Heavy Lenses

There are 3 events with best–fit masses greater than 2 $M_\odot$: events 96–BLG–5, 98–BLG–6, and 99-BLG–22. Event 96–BLG–5 is considered an exceptional parallax candidate, with $\Delta\chi^2 = 2354$. While the event was ongoing, near date 1700 in Figure 5.11, the lightcurve was fit for parallax, which predicted the future behavior of the event near day 1800. Since this secondary peak was predicted while evaluating the lightcurve in the context of the parallax microlensing model, this is interpreted as a clear sign of a legitimate parallax signal, even though the lightcurve might seem unusual compared to typical parallax microlensing events. In fact, the GMAN observations were specially scheduled to detect or limit this exact predicted effect. The result is a constraint on what is likely the heaviest mass lens yet detected – Table 5.4 indicates a best fit mass of 73 $M_\odot$. If such a lens were a normal main sequence star, it would dominate the apparent brightness and color of the lensed object. Table 5.3 indicates that only $\sim 10\%$ of the object's brightness is lensed, but this is not nearly enough light to account for a 73 $M_\odot$ main–sequence lens. The only plausible explanation for this lens is a massive black hole, very likely a stellar remnant from the supernova of a massive star. The full confidence limits resulting from the 96–BLG–5 likelihood analysis are shown below:

	$+3\sigma$	$+2\sigma$	$+1\sigma$	median	-1σ	-2σ	-3σ
$M_l(M_\odot)$	1252	566	176	73	33	7.3	3.7
D_l(kpc)	0.09	0.2	0.6	1.3	2.4	5.4	6.6 .

It is thus very unlikely that this lens weighs less than $\sim 4\ M_\odot$. The significance of this event – *this represents the first detection of an isolated stellar mass black hole.*

It is possible the other 2 events with $M_l > 2$ M$_\odot$ are also stellar remnants, but the evidence is less compelling. Both lenses are less than $2-\sigma$ away from a typical main sequence lens, $M_l \sim 0.3$ M$_\odot$. The same can be said about the 4 events with $M_l \sim 1$ M$_\odot$. However, the distribution in masses is suggestive of a population of dark stellar remnant lenses (Gould 2000).

Light Lenses

Also noteworthy are 3 events, 179.22619.3190, 97–BLG–25, and 99–BLG–18, where the lens masses are merely several thousandths of a solar mass. 179.22619.3190 has an unusual morphology (Figure 5.1) which might be explained by a variety of lensing (or even non–lensing) phenomena – it is considered the weakest candidate of the group. The remaining 2 have very short standard and parallax $\widehat{t}$ values, implying the parallax interpretation might not be appropriate. In fact, 97–BLG–25 (Figure 5.19) is the only event where the addition of the GMAN data *lessens* the $\Delta\chi^2$ between standard and parallax fits, compared to fits with only the MACHO data. 99–BLG–18 is the only of these 3 events where there is no obvious red flag – its $3-\sigma$ upper limit on mass is $M_l < 0.04$ M$_\odot$.

5.3 Parallax Non-Detections

For several of the events covered by GMAN, the lack of a parallax signal provides significant constraints on the properties of the lensing object. This leads to an exclusion region in the (D_l, M_l) plane defined by Equation 3.17.

We quantify a null parallax detection by fixing $\tilde{v}$ in a series of parallax microlensing fits, in logarithmic intervals between 1 and 10,000. All other fit parameters are free to minimize. We define a significant constraint as when the parallax fit with $\tilde{v}$ fixed increases by $\Delta\chi^2 = 25$ from the best standard microlensing fit. This establishes $\tilde{v}_{\rm min}$ for the lens, given our lightcurve coverage. Table 5.5 lists a select set of events whose lightcurves constrain $\tilde{v} > 25\,{\rm km\,s^{-1}}$, or whose lightcurves are densely covered.

The corresponding lightcurves, including standard microlensing fits, are presented in the odd numbered Figures 5.35–5.52. The even numbered Figures 5.35–5.52 show the evolution of $\Delta\chi^2$ vs. fixed $\tilde{v}$. The horizontal line is the threshold $\Delta\chi^2 = 25$, and the parallax limit is

defined as the location where the *solid* line representing $\Delta\chi^2$ crosses this threshold.

5.3.1 Conclusions

95-BLG-13

The most significant constraint on $\tilde{v}$ comes from the coverage of event 95–BLG–13, which is densely covered by GMAN observations (Figure 5.35). The increase in χ^2 as a function of fixed $\tilde{v}$ is shown in Figure 5.36. A threshold of $\Delta\chi^2 = 25$ is reached when $\tilde{v} \sim 96\,\mathrm{km\,s^{-1}}$. A minimum mass as a function of x may be determined given the minimum $\tilde{v}$ by evaluating the right side of Equation 3.17. The value of the best standard fit $\widehat{t}$, the limiting value of $\tilde{v}$, and the value of this minimum mass function are given in Table 5.6 for all parallax null detections.

99-LMC-2

A significant limit is also set on $\tilde{v}$ for event 99–LMC–2 : $\tilde{v}_{min} = 43.1\,\mathrm{km\,s^{-1}}$. However, parallax only provides a somewhat weak constraint for events seen towards the LMC. For example, a typical Galactic halo lens is expected to be at a distance of $\sim 10\,\mathrm{kpc}$ along the line of sight to the LMC. In this case $x = 0.2$, and our 99–LMC–2 $\tilde{v}$ constraint yields $M_{l,min} = 0.03\ \mathrm{M}_\odot$. Practically, this is not a very useful conclusion, considering the LMC microlensing signal is consistent with $M_l \sim 0.5\ \mathrm{M}_\odot$ (Alcock et al. 2000a). However, for lenses within our thick or thin Galactic disk, this constraint becomes more significant. For a thick disk lens at, for instance 1 kpc, the constraint becomes $M_{l,min} = 0.4\ \mathrm{M}_\odot$, within the range of Galactic dark matter masses.

The standard microlensing fit indicates blending fractions of $f_{MACHO_R} = 0.78, f_B = 0.88$. If we attribute all of the unlensed flux to the lens, it would have an apparent magnitude of $R = 22.3$. Note this is a maximum allowed brightness for the lens.

The low mass isochrones of Girardi et al. (2000) are used to estimate the physical properties of candidate main sequence, thick disk lenses. It is assumed the thick disk metallicity is $z = 0.001$, with its constituent objects 10 Gyr old (e.g, Ng et al. 1997). For each entry in the Girardi et al. (2000) isochrones, the distance modulus to the object is determined for it to appear with $R = 22.3$. This distance modulus will increase with

Table 5.1: Information on the lensed MACHO objects and de–blended source stars for parallax events. The event name, internal MACHO ID, and ecliptic latitude and longitude are presented. Also included are the V–band brightness and $V-R$ colors of the lensed MACHO object, as well as for the actual lensed source (determined from blending parameters in the parallax fit).

Event	MACHO Id	λ	β	MACHO V	Object $V-R$	Lensed V	Source $V-R$
...	179.22619.3190	272.0	-2.7	21.01	1.35	21.00	1.27
101-B	101.21689.315	271.6	-4.0	17.50	1.09	17.70	1.07
104-C	104.20251.50	270.8	-4.6	17.32	0.92	17.27	0.92
124-A	124.22157.151	271.8	-7.5	17.18	0.93	...	...
95-BLG-27	109.21024.5007	271.2	-5.0	20.23	0.69	22.51	0.79
96-BLG-5	104.20906.3973	271.1	-4.3	19.87	0.86	22.70	0.89
96-BLG-12	104.20382.803	270.9	-4.5	17.82	0.94	17.88	0.93
96-BLG-28	114.20496.5206	270.9	-5.6	20.00	0.85	20.70	0.77
97-BLG-8	118.18529.538	269.9	-6.7	19.54	1.04	19.96	1.04
97-BLG-25	116.23864.503	272.6	-6.4	17.86	0.82	18.73	0.81
97-BLG-43	114.19583.5176	270.4	-5.8	19.57	0.79	21.17	0.74
98-BLG-1	104.20910.7700	271.1	-4.0	19.37	0.85	19.84	0.85
98-BLG-6	402.48103.1719	269.5	-5.3	19.55	1.06	19.50	1.09
99-BLG-1	121.22423.1032	271.9	-7.1	18.85	0.87	...	...
99-BLG-8	403.47849.756	269.2	-6.2	15.82	1.32	16.60	1.29
99-BLG-18	108.19204.267	270.2	-5.1	16.74	1.03	...	...
99-BLG-22	109.20893.3423	271.1	-5.1	19.77	0.93	20.43	0.71

mass – put another way, the implied mass increases the farther away the object is. For each distance modulus, the fractional distance to the source x is evaluated, assuming the source is at 50 kpc. $M_{l,min}$ is then established using $0.0084 \times (1-x)/x$ from Table 5.6. As the distance x increases, this minimum mass will decrease. A limit is established at the distance where this minimum mass crosses the Girardi et al. (2000) implied mass necessary to account for the blended flux. This limit occurs for lens masses weighing approximately 0.18 $M_\odot$, located at $x = 0.05$, ~ 2.5 kpc along the line of sight to the source, or 2.5 scale heights above the Galactic midplane. This configuration is marginally unlikely. All main sequence lenses closer than 2.5 kpc can be excluded using this combination of microlensing and photometric parallax. However, if the lens is a stellar remnant, this analysis is not applicable.

Table 5.2: Comparison of standard and parallax microlensing fits, for datasets excluding and including the GMAN follow–up data. The fits labeled "M:S" and "M:P" represent standard and parallax microlensing fits using the MACHO data only. The improvement in χ^2 between these 2 fits is shown in the last column. Fits "M+G:S" and "M+G:P" include all available GMAN data, and the overall χ^2 improvement for the entire data–set is also shown in the last column. Reported uncertainties in the final significant digit(s) are the maximum extent of the surface in parameter space which has a χ^2 greater than the best–fit value by 1.

[a] Blending fits did not converge, and these values represent the best microlensing fits without accounting for blending.

Event	Fit	t_0	$\widehat{t}$ (days)	$u_{\rm min}$	$\tilde{v}$ ($\rm km\,s^{-1}$)	ϕ (rad)	$\Delta\chi^2$
179.22619.3190	M:S	1623.40 (46)	231 (19)	0.165 (16)	···	···	···
···	M:P	1630.70 (74)	27.3 (84)	-0.41 (13)	26.41 (25)	-1.742 (23)	104
101-B	M:S	593.06 (10)	187.8 (38)	0.1704 (52)	···	···	···
···	M:P	569.3 (67)	222 (10)	0.553 (36)	30.4 (34)	-59.454 (96)	60
104-C	M:S	493.940 (62)	354.7 (58)	0.0737 (17)	···	···	···
···	M:P	509.6 (11)	213.1 (51)	0.171 (18)	70.5 (58)	-0.998 (69)	1057
124-A[a]	M:S	418.49 (30)	139.3 (12)	0.00 (10)	···	···	···
···	M:P	561.2 (28)	77.9 (39)	1.271 (45)	14.02 (26)	-1.277 (29)	83
95-BLG-27	M:S	1321.60 (15)	305 (36)	0.0554 (77)	···	···	···
···	M:P	1325.3 (70)	456 (71)	-0.174 (21)	29.5 (19)	-6.36 (15)	52
···	M+G:S	1321.800 (56)	437 (50)	0.0349 (42)	···	···	···
···	M+G:P	1316.3 (33)	536 (88)	-0.163 (21)	27.5 (10)	-0.264 (63)	133
96-BLG-5	M:S	1739.1 (17)	1310 (154)	0.208 (30)	···	···	···
···	M:P	1763.1 (18)	2351 (413)	0.038 (12)	37.7 (16)	-1.32 (13)	315
···	M+G:S	1754.1 (18)	2110 (732)	0.107 (42)	···	···	···
···	M+G:P	1763.6 (13)	3418 (1795)	0.0105 (60)	30.8 (12)	-0.833 (60)	2354
96-BLG-12	M:S	1758.30 (26)	1079 (56)	0.0223 (13)	···	···	···
···	M:P	1735.5 (11)	424 (26)	-0.023 (10)	47.5 (18)	-0.960 (61)	3595
···	M+G:S	1767.800 (41)	638 (14)	0.0185 (4)	···	···	···
···	M+G:P	1742.80 (37)	297.4 (54)	0.1872 (43)	39.03 (51)	-2.110 (12)	5713
96-BLG-28	M:S	1748.60 (15)	192 (19)	0.0310 (38)	···	···	···
···	M:P	1728.30 (65)	163.12 (91)	0.8894 (91)	20.27 (12)	-9.1395 (89)	7
···	M+G:S	1749.000 (40)	208 (20)	0.0255 (27)	···	···	···
···	M+G:P	1748.40 (26)	235.20 (61)	0.7051 (13)	19.922 (47)	-21.9200 (33)	28
97-BLG-8	M:S	1952.200 (31)	121.9 (32)	-0.0434 (17)	···	···	···
···	M:P	1974.00 (67)	139.6 (32)	0.585 (11)	-27.37 (54)	-3.483 (12)	37
···	M+G:S	1952.100 (20)	130.7 (30)	0.0388 (11)	···	···	···
···	M+G:P	1976.2 (33)	145.6 (34)	0.566 (27)	26.4 (21)	-0.384 (37)	59

Table 5.2: Continued

Event	Fit	t_0	$\widehat{t}$ (days)	$u_{\rm min}$	$\tilde{v}$ (km s^{-1})	ϕ (rad)	$\Delta\chi^2$
97-BLG-25	M:S	1971.20 (15)	50.5 (34)	0.302 (32)	···	···	···
···	M:P	2008.60 (88)	18.9 (23)	-0.38 (15)	22.75 (34)	-7.702 (34)	37
···	M+G:S	1971.30 (15)	51.6 (34)	0.293 (30)	···	···	···
···	M+G:P	2008.70 (85)	19.5 (21)	-0.32 (14)	22.75 (35)	-7.692 (33)	34
97-BLG-43	M:S	2019.700 (53)	123.0 (88)	-0.0243 (20)	···	···	···
···	M:P	2058.30 (72)	417.3 (78)	-0.2601 (48)	10.07 (15)	-5.8406 (81)	20
···	M+G:S	2019.700 (43)	143 (13)	0.0202 (22)	···	···	···
···	M+G:P	2054.90 (43)	313.1 (44)	-0.1629 (26)	15.36 (15)	-5.670 (12)	25
98-BLG-1	M:S	2266.00 (22)	315 (18)	0.0726 (52)	···	···	···
···	M:P	2305.9 (15)	330.1 (62)	0.4956 (50)	21.57 (32)	11.991 (21)	79
···	M+G:S	2266.00 (22)	324 (17)	0.0702 (47)	···	···	···
···	M+G:P	2290.6 (32)	300 (16)	0.264 (39)	29.9 (30)	-0.468 (38)	82
98-BLG-6	M:S	2398.20 (76)	323 (26)	0.408 (49)	···	···	···
···	M:P	2380.5 (35)	464 (53)	0.204 (50)	-75.1 (96)	-17.75 (22)	51
···	M+G:S	2395.10 (47)	257 (27)	0.497 (77)	···	···	···
···	M+G:P	2380.0 (42)	400 (40)	0.277 (55)	80 (10)	4.01 (21)	158
99-BLG-1[a]	M:S	2719.80 (43)	440.2 (38)	0.2927 (9)	···	···	···
···	M:P	2709.4 (15)	-210.0 (82)	0.294 (16)	36.18 (78)	-13.906 (40)	1033
···	M+G:S	2720.40 (39)	418.2 (32)	0.2879 (9)	···	···	···
···	M+G:P	2711.9 (10)	221.5 (44)	0.2332 (47)	43.22 (65)	-1.846 (22)	1846
99-BLG-8	M:S	2732.10 (12)	159.5 (43)	0.607 (26)	···	···	···
···	M:P	2728.50 (41)	295 (22)	0.106 (16)	-57.6 (29)	-4.794 (26)	161
···	M+G:S	2731.900 (77)	134.21 (27)	0.8321 (9)	···	···	···
···	M+G:P	2729.50 (20)	278.9 (26)	0.1131 (4)	56.16 (56)	-1.604 (10)	518
99-BLG-18[a]	M+G:S	2678.500 (66)	40.04 (23)	0.4757 (20)	···	···	···
···	M+G:P	2704.2 (19)	22.0 (12)	-2.128 (92)	31.95 (79)	-2.251 (46)	29
···	M+G:S	2678.500 (56)	40.08 (21)	0.4687 (17)	···	···	···
···	M+G:P	2711.00 (11)	18.62 (20)	-2.757 (39)	27.88 (23)	-2.169 (11)	50
99-BLG-22	M:S	2742.00 (42)	1660 (303)	0.0170 (33)	···	···	···
···	M:P	2746.7 (54)	929 (87)	-0.0480 (64)	-49.3 (71)	-1.88 (73)	15
···	M+G:S	2742.30 (16)	1676 (319)	0.0167 (32)	···	···	···
···	M+G:P	2721.6 (70)	674 (80)	0.108 (16)	25.6 (44)	-3.34 (16)	34

Table 5.3: Comparison of blending fractions for standard and parallax microlensing fits. Fits are the same as presented in Table 5.2. Reported uncertainties in the final significant digit(s) are the maximum extent of the surface in parameter space which has a χ^2 greater than the best–fit value by 1.

[a] Blending fits did not converge, and these values represent the best microlensing fits without accounting for blending.

Event	Fit	f_{MACHO_R}	f_{MACHO_B}	f_{CTIO_R}	f_{UTSO_R}	f_{UTSO_V}	f_{WISE_R}
179.22619.3190	M:S	0.63 (9)	0.71 (12)	···	···	···	···
···	M:P	0.93 (88)	1.04 (106)	···	···	···	···
101-B	M:S	0.77 (3)	0.79 (4)	···	···	···	···
···	M:P	0.81 (5)	0.83 (6)	···	···	···	···
104-C	M:S	0.74 (2)	0.72 (2)	···	···	···	···
···	M:P	1.05 (6)	1.04 (6)	···	···	···	···
124-A[a]	M:S	1.00 (0)	1.00 (0)	···	···	···	···
···	M:P	1.00 (0)	1.00 (0)	···	···	···	···
95-BLG-27	M:S	0.28 (4)	0.25 (3)	···	···	···	···
···	M:P	0.19 (4)	0.16 (3)	···	···	···	···
···	M+G:S	0.18 (2)	0.16 (2)	0.18 (2)	0.17 (2)	0.17 (2)	0.24 (8)
···	M+G:P	0.14 (2)	0.12 (2)	0.16 (3)	0.17 (3)	0.16 (3)	0.14 (4)
96-BLG-5	M:S	0.31 (5)	0.29 (5)	···	···	···	···
···	M:P	0.12 (2)	0.11 (2)	···	···	···	···
···	M+G:S	0.16 (6)	0.15 (6)	0.16 (6)	···	···	···
···	M+G:P	0.08 (4)	0.07 (4)	0.08 (4)	···	···	···
96-BLG-12	M:S	0.13 (0)	0.13 (0)	···	···	···	···
···	M:P	0.42 (5)	0.43 (5)	···	···	···	···
···	M+G:S	0.27 (0)	0.27 (0)	0.29 (0)	···	···	···
···	M+G:P	0.93 (4)	0.95 (4)	0.99 (4)	···	···	···
96-BLG-28	M:S	0.47 (6)	0.53 (8)	···	···	···	···
···	M:P	0.77 (2)	0.86 (3)	···	···	···	···
···	M+G:S	0.40 (5)	0.45 (6)	0.51 (7)	···	···	···
···	M+G:P	0.48 (1)	0.54 (1)	0.57 (2)	···	···	···
97-BLG-8	M+G:S	0.73 (3)	0.74 (4)	···	···	···	···
···	M+G:P	0.73 (3)	0.74 (3)	···	···	···	···
···	M+G:S	0.67 (2)	0.67 (2)	0.87 (3)	···	···	···
···	M+G:P	0.67 (2)	0.68 (2)	0.92 (4)	···	···	···

Table 5.3: Continued

Event	Fit	f_{MACHO_R}	f_{MACHO_B}	f_{CTIO_R}	f_{UTSO_R}	f_{UTSO_V}	f_{WISE_R}
97-BLG-25	M:S	0.64 (12)	0.66 (12)	···	···	···	···
···	M:P	0.44 (7)	0.45 (7)	···	···	···	···
···	M+G:S	0.62 (11)	0.63 (11)	0.69 (12)	···	···	···
···	M+G:P	0.44 (6)	0.45 (6)	0.48 (7)	···	···	···
97-BLG-43	M:S	0.22 (1)	0.23 (2)	···	···	···	···
···	M:P	0.22 (0)	0.23 (0)	···	···	···	···
···	M+G:S	0.19 (2)	0.20 (2)	0.38 (4)	···	···	···
···	M+G:P	0.21 (0)	0.23 (0)	0.46 (1)	···	···	···
98-BLG-1	M:S	0.62 (6)	0.63 (6)	···	···	···	···
···	M:P	0.76 (2)	0.76 (2)	···	···	···	···
···	M+G:S	0.60 (5)	0.61 (5)	0.49 (4)	···	···	···
···	M+G:P	0.65 (5)	0.65 (5)	0.50 (3)	···	···	···
98-BLG-6	M:S	2.27 (148)	1.99 (98)	···	···	···	···
···	M:P	0.75 (28)	0.73 (27)	···	···	···	···
···	M+G:S	3.58 (488)	2.65 (240)	2.93 (289)	···	···	···
···	M+G:P	1.07 (43)	1.03 (40)	1.10 (44)	···	···	···
99-BLG-1[a]	M:S	1.00 (0)	1.00 (0)	···	···	···	···
···	M:P	1.00 (0)	1.00 (0)	···	···	···	···
···	M+G:S	1.00 (0)	1.00 (0)	1.00 (0)	···	···	···
···	M+G:P	1.00 (0)	1.00 (0)	1.00 (0)	···	···	···
99-BLG-8	M:S	3.50 (124)	3.67 (136)	···	···	···	···
···	M:P	0.44 (7)	0.46 (8)	···	···	···	···
···	M+G:S	5.92 (7)	6.24 (9)	6.66 (15)	···	···	7.76 (56)
···	M+G:P	0.47 (0)	0.49 (0)	0.52 (0)	···	···	0.54 (1)
99-BLG-18[a]	M:S	1.00 (0)	1.00 (0)	···	···	···	···
···	M:P	1.00 (0)	1.00 (0)	···	···	···	···
···	M+G:S	1.00 (0)	1.00 (0)	1.00 (0)	···	···	···
···	M+G:P	1.00 (0)	1.00 (0)	1.00 (0)	···	···	···
99-BLG-22	M:S	0.09 (1)	0.12 (2)	···	···	···	···
···	M:P	0.26 (4)	0.36 (6)	···	···	···	···
···	M+G:S	0.09 (1)	0.12 (2)	0.18 (3)	···	···	···
···	M+G:P	0.42 (9)	0.58 (14)	0.92 (26)	···	···	···

Table 5.4: List of most likely lens mass and distance values determined from evaluation of the likelihood function Equation 3.18, for events with parallax detections. Errors correspond to $1-\sigma$ confidence intervals.

[a] Blending fits did not converge, and these values represent the best microlensing fits without accounting for blending.

Event	$\tilde{v}$ ($\mathrm{km\,s^{-1}}$)	D_l (kpc)	M_l ($\mathrm{M_\odot}$)
179.22619.3190	26.41	$1.2^{+1.2}_{-0.7}$	$0.0038^{+0.0064}_{-0.0023}$
101-B	30.4	$1.0^{+1.9}_{-0.7}$	$0.39^{+0.77}_{-0.29}$
104-C	70.5	$1.9^{+1.1}_{-0.8}$	$0.93^{+0.91}_{-0.45}$
124-A[a]	14.02	$1.0^{+1.0}_{-0.6}$	$0.010^{+0.017}_{-0.006}$
95-BLG-27	27.5	$1.3^{+1.1}_{-0.7}$	$1.5^{+2.2}_{-0.8}$
96-BLG-5	30.8	$1.3^{+1.1}_{-0.7}$	73^{+104}_{-39}
96-BLG-12	39.03	$1.2^{+1.5}_{-0.7}$	$0.94^{+1.66}_{-0.61}$
96-BLG-28	19.922	$0.97^{+1.36}_{-0.60}$	$0.20^{+0.38}_{-0.14}$
97-BLG-8	26.4	$1.2^{+1.1}_{-0.7}$	$0.10^{+0.15}_{-0.06}$
97-BLG-25	22.75	$1.1^{+1.0}_{-0.6}$	$0.0016^{+0.0026}_{-0.0009}$
97-BLG-43	15.36	$1.1^{+1.1}_{-0.6}$	$0.19^{+0.31}_{-0.11}$
98-BLG-1	29.9	$1.3^{+1.1}_{-0.7}$	$0.53^{+0.75}_{-0.28}$
98-BLG-6	80	$2.9^{+3.1}_{-1.8}$	$2.5^{+6.0}_{-1.9}$
99-BLG-1[a]	43.22	$1.2^{+1.2}_{-0.7}$	$0.65^{+1.04}_{-0.38}$
99-BLG-8	56.16	$1.6^{+1.3}_{-0.8}$	$1.3^{+1.7}_{-0.7}$
99-BLG-18[a]	27.88	$1.1^{+1.3}_{-0.7}$	$0.0021^{+0.0037}_{-0.0013}$
99-BLG-22	25.6	$0.97^{+1.67}_{-0.62}$	$2.8^{+5.4}_{-2.0}$

Table 5.5: Information on the lensed MACHO objects and de–blended source stars for events which show no significant signs of parallax. The event name, internal MACHO ID, and ecliptic latitude and longitude are presented. Also included are the V–band brightness and $V-R$ colors of the lensed MACHO object, as well as for the actual lensed source (determined from blending parameters in the standard microlensing fit).

Event	MACHO Id	λ	β	MACHO V	Object $V-R$	Lensed V	Source $V-R$
95-BLG-1	113.18292.2374	269.8	-5.2	19.17	1.05	19.48	1.07
95-BLG-13	102.22466.140	272.0	-4.3	16.82	0.96	16.86	0.95
95-BLG-19	102.23635.1426	272.6	-4.3	18.82	0.69	19.00	0.64
95-BLG-26	105.21161.7671	271.2	-4.6	18.78	0.75	18.96	0.76
96-BLG-1	104.20645.3129	271.0	-4.4	17.69	1.07	17.85	1.06
97-BLG-18	104.20121.1692	270.7	-4.6	18.59	0.88	19.14	0.88
97-BLG-26	118.18797.1397	270.0	-6.2	19.33	1.28	19.29	1.30
97-BLG-56	403.47671.57	269.0	-6.1	16.09	1.33	16.30	1.35
99-LMC-2	79.5863.4522	321.3	-85.1	21.02	0.44	21.18	0.36

Table 5.6: Events which show no significant signs of parallax. The standard microlensing fit $\widehat{t}$ is listed, as well as the minimum allowed value of $\tilde{v}$. This value is determined by fitting the event with $\tilde{v}$ fixed in logarithmic intervals from 1 to $10,000$, and allowing all other parameters to be fit for. This parallax limit is established when the change in χ^2 from the best standard fit exceeds 25. The bottom set of events have weak parallax limits, but good coverage of the event lightcurve. The final column represents the minimum mass function of the lens assuming sources at 8.5 kpc, except for 99–LMC–2, where the source is assumed at 50 kpc.

Event	$\widehat{t}$	$\tilde{v}_{min}$	$(M_{l,min}\frac{x}{1-x})$ $M_\odot$
95-BLG-13	155.1	95.7	0.26
96-BLG-1	165.8	27.1	0.024
97-BLG-18	208	45.5	0.11
97-BLG-26	122.2	49.7	0.044
97-BLG-56	41.04	30.9	0.0019
99-LMC-2	148.9	43.1	0.0084
95-BLG-1	55.7	9.1	0.00031
95-BLG-19	70.0	5.3	0.00017
95-BLG-26	43.3	22.2	0.0011

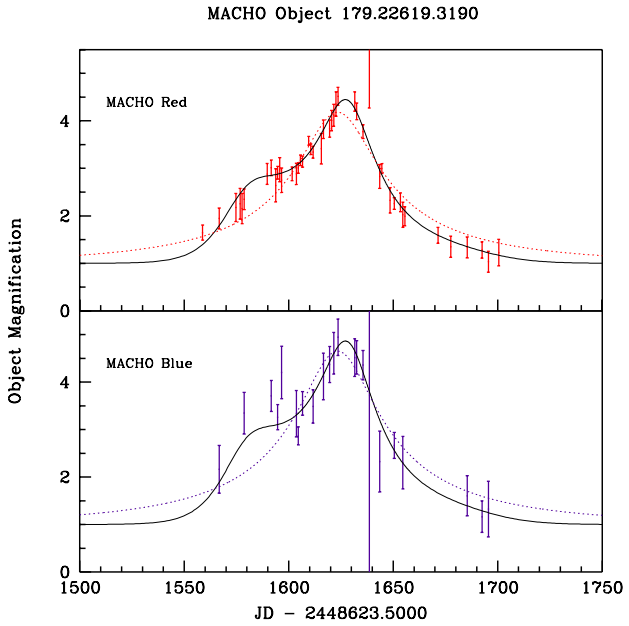

Figure 5.1:
Lightcurve of MACHO object 179.22619.3190, including parallax (*solid* line) and standard (*dotted* line) microlensing fits.

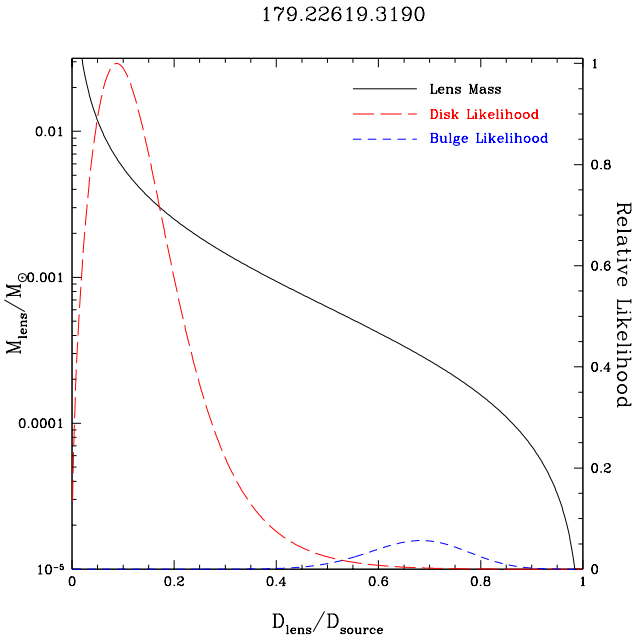

Figure 5.2:
179.22619.3190 lens mass plotted as a function of its distance, using Equation 3.17, as the *solid* line. The *dashed* and *dotted* likelihood curves show relative probabilities of disk and bulge lenses as a function of distance.

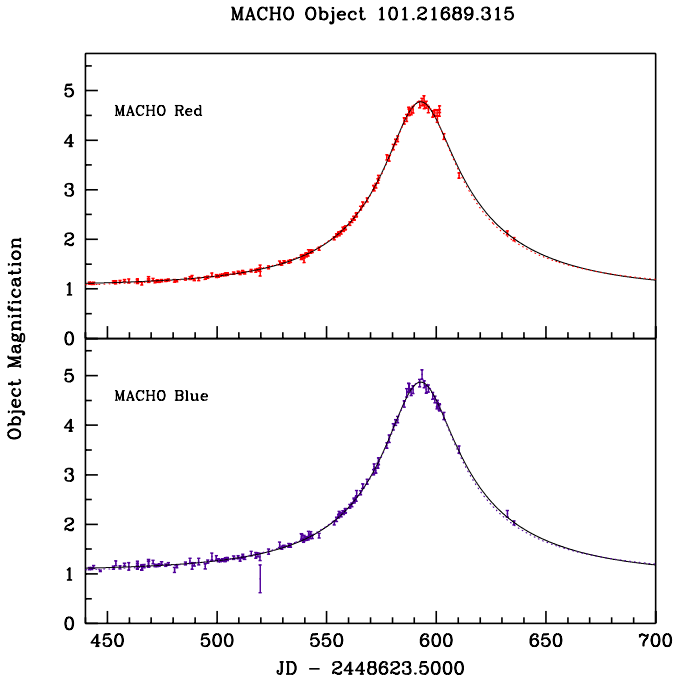

Figure 5.3: Lightcurve of MACHO event 101–B, including parallax (*solid* line) and standard (*dotted* line) microlensing fits.

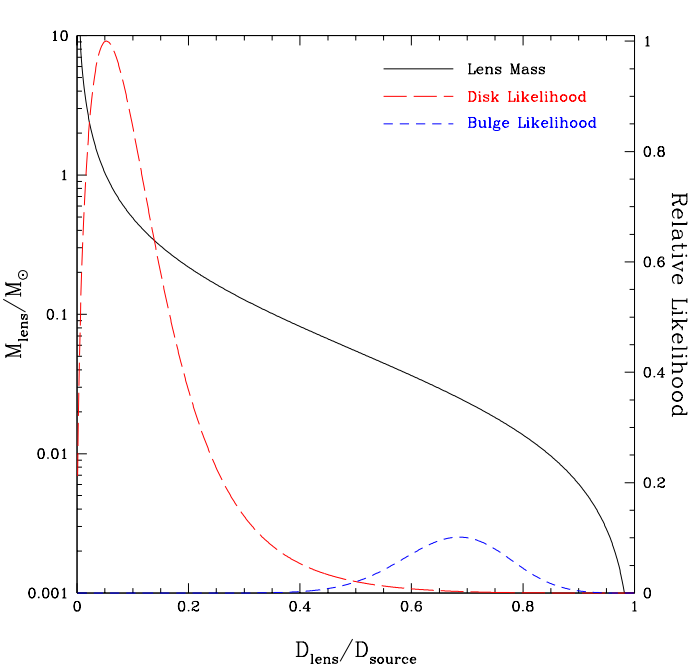

Figure 5.4: 101–B lens mass, Galactic disk likelihood, and Galactic bulge likelihood, plotted as a function of lens distance.

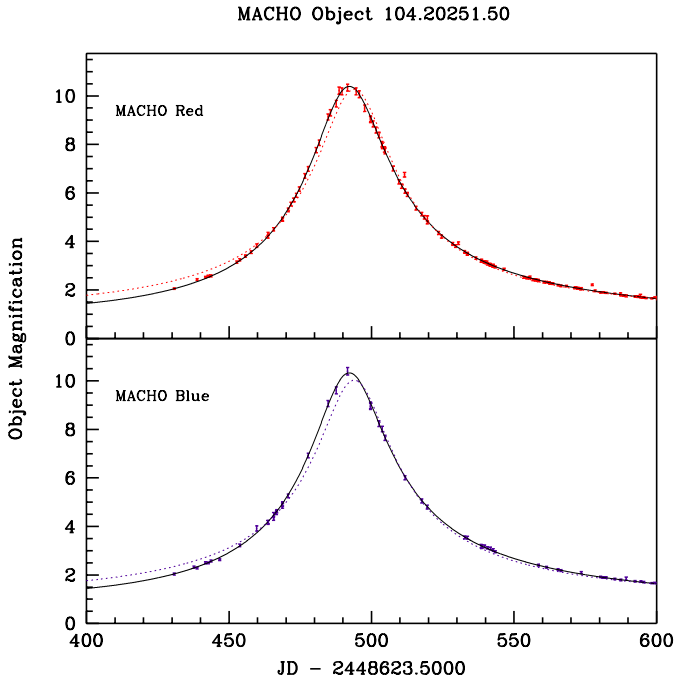

Figure 5.5: Lightcurve of MACHO event 104-C, including parallax (*solid* line) and standard (*dotted* line) microlensing fits.

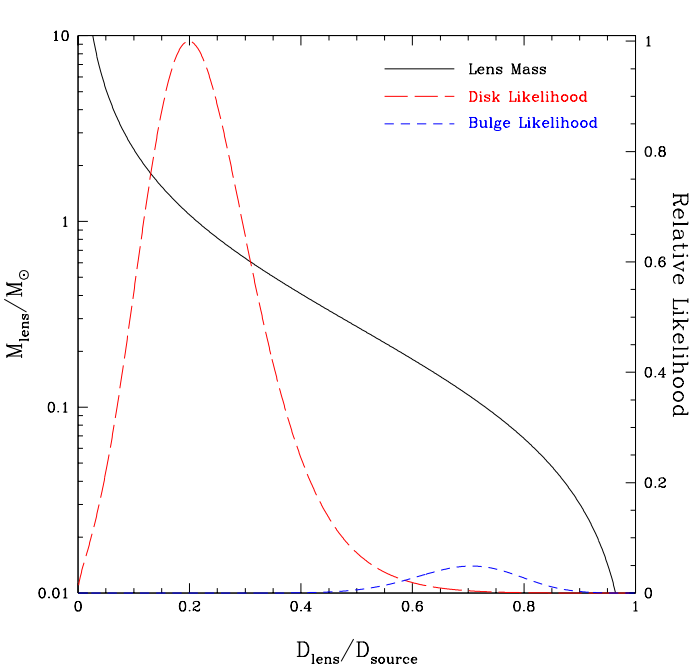

Figure 5.6: 104-C lens mass, Galactic disk likelihood, and Galactic bulge likelihood, plotted as a function of lens distance.

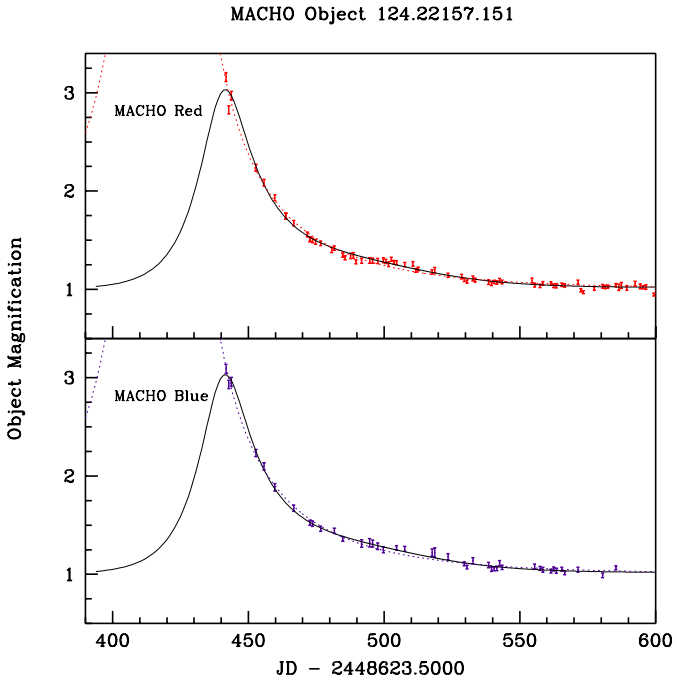

Figure 5.7: Lightcurve of MACHO event 124-A, including parallax (*solid* line) and standard (*dotted* line) microlensing fits.

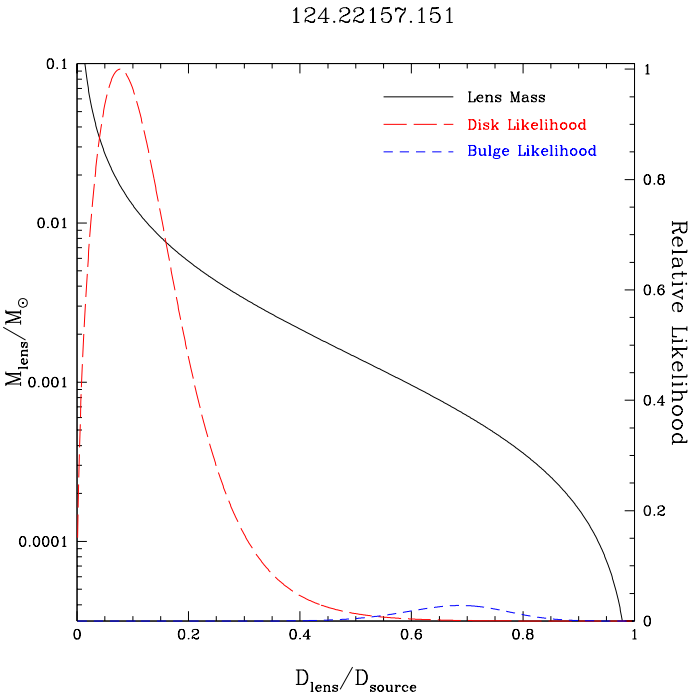

Figure 5.8: 124-A lens mass, Galactic disk likelihood, and Galactic bulge likelihood, plotted as a function of lens distance.

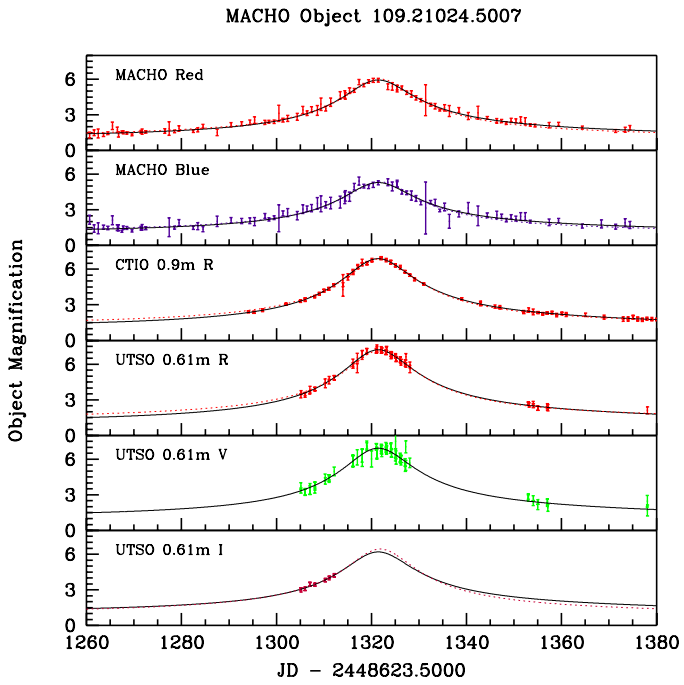

Figure 5.9: Lightcurve of MACHO event 95-BLG-27, including parallax (*solid* line) and standard (*dotted* line) microlensing fits.

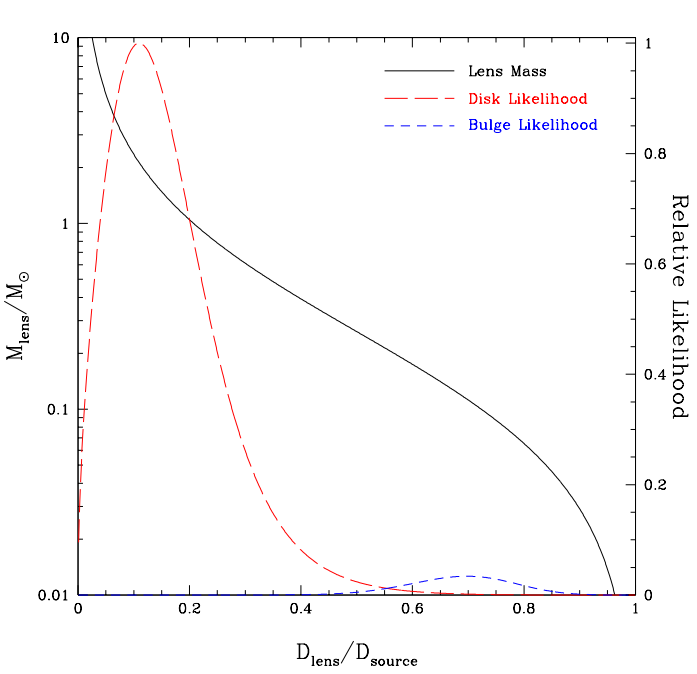

Figure 5.10: 95-BLG-27 lens mass, Galactic disk likelihood, and Galactic bulge likelihood, plotted as a function of lens distance.

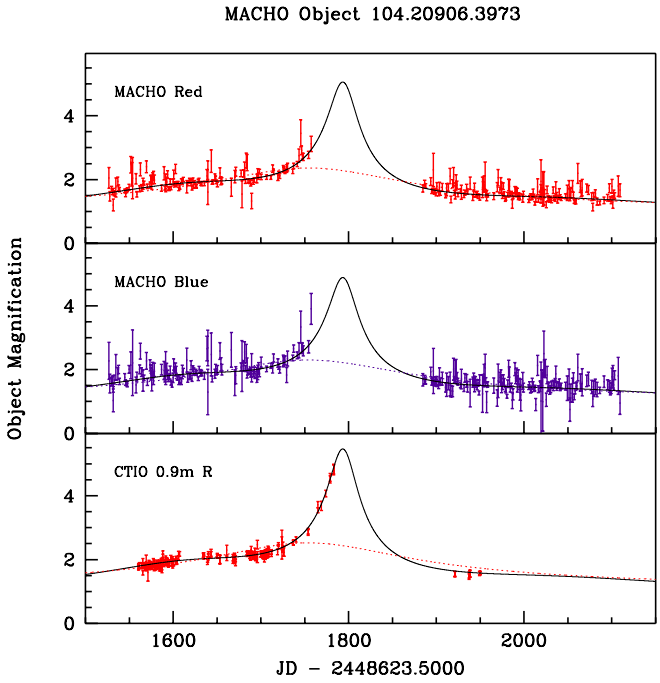

Figure 5.11: Lightcurve of MACHO event 96-BLG-5, including parallax (*solid* line) and standard (*dotted* line) microlensing fits.

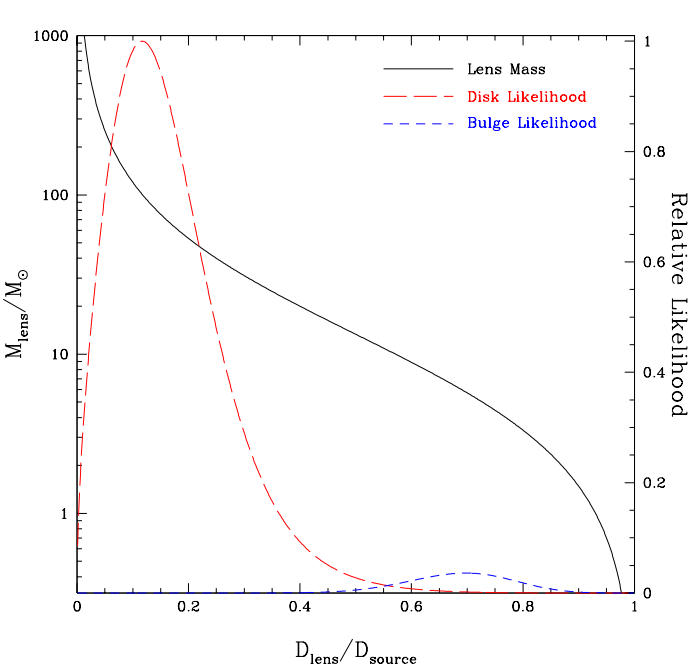

Figure 5.12: 96-BLG-5 lens mass, Galactic disk likelihood, and Galactic bulge likelihood, plotted as a function of lens distance.

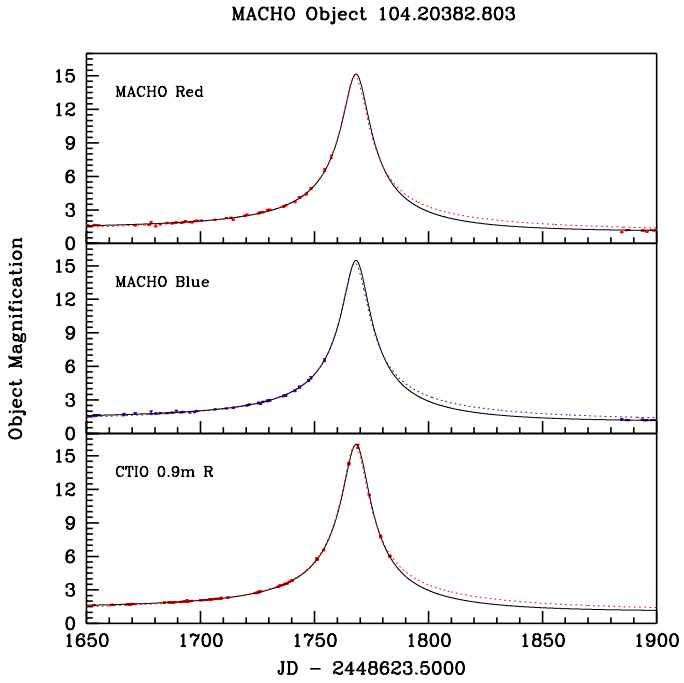

Figure 5.13: Lightcurve of MACHO event 96-BLG-12, including parallax (*solid* line) and standard (*dotted* line) microlensing fits.

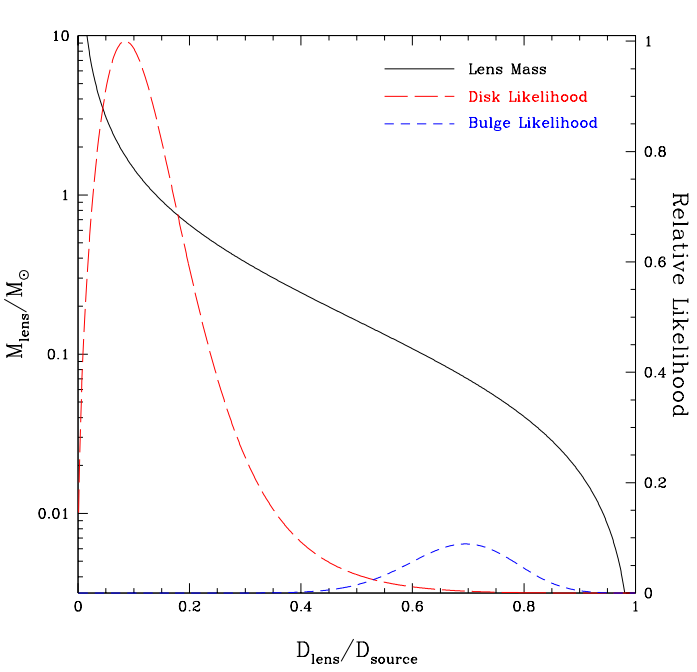

Figure 5.14: 96-BLG-12 lens mass, Galactic disk likelihood, and Galactic bulge likelihood, plotted as a function of lens distance.

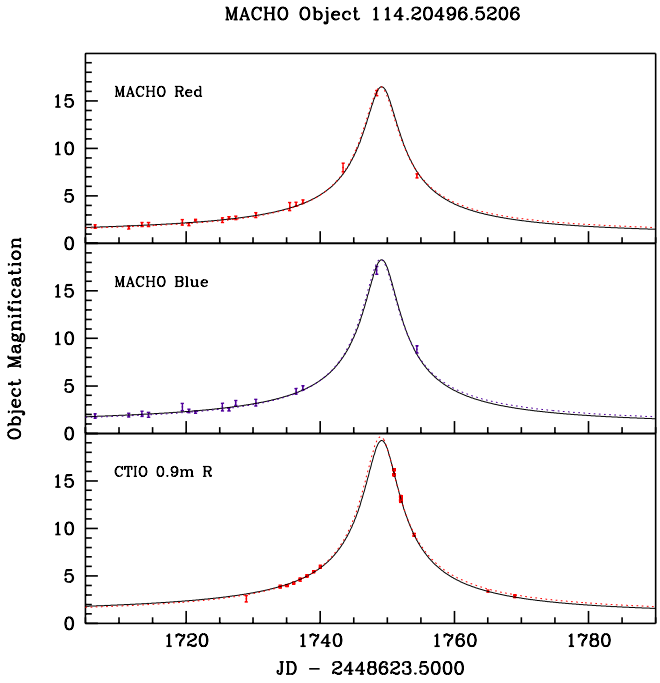

Figure 5.15:
Lightcurve of MACHO event 96-BLG-28, including parallax (*solid* line) and standard (*dotted* line) microlensing fits.

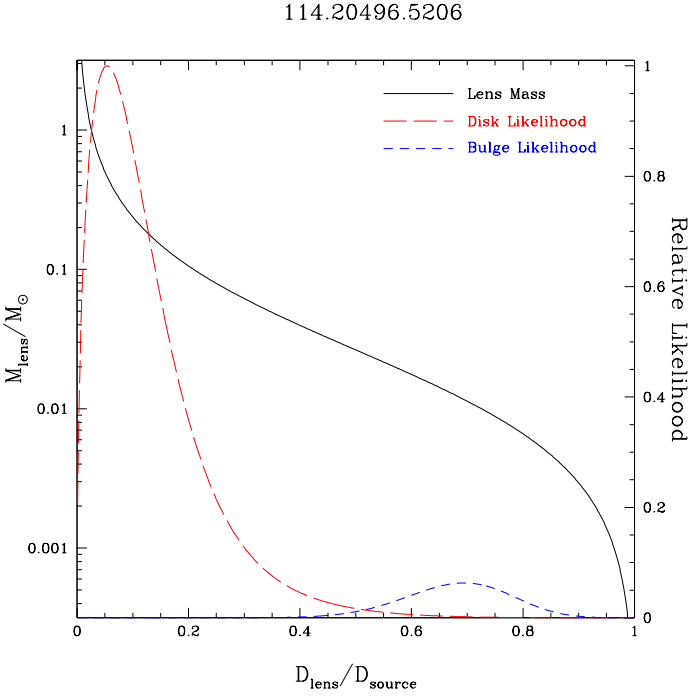

Figure 5.16:
96-BLG-28 lens mass, Galactic disk likelihood, and Galactic bulge likelihood, plotted as a function of lens distance.

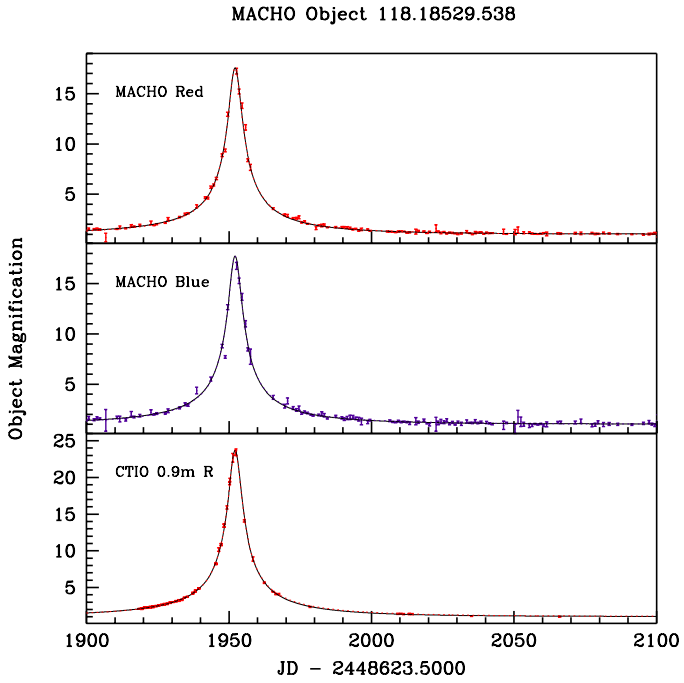

Figure 5.17:
Lightcurve of MACHO event 97-BLG-8, including parallax (*solid* line) and standard (*dotted* line) microlensing fits.

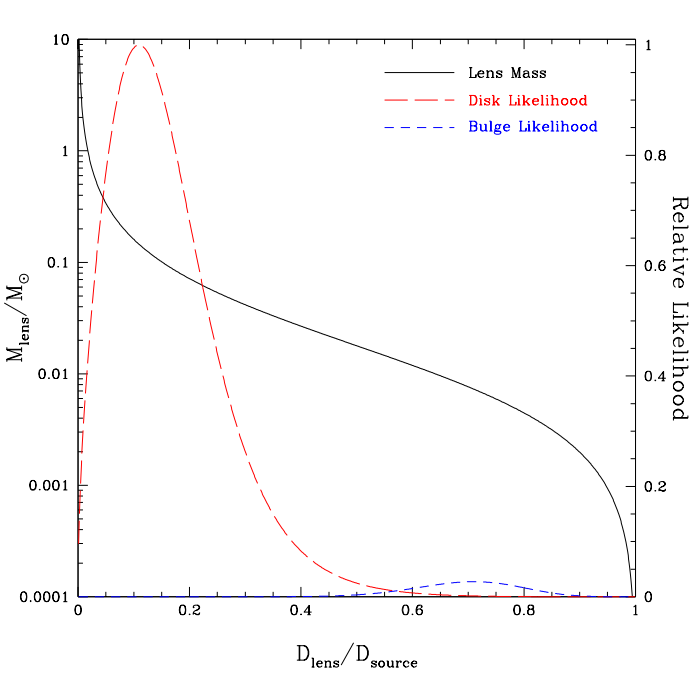

Figure 5.18: 97-BLG-8 lens mass, Galactic disk likelihood, and Galactic bulge likelihood, plotted as a function of lens distance.

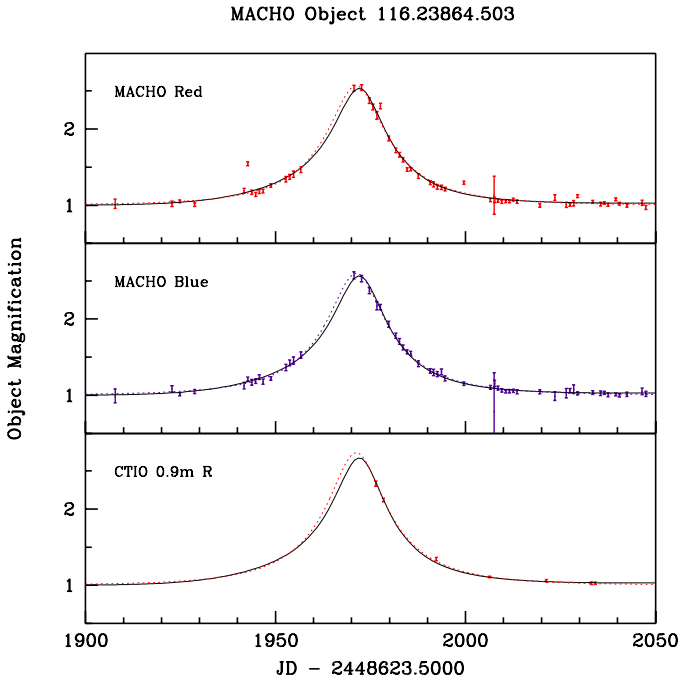

Figure 5.19:
Lightcurve of MACHO event 97-BLG-25, including parallax (*solid* line) and standard (*dotted* line) microlensing fits.

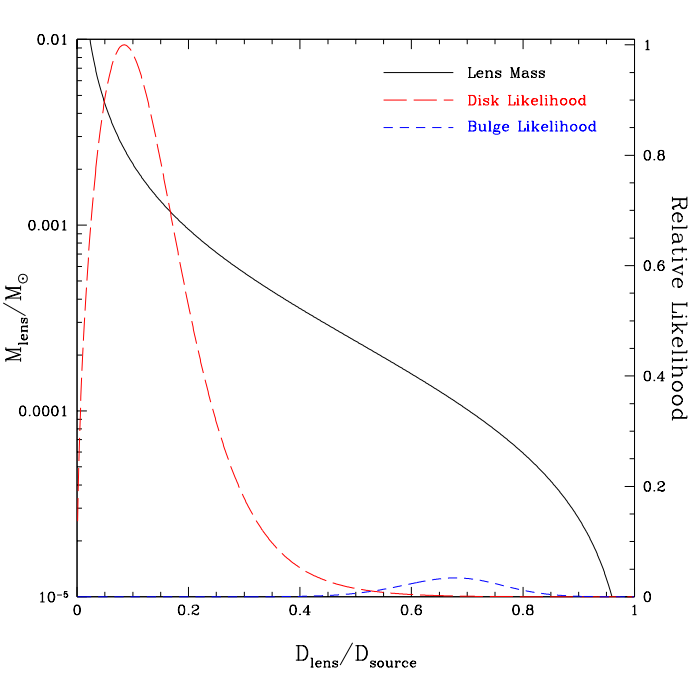

Figure 5.20: 97-BLG-25 lens mass, Galactic disk likelihood, and Galactic bulge likelihood, plotted as a function of lens distance.

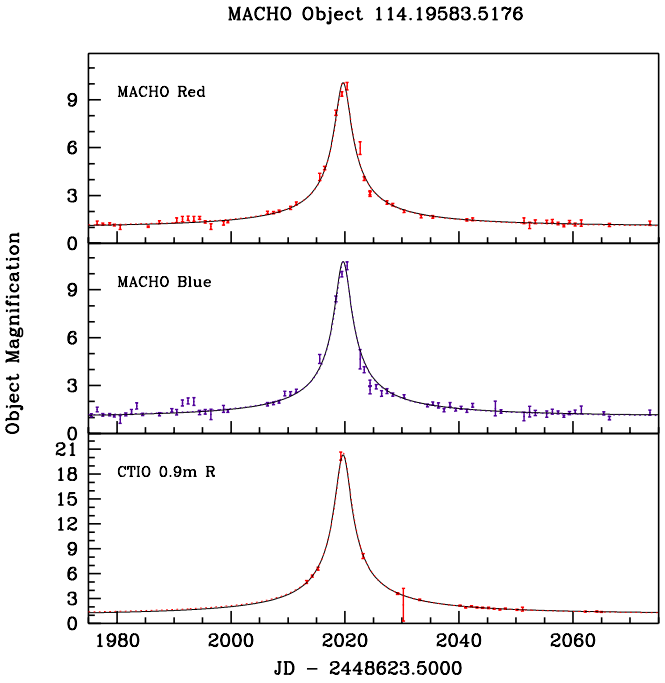

Figure 5.21: Lightcurve of MACHO event 97-BLG-43, including parallax (*solid* line) and standard (*dotted* line) microlensing fits.

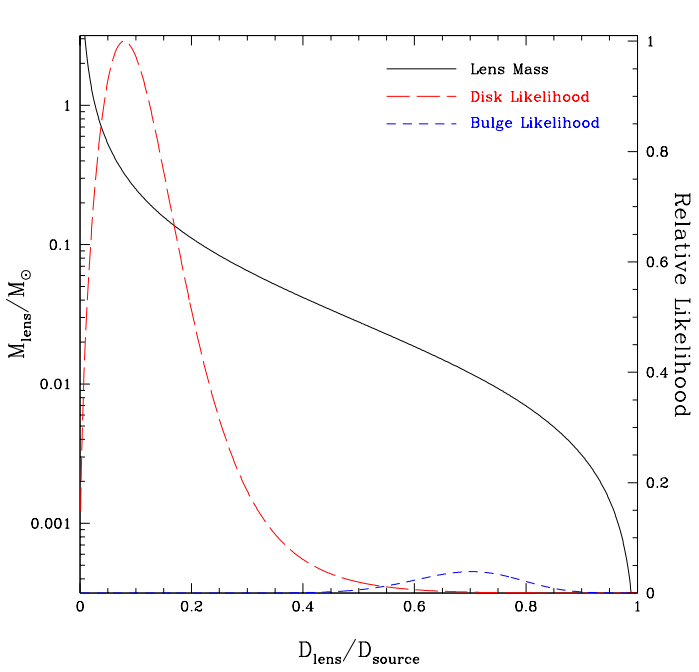

Figure 5.22: 97-BLG-43 lens mass, Galactic disk likelihood, and Galactic bulge likelihood, plotted as a function of lens distance.

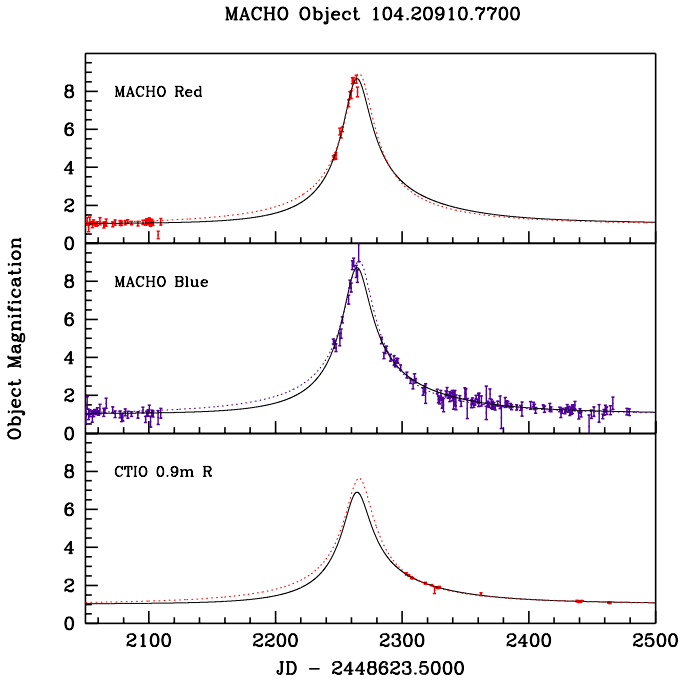

Figure 5.23: Lightcurve of MACHO event 98-BLG-1, including parallax (*solid* line) and standard (*dotted* line) microlensing fits.

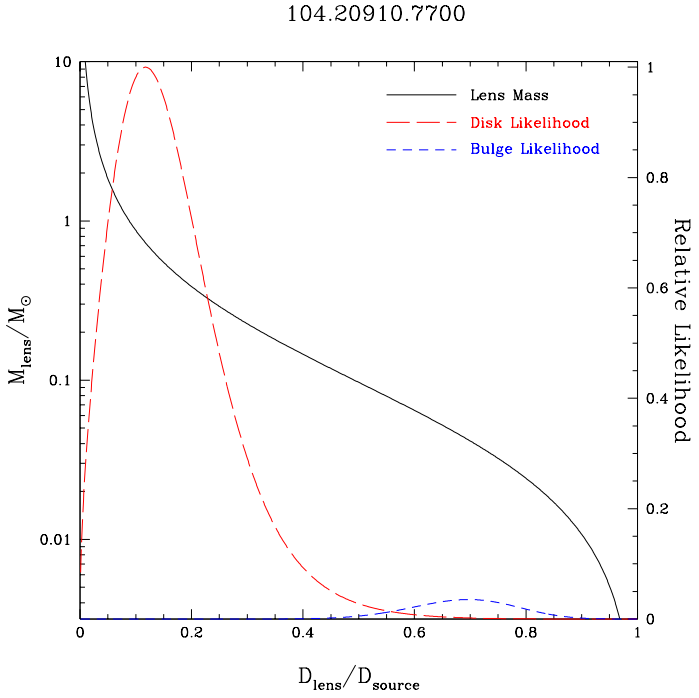

Figure 5.24:
98-BLG-1 lens mass, Galactic disk likelihood, and Galactic bulge likelihood, plotted as a function of lens distance.

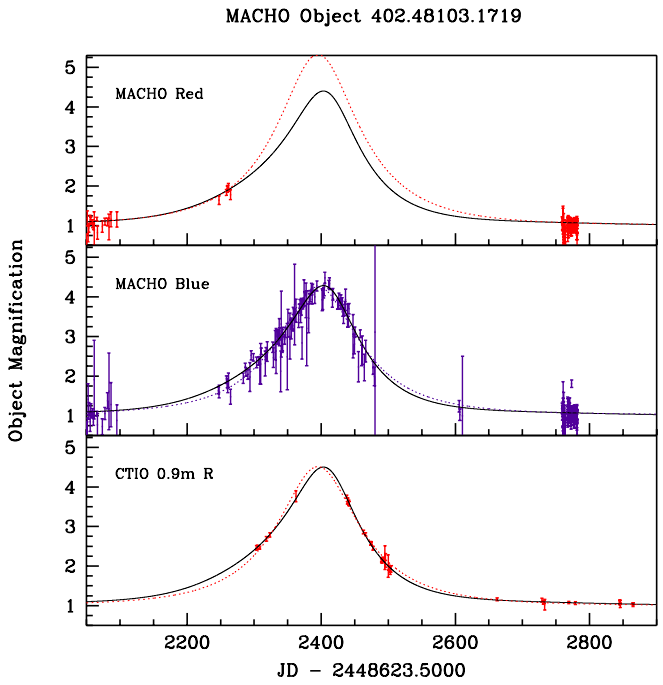

Figure 5.25: Lightcurve of MACHO event 98-BLG-6, including parallax (*solid* line) and standard (*dotted* line) microlensing fits.

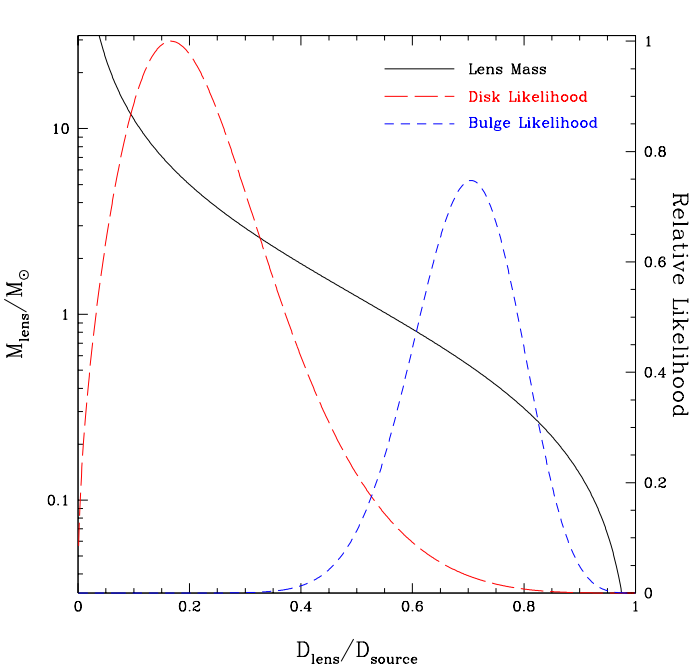

Figure 5.26:
98-BLG-6 lens mass, Galactic disk likelihood, and Galactic bulge likelihood, plotted as a function of lens distance.

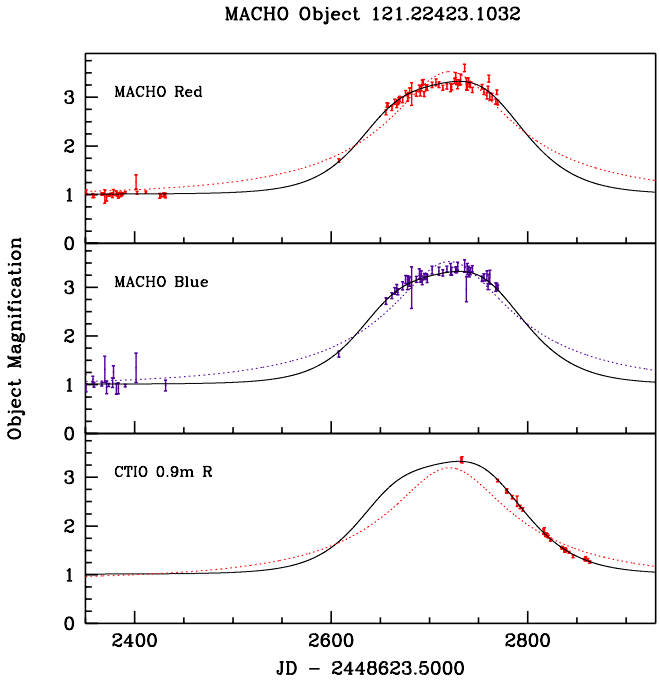

Figure 5.27:
Lightcurve of MACHO event 99-BLG-1, including parallax (*solid* line) and standard (*dotted* line) microlensing fits.

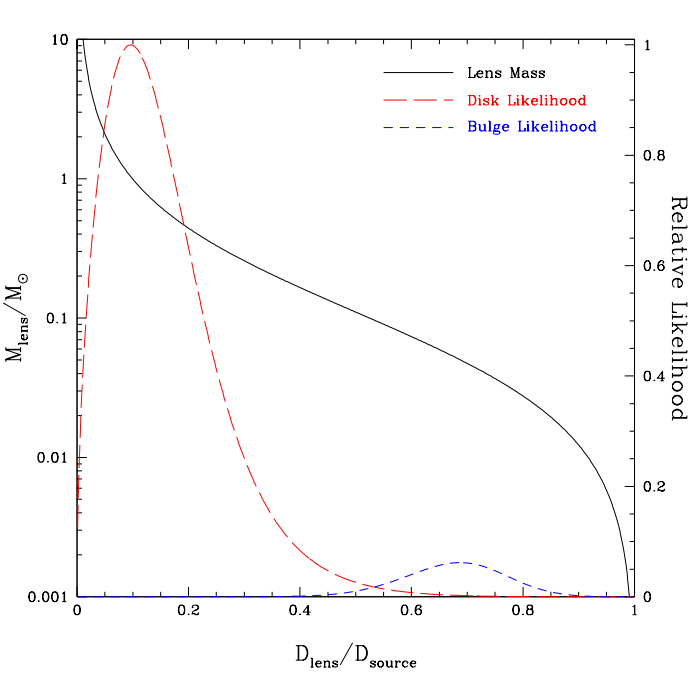

Figure 5.28: 99-BLG-1 lens mass, Galactic disk likelihood, and Galactic bulge likelihood, plotted as a function of lens distance.

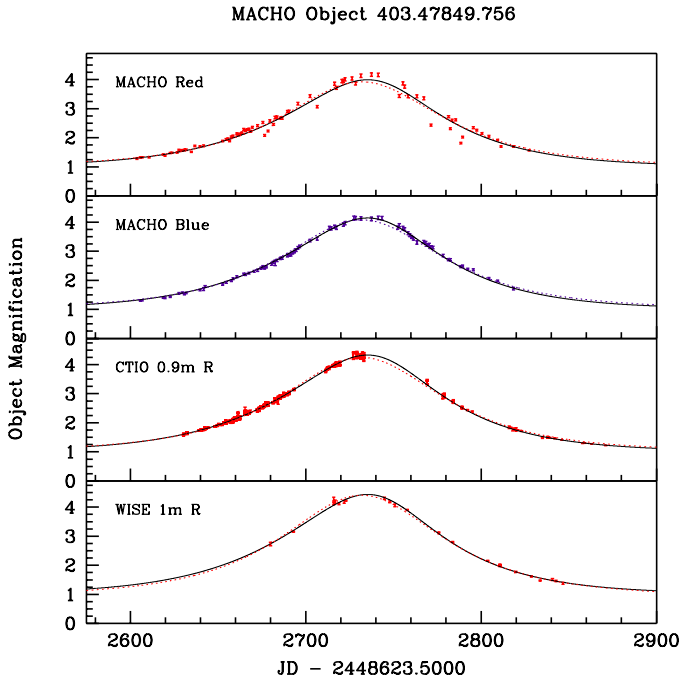

Figure 5.29: Lightcurve of MACHO event 99-BLG-8, including parallax (*solid* line) and standard (*dotted* line) microlensing fits.

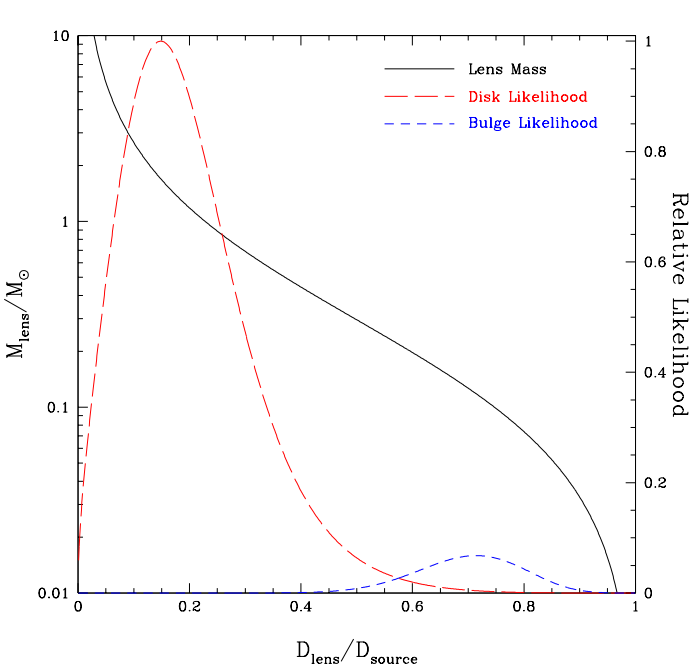

Figure 5.30:
99-BLG-8 lens mass, Galactic disk likelihood, and Galactic bulge likelihood, plotted as a function of lens distance.

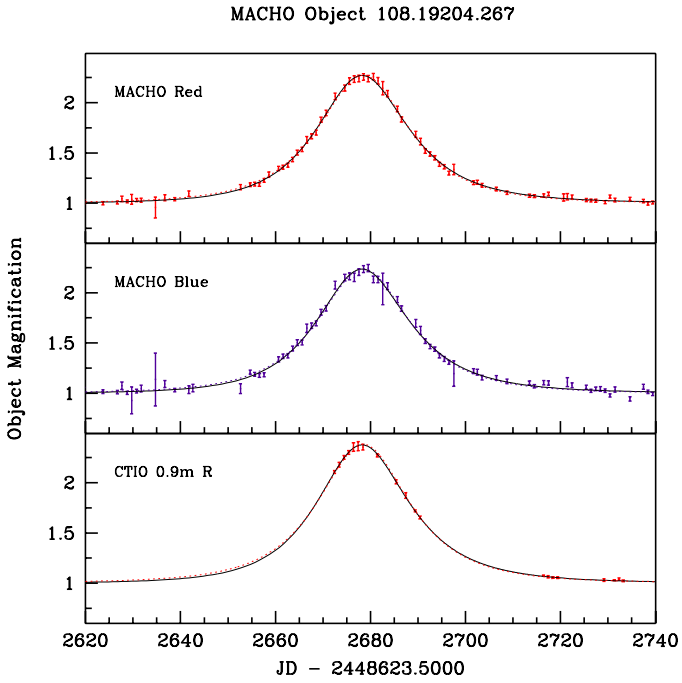

Figure 5.31:
Lightcurve of MACHO event 99-BLG-18, including parallax (*solid* line) and standard (*dotted* line) microlensing fits.

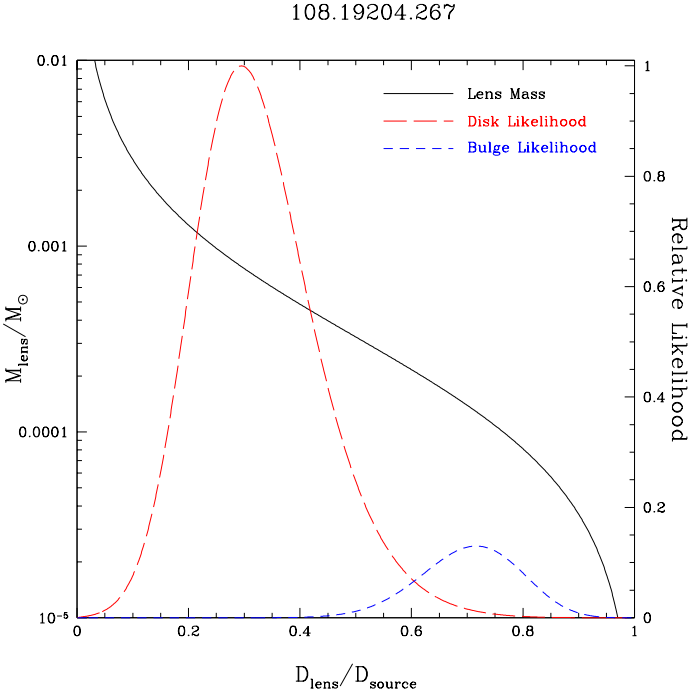

Figure 5.32: 99-BLG-18 lens mass, Galactic disk likelihood, and Galactic bulge likelihood, plotted as a function of lens distance.

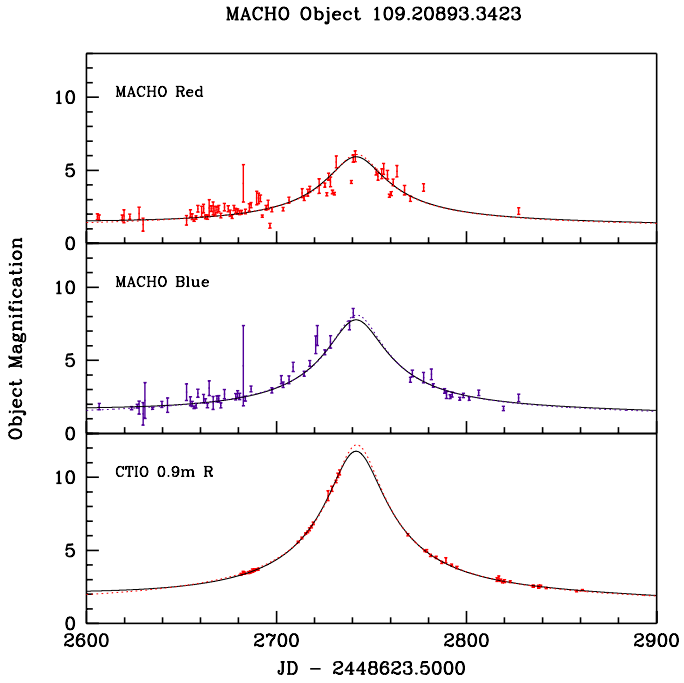

Figure 5.33: Lightcurve of MACHO event 99-BLG-22, including parallax (*solid* line) and standard (*dotted* line) microlensing fits.

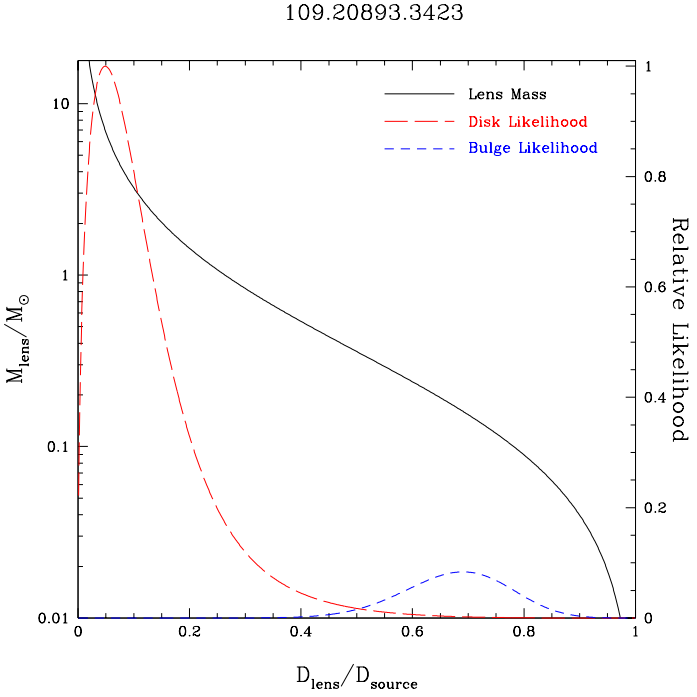

Figure 5.34: 99-BLG-22 lens mass, Galactic disk likelihood, and Galactic bulge likelihood, plotted as a function of lens distance.

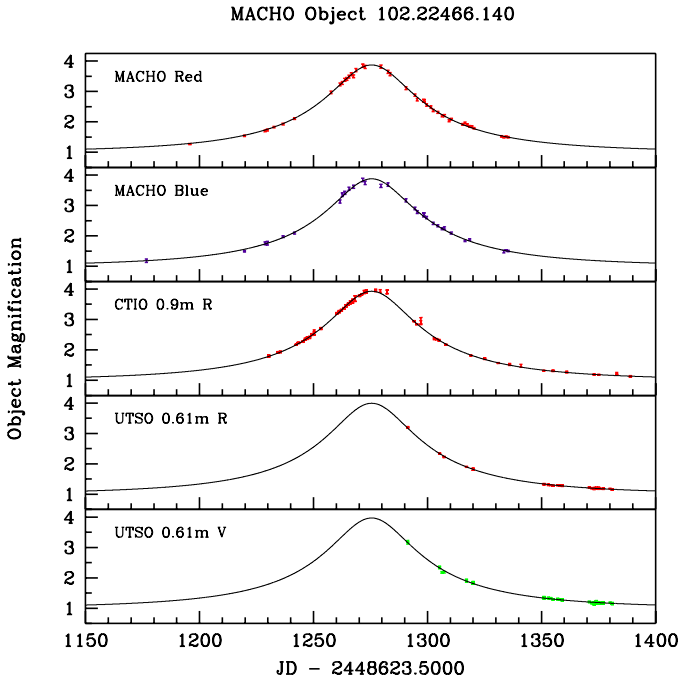

Figure 5.35: Lightcurve of MACHO event 95-BLG-13, including the standard (*solid* line) microlensing fit.

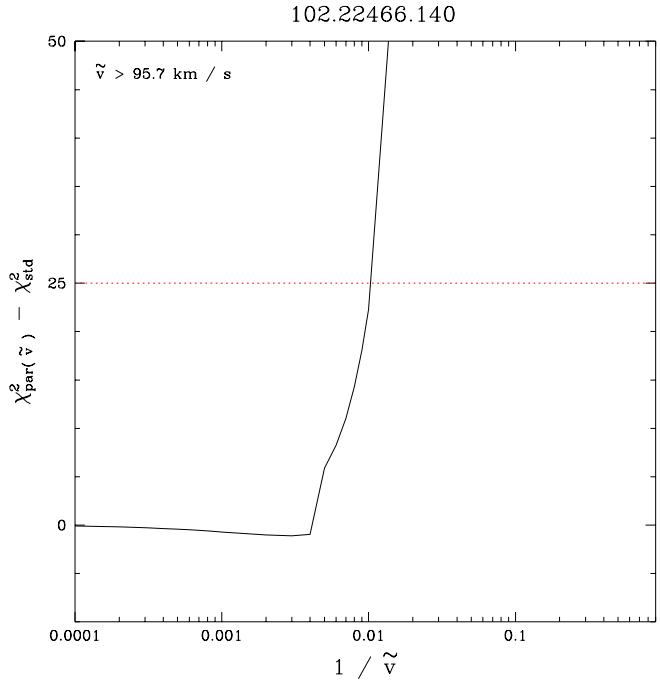

Figure 5.36: Change in the 95-BLG-13 microlensing fit χ^2 between the standard microlensing fit and the best parallax fit with $\tilde{v}$ fixed. A significant limit is established at $\Delta\chi^2 = 25$, implying $\tilde{v} > 95.7\,\mathrm{km\,s^{-1}}$.

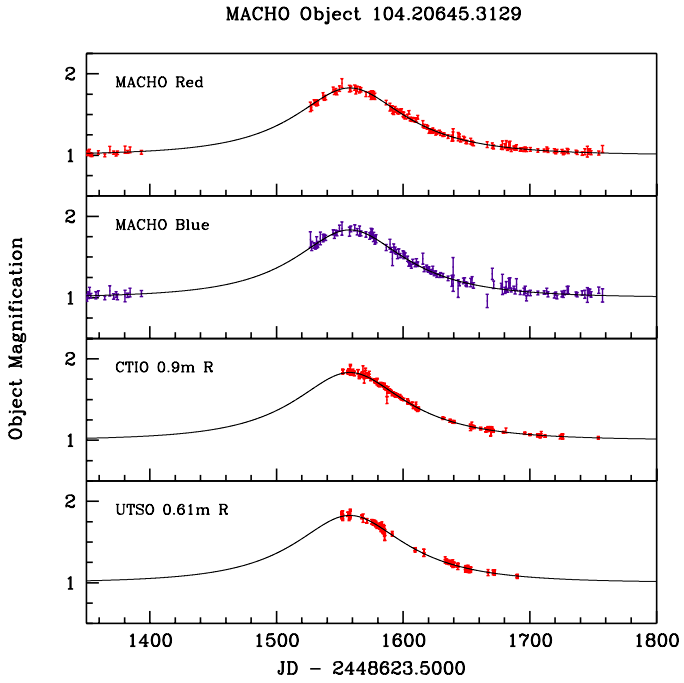

Figure 5.37: Lightcurve of MACHO event 96-BLG-1, including the standard (*solid* line) microlensing fit.

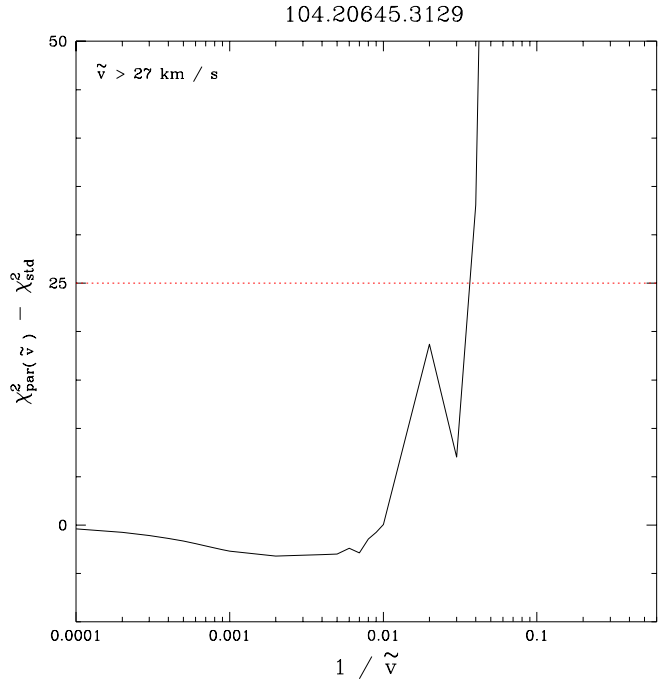

Figure 5.38: Change in the 96-BLG-1 microlensing fit χ^2 between the standard microlensing fit and the best parallax fit with $\tilde{v}$ fixed. A significant limit is established at $\Delta\chi^2 = 25$, implying $\tilde{v} > 27.1\,\mathrm{km\,s^{-1}}$.

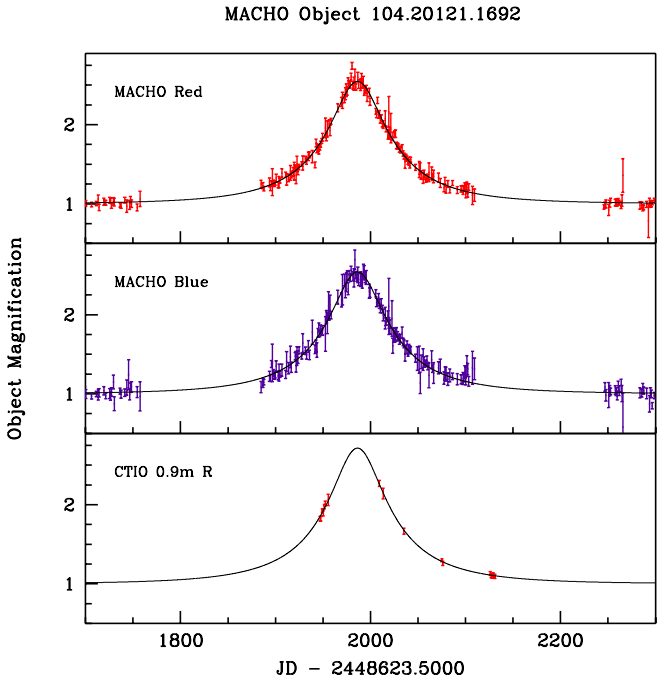

Figure 5.39: Lightcurve of MACHO event 97-BLG-18, including the standard (*solid* line) microlensing fit.

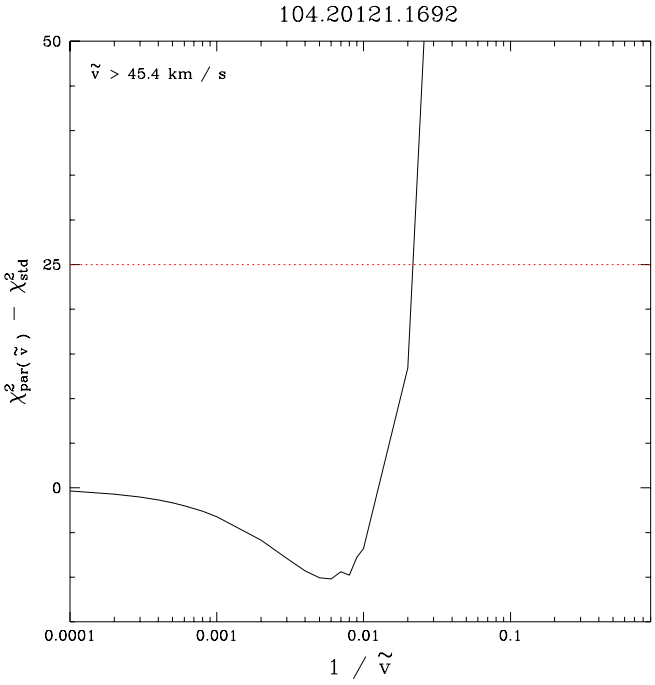

Figure 5.40: Change in the 97-BLG-18 microlensing fit χ^2 between the standard microlensing fit and the best parallax fit with $\tilde{v}$ fixed. A significant limit is established at $\Delta\chi^2 = 25$, implying $\tilde{v} > 45.5\,\mathrm{km\,s^{-1}}$.

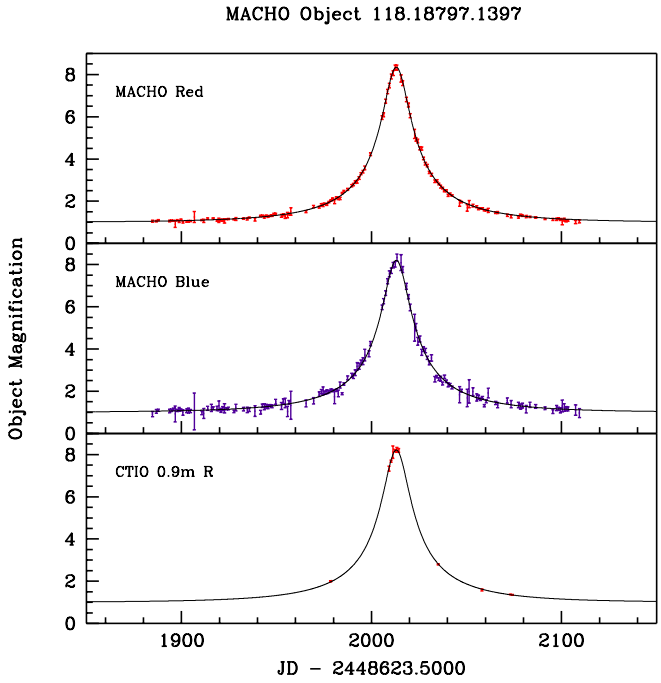

Figure 5.41: Lightcurve of MACHO event 97-BLG-26, including the standard (*solid* line) microlensing fit.

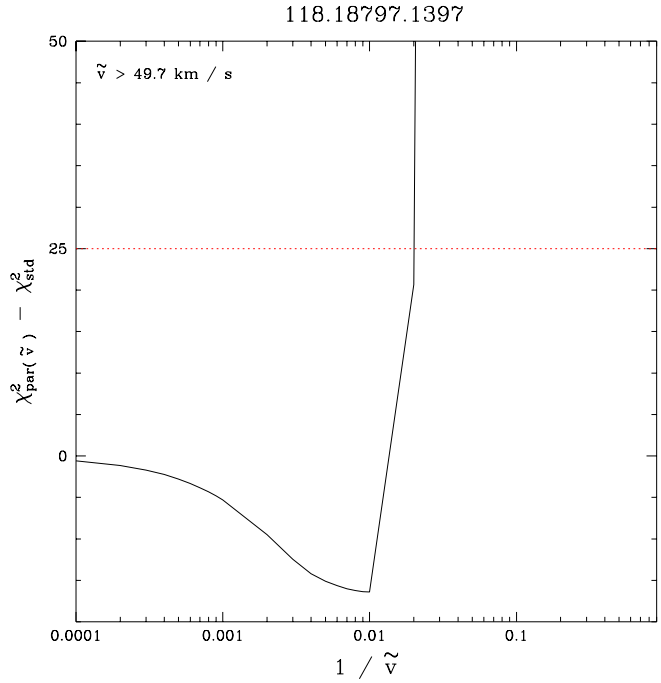

Figure 5.42: Change in the 97-BLG-26 microlensing fit χ^2 between the standard microlensing fit and the best parallax fit with $\tilde{v}$ fixed. A significant limit is established at $\Delta\chi^2 = 25$, implying $\tilde{v} > 49.7\,\mathrm{km\,s^{-1}}$.

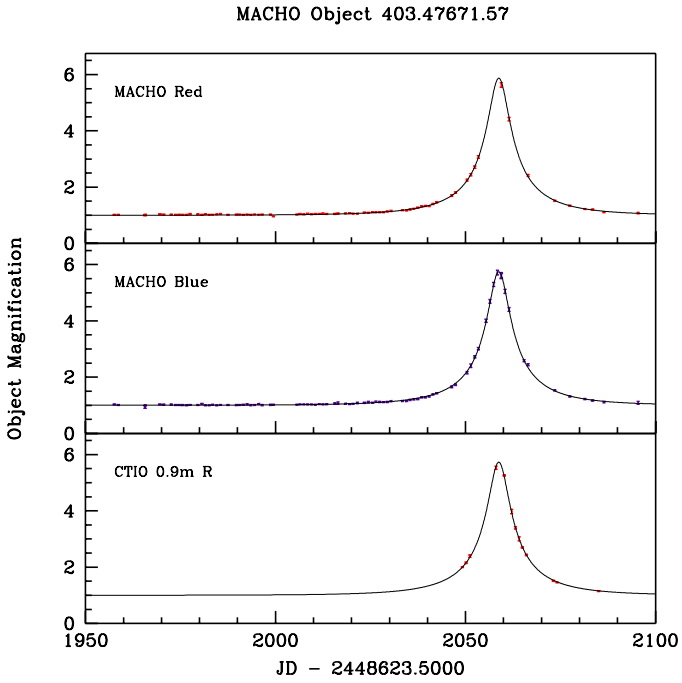

Figure 5.43: Lightcurve of MACHO event 97-BLG-56, including the standard (*solid* line) microlensing fit.

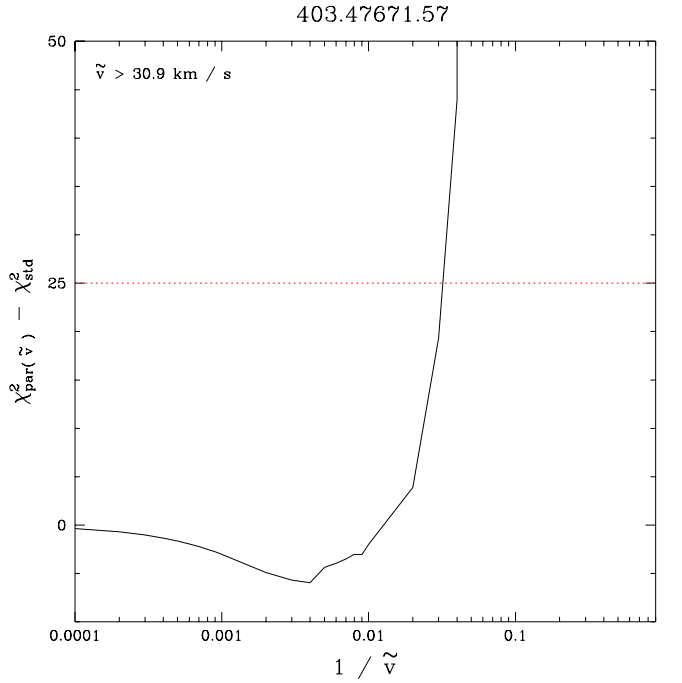

Figure 5.44: Change in the 97-BLG-56 microlensing fit χ^2 between the standard microlensing fit and the best parallax fit with $\tilde{v}$ fixed. A significant limit is established at $\Delta\chi^2 = 25$, implying $\tilde{v} > 30.9\,\mathrm{km\,s^{-1}}$.

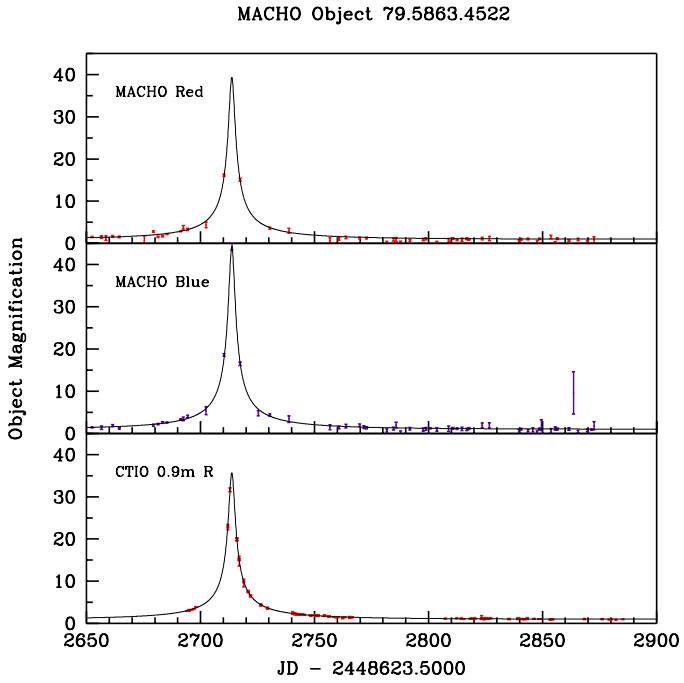

Figure 5.45: Lightcurve of MACHO event 99-LMC-2, including the standard (*solid* line) microlensing fit.

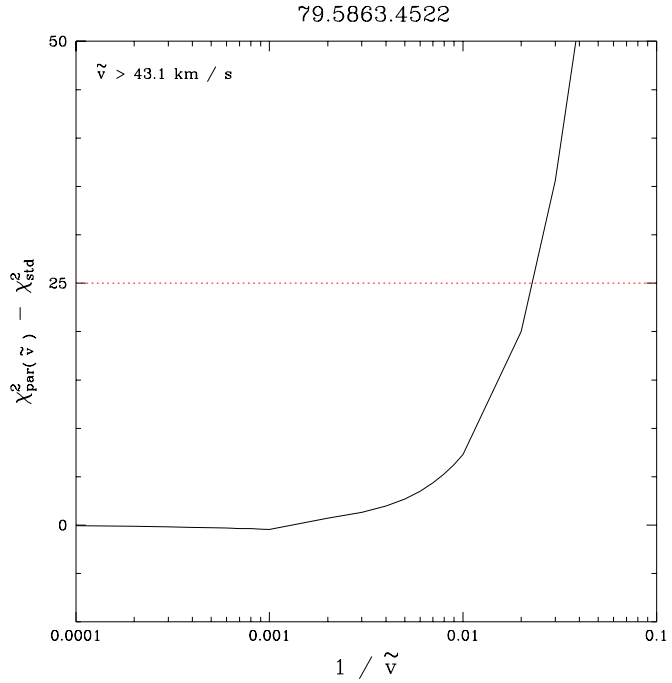

Figure 5.46: Change in the 99-LMC-2 microlensing fit χ^2 between the standard microlensing fit and the best parallax fit with $\tilde{v}$ fixed. A significant limit is established at $\Delta\chi^2 = 25$, implying $\tilde{v} > 43.1\,\mathrm{km\,s^{-1}}$.

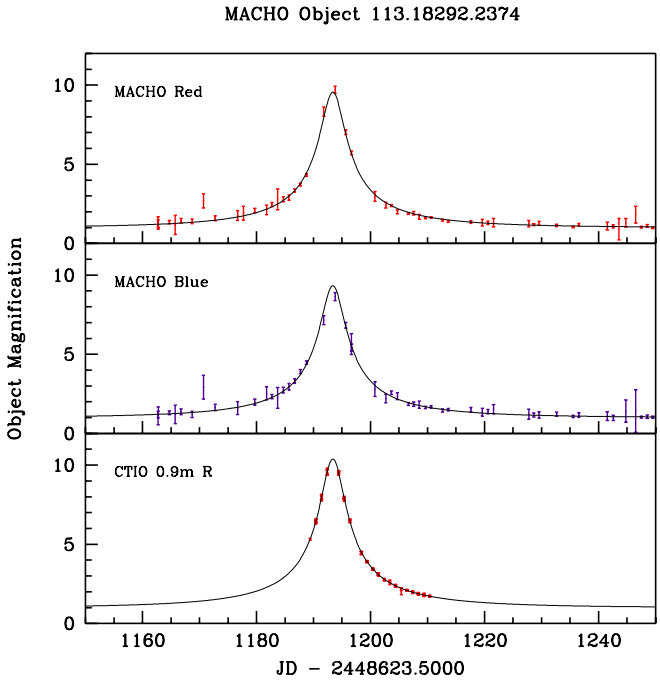

Figure 5.47: Lightcurve of MACHO event 95-BLG-1, including the standard (*solid* line) microlensing fit.

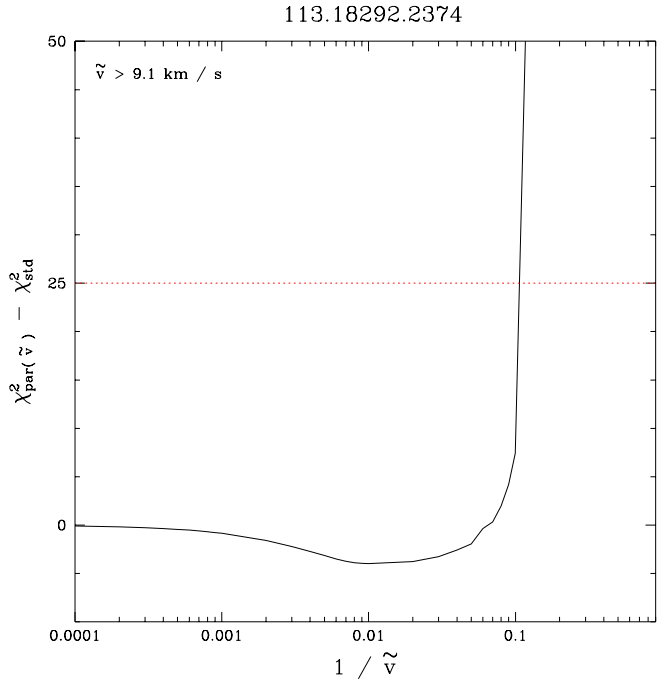

Figure 5.48: Change in the 95-BLG-1 microlensing fit χ^2 between the standard microlensing fit and the best parallax fit with $\tilde{v}$ fixed. A significant limit is established at $\Delta\chi^2 = 25$, implying $\tilde{v} > 9.1\,\mathrm{km\,s^{-1}}$.

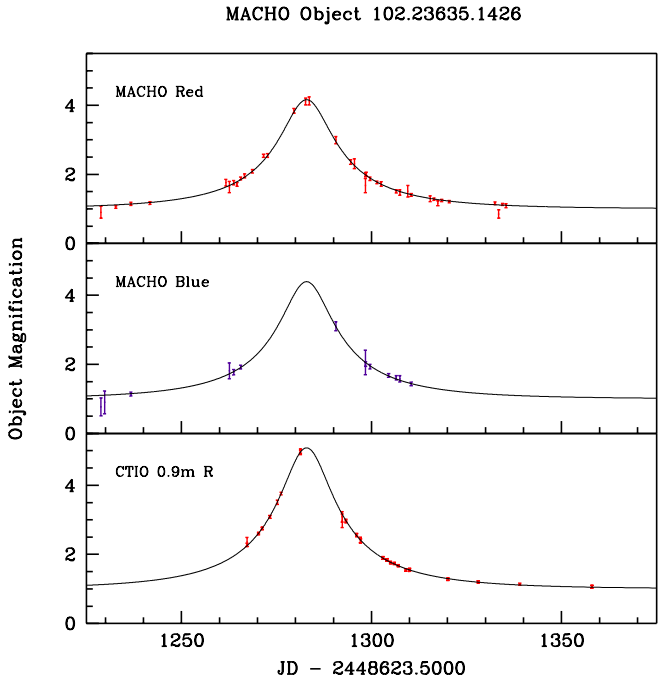

Figure 5.49: Lightcurve of MACHO event 95-BLG-19, including the standard (*solid* line) microlensing fit.

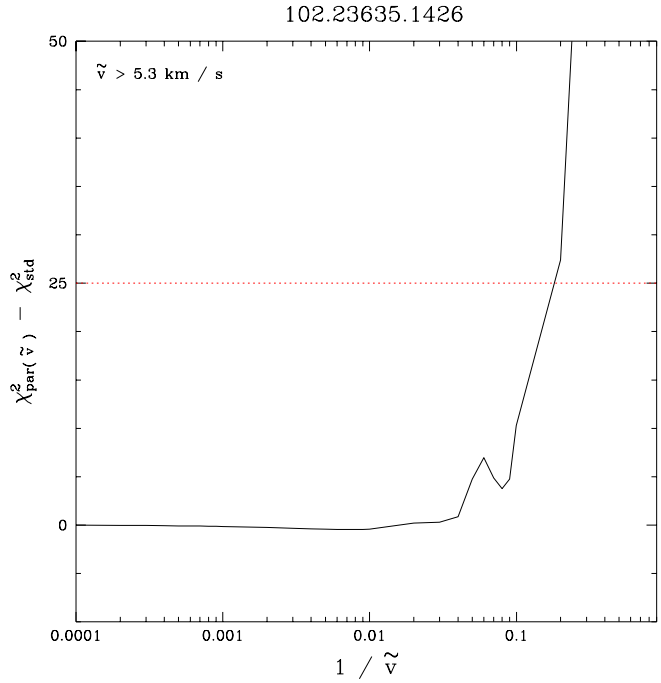

Figure 5.50: Change in the 95-BLG-19 microlensing fit χ^2 between the standard microlensing fit and the best parallax fit with $\tilde{v}$ fixed. A significant limit is established at $\Delta\chi^2 = 25$, implying $\tilde{v} > 5.3\,\mathrm{km\,s^{-1}}$.

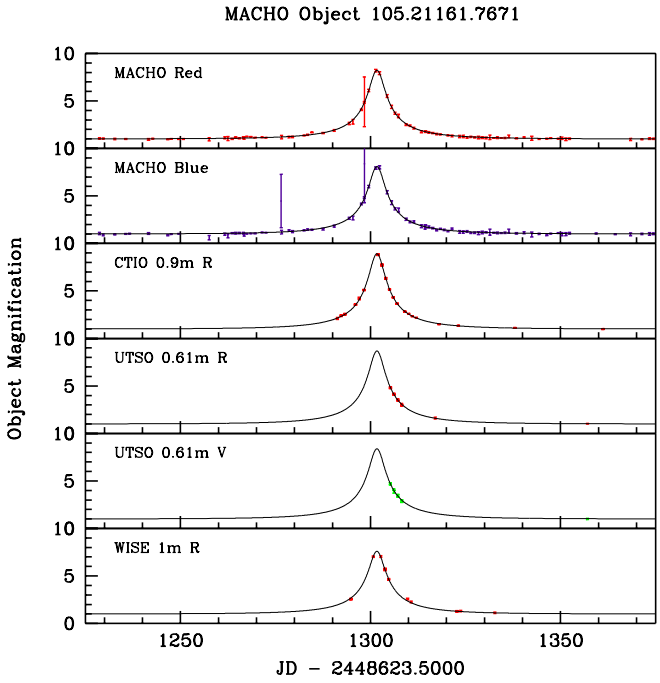

Figure 5.51: Lightcurve of MACHO event 95-BLG-26, including the standard (*solid* line) microlensing fit.

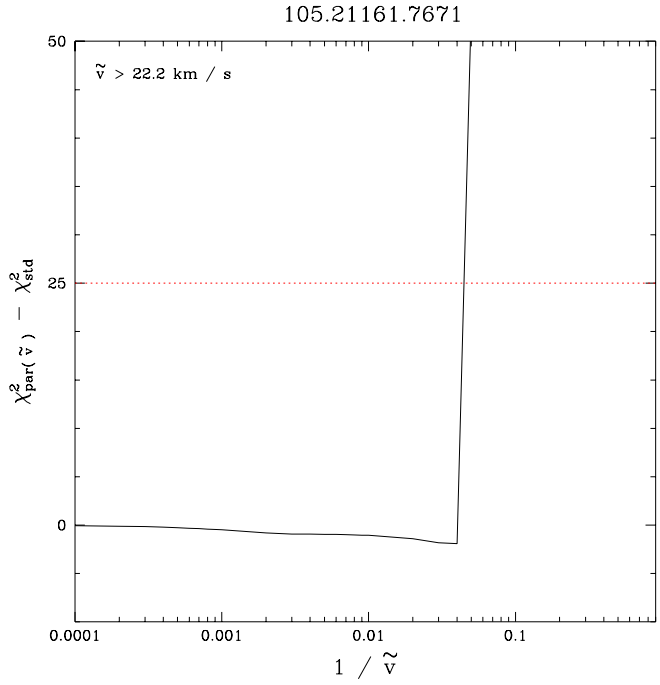

Figure 5.52: Change in the 95-BLG-26 microlensing fit χ^2 between the standard microlensing fit and the best parallax fit with $\tilde{v}$ fixed. A significant limit is established at $\Delta\chi^2 = 25$, implying $\tilde{v} > 22.2\,\mathrm{km\,s^{-1}}$.

Chapter 6

EXOTIC MICROLENSING: EXTENDED SOURCE EFFECTS

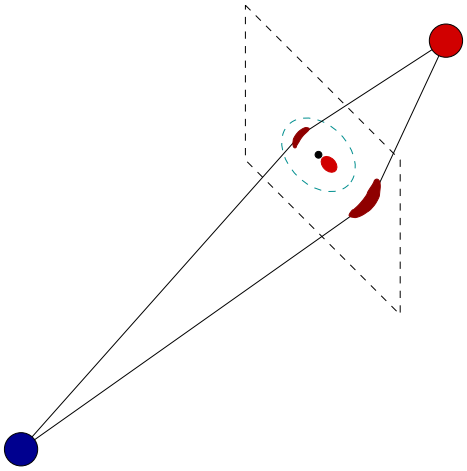

6.1 Extended Source Theory

The effects of extended source size become apparent in the limit of a large source, high magnification event, where the lens impact parameter is of the order of the projected source radius (Gould 1994; Nemiroff & Wickramasinghe 1994; Witt & Mao 1994; Peng 1997). In this case, the source position $\vec{s}$ is parameterized as

$$\vec{s}(\phi) = s_o\hat{x} + R_*\left(\cos(\phi)\hat{x} + \sin(\phi)\hat{y}\right) \qquad 0 \leq \phi \leq 2\pi. \tag{6.1}$$

R_* represents the radius of the source star, with $\hat{x}$ and $\hat{y}$ defining the plane containing the source disk. This modifies the image solutions to the lens equation

$$\left(\frac{\vec{i}}{R_{\rm E}}\right)_{\pm}(\phi) = \frac{[u + u_*\cos(\phi), u_*\sin(\phi)]}{2}\left(1 \pm \sqrt{1 + \frac{4}{u^2 + 2uu_*\cos(\phi) + u_*^2}}\right) \tag{6.2}$$

In this situation, an extra parameter is included in the microlensing solution

$$u_* = x\frac{R_*}{R_{\rm E}}. \tag{6.3}$$

Here u_* represents the projection of R_* into the lens plane, scaled by $R_{\rm E}$ (Equation 3.3). Note that as $R_* \rightarrow 0$ we recover the point source equation for $\vec{s}$ (Equation 3.1) and the solutions of the lens equation Equation 3.4. If we measure $u(t)$ with respect to the center of the source disk, it is not modified by this new parameterization. However, since the observed magnification is a function of the derivative of Equation 6.2, $A(t)$ is modified to (Witt & Mao 1994)

$$A(t) = \frac{2}{\pi u_*} + \frac{1+u_*^2}{\pi u_*^2}\left(\frac{\pi}{2} + \arcsin\frac{u_*^2-1}{u_*^2+1}\right) \tag{6.4}$$

for $u = u_*$, and

$$\begin{aligned} A = & \frac{2(u-u_*)^2}{\pi u_*^2(u+u_*)}\frac{1+u_*^2}{\sqrt{4+(u-u_*)^2}}\ \Pi\left(\frac{\pi}{2}, n, k\right) \\ & + \frac{u+u_*}{2\pi u_*^2}\sqrt{4+(u-u_*)^2}\ E\left(\frac{\pi}{2}, k\right) \\ & - \frac{u-u_*}{2\pi u_*^2}\ \frac{8+(u^2-u_*^2)}{\sqrt{4+(u-u_*)^2}}\ F\left(\frac{\pi}{2}, k\right) \end{aligned} \tag{6.5}$$

for $u \neq u_*$, where

$$\begin{aligned} n &= \frac{4uu_*}{(u+u_*)^2} \\ k &= \sqrt{\frac{4n}{4+(u-u_*)^2}} \end{aligned}$$

and F, E, and Π are elliptic integrals of the first, second and third kind.

To account for limb–darkening of the source, an appropriate limb–darkening law and coefficients must be determined for the source star. The amplification is then integrated over the face of the star, properly weighted by the brightness profile. The limb–darkening law we will choose is of the form (e.g. Claret, Diaz-Cordoves, & Gimenez 1995)

$$I_\lambda(\mu)/I_\lambda(1) = 1 - a(1-\mu) - b(1-\mu)^2. \tag{6.6}$$

Here μ is the cosine of the angle between the observer's line of sight and the emerging stellar radiation, and a and b are model parameters dependent primarily upon the effective temperature and surface gravity of the star.

Figure 6.1 compares point source and extended source lightcurves for various impact parameters $u_{\rm min}$. In each case, the size of the source star is fixed at $0.25 R_{\rm E}$. Note the effects are most significant when the lens is close to (or over) the source face. These deviations diminish in amplitude as the lens moves away from the source. This indicates high–magnification (low impact parameter) events, or events where the source is expected to have a large angular radius (such as a red giant source star) are most likely to reveal such deviations. Observing densely the peaks of high magnification events provides the best means to detect or limit extended source effects.

Appropriately fitting light–curve deviations with the extra parameter u_* provides a second constraint equation for the three lens parameters, the angular size of the source in units of the lens's Einstein radius. If we estimate the linear radius and distance of the source star from photometry and spectroscopy, we have an estimate of the lens proper motion relative to the source. Such a situation is rare, and is expected in only $\sim 5\%$ of events towards the Galactic bulge (Gould & Welch 1996).

By combining Equation 3.3 and Equation 6.3, our measurement of u_* allows a measurement of the angular size of the lens' Einstein ring radius

$$\theta_{\rm E} \equiv \frac{R_{\rm E}}{D_l} = \frac{R_*}{u_* D_s} = \frac{\theta_*}{u_*}. \tag{6.7}$$

The lens proper motion can then be determined

$$\mu \equiv \frac{v_\perp}{D_l} = \frac{2\ R_{\rm E}}{D_l\ \widehat{t}} = \frac{2\ \theta_{\rm E}}{\widehat{t}} = \frac{2\ \theta_*}{\widehat{t}\ u_*}. \tag{6.8}$$

Recall, $\widehat{v} \equiv \mu\ D_s$, and Equation 3.13 can be used to relate the mass and distance of the lens.

6.2 95-BLG-30

The source star in Alert 95-BLG-30 is located at α =18:07:04.26, $\delta = -$27:22:06 (J2000). The MACHO project's identifier for this star is 101.21821.128. Alert 95-BLG-30 was detected by the MACHO Alert system at $A \sim 1.8$ on Jul 24, 1995, approximately 22 days before the observed peak.

The location of the source star in an optical color–magnitude diagram (CMD), $V = 16.21$ and $(V - R) = 1.39$, indicates this star passes the "clump giant" cuts defined in Alcock et al. (1997d). Figure 6.2 shows a single epoch CMD for a 2×2 arcmin field surrounding the source star, which is indicated with a circle. We may be reasonably sure then that this star is located in the Galactic bulge and has a large radius. Microlensing fits to the rising portion of the light–curve predicted a high–magnification event for the giant source, which presented the possibility of source star resolution.

Subsequent observations indicated deviations from the standard microlensing model at $A \sim 20$, approximately 2 days before the projected peak. At this time, we mounted an aggressive program of photometry and spectroscopy to study these deviations thoroughly. Follow–up observations continued nightly past the observed peak until the star returned to its baseline state. Intermittent observations followed to determine accurately the baseline flux as measured at each site.

Figure 6.3 displays the MACHO 1995 bulge season light–curve of Alert 95-BLG-30 [6]. The alert date is indicated with an arrow, after which time the light–curve becomes heavily sampled with follow–up data. Data from all follow–up observatories have been included after determining the baseline flux in each passband. No microlensing fits are included in the figure, but it is apparent that the data conform to the symmetric and achromatic shape expected of gravitational microlensing events, at least for magnification $A \leq 20$.

This conclusion is confirmed after fitting a normal microlensing curve to the combined dataset. Event parameters for this fit (Fit 1 hereinafter) are listed in Table 6.1, and χ^2 statistics for each passband are listed in Table 6.2. However, near the peak of the event the data deviate from the expected light–curve (see Figure 6.4). This type of deviation is not unexpected in a high magnification microlensing event. We note that the standard point–source microlensing model allows infinite magnification when the source and lens are aligned. When the extended size of the source is considered, the magnification is limited, as the entirety of the source disk cannot be perfectly aligned with the lens. If we include an

[6] We report an uncatalogued CCD trap which allowed several contaminated MACHO–red observations to pass through our processing stream. The majority of these were removed from the data set based upon their proximity to the bad columns and psf FWHM.

Table 6.1: Comparison of event parameters between microlensing fits for MACHO Alert 95–BLG–30. Statistics are derived from simultaneous fits on all passbands. Reported uncertainties in the final significant digit(s) are the maximum extent of the surface in parameter space which has a χ^2 greater than the best–fit value by 1.

[a] Fit 1 is the best standard microlensing fit to the data, Fit 2 incorporates the extended size of the source star, and Fit 3 takes into account limb–darkening of the source.
[b] JD – 2448623.50.
[c] Einstein diameter crossing time.
[d] Lens angular velocity, relative to the source, is in $\mathrm{km\,s^{-1}\,kpc^{-1}}$ and assumes a $61 \pm 12 \mathrm{R}_\odot$ source at 9 kpc.

Fit [a]	t_0 [b]	$\widehat{t}$ [c]	$u_{\min}$	u_*	μ [d]
1	1321.2 (1)	67.70 (13)	0.04069 (12)	0	···
2	1321.2 (1)	67.36 (1)	0.05579 (1)	0.07335 (1)	22.1 (30)
3	1321.2 (1)	67.28 (27)	0.05408 (20)	0.07561 (9)	21.5 (29)

Table 6.2: Individual microlensing statistics for MACHO and GMAN observations of Alert 95–BLG–30. The number of constraints per passband for fits 1, 2, and 3 are four, five, and five, respectively.

[a] Average error, in magnitudes, for each passband.

Passband	# Observations	$\bar{dm}$ [a]	Fit 1 χ^2	Fit 2 χ^2	Fit 3 χ^2
MACHO R	205	0.018	980.33	847.49	839.15
MACHO V	292	0.023	1069.65	964.16	963.86
CTIO R	103	0.019	307.58	124.97	126.51
MJUO R	41	0.019	184.56	46.68	42.62
UTSO V	55	0.020	101.34	48.64	50.28
UTSO R	96	0.013	488.20	82.91	90.09
WISE R	12	0.013	80.71	13.76	7.22
TOTAL	804		3212.40	2128.64	2119.76

extra parameter in the fit to account for the angular size of a constant surface brightness source star (Fit 2), we reduce χ^2 by 1084. The deviations near the peak of MACHO 95-BLG-30 are significantly reduced with this model, which we interpret as clear justification for the extended source microlensing interpretation.

The data in Table 6.2 indicate an extended source fit χ^2 per degree of freedom of approximately 1 for the GMAN follow–up data. The implication here is that the data scatter around the fit is what one would statistically expect due to measurement error. Thus, the data are in excellent agreement with the extended source microlensing fit, considering our

photometry is at the $1-2\%$ level, as indicated in column 3 of Table 6.2. However, the MACHO data exhibit χ^2_{dof} between $3-4$, which formally indicates a poor fit to the data. While it is obvious that this is indeed a gravitational microlensing event, such a poor fit might cast doubt on the extended source interpretation. Fits to data of magnification $A < 10$, which should be negligibly affected by extended source effects, display the same excessive scatter around the fit. We therefore conclude that the majority of this scatter is contained in baseline measurements, and should not adversely affect our interpretation of the data.

Figure 6.3 also presents a scaled schematic of this microlensing event using event parameters derived from fits with a limb–darkened source star (Table 6.1, Fit 3). Included are the lens's Einstein radius expressed as $\widehat{t}/2$, and the source radius scaled to 0.0756 $R_{\rm E}$. The trajectory of the lens across the extended face of the source star is shown with $u_{\rm min}/u_* = 0.715$.

Figure 6.4 provides a visual comparison between the best standard microlensing fit to the data (*dashed* line) and microlensing of a limb–darkened extended source (*solid* line). Each passband was fit independently with a baseline parameter, while event parameters were derived from joint fits on the combined dataset. All fits were performed in the MINUIT environment (James 1994).

6.2.1 Determination of Stellar Parameters

Analysis of the stellar parameters of the source star in MACHO 95-BLG-30 (hereinafter referred to as the source star) is required if we are to use the additional information provided by u_* to characterize the lensing object. The most important parameters are its distance (D_s) and radius (R_*). Also valuable are estimates of the source temperature and surface gravity, which will help define the limb–darkening coefficients.

Figure 6.2 shows the fiducial line for the red giant branch of the metal–rich globular cluster NGC 6553 from Ortolani, Barbuy, & Bica (1990), plotted over the optical CMD for a 2×2 arcmin field surrounding the source star. We note that the horizontal branch (HB) in this field is inclined like that of NGC 6553, due to the effect of differential reddening. Even though the morphology of the red giant branch of this cluster is similar to that of the MACHO field surrounding the microlensing event, the magnitude of the source star is fainter than expected, after we account for the different reddenings and distances to these

Table 6.3: 95-BLG-30: Photometry of the Source Star

Observed	Extinction	Dereddened	Abs Mag, 8 kpc	Abs Mag, 9 kpc
$V = 16.21$	$A_V = 1.35$	$V_0 = 14.86$	$M_V = +0.34$	$M_V = +0.09$
$K = 9.98$	$A_K = 0.15$	$K_0 = 9.83$	$M_K = -4.69$	$M_K = -4.94$
$V - R = 1.39$	$E(V-R) = 0.34$	$(V-R)_0 = 1.05$		
$J - K = 1.12$	$E(J-K) = 0.23$	$(J-K)_0 = 0.89$		
$H - K = 0.26$	$E(H-K) = 0.08$	$(H-K)_0 = 0.18$		
$V - K = 6.23$	$E(V-K) = 1.21$	$(V-K)_0 = 5.03$		
Bolometric		$BC_K = -2.7 \pm 0.1$	$M_{\rm bol} = -2.0$	$M_{\rm bol} = -2.25$

sources (we adopt a bulge distance of 8 kpc). The smaller apparent luminosity could be due to differences in age, metallicity, or distance. From this diagram, we tentatively conclude that this star is either more metal-rich, or more distant than 8 kpc (or both) than the giants of similar color in NGC 6553.

Reddening

The reddening is patchy in the MACHO field where the source star is located. Figure 6.5 shows the amplitude vs. color of all the RR Lyr that we found in this field. The reddening vector is horizontal in this figure, so the color spread is mostly due to differential reddening within the field, as the RRab sequence in such a diagram should be very tight (Bono et al. 1997). There appear to be two zones of different obscuration, with $E(B-V)$ ranging from 0.3 to 0.8 mag. The source star appears to be located in the region with smaller reddening, as measured from the colors of the three closest RR Lyr. We identified a total of two bulge RR Lyr type ab, and one RR Lyr type c, within 2 arcmin of the source star. The locations of these 3 RR Lyr are shown in the optical CMD (Figure 6.2) as triangles. The mean color of the two RRab is $V - R = 0.54$, and the mean color of the RRc is $V - R = 0.46$. From these colors we deduce $E(V-R) = 0.34 \pm 0.05$. Using the extinction law of Rieke & Lebofsky (1985), we obtain $A_V = 1.36$, $E(B-V) = 0.44$, $A_K = 0.15$, $E(V-K) = 1.21$, $E(J-H) = 0.15$, $E(H-K) = 0.08$, and $E(J-K) = 0.23$. The observed and dereddened photometric measurements of the source star are listed in Table 6.3.

Infrared Photometry

We observed the field of the source star with the CIRIM camera on the CTIO 1.5m telescope. The f/13.5 configuration yields a pixel scale of 0.65 arcsec pixel^{-1}. The detector is a 256×256 HgCdTe NICMOS 3 array. Conditions on the night of September 24, 1996 were photometric. We used the J, H, and K_s filters, and a five-position on-source dithering pattern optimally to expose the target field and collect the necessary frames for sky flats. Six 10–second coadds were obtained at each position in the dithering pattern for total exposures of 300 seconds in each filter. The individual IR images were reduced following standard procedure using dark and sky frames, then shifted and combined to create the final images, which cover about 2 arcmin on a side. The photometric calibration was obtained by observing the UKIRT Faint Standard Star no. 1 (G158–100) just prior to observing the field of the source star. The standard star and program field were observed at identical airmasses ($X = 1.2$), thus no extinction corrections were necessary. We find $K = 9.98$, $(J - K) = 1.12$, and $(H - K) = 0.26$ mag for the source star. We estimate an uncertainty of 0.05 mag in J, H, and K from the photon statistics and aperture corrections. Figure 6.6 shows the optical–IR color–color diagram of stars one magnitude brighter than the horizontal branch in the 2×2 arcmin field surrounding the source star, along with the sequences corresponding to field giants, field dwarfs, and Baade's Window giants from Frogel & Whitford (1987). The colors of the source star are similar to Baade's Window M giants, and we conclude that it is unlikely to be a field dwarf.

Figure 6.7 shows an expanded version of the reddening corrected K_0 vs $(V-K)_0$ optical–IR CMD for the bright stars found in this field. Overplotted are the fiducial lines corresponding to the red giant branches of the metal–rich globular clusters 47 Tuc from Frogel, Persson, & Cohen (1981) and the metal-rich globular cluster NGC 6553 from Guarnieri, Renzini, & Ortolani (1997), assuming a distance of 8 kpc for both populations. Figure 6.7 shows again that the source star is relatively faint with respect to the giants in these clusters. This suggests that the star is either more metal-rich than $[Fe/H] = -0.4$, and/or more distant than 8 kpc. As an additional comparison, we have plotted data from Frogel & Whitford (1987) for spectral type M3–5 giants from Baade's Window (assuming a dis-

tance of 8 kpc), and our own estimated fiducial line for these stars. If we assume a solar composition for the source star ($[Fe/H] = 0$), we obtain a distance of about 10 kpc. The uncertainty in this distance is large; it assumes that all of the scatter about the fiducial line of BW giants is due to the line–of–sight depth of the bulge. It is possible that the source star is on the metal–rich tail of the distribution of bulge giant metallicities. Comparing the two globular cluster tracks in Figure 6.7 gives one a sense of the dependence of the red giant branch fiducial lines on metallicity. If the location of the source star in the CMD were entirely due to metallicity, it would be an extremely metal–rich star, which is less probable than a combination of distance and metallicity effects at work. Given the position of the source star in the CMD at the outer envelope of giants observed in Baade's Window, we conclude that the source star is likely located on the "far" side of the bulge. Note that we would expect a giant star in the Sagittarius dwarf galaxy to be about 2 magnitudes fainter than the observed K_0 magnitude of the source star (see also Chapter 6.2.1 below).

Spectroscopy

We have obtained spectra of the source star in several different observing runs, as will be discussed in Chapter 6.2.3. Here we analyze the spectra taken at the 4m Blanco telescope at CTIO with the R–C spectrograph and the Loral $3K_1$ detector during the nights of 14 and 15 August, and 27 September, 1995. The first two spectra were taken 0.5 days before and after, respectively, the peak of the microlensing event, while the lens was still in transit across the source face. The wavelength coverage of these spectra is from λ6230 to λ9340 Å. A HeNeAr comparison lamp was used, which provided the wavelength calibration. The exposures were 60 seconds long, and were taken at an airmass of 1.7. All the spectra were reduced in the standard way. The dispersion was 1Å pixel^{-1}, and the resolution was 5Å, as measured from the FWHM of the lines.

The additional spectrum from 27 September, 1995 was taken at an airmass of 1.1, with a total exposure time of 500 seconds. No independent wavelength calibration was obtained for this spectrum. The dispersion was 2Å pixel^{-1}, and the resolution was 8Å. The wavelength coverage of this spectrum, shown in Figure 6.8, was from λ3890 to λ9830 Å. This spectrum, taken 42.3 days after peak magnification, is very similar to the near–peak spectra. This

further supports the microlensing interpretation, where the overall colors or spectral type must not change.

Spectral Typing

We determined the spectral type of the source star by direct comparison with the digital spectral atlas of late-type stars of Turnshek (1985) and Kirkpatrick, Henry, & McCarthy (1991). This comparison was done visually after rebinning our CTIO spectra to lower resolution, and paying close attention to the match of the prominent TiO bands. There is a very close match of the spectra shown in Figure 6.8 with a spectral type M4 III, and we adopt this classification for the source star. The uncertainty in this classification is estimated to be one spectral subtype.

Using the spectral type we can check our estimate of the reddening of the source star by adopting the unreddened optical and infrared colors of the same type bulge giants. For an M4 III bulge star, Frogel & Whitford (1987) give $(J-K)_0 = 0.90$ and $(H-K)_0 = 0.18$. and from the observed infrared colors we compute $E(J-K) = 0.22$, and $E(H-K) = 0.08$, respectively. These reddening values are in excellent agreement with the reddening derived from the optical photometry of the RR Lyr in this field (see Table 6.3).

CaII Triplet

The CTIO spectra allows us to determine independently the surface gravity (g) of the source star. The spectral region covered includes the CaII triplet, which is strong and very sensitive to $\log g$. Other spectral lines in the region from λ6400 Å to λ9200 Å can be used for this purpose in M–type stars, like the NaI doublet at $\lambda\lambda 8183, 8195$Å (Kirkpatrick, Henry, & McCarthy 1991). However, the lines of the CaII triplet are the most suitable ones, because they have been studied and calibrated by a number of authors (Jones, Alloin, & Jones 1984; Humphreys & Graham 1986; Diaz, Terlevich, & Terlevich 1989; Alloin & Bica 1989; Jorgensen, Carlsson, & Johnson 1992; Erdelyi-Mendes & Barbuy 1991).

We measured the equivalent width of the CaII lines at λ8498.06 Å, λ8542.14 Å, and λ8662.17 Å in the three spectra obtained with two different resolutions, obtaining $EW = 11.0 \pm 0.5$ Å, where the uncertainty is dominated by the location of the continuum. We used

the local continuum bands at λ8480 Å, λ8635 Å, and λ8905 Å, defined by Jones, Alloin, & Jones (1984), Diaz, Terlevich, & Terlevich (1989), and Alloin & Bica (1989), in order to make a direct comparison with their measurements and models. Note that the resolution of our spectra is similar to these other works.

We have also compiled published data (spectral type, $T_{\rm eff}$, log g, and CaII$-EW$) on M–type stars, covering a wide range of temperatures and gravities. In some cases only the two strongest lines of the CaII triplet are measured, and we have scaled these accordingly in order to include the weaker line. Figure 6.9 shows the equivalent width vs M spectral subtype for dwarfs (V), giants (III), and supergiants (I). The position of the source star is shown with the box. This figure confirms the conclusions drawn from the IR photometry and spectral classification – the source is a giant star.

Figure 6.10 shows equivalent width vs log g. The dotted lines show the $\pm 1\sigma$ measurements for the source star. From this figure we conclude that log $g = 1.0 \pm 0.2$. A similar value is obtained by applying the empirical relations found by Alloin & Bica (1989) and Diaz, Terlevich, & Terlevich (1989), and by slightly extrapolating the models of Jorgensen, Carlsson, & Johnson (1992) and Erdelyi-Mendes & Barbuy (1991).

Diaz, Terlevich, & Terlevich (1989) conclude that there is an almost one–to–one correlation between the CaII triplet EW and surface gravity for stars with solar and higher metallicity. Note that we have assumed solar abundances for the source star. The strength of the CaII triplet is expected to increase with increasing metallicity, and thus if $[Fe/H] > 0$, then log $g > 1.0$. We caution that the behavior of this spectral feature as a function of metallicity has not been thoroughly investigated for M–type stars, and we will ignore here this potential source of uncertainty. It does not, however, affect our eventual estimate of the lens proper motion.

Radial Velocity

We have also measured the radial velocity of the source star. Unfortunately, we did not measure radial velocity standards, and have to rely on a wavelength calibration based on the HeNeAr lamps. From the two CTIO spectra of the August run we obtain $V_r = -80 \pm 5$ km s^{-1}. Even though the spectra from the August run have high enough resolution to measure

velocities good to < 10 km s^{-1}, we consider that the most important source of uncertainty is the zero point.

We consider the possibility that the source star may be located in the Sgr dwarf galaxy. The Sgr dwarf galaxy discovered by Ibata, Gilmore, & Irwin (1994) is much more extended than previously thought. RR Lyr belonging to this galaxy have been identified in fields close to the Galactic plane (Alard 1996; Alcock et al. 1997e). In fact, the Sgr galaxy extends as far as the field containing the source star, as shown by the one Sgr RR Lyrae type ab discovered in this field by Alcock et al. (1997e). However, the radial velocity measured here rules out membership to the Sgr dwarf galaxy, which has $V_r = +150$ km s^{-1}.

The radial velocities of bulge giants in off-axis bulge fields have been measured by Minniti (1996) and Minniti et al. (1996). At the position of the MACHO field, the mean heliocentric radial velocity of bulge stars is estimated to be about 25 km s^{-1}, with a velocity dispersion $\sigma = 80$ km s^{-1}. The radial velocity of the source star is, therefore, consistent with the velocities of bulge giants, supporting our assumption that this star belongs to the bulge population.

Stellar Parameters

We will derive the stellar parameters M, $T_{\rm eff}$, L, and R for the source star in a variety of ways and compare the different values to estimate our uncertainties. When needed, we assume the solar values: $T_\odot = 5730K$, $\log g_\odot = 4.44$, and $M_{{\rm bol}\odot} = 4.72$ mag. The following equations relate various stellar parameters:

$$(L/L_\odot) = (R/R_\odot)^2 (T_{\rm eff}/T_\odot)^4$$

$$(g/g_\odot) = (M/M_\odot)(R/R_\odot)^{-2}$$

We begin with the most simple method, adopting the typical stellar parameters of an M4 giant in the galactic bulge. We would expect the mass of the source star to be $\sim 1 M_\odot$, the mass appropriate for a bulge giant according to the estimated age of the bulge (e.g. Holtzman et al. 1993). Using only the spectral type information (M4 III), we obtain $T_{\rm eff} = 3430$, $M_{\rm bol} = -2.7$ from Lang (1992), which gives $R = 85 R_\odot$. Also, for an M4 III star, $R = 83 R_\odot$, and $T_{\rm eff} = 3600$ from the recent calibrations of Dyck et al. (1996). These

values are averages over several spectral sub-types. The dependence of radius on spectral type is such that for an M3 III star $R \approx 60 R_\odot$, and for an M5 III star $R \approx 100 R_\odot$.

The IR colors allow us to measure the effective temperature. For $(J-K)_0 = 0.89$, $T_{\rm eff} = 3900 \pm 270$ from the calibration of Feast (1996). For $(V-K)_0 = 5.03$, $T_{\rm eff} = 3600$ from the recent calibration of Bessell, Castelli, & Plez (1998). The optical photometry also allows us to estimate the temperature of the source star. For $(V-R)_0 = 0.93$, we find $T_{\rm eff} = 3800 \pm 200$ by differential comparison with the giant star III-17 member of the globular cluster NGC 6553 analyzed by Barbuy et al. (1992). Comparing these values of temperature with those derived from the spectral type information, we adopt a temperature of $T_{\rm eff} = 3700 \pm 250$ for the source star, or $\log(T/T_\odot) = -0.19 \pm 0.03$.

Numerous bolometric corrections exist in the literature. We find $BC_K(J-K) = 2.6$ and $BC_K(V-K) = 2.7$ from Frogel & Whitford (1987) and Bessell, Castelli, & Plez (1998), $BC_H(M \text{ giants}) = 2.6$ from Bessell & Wood (1984), and $BC_V(M4III) = -2.2$ (Lang 1992). These give $m_{\rm bol} = 12.4$, 12.5, 12.6, and 12.6, respectively. We adopt $m_{\rm bol} = 12.5 \pm 0.1$ for the source star.

In order to compute the absolute magnitudes, we must assume a distance to the star. Adopting a distance of 8 kpc, or $(m-M)_0 = 14.52$, we obtain the absolute magnitudes $M_V = +0.34$, $M_K = -4.69$, and $M_{\rm bol} = -2.0$ mag. This gives $\log(L/L_\odot) = 2.69 \pm 0.04$. We can immediately derive the radius, $\log(R/R_\odot) = 1.72 \pm 0.06$ or $R = 53 \pm 8 R_\odot$. However, the uncertainty here is underestimated given the systematic uncertainty in the adopted distance. From our arguments in Chapter 6.2.1 , we adopt the distance to the source star of 9 ± 1 kpc, giving a distance modulus $(m-M)_0 = 14.77 \pm 0.25$. Re–calculating the radius at this distance and incorporating the added uncertainty, we find $M_{\rm bol} = -2.25 \pm 0.27$ and thus $R = 61 \pm 12 R_\odot$.

Lastly, we derive the mass of the source star using the measured value of $\log g$ (Chapter 6.2.1). We find $\log(g/g_\odot) = -3.44 \pm 0.08$ and $M \sim 0.8 - 2.5 M_\odot$. The mass derived in this manner is quite uncertain. The largest mass values are unlikely given the age of the bulge $t \approx 10$ Gyr (Holtzman et al. 1993). However, a mass slightly larger than 1 $M_\odot$ is consistent with the source star having a high metallicity.

To summarize, we adopt the following stellar parameters for the source star in MACHO

Table 6.4: Limb darkening coefficients for Equation 6.6 used to approximate the brightness profile of the source star in MACHO Alert 95–BLG–30.

Passband	a	b
MACHO V	1.140	-0.284
MACHO R	0.825	-0.051
Standard V	1.072	-0.228
Standard R	0.910	-0.108

Alert 95-BLG-30, which we categorize as an M4 bulge giant:

$$L = 600 \pm 200 L_{\odot},$$

$$T_{\rm eff} = 3700 \pm 250 K,$$

$$log\ g = 1.0 \pm 0.2,$$

$$R = 61 \pm 12 R_{\odot},$$

$$D = 9 \pm 1\ kpc,$$

$$M \approx 1.0 M_{\odot},$$

$$[Fe/H] \approx 0.$$

6.2.2 Determination of Event Parameters

Effect of Limb–Darkening on the Photometry

We now integrate an approximate limb–darkening law into the microlensing model, to extract more realistic event parameters than those derived with a constant surface brightness disk. Limb–darkening coefficients for GMAN's standard R and V passbands exist in the literature for $T_{\rm eff}$ = 3500 K, log g=1 for the quadratic form of Equation 6.6 (Claret, Diaz-Cordoves, & Gimenez 1995; Díaz-Cordovés, Claret, & Giménez 1995). Limb–darkening coefficients were also calculated for MACHO's non–standard passbands (Claret 1997, private communication). These coefficients are listed in Table 6.4.

Including this brightness profile in the extended source model further improves the fit χ^2 by 9 (see Table 6.2, Fit 3). While this improvement is formally significant, its interpretation here appears unclear. Comparison of fits 2 and 3 in Table 6.2 shows no clear trend between

data sets, which effectively washes out any overall conclusions about the significance of the model. However, we do regard the limb–darkened parameters as the more realistic interpretation of the data. Comparison of optical and *infrared* photometry during a lens transit should detect significant color terms as a result of source limb–darkening (Gould & Welch 1996), which would then provide a more robust test of stellar atmosphere models.

Implications for Lens Mass

The limb–darkened fit to finite source microlensing provides a direct measurement of $u_* \equiv \theta_*/\theta_E = 0.0756$, i.e. the angular size of the star as a fraction of the Einstein ring angle. To convert this into physical units, we need an estimate of the angular radius θ_* of the source star. The analysis in Chapter 6.2.1 indicates $R_* = 61\mathrm{R}_\odot$ and $D_s = 9\,\mathrm{kpc}$, giving $\theta_* = 31.5\,\mu\mathrm{arcsec}$ and thus $\theta_E = 0.417\,\mathrm{milliarcsec}$. The Einstein diameter crossing time $\widehat{t}$ is measured similarly to the usual point–source case, so this provides the proper motion of the lens with respect to the source star $\mu \equiv 2\theta_E/\widehat{t} = 21.5\,\mathrm{km\,s^{-1}\,kpc^{-1}} = 4.51\,\mathrm{mas/yr}$.

Simply adding the fractional errors of R_* and D_s in quadrature leads to a 23% uncertainty in the lens proper motion. However, the uncertainty in D_s has been included in the uncertainty in R_* (see Chapter 6.2.1), so this represents an over–estimate of the uncertainty in μ. A similar solution for the lens proper motion may be obtained by deriving the angular size of the source star from $T_{\rm eff}$ and $m_{\rm bol}$ (Gray 1992). These parameters are more tightly constrained than R_* and D_s, and lead to a smaller fractional error in θ_*. The uncertainty in the angular size of the source star, and therefore of the lens proper motion, is approximately twice the uncertainty in $T_{\rm eff}$, or 13.5%.

Evaluating Equation 3.13 for the observed values of $\widehat{v} = 193\,\mathrm{km\,s^{-1}}$, $\widehat{t} = 67.3$ days, we have $M(x) = 0.192\,M_\odot\,x/(1-x)$, thus the lens may be either a low-mass star roughly half–way to the source, or a more massive star closer to the source. Figure 6.11 shows $M(x)$ for the event parameters given in Table 6.2 (Fit 3), and the radius and distance of the source star obtained in Chapter 6.2.1. Since our proper motion error is dominated by uncertainty in the source radius, we also include $M(x)$ contours for $R_* = 61 \pm 12 R_\odot$.

Figure 6.11 shows the result of Equation 3.16 as a function of lens distance, for the observed $\widehat{v} = 193\,\mathrm{km\,s^{-1}}$, and assuming $D_s = 9\,\mathrm{kpc}$. The lower *solid* line shows disk lenses

only, and the upper *solid* line shows the sum of disk + bulge lenses; the relative areas indicate that there is about an 80% probability that this lens belongs to the bulge.

We define a median distance $x_{\rm med}$ such that half of the integrated likelihood arises from $x < x_{\rm med}$, giving $x_{\rm med} = 0.77$ and a median mass estimate of $M_{\rm med} = 0.67\,M_\odot$. Similarly, we define a 90% confidence interval (x_1, x_2) such that 5% of the integrated likelihood arises from each of $x < x_1$ and $x > x_2$; the resulting interval is $0.52 < x < 0.943$, which translates into a mass interval of 0.21 to $3.2\,M_\odot$. These results are relatively insensitive to the details of the galactic model, since the constraints on x are dominated by the drop in ρ_{Bulge} for $x \lesssim 0.6$ and by the geometrical factor $\sqrt{x(1-x)}$ for $x \to 1$.

For reference, Figure 6.12 shows $\hat{v} \int \mathcal{L}(x;\hat{v})\,dx$, i.e. the lensing rate per unit $\log \hat{v}$ for disk and bulge lenses. The observed value of $\hat{v} = 193\,{\rm km\,s^{-1}}$ is well within the range of expected values. The areas under the two curves reflect the fact that bulge lenses produce about 3 times the event rate of disk lenses for the above models. This figure shows that there is a large overlap in the distributions; events with $\hat{v} \lesssim 150\,{\rm km\,s^{-1}}$ are produced almost entirely by bulge lenses, but the more common events with larger $\hat{v}$ arise from both disk and bulge lenses; thus, proper motion measurements towards the bulge are not as useful as parallax measurements for constraining the lens distance. (This has been previously noted by Han & Gould 1995).

Note that this is distinctly different from the LMC case, where either proper motion or parallax measurements provide a good separation of the various lensing populations (Gould 1996).

Constraints on Lens Luminosity

As seen above, if the lens is more distant than $x > 0.9$, it has a relatively large mass. If it is a hydrogen-burning star, we can constrain this possibility as follows. For the above proper motion of $\mu \approx 4.5$ mas/year, the lens is completely unresolved from the source during our observations, thus the observed light–curve of our 'object' is simply the sum of that from the source, the lens and possibly other superposed stars.

Any flux from the lens would add a constant un–magnified baseline which would distort the microlensing fit. Although in most cases this additional flux would be a small fraction

of the flux of the source star, with the high precision measurements here this would be detectable even if the lens is considerably fainter than the source.

We have fit blended microlensing to data of magnification $A < 10$. We note that the χ^2_{dof} of all light–curves in these blended fits are similar to those in the extended source fits. We therefore exclude the MACHO data in our lens brightness estimate due to excessive baseline scatter; however, this turns out to be unimportant. The most follow–up data with $A < 10$ are contained in the CTIO and UTSO observations. For the CTIO R, UTSO R, and UTSO V passbands, we find $(1 - f) \approx (-0.021 \pm 0.016), (-0.019 \pm 0.017)$, and (-0.015 ± 0.016), respectively, consistent with zero flux from the lens. For completeness, we note that similar results are obtained from the MACHO data, with $(1-f) \approx (-0.012 \pm 0.017)$ and (-0.026 ± 0.018) for MACHO V and MACHO R, respectively. MJUO and Wise data did not contain enough baseline observations to determine accurately the amount of unlensed flux. In the following, we take 0 ± 0.02 as a conservative limit.

If the lens is a main-sequence star, we may predict its apparent brightness using the mass-distance relation of Equation 3.13. Assuming a main-sequence V-band mass-luminosity relation $L/L_\odot = (M/M_\odot)^{3.5}$, and 1.5 magnitudes of extinction, we find that the apparent brightness of a main-sequence lens would be e.g. 1% of that of the source star for $x = 0.83$, and 10% for $x = 0.90$. Note that the implied lens brightness *increases* with distance since the rapid rise in $M(x)$ outweighs the r^{-2} term; note also that a giant lens is excluded at any distance.

Instead of applying a sharp limit $x < 0.88$, it is more rigorous to multiply the likelihood function of Equation 3.16 by the Gaussian probability that the lens brightness is consistent with the above constraint on $(1 - f)$. This causes a rapid roll-off in the likelihood function for $D_l > 7.5\,\mathrm{kpc}$, as shown by the dotted curves in Figure 6.11. Assuming a main-sequence lens, we can re-compute the constraints on x and M from the likelihood function with the brightness factor, giving a median $x = 0.73$, a mass of $M_{med} = 0.53\,M_\odot$, and 90% confidence intervals of $0.48 < x < 0.84$ and $0.18 < M < 1.05\,M_\odot$. Thus, the inclusion of the lens brightness constraint reduces the median mass only slightly, but considerably strengthens the upper limit.

Table 6.5: 95-BLG-30: Spectral Observations Summary

JD	Telescope & Instrument	Dispersion	Resolution	Coverage	S / N
2449944.234	CTIO 4m/RC Sp.	1.0 Å pix^{-1}	4.0Å	6230–9340Å	~ 100
2449945.211	CTIO 4m/RC Sp.	1.0 Å pix^{-1}	4.0Å	6230–9340Å	~ 100
2449947.221	Keck 10m/HIRES	0.04 Å pix^{-1}	0.2Å	4309–6739Å	92-256
2449947.524	MSO 74"/Cass. Sp.	0.9 Å pix^{-1}	4.6Å	6240–6770Å	106
2449948.223	Keck 10m/HIRES	0.04 Å pix^{-1}	0.2Å	4835–7282Å	166-296
2449948.504	MSO 74"/Cass. Sp.	0.9 Å pix^{-1}	4.6Å	6240–6770Å	117
2449949.509	MSO 74"/Cass. Sp.	0.9 Å pix^{-1}	4.6Å	6240–6770Å	113
2449950.322	Keck 10m/HIRES	0.04 Å pix^{-1}	0.2Å	3750–6065Å	20-141
2449950.523	MSO 74"/Cass. Sp.	0.9 Å pix^{-1}	4.6Å	6240–6770Å	91
2449951.498	MSO 74"/Cass. Sp.	0.9 Å pix^{-1}	4.6Å	6240–6770Å	96
2449952.508	MSO 74"/Cass. Sp.	0.9 Å pix^{-1}	4.6Å	6240–6770Å	72
2449953.494	MSO 74"/Cass. Sp.	0.9 Å pix^{-1}	4.6Å	6240–6770Å	78
2449954.513	MSO 74"/Cass. Sp.	0.9 Å pix^{-1}	4.6Å	6240–6770Å	66
2449987.000	CTIO 4m/RC Sp.	2.0 Å pix^{-1}	8.0Å	3890–9830Å	~ 100

6.2.3 Spectral Variation during MACHO 95-BLG-30

In addition to the CTIO observations discussed in Chapter 6.2.1, we have obtained spectra at Mount Stromlo and Keck [7] Observatories. Table 6.5 lists the complete catalogue of spectroscopic observations of this event. Figure 6.13 schematically shows the location of the lens with respect to the source when these different observations were made. Nightly spectra of the source star were taken between August 18 and 25, 1995 (from 2.8 to 9.8 days after peak magnification), with the Cassegrain spectrograph at the MSO 74–inch telescope. They cover the wavelength interval 6240–6770 Å, with a dispersion of 0.90 Å per pixel, and a resolution FWHM = 4.6 Å as determined from the comparison lamp spectra. The total exposures were typically 1000 seconds long. These MSO spectra are wavelength calibrated and sky subtracted, but not fluxed. The S/N per resolution element is listed in Table 6.5, along with other relevant data.

The CTIO and MSO spectra have similar resolution, with the exception of the September 27 CTIO spectrum, which has lower resolution. We rebinned the CTIO and MSO spectra in order to compare them directly. Figure 6.14 shows the spectral sequence, which constitutes one of the most extensive and homogeneous series of spectroscopic observations of a microlensing event to date (see also Benetti, Pasquini, & West 1995 and Lennon et al.

[7] The Keck telescope project was made possible by a generous grant from the W.M. Keck Foundation.

1996). It is clear that the microlensing does not change the spectral type of the star, nor does it strongly affect the major spectral features. However, subtle effects may appear in some spectral lines, as discussed by Valls-Gabaud (1995) and Loeb & Sasselov (1995), which warrants a more careful comparison among the spectra.

Before this discussion, we note that the MSO spectrum of August 18 (the first spectra taken *after* the lens transit) is anomalous, showing a dip at λ6520Å that looks like an unidentified bandhead. Although we have examined several possible sources for this feature, including checking the flat fields and comparing the spectra of other stars in the field, the cause of this dip is still unexplained.

Each spectrum was divided by the median combination of all spectra (this operation was repeated before and after continuum subtraction, in order to account for possible differences due to flux calibration of the CTIO spectra but not of the MSO ones). Figure 6.15 shows the sequence of these ratios. While there are no strong deviations, the two spectra taken closest to maximum magnification show stronger Hα than the rest. Also, these two spectra show stronger TiO bands than the following ones. The total TiO absorption, however, started to climb steadily after 18 August, 1995. We measured the equivalent widths of several spectral features of interest within 6240–6770 Å with the SPLOT package within IRAF. Figure 6.16 shows the equivalent width of Hα, and the combined intensity of 4 TiO bands in the 6650–6750 Å region. Included are conservative error bars based upon uncertainty in placing the local continuum. The equivalent width of the Hα line was scaled to the equivalent width measured in the HIRES spectra of 18 and 19 August, 1995. These equivalent widths were measured with respect to the local pseudo continuum, in the same way for all the spectra, in order to avoid systematic effects.

While we cannot explain in detail the behavior of these spectral features, changes in the equivalent width of these lines have been predicted by Loeb & Sasselov (1995). These changes are due to limb brightening effects in the cores of resonance lines (like Hα) due to a very extended photosphere. Resonant line scattering may also affect the optical TiO bands in the case of M giants like the MACHO 95-BLG-30 source (Sasselov 1997). Detailed modeling of the spectra of this event in particular is needed, as this will help with the interpretation of forthcoming similar events.

Three spectra were also taken in the nights of August 18, August 19, and August 21, about 5 hours later than the MSO spectra, using HIRES at the Keck 10–m telescope. These high resolution spectra also have high S/N, as listed in Table 6.5, which includes the S/N per resolution element of the lowest and highest orders. The spectra of August 18, August 19, and August 21 consist of 30, 25, and 40 orders, respectively. The blue region below about 4000Å covered in the August 21 spectrum does not have much information due to low counts. We have checked different resonance lines (CaII, Hα, Hβ, Hγ, etc), finding no large variations. The August 21 spectrum has coverage extending to the blue, including the Ca H and K lines, but misses the Hα line. The spectra of August 18 and 19 do not include these Ca lines. The Hα equivalent width differs by only 4% between August 18 and 19, as measured from the high quality HIRES spectra (1.087 vs 1.039Å). This variation occurs in the core of the line. Otherwise, there is no significant change between the Hα profiles of August 18 and 19. The strong TiO band heads at $\lambda\lambda$ 4954, 5166, and 5447 Å are present in all three HIRES spectra. The difference of about 10% in strength of these bands between August 18 and 21 seen in the MSO spectra is confirmed.

We have also fit the NaI (D) line profiles in the HIRES spectra with an interstellar cloud model which uses 12 clouds over the velocity range $-60.8\,\mathrm{km\,s^{-1}}$ to $+202.3\,\mathrm{km\,s^{-1}}$. The clouds with extreme velocities only fit one line of the Na doublet because of problems with the continuum determination and blending with other lines. The interstellar clouds indicate that the star is at a great distance and therefore it is certainly a giant, as discussed in Chapter 6.2.1.

We also measured the radial velocities of the MSO spectra using the cross-correlation routine FXCOR within IRAF. From the MSO spectra, we measure a mean velocity of $V_r = -76 \pm 4\,\mathrm{km\,s^{-1}}$, which is in excellent agreement with the mean velocity of $V_r = -80 \pm 5\,\mathrm{km\,s^{-1}}$ from the CTIO spectra, reduced and calibrated independently (Chapter 6.2.1). The velocities of the eight MSO spectra agree with each other within an rms of $12\,\mathrm{km\,s^{-1}}$. We measured also the radial velocity of the August 21 HIRES spectrum, $V_r = -86.2 \pm 3.9\,\mathrm{km\,s^{-1}}$, using the strong Cr lines at $\lambda\lambda$ 4254, 4274, and 4289 Å. All these velocities are in excellent agreement, and we adopt a final value of $V_r = -81 \pm 5\,\mathrm{km\,s^{-1}}$ for the source star in MACHO 95-BLG-30.

Subtle radial velocity variations (of the order of $1-2\,\mathrm{km\,s^{-1}}$) may also be expected during microlensing events such as this one (Maoz & Gould 1994), and can give an independent measurement of the proper motion. Alternatively, combining the radial velocity variation with the extended source magnification effect, one can determine the projected rotation velocity of the star (Gould 1997). We note that detecting such velocity differences may be possible using the HIRES spectra, after detailed corrections and modeling that are beyond the scope of the present paper.

In summary, we have obtained a large number of spectra of the microlensed source star during MACHO Alert 95-BLG-30. These spectra show subtle variations, which support the predictions of existing microlensing and stellar models. These spectra demonstrate that differential magnification of an extended source star during a gravitational microlensing event may be used to probe otherwise inaccessible stellar atmosphere "fine structure".

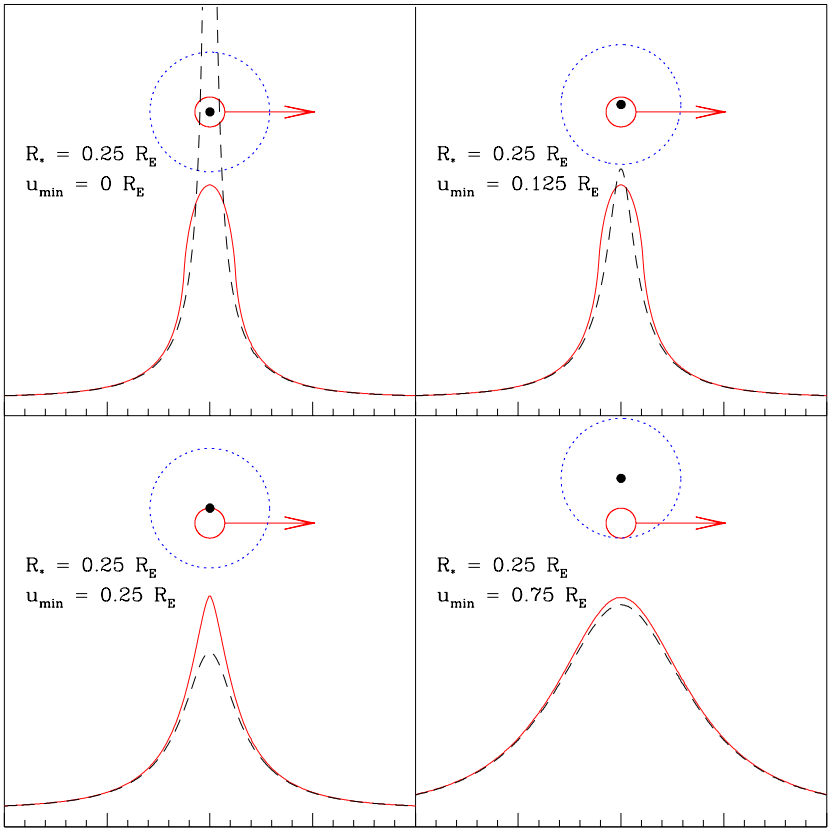

Figure 6.1:
Four example lightcurves illustrating the effect of extended source size on a microlensing lightcurve. The upper schematic shows an extended source as a *solid* circle, and the lensing object as the *solid* point, surrounded by its *dotted* Einstein ring. The source radius is $0.25R_{\rm E}$. The lens impact parameter $u_{\rm min}$ is measured with respect to the center of the source star. The bottom schematic represents the event lightcurve in the case of an extended source (*solid* line) and a point source (*dashed* line). Note the maximum magnification of a extended source with $u_{\rm min} = 0$ is finite (upper left panel). The peak of the lightcurve is the best region to detect or set limits on extended source effects.

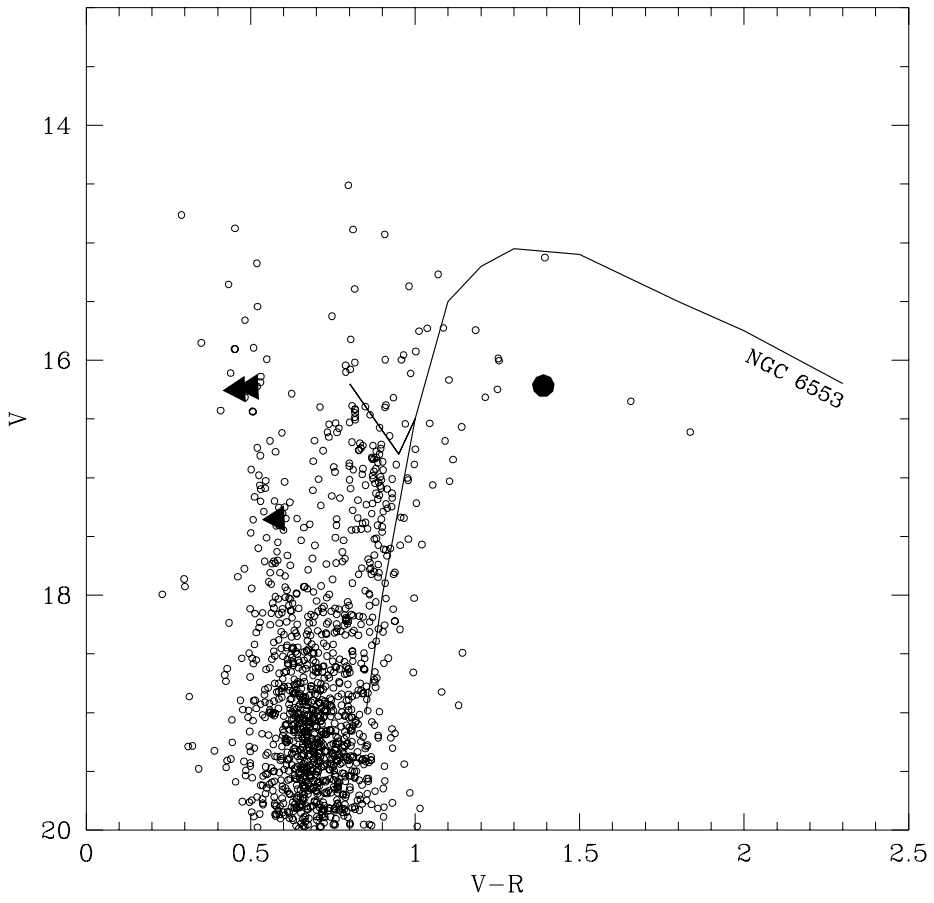

Figure 6.2:
Single epoch optical V vs $V-R$ color–magnitude diagram of the field surrounding the 95–BLG–30 source star, which is indicated with a *filled* circle. Three RR Lyr used to estimate the reddening are plotted as triangles. The fiducial loci of the giant branch of the metal–rich globular cluster NGC 6553 ($[Fe/H] = -0.2$) from Ortolani et al. (1990) is also indicated.

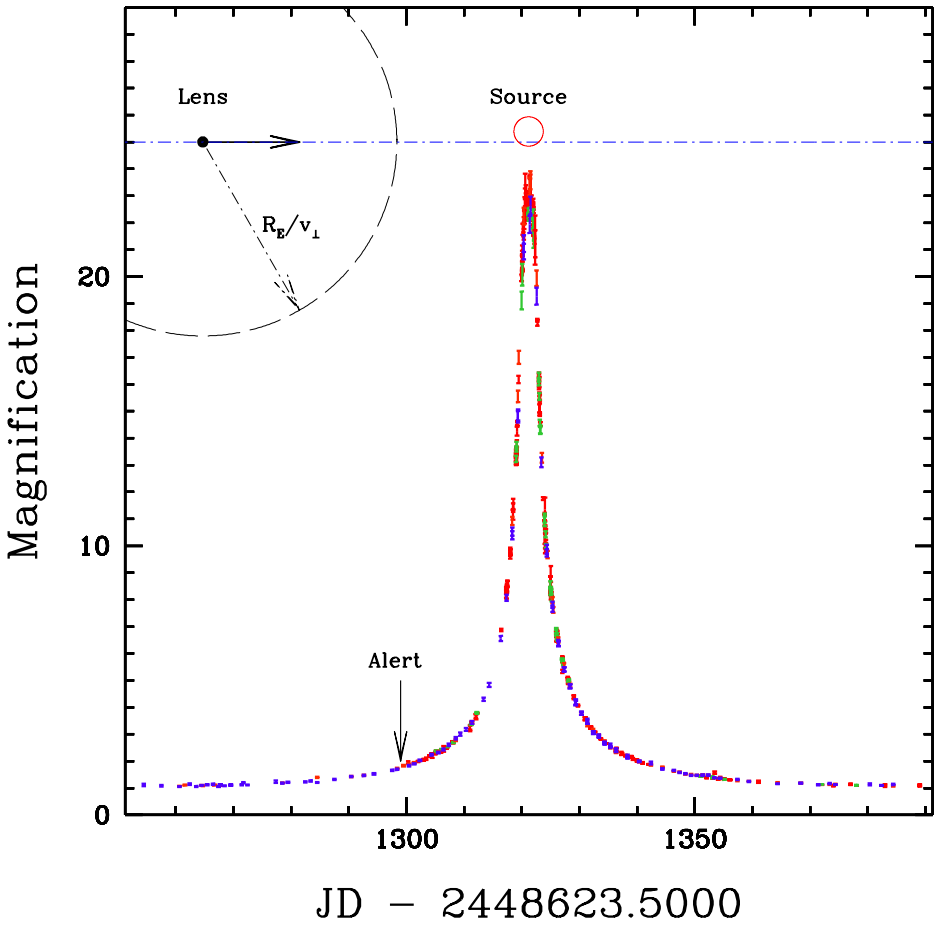

Figure 6.3:
1995 light–curve of MACHO Alert 95–BLG–30. The data represent MACHO–GMAN observations of this event in all passbands within a window of 70 days around peak magnification. The date this event was detected by the MACHO Alert system is indicated with an arrow. An additional schematic relates the scale of the lens's Einstein radius to the angular size of the source star, and indicates transit of the lens across the source face.

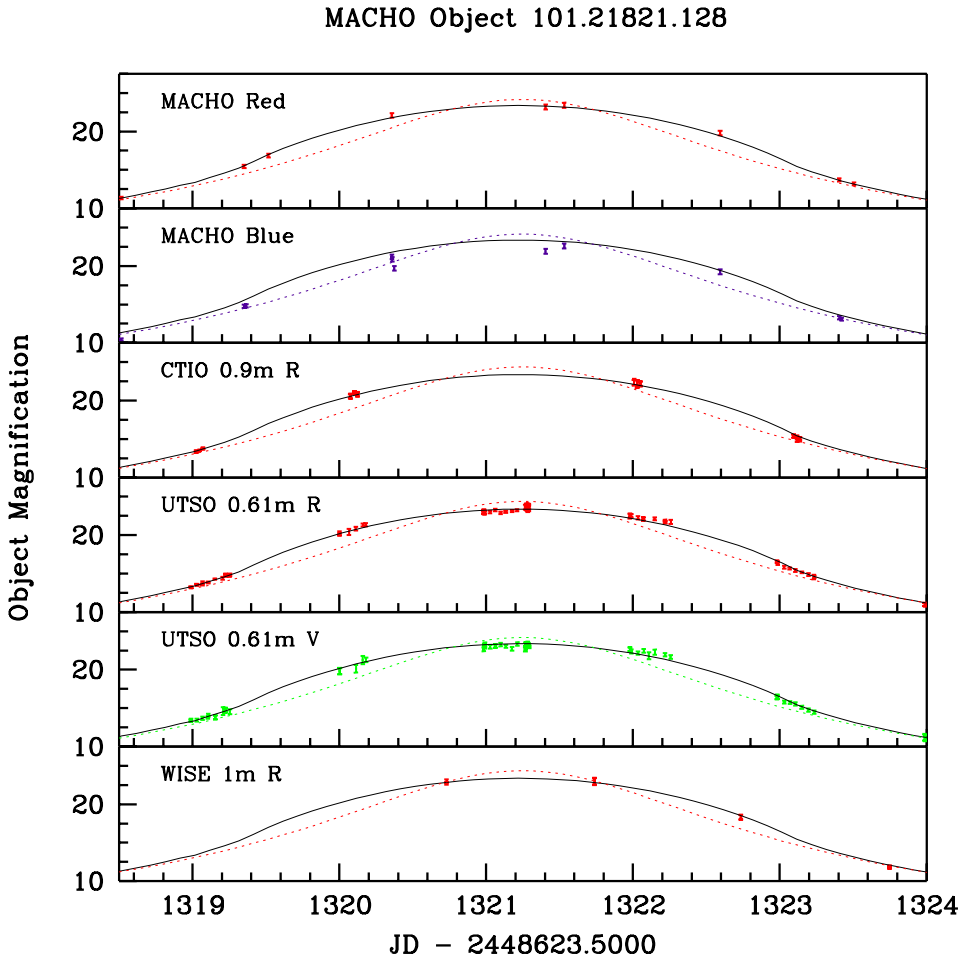

Figure 6.4:
Peak of MACHO Alert 95–BLG–30, showing the best standard microlensing fit to the data (*dashed* line) and an extended source microlensing fit incorporating source limb–darkening (*solid* line).

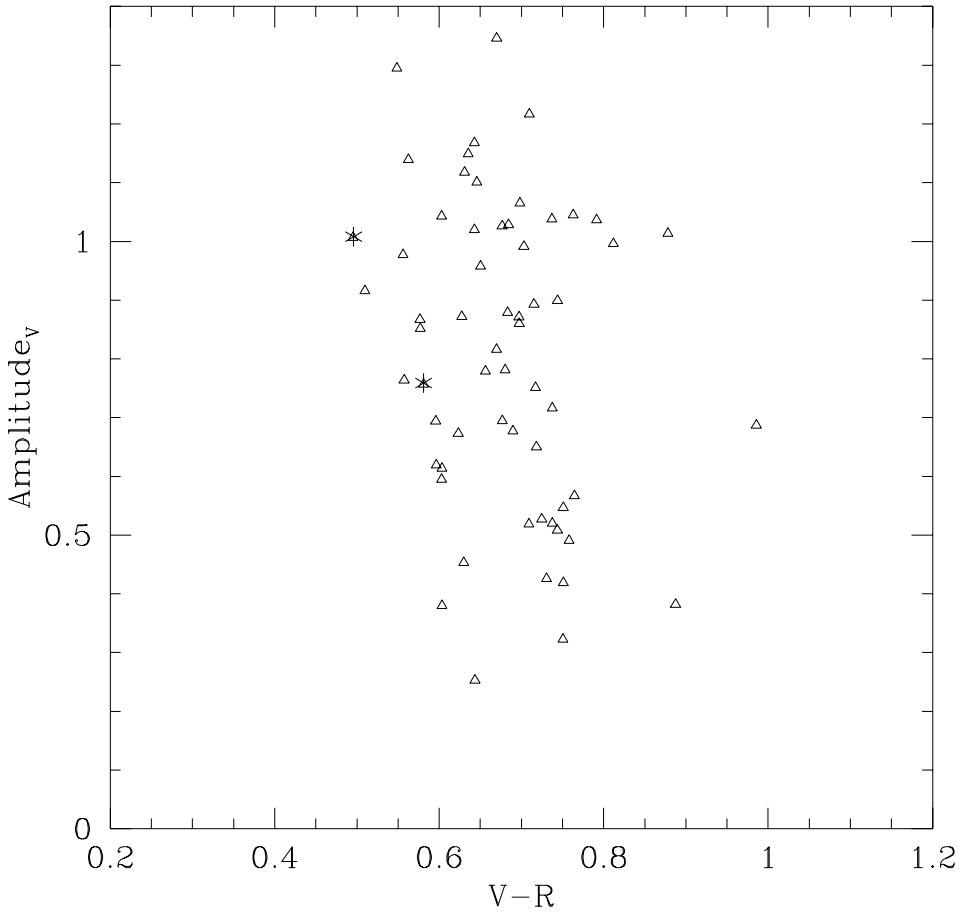

Figure 6.5:
Amplitude vs. color of the RR Lyr type ab in the MACHO field where the 95–BLG–30 source is located. The two RRab closest to the source star are indicated with asterisks. We find $A_V = 1.35$ mag.

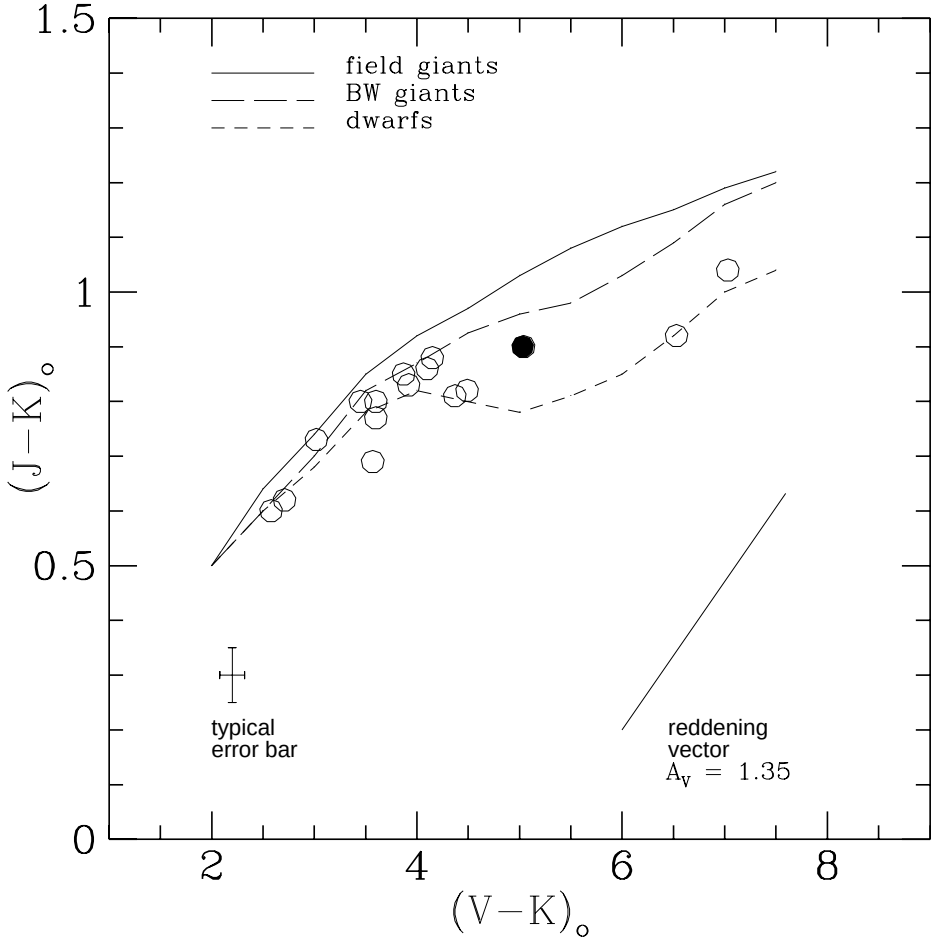

Figure 6.6:
Optical–infrared $(V-K)_0$ vs $(J-K)_0$ color–color diagram for the giants brighter than 1 mag above the horizontal branch in the 95–BLG–30 field. The fiducial loci of field giants, dwarfs, and Baade's Window giants from Frogel & Whitford (1987) are indicated with the *solid*, *short-dashed*, and *long-dashed* lines, respectively.

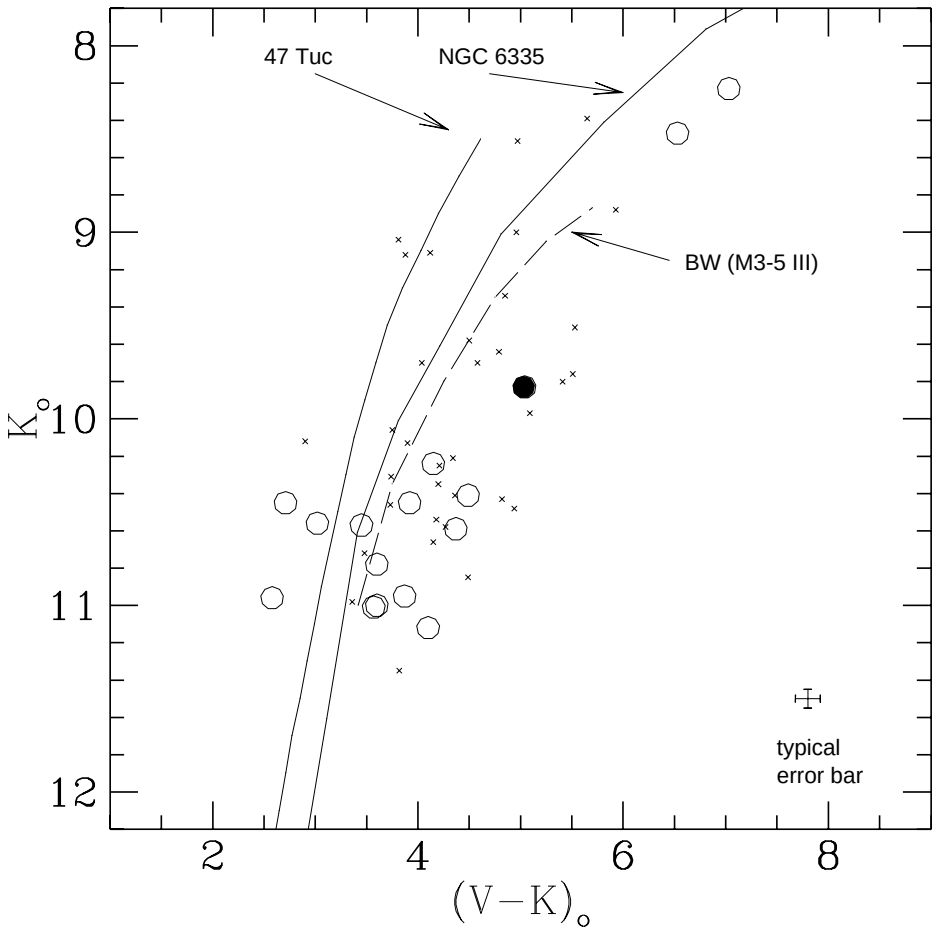

Figure 6.7: Optical–IR K_0 vs $(V-K)_0$ color–magnitude diagram of the 95–BLG–30 field. The fiducial loci of the giant branches of the metal–rich globular clusters 47 Tuc ($[Fe/H] = -0.7$), and NGC 6553 ($[Fe/H] = -0.2$) from Guarnieri et al. (1996) are indicated. Additionally, we have plotted BW M3–5 giants (Frogel & Whitford, 1987) as small crosses and drawn our own estimated fiducial line through these points.

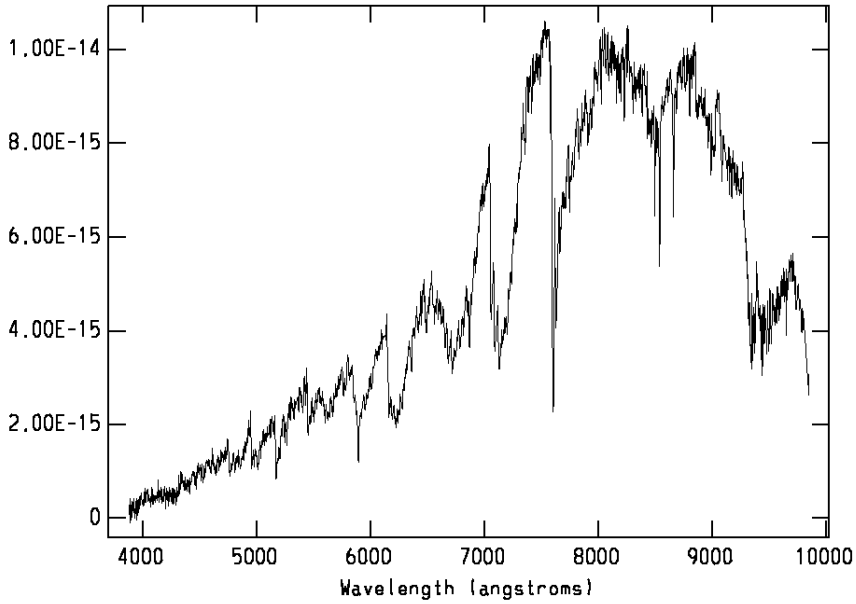

Figure 6.8: Baseline spectrum of the 95–BLG–30 source star obtained at CTIO on September 27, 1995, 42 days after maximum magnification. The flux calibration is unreliable beyond 9000Å.

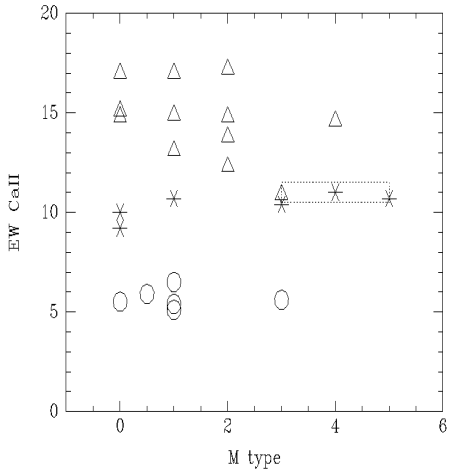

Figure 6.9: CaII equivalent width in Å *vs* M spectral sub-type for dwarfs (*circles*), giants (*asterisks*), and supergiants (*triangles*). The box encloses the $\pm 1\sigma$ measurements of the source star in MACHO 95–BLG–30.

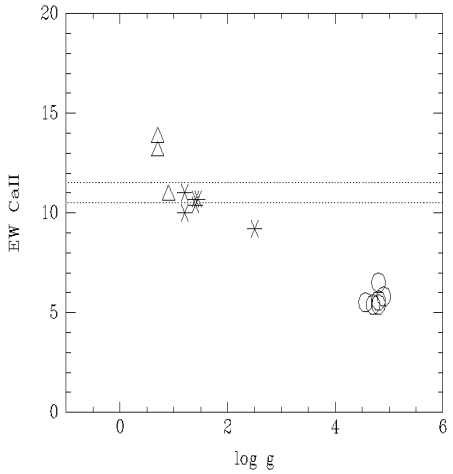

Figure 6.10: CaII equivalent width in Å *vs* $\log g$, with the *dotted* lines indicating the CaII equivalent width of the source star in MACHO 95–BLG–30 ($\pm 1\sigma$).

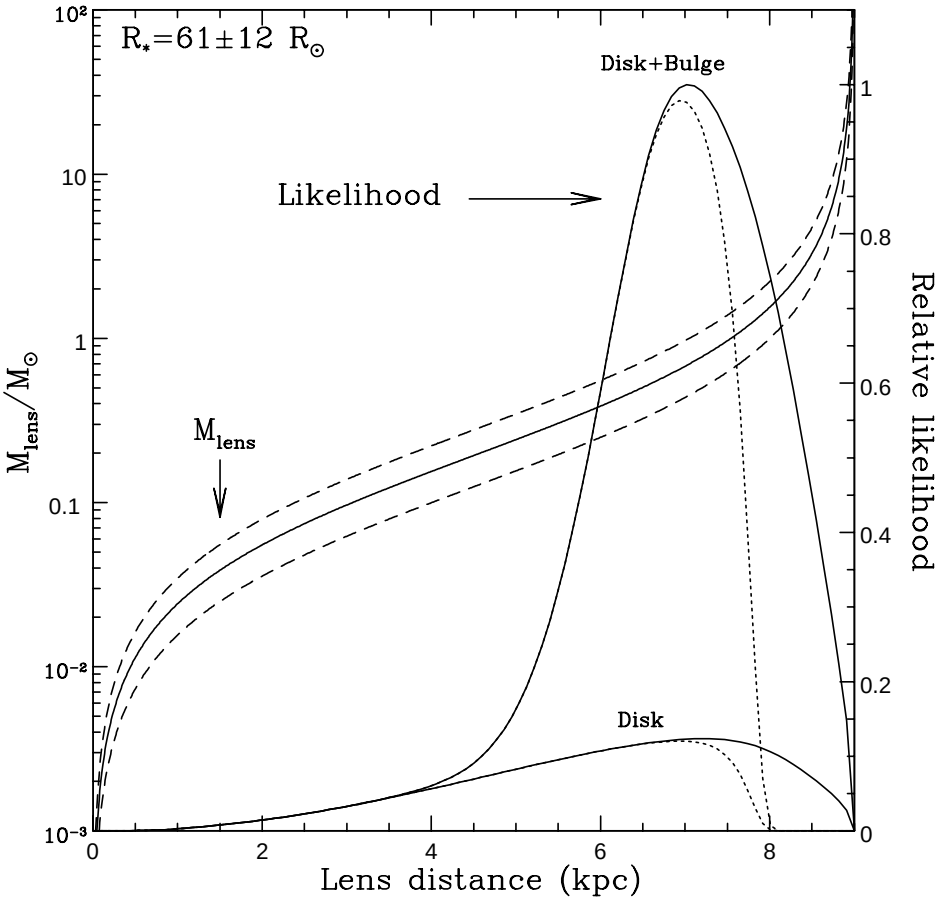

Figure 6.11:
95–BLG–30 lens mass plotted as a function of its distance, using Equation 3.13. This assumes a $61R_\odot$ source, with error contours provided at $\pm 12R_\odot$, and event parameters listed in Table 6.2 (Fit 3). The *solid* likelihood curves show relative probabilities for disk and bulge lenses as a function of their distance. The *dotted* lines include an upper limit on the brightness of a main–sequence lens set from the microlensing blend fractions.

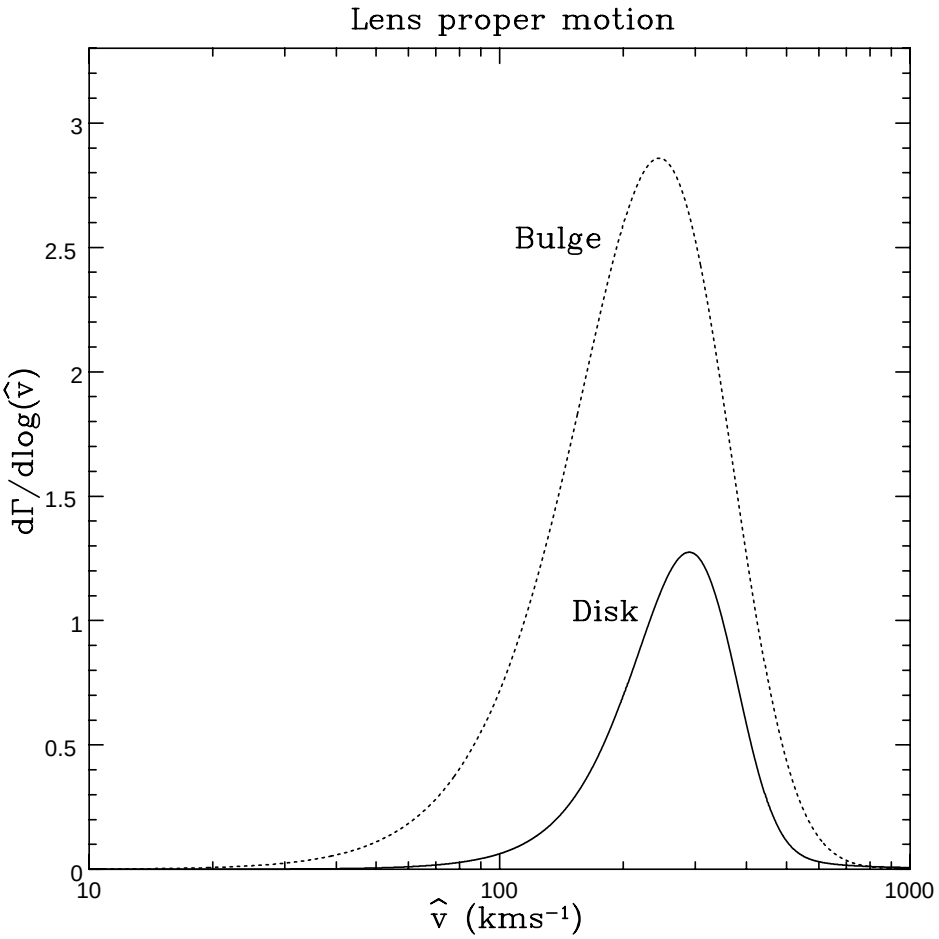

Figure 6.12:
Lensing rates per unit log $\widehat{v}$ for Galactic disk and bulge lenses, indicated with the *solid* and *dashed* lines, respectively.

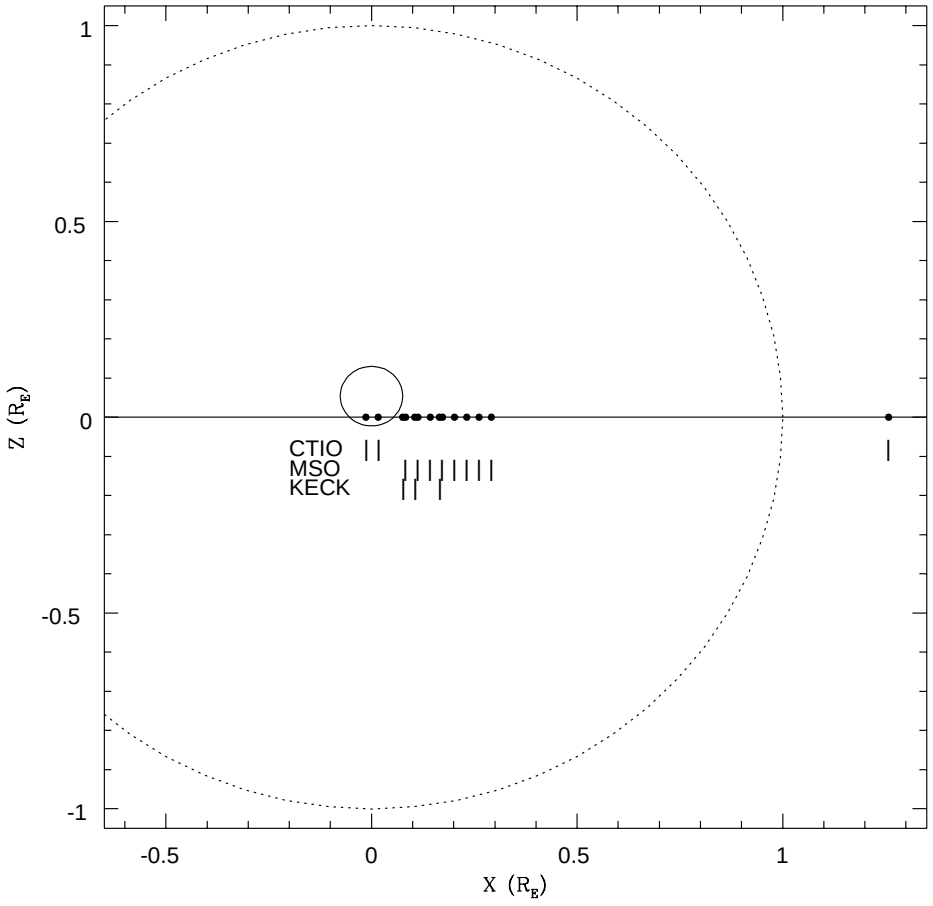

Figure 6.13:
95–BLG–30 spectral observations listed in Table 6.5 plotted on the source plane. The relative sizes of the source star (*solid* circle) and the lens's Einstein radius (*dotted* circle) are plotted to scale, in units of $R_{\rm E}$. The *solid* points show the position of the lens at the different times when spectra were taken. The observatories where the spectra were taken are indicated with the tick marks.

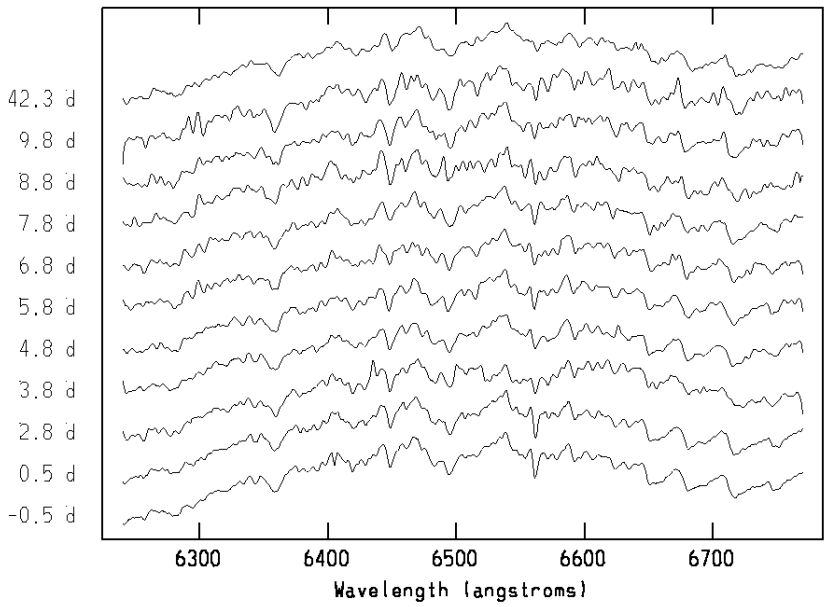

Figure 6.14:
Spectra of the 95–BLG–30 source star taken at CTIO and MSO. All of these have similar resolution, except for the top one. Note Hα at λ6563 Å, and the TiO band–heads at $\lambda\lambda$ 6647, 6676, 6711, and 6742 Å. Days from the peak of the microlensing event are indicated along the vertical axis.

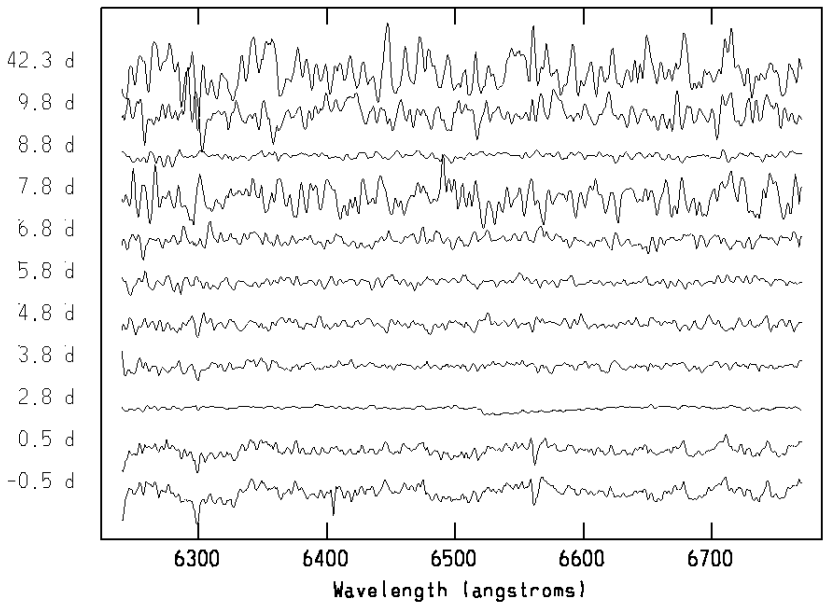

Figure 6.15:
Same as Figure 6.14, showing the spectra divided by the median combination of all. These have been displaced in the vertical direction and arbitrarily scaled, such that the flattest spectra here actually display the largest range of excess from the median combination. Note the changes in Hα and the TiO bands in the two spectra nearest peak magnification.

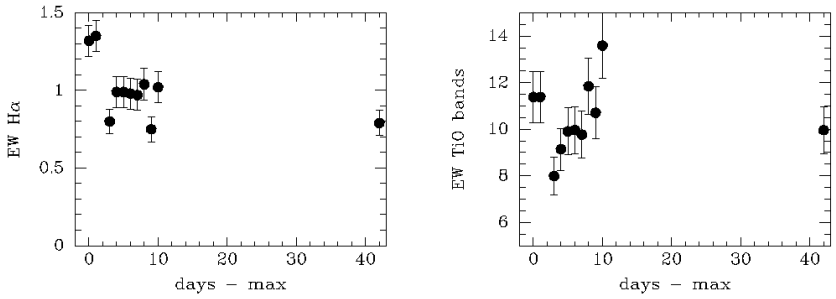

Figure 6.16:
Temporal evolution of the 95–BLG–30 equivalent width in Å of Hα and the TiO band–heads, measured with respect to the local pseudo–continuum. The EW plotted in the right panel are the sum of the TiO bands at $\lambda\lambda$ 6647, 6676, 6711, and 6742 Å.

Chapter 7

EXOTIC MICROLENSING: BINARY LENS EVENTS

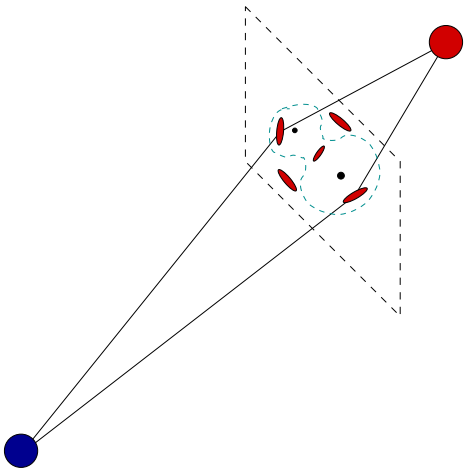

7.1 Binary Lens Theory

Binary lensing is described by the generalization of Equation 3.1 to the case of two deflectors:

$$\vec{s} = \vec{i} - R_{\rm E}^2 \left(\epsilon_1 \frac{\vec{i} - \vec{l}_1}{(\vec{i} - \vec{l}_1)^2} + \epsilon_2 \frac{\vec{i} - \vec{l}_2}{(\vec{i} - \vec{l}_2)^2} \right) \ , \tag{7.1}$$

where $\epsilon_1 + \epsilon_2 \equiv 1$, and refer to the mass fraction of each lens. $R_{\rm E}$ now refers to the Einstein ring radius of the complete lens system $(M_1 + M_2)$.

As with the single lens, Equation 7.1 represents a mapping from the image plane to the source plane. This mapping is well behaved, but the inverse mapping from the source plane to the image plane is multi–valued, with each point on the source plane mapping into either 3 or 5 points on the image plane. The boundaries between the regions of 3 and 5 images in the image plane are referred to as critical curves. These critical curves map into closed caustic curves (or caustics) in the source plane. The shape of a caustic curve is characterized by inwardly curved segments joined at outwardly spiked cusps.

A binary lens lightcurve can be described by 7 parameters, if the orbital motion of the lensing objects is neglected. These parameters include the 3 parameters for a single lens fit $\widehat{t}$, $u_{\rm min}$, and t_0, where $u_{\rm min}$ and t_0 are now measured with respect to the lensing system's center of mass. The 3 intrinsic binary parameters are the binary lens separation (scaled by $R_{\rm E}$), a; the mass fraction, ϵ_1; and the angle between the lens axis and the source trajectory, θ. A final parameter may be added if the source star crosses a caustic, the source radius crossing time $t_* = \theta_*/\mu$. This represents the time it takes the lens to move relative to the source by an angle equal to the source angular radius – typically an hour to a day. This may be constrained by observing the caustic crossing duration $2t_*/\sin\phi$, where ϕ is the angle between the relative motion vector and the caustic line. This parameter is sensitive to the assumed limb darkening model. An additional blending parameter f must also be included for each passband. An excellent treatment of binary microlensing can be found in Dominik (1998b).

When a source crosses near or over a caustic, the event lightcurve can differ quite significantly from the standard microlensing lightcurve. During a caustic crossing, the determinant of the lens mapping in Equation 7.1 goes to zero. This divergence of the magnification factor implies that a point source located on a caustic curve becomes infinitely bright. In this situation, two of the images either merge and disappear, or are created, such that the number of images is greater within the region bounded by the caustic surface. For a realistic source brightness profile, the observed magnification is the weighted mean of the magnification factor over the source, which always leads to finite values. If one is able to observe a caustic crossing, the temporal width of the transit provides a measurement of t_*, if ϕ is sufficiently constrained by the global microlensing fit. An estimate of the true angular source size then yields the proper motion of the lensing system with respect to the source star.

Figure 7.1 demonstrates a typical caustic–crossing binary lensing system. The upper region of each panel in Figure 7.1 represents the lensing encounter seen in the source plane. The angular size of the source is represented by the circle, and the cuspy lines represent the caustic structure induced by the binary lens. This may be thought of as representing the local maximum in the isomagnification contours – it is a 2–dimensional analog of the point caustic seen in single lens microlensing. The corresponding microlensing lightcurve is shown

in the bottom of each panel – note it is considerably different than the typical microlensing lightcurve. The figure begins in the upper left–hand corner, after the source has passed within the caustic structure. The lightcurve exhibits a sharp feature whose temporal width is brief, but whose passage may be noted by the enhanced lightcurve magnification. The lightcurve evolves to the right along the top row, as the source moves through the caustic structure 5 and 10 days after the original caustic crossing. If the lightcurve is sampled well enough, the time of the source exiting the caustic region may be predicted. Resolution of extended source effects during this caustic crossing leads to the lens proper motion, similar to Chapter 6. In general, once a caustic crossing event is detected (the first caustic crossing is unlikely to be resolved due to its short duration), one is guaranteed a second caustic crossing. This situation is seen in the middle set of panels, which are centered on the source and demonstrate the caustic line sweeping across its face. The temporal width, which can be measured by sampling and fitting the lightcurve shape below, yields the lens proper motion once the source angular radius is determined. In this figure, the lens proper motion is $\theta_*/0.11$ days. Note, the timesteps in these middle panels are brief, and indicate that considerable information about the lensing system is encoded in ~ 2.5 hours of the source lightcurve profile. It is thus imperative that predictions be made about the timing of second caustic crossings. The bottom panel shows the global lightcurve as the view zooms out and the source moves away from the caustic region.

Resolving this effect provides an especially important constraint in binary lensing events seen towards the Magellanic Clouds, where there is a distinct difference between the expected relative proper motion of a binary lens in the Galactic dark halo ($\mu \sim 30\,\mathrm{km\,s^{-1}\,kpc^{-1}}$), and of a binary lens in the Magellanic Clouds, where the relative proper motion is a function of the velocity dispersion in the Cloud ($\mu \sim 1\,\mathrm{km\,s^{-1}\,kpc^{-1}}$).

7.1.1 Estimates of the Binary Lensing Rate

The overall phenomenology of lensing by two point masses is well known (e.g. Schneider & Weiss 1986), and the lightcurve morphology expected in the Galactic microlensing limit well established (e.g. Mao & Paczyński 1991, Mao & Di Stefano 1995, and Di Stefano & Perna 1997). Mao & Paczyński (1991) predicted that $\sim 7\%$ of all events seen towards the

Galactic bulge should show strong evidence of lens binarity, and that as many as $\sim 3\%$ of bulge events might show evidence of a high mass ratio (planetary) binary system, depending upon the abundance of giant planets. The prospect of detecting extra–solar planets through lens binarity has led to much investigation (Gould & Loeb 1992; Bolatto & Falco 1994; Bennett & Rhie 1996; Peale 1997; Gaudi, Naber, & Sackett 1998), and distinct methods and detection rates for multiple classes of planetary lensing (Griest & Safizadeh 1998; Di Stefano & Scalzo 1999a; Di Stefano & Scalzo 1999b).

The question of the fractional binary lensing rate has recently been analyzed in more detail by Di Stefano (2000), who argues that, in the extreme case where *all* lenses are binaries, $\sim 6\%$ of all events should exhibit caustic crossings. This fraction will obviously decrease if some lenses are single. Thus the majority of binary lensing events should result in multiply–peaked lightcurves or low amplitude deviations from single lens lightcurves, without caustic features. However, Di Stefano (2000) appears to underestimate the observational bias towards low impact parameter (small $u_{\rm min}$) events. Di Stefano (2000) considers all events with $u_{\rm min} \leq 1$ to be detectable if they are sampled frequently, but in fact the MACHO analysis and Alert System trigger both explicitly exclude lensing events with $u_{\rm min} \gtrsim 0.75$. Additional cuts on the signal to noise of the stellar brightening also discriminate against the large $u_{\rm min}$ events, which may lie within the relatively large error bars ($\sim 7\%$) of survey system photometry. Furthermore, most of the events seen towards both the Galactic bulge and the Magellanic Clouds are significantly blended, such that the true $u_{\rm min}$ value is generally smaller than the observed value used for event selection. Figure 2 of Di Stefano (2000) indicates that the fraction of caustic crossing events would be substantially higher if a smaller $u_{\rm min}$ cut (*i.e.* $u_{\rm min} \lesssim 0.3$) were used to better reflect the survey team's event selection criteria.

7.1.2 Previous Binary Lens Observations

The first unambiguous case of binary microlensing was reported by the OGLE collaboration (OGLE–7, Udalski et al. 1994), and later corroborated with data from the MACHO database (Bennett et al. 1995; Mao et al. 1994). Subsequent binary lens event publications include DUO 2 (Alard, Mao, & Guibert 1995), MACHO 95–BLG–12 (Pratt et al. 1996;

Albrow et al. 1997), MACHO LMC–1 (Rhie & Bennett 1996; Dominik & Hirshfeld 1996), MACHO LMC–9 (Bennett et al. 1996b), MACHO 97–BLG–28 (Albrow et al. 1999c), and MACHO 98–SMC–1 (Alcock et al. 1999a; Afonso et al. 2000). In addition, there have been a number of binary lensing events discovered in progress and announced on the web sites of the various microlensing survey and follow–up programs (see Chapter 4).

7.2 Binary Lens Detections

We have not made a complete assessment of our binary lens detection efficiency, and the events presented here were selected by a variety of different mechanisms. Most were originally discovered with the MACHO Alert System, and were subsequently observed to deviate from the standard microlensing lightcurve. Other events were discovered via our normal analysis procedure (see Alcock et al. 1997a), difference imaging analysis (DIA) on a subset of our database (Alcock et al. 1999b), or during testing of the Alert System software. It should be emphasized that for some of these fits there are probably degeneracies between model parameters. That is, the fit presented is not unique, but does represent a local minimum in parameter space. Is it likely that for some of these events, particularly the poorly sampled ones, there are different lens configurations whose lightcurves, as sampled by our observations, are similar to the fits presented here (see Dominik 1999). There are, however, systematic approaches to determining all physical solutions for a set of microlensing data (e.g. Di Stefano & Perna 1997 and Albrow et al. 1999a).

Characteristics of the MACHO objects that received the lensed flux are presented in Table 7.4. Each object is given an event name in addition to the MACHO star ID number which has been previously assigned. For each object, we include the transformation to Cousins V and $V-R$, calibrated using Alcock et al. (1999c). From the blending parameters included in the binary microlensing fit, we can also estimate the true brightness and color of the star which was lensed. This information is also included in Table 7.4. For all events, we will refer to the (sometimes blended) object identified in the MACHO database as the 'object', and refer to the 'source' as the actual star in the blend which was lensed. Fit parameters for these binary microlensing events are given in Tables 7.5 and 7.6. For each event, we present a lightcurve of these fits, as well as a schematic of the critical and caustic

curves induced by the binary lens (Figures 7.7–7.48).

Figure 7.49 and Figure 7.50 display the distribution of V, $V-R$ for neighboring sources in the same 5'x5' "chunk" (1/64 of MACHO's focal plane) as the lensed object, for Magellanic Cloud and Galactic bulge sources, respectively. The solid circle indicates the location of the MACHO object, and the open circle represents the location of the lensed source, as determined from the blending parameters.

7.2.1 98-SMC-1 (208.15683.4237)

Discovery and Observations

The source star in MACHO Alert 98–SMC–1 is located at α =00:45:35.2, $\delta = -72$:52:34.1 (J2000). MACHO Alert 98–SMC–1 was announced May 25.9 UT after the source had apparently brightened by ~ 0.9 mag. The baseline magnitude and color of the MACHO object had been constant over 5 years of observations, at $V = 21.37 \pm 0.10, V - R = 0.14 \pm 0.05$. Our binary microlens fit presented in Chapter 7.2.1 indicates that the lensed source has a brightness of $V = 22.05 \pm 0.15, V - R = 0.03 \pm 0.10$, with the additional unlensed flux provided by other sources within the seeing disk (as quite commonly occurs in these crowded fields).

Follow–up observations were scheduled nightly on the CTIO 0.9m telescope, which showed a gradual rise in the lightcurve until June 6.5 UT, when it was noticed the source had brightened suddenly by 1.5 mag. Photometry from the subsequent night confirmed that this was a likely caustic crossing event, and an IAU Circular was submitted alerting the astronomical community to the first real–time detection of a binary lensing event towards the Magellanic Clouds (Becker, Rhie, & Bennett 1998).

Continued observations allowed an estimate on the date of the second caustic crossing of June 19.3 ± 1.5 UT (Bennett & Rhie 1998) to be issued June 15.3. This error bar was estimated based upon prior experience predicting caustic crossings (see Bennett & Marshall 1996), and also because the path of the source was expected to cross the caustic at a small angle, so that a small error in the source trajectory translated into a large error in the time of the caustic crossing. Data from June 15 caused a revision of the caustic crossing time to June 19.2 ± 1.5 UT, and June 17 data forced a revised prediction of June 18.2.

Figure 7.2 shows the joint MACHO/GMAN/EROS light curve for 98–SMC–1 : dual color lightcurves from the MACHO Project's Mt. Stromlo 1.3m telescope, the CTIO 0.9m telescope, and the EROS Project's 1.0m Marly telescope at La Silla (Palanque-Delabrouille 1997). The CTIO lightcurves are for the standard R and B bands, while the MACHO and EROS lightcurves are for their respective non–standard passbands. The MACHO and EROS data were reduced with the SoDOPHOT photometry package used for routine reduction of MACHO data, while the CTIO data were reduced with ALLFRAME (Stetson 1994). In each case, the photometric error estimates reported by the photometry code are used, with minimum errors of 0.014, 0.01, and 0.005 added in quadrature for the MACHO, EROS, and CTIO data, respectively. The CTIO error estimates are also multiplied by 1.5, although this appears to overestimate the errors for this event. Each lightcurve is normalized to the best fit unlensed flux of the source, so that the brightness of any unlensed (blended) sources has been subtracted out. The overall structure is consistent with a caustic crossing binary lens event.

Figure 7.3 shows a close–up of the latter part of the lightcurve for the MACHO–R, CTIO–R, and EROS–B data. The CTIO–R band data were generally taken over a period of less than 1.5 hours, and have been binned nightly for every night except for June 18.

Analysis

Once it was realized that 98–SMC–1 was a likely binary microlensing event, it was modeled using the binary lens fitting code developed by Bennett & Rhie (1996). Starting with the data available on June 8, we began a series of Monte Carlo searches that initially resulted in several possible binary microlensing fits. By June 14, only one good fit remained, and an accurate caustic crossing prediction was announced (Bennett & Rhie 1998). This preliminary lightcurve and fit parameters were posted on the WWW [8].

Table 7.1 shows the June 15 pre–caustic crossing fit parameter estimates (as the first line) and the current best fit parameters with errors in the second line. Note that the parameters have changed only slightly between the pre–caustic crossing fit and the current fit. The

[8] see **http://darkstar.astro.washington.edu/98–SMC–1_lev2.html** and **http://bustard.phys.nd.edu/MPS/98–SMC–1/**

Table 7.1: Line 1 presents the preliminary binary lens fit parameters announced on June 15, before the second caustic crossing. The second line shows the current best fit binary lens parameters used in the analysis.

[a] Date in June UT.

t_0 [a]	$\widehat{t}$ (days)	$u_{\rm min}$	a	θ (rad)	ϵ_1	t_* (days)
14.5	149	0.043	0.678	-0.205	0.276	···
14.931 (15)	147.58 (41)	0.04628 (12)	0.66365 (84)	-0.1803 (18)	0.27929 (57)	0.116 (10)

Table 7.2: 98-SMC-1: Binary Microlensing Fit Blending Parameters

$f_{\rm CTIO\ R}$	$f_{\rm CTIO\ B}$	$f_{\rm EROS\ R}$	$f_{\rm EROS\ B}$	$f_{\rm MACHO\ R}$	$f_{\rm MACHO\ V}$
0.79	1.00	0.83	0.40	0.47	0.56

fit lightcurves are shown in Figures 7.2 and 7.3, and the parameters of the fit are shown in Tables 7.1 and 7.2. Fit statistics are shown in Table 7.3. We have used a simple linear limb darkening model (Claret, Diaz-Cordoves, & Gimenez 1995) with coefficients 0.482, 0.620, 0.506, 0.697, 0.460, and 0.561 for the MACHO–R, MACHO–V, CTIO–R, CTIO–B, EROS–R, and EROS–B passbands, respectively. Note that the χ^2 per degree of freedom is less than 1 for every passband, except for the MACHO passbands where it is somewhat larger than 1. The excess fit χ^2 in the MACHO data is partially due to excess scatter in the baseline, and from very high airmass observations on June 18.

However, assuming a single source, the uniqueness of this fit seems sound. The MACHO data characterize the full lightcurve. Each night of CTIO observations, begun soon after MACHO's initial alert, constrains the overall lightcurve at the $\lesssim 3\%$ level. Especially important constraints are the flux preceding the first caustic crossing, the minimum flux between caustics, and the magnitude of the cusp passage after the second caustic crossing, which strongly constrains θ and avoids fit uncertainties present in other analyses of this event (Albrow et al. 1999b; Afonso et al. 1998). The two fits presented by the PLANET collaboration (Albrow et al. 1999b), for example, both appear inconsistent with the pre–caustic crossing MACHO and CTIO data. However, PLANET was able to densely sample

Table 7.3: 98-SMC-1: Fit Statistics

[a] Average photometric error, in magnitudes, before alert.
[b] Average photometric error, in magnitudes, after alert.
[c] The binary lens fit contains 7 global constraints, plus 2 additional baseline constraints per passband.

Passband	# Observations	$\bar{dm}$ [a]	$\bar{dm}$ [b]	Binary Lens Fit χ^2 [c]
CTIO R	84	···	0.041	44.4
CTIO B	22	···	0.045	10.4
EROS R	38	···	0.20	19.5
EROS B	38	···	0.077	12.2
MACHO R	704	0.55	0.10	921.5
MACHO V	712	0.49	0.093	763.9
TOTAL	1598			1771.9

the peak of the caustic crossing, measuring to high precision the time taken by the caustic to transit the source. The EROS data used in this analysis strongly constrain the falling slope and end–point of the caustic crossing, which leads to our estimate of the lens velocity projected to the SMC.

Projected Lens Velocity ($\hat{v}$)

In order to convert the fit parameter t_* to a projected velocity $\hat{v}$, we need to estimate the radius of the source star. The color of the lensed star is $V - R = 0.03$, which may be determined from the microlensing fit or simply from the mean color of the MACHO observations on June 17, when the entire star was highly magnified. Assuming $E(V-R) = 0.03$ and $T_{\rm eff} = 8000K$ (Albrow et al. 1999b), we obtain $R_* = 1.4 \pm 0.1 {\rm R}_\odot$ and $M_V = 2.8 \pm 0.3$ (Bertelli et al. 1994; Lang 1992). For an assumed source distance of 60 kpc, this yields $m_V = 21.8 \pm 0.3$, which is consistent with the value $m_V = 22.05 \pm 0.15$ determined from the microlensing fit and the MACHO photometric zero point determination.

If we divide the stellar radius of $R_* = 1.4 \pm 0.1 {\rm R}_\odot$ by the stellar radius crossing time $t_* = 0.116 \pm 0.010$ days, we obtain a projected velocity of $\hat{v} = 84 \pm 9\,{\rm km\,s^{-1}}$, which can be used to estimate the location of the lens.

We evaluate Equation 3.16 over $\hat{v}$ separately for lenses either in the dark halo or the SMC. Figure 7.4 shows the predicted $\hat{v}$ distributions as calculated from Equation 3.16 with the measured $\hat{v}$ value indicated. The distributions peak at $\sim 60\,{\rm km\,s^{-1}}$ for SMC lenses and

$1500\,\mathrm{km\,s^{-1}}$ for halo lenses. (Note that since Figure 7.4 has a logarithmic $x-$axis, what is actually plotted is $\hat{v}\mathcal{L}(\hat{v}) = d\Gamma/d\log\hat{v}$, so areas under these curves represent relative probabilities.) The peak for SMC lenses occurs at a value larger than $30\,\mathrm{km\,s^{-1}}$ for several reasons: $\hat{\mathbf{v}}$ has two components, it is the *relative* source–lens motion, and there is the factor of $v_\perp$ in the event rate per lens. Integrating these curves we find that only 0.15% of halo lenses would have a $\hat{v} \leq 84\,\mathrm{km\,s^{-1}}$, while $\sim 31\%$ of SMC lenses would have a $\hat{v}$ larger than this value. *Thus it is highly probable that this binary lens is located in the SMC .*

Since this event is likely due to a lens in the SMC, and the previously discovered SMC event also may be due to an SMC lens (Palanque-Delabrouille et al. 1998; Alcock et al. 1997c), it is interesting to discuss the measured vs. expected optical depth for SMC self–lensing. We have not yet performed a careful efficiency calculation for the SMC, but with about 2.2 million stars monitored over about 5.1 years, and using SMC sampling efficiencies of about 30%, we estimate an observed optical depth $\tau_{est} = 2 - 3 \times 10^{-7}$ for the two known SMC events. For SMC self–lensing, (Palanque-Delabrouille et al. 1998) use a prolate ellipsoid model aligned along the line–of–sight to predict optical depths between 1×10^{-7} and 1.8×10^{-7}, depending upon the extent of the SMC along the line–of–sight. Given the small number of events, this estimate is quite consistent with the observed optical depth. For completeness, we note that the predicted optical depth for halo lensing towards the SMC is about 6×10^{-7} for a 100% Macho halo.

Joint Analysis of All Microlensing Datasets

After the publication of each microlensing team's analysis of 98–SMC–1 by EROS (Afonso et al. 1998), OGLE (Udalski et al. 1998), MACHO/GMAN (Alcock et al. 1999a), MPS (Rhie et al. 1999), and PLANET (Albrow et al. 1999b), a joint paper was published which made use of these joint data to best constrain the lensing system (Afonso et al. 2000). This analysis leads to two solutions for the properties of the lensing system, a "close" binary and "wide" binary degeneracy. However, both solutions lead to low lens proper motions, $\mu_1 = 1.30 \pm 0.08\,\mathrm{km\,s^{-1}}$ and $\mu_2 = 1.76 \pm 0.11\,\mathrm{km\,s^{-1}}$. This corresponds to $\hat{v}_1 = 78\,\mathrm{km\,s^{-1}}$, $\hat{v}_2 = 106\,\mathrm{km\,s^{-1}}$, which Figure 7.4 indicates are well within the likelihood envelope for SMC lenses, and well outside the expected distribution of Galactic halo lens $\hat{v}$.

An auxiliary result of the analysis of Afonso et al. (2000) are limb–darkening parameters for the source star, which has an angular radius of ~ 85 *nano* arcseconds. Unfortunately, there have been no prior models of such a metal–poor star, and Afonso et al. (2000) are unable to compare the derived limb–darkening coefficients to theory.

7.2.2 LMC-1 (79.5628.1547)

This event was the first LMC microlensing event reported by the MACHO collaboration (Alcock et al. 1993). The lensed object does not significantly change color during the event, and its color and magnitude indicate that it is a slightly reddened red clump giant star in the LMC. We thus expect *a priori* that a large fraction of the MACHO object's brightness should be lensed. A difference image photometry (DIP, Tomaney & Crotts 1996a) analysis of the event images indicates a very small centroid shift between the photometered object and lensed source, 0.1 ± 0.1", also suggesting the clump giant was lensed.

The lightcurve is consistent with single lens microlensing, except for a shoulder shortly after the lightcurve peak. This suggests a short timescale structure which was not resolved at the sampling of the survey system. Binary fits for this event have been done by Dominik & Hirshfeld (1996), and the two fits displayed in Figure 7.7 were previously presented by Rhie & Bennett (1996). The similarity to standard microlensing implies the fit resides in a class of fits with small lens separations (*solid* fit in Figure 7.7, and Figure 7.8) or large mass ratios (*dashed* fit in Figure 7.7, and Figure 7.9).

The measured $\widehat{t} \sim 35$ days for both of these fits yields an expectation value for the mass of the lensing system of ~ 0.1 $M_{\odot}$ (Alcock et al. 1993; Dominik 1998a). For the large mass ratio fit, this implies a secondary companion of ~ 1 Jupiter mass. However, since there were no follow–up efforts in place at the time of this event, this degeneracy between fits cannot be broken.

7.2.3 LMC-9 (80.6468.2746)

LMC–9 is the most anomalous lensing event discovered toward the LMC, and it displays the lightcurve structure of a typical caustic crossing binary lens event with similar mass lenses (see Figure 7.10). Prior analysis of this event can be found in Bennett et al. (1996b). The

lensed object appears to be on the red side of the LMC main sequence, at the level of the clump. However, the fits suggest only $\sim 1/5$ of this light is lensed, and so the source likely resides further down the main sequence as a late A or early F star. The lensed source does appear 0.4 ± 0.1" from the MACHO object, based upon DIP analysis.

The first caustic crossing appears to be resolved with two observations on its rise. If we assume the source is not itself a binary, we can estimate the source radius as 1.5 ± 0.2 $R_\odot$ from its color and magnitude. The measured $t_* = 0.65 \pm 0.10$ days yields a lens velocity projected to the LMC (assumed to be at 50 kpc) of $19 \pm 4\,\mathrm{km\,s^{-1}}$, considerably lower than what one would expect from a halo lens. In fact, this velocity is low enough that it is only marginally consistent with a lens in the disk of the LMC, and would not be consistent with any LMC models including velocity dispersions in excess of the measured values (Bennett et al. 1996b).

Aubourg et al. (1999) have suggested an LMC model with a self–lensing optical depth large enough to explain the excess of lensing events observed towards the LMC. Aubourg et al. (1999) achieve a high microlensing optical depth without violating the virial relation between velocity dispersion and microlensing optical depth (Gould 1995) by arguing that the velocity dispersion of the lens population is much higher than the velocity dispersion of the stars with measured radial velocities (Cowley & Hartwick 1991; Zaritsky et al. 1999). However, even in such a model our projected velocity of $19 \pm 4\,\mathrm{km\,s^{-1}}$ for LMC–9 would not be consistent with a lens in the LMC.[9]

Thus, there are two possible interpretations of the LMC–9 caustic crossing observations:

1. They imply that the lens resides in an LMC disk which contains enough mass to generate only a fraction of the observed LMC lensing events, or

2. The source star is itself a binary, and the two caustic crossing observations do not constrain the lens proper motion or its location.

Both of these possibilities have an *a priori* probability of about 10%. Clearly, better photometric coverage of the caustic crossings could have resolved this issue.

---

[9] An early version of Aubourg et al. (1999) incorrectly suggested that their model was consistent with the LMC–9 projected velocity (Aubourg 1999, private communication).

7.2.4 LMC-10 (18.3324.1765)

We include LMC–10 as a binary candidate as an example of variability which passes our microlensing cuts (Alcock et al. 1997a), and yet is almost certainly not standard single lens microlensing due to its asymmetry (Figure 7.12). Explanations for this event include intrinsic stellar variability (we detect no recurrence of this behavior in 5 further years of observations), a background supernova (we find no obvious host galaxy down to R $\sim$ 21), or possibly a weakly perturbed binary microlensing event. Such lightcurves are thought to compose a significant fraction of all binary lensing events (Di Stefano 2000). The best fit lightcurve does have a pair of caustic crossing, but they are separated by about 4 hours and occurred during daylight hours in Australia. For $t_* < 0.2$ days, these caustic crossings would not have been observable from Australia, and the fit is a plausible explanation of the lightcurve. The microlensing interpretation of this event would be much more secure if such a lightcurve were seen in a time reversed order, since the observed rapid rise followed by a slow decay is common in known types of stellar variability. The one observational test that can still be performed is to obtain high resolution HST images of this object. The centroid of the variable source is well constrained by the DIP method of Tomaney & Crotts (1996a), and appears 1.0 ± 0.2" from the MACHO object. If the binary lens interpretation is correct, then this centroid should be centered on a $R = 21.4$ star. Alternatively, the HST frame might also reveal a background galaxy which will make the supernova explanation most plausible.

7.2.5 OGLE-7/MACHO-119-A (119.20226.2119)

This caustic crossing event was initially detected by the OGLE collaboration (Udalski et al. 1994), and later verified with data from the MACHO database (Mao et al. 1994). As OGLE–7, it was the first reported case of binary microlensing. 119–A is a moderately blended event, with $f \sim 0.4$, and the source appears to be located near the top of the bulge main sequence.

The fit presented in Figure 7.14, and the geometry of the lensing encounter in Figure 7.15, are qualitatively similar to the analysis of Udalski et al. (1994). A comparison of event parameters (MACHO:OGLE) yields $\widehat{t} = (169 : 160), u_{\rm min} = (0.08 : 0.05), a = (1.05 :$

$1.14), \epsilon_1 = (0.55 : 0.50), \theta = (-0.94 : 0.84)$, where the difference in θ is due to a different orientation of coordinate systems. Fortunately, the MACHO dataset provides better sampling of the lightcurve, and thus more tightly constrains the global fit. The data presented here include 2 observations on the falling portion of the second caustic crossing, yielding an additional constraint of $t_* = 0.21 \pm 0.03$ days.

7.2.6 MACHO-403-C (403.47793.2961)

Event 403–C exhibits a series of photometric deviations near Aug 18, 1996 (day 1690 in Figure 7.16) which are, for the most part, achromatic. It is plausible these deviations are due to gravitational microlensing. However, this event does not appear to be consistent with single lens microlensing, and is only marginally consistent with binary microlensing. The sparse sampling and relatively large error bars prevent tight constraints on the binary microlensing event parameters.

7.2.7 94-BLG-4 (118.18141.731)

94–BLG–4 exhibits features similar to LMC–1, with a high-σ deviation near the peak of the event which is unresolved by the survey system. This event was initially reported in Bennett et al. (1997), after discovery during testing of the MACHO Alert System. The 2 observations apparently taken between caustic crossings are not enough to completely constrain the lensing system, thus Figure 7.18 and Figure 7.19 are probably not unique interpretations of this sparsely sampled lightcurve.

The lensed object is a clump giant, with $V = 17.9, V-R = 1.1$, based upon its position in Figure 7.50. The binary fit blend fraction of $f \sim 1$ indicates the clump giant itself was lensed, avoiding fit ambiguities introduced by unknown or unconstrained blend fractions, which directly influence our measurement of $\widehat{t}$. The event duration is relatively short, $\widehat{t} = 10.7$ days. If we assume "typical" parameters for the lensing object ($v_\perp = 150\,\mathrm{km\,s^{-1}}$ and a distance 80% of the way to the Galactic bulge) we arrive at the relationship $\widehat{t} \sim 70\sqrt{m/\mathrm{M}_\odot}$ days (Paczyński 1991). This implies an overall lens mass of 0.02 $\mathrm{M}_\odot$ – however, we expect the shortest of our events to be drawn from lenses residing closer to the source, so the actual mass is likely to be much larger than this. If we take an upper limit of 0.2 $\mathrm{M}_\odot$ as the total

lens mass, then the mass ratio of 1/18 implies a secondary lens of $\lesssim 10$ Jupiter masses, for this particular fit.

7.2.8 95-BLG-12 (120.21263.1213)

This 12th Alert of the 1995 bulge season was detected on May 15, at a magnification of $A \sim 2$. Real–time follow–up observations by both GMAN (Pratt et al. 1996) and PLANET (Albrow et al. 1997) detected deviations from the standard fit near Jun 5, making 95–BLG–12 the first binary event detected in real–time. Data on this event from the PLANET collaboration are presented in Albrow et al. (1998).

The lensed object is located on the subgiant branch of the bulge, below the clump. However, because subgiants are rare, we expect that the majority of objects in this location of the color–magnitude diagram are actually blends of multiple fainter stars. Thus, it is no surprise that the binary lens fit indicates blend fractions of $\sim 0.2 - 0.3$. 95–BLG–12 is a good example of a significantly perturbed, non–caustic crossing binary lensing event (Figure 7.20). The multiple peaks are caused by the source approaching cusps in the caustic curve, as displayed in Figure 7.21. The extensive follow–up data are able to constrain the event at nearly the 1% level for much of its duration.

7.2.9 96-BLG-3 (119.19444.2055)

This event was discovered at the beginning of the 1996 bulge season, and announced by the MACHO Alert System on Mar 12, 1996. After an initial peak (due to a cusp approach) which resembled a normal lensing event, the star jumped to a large magnification on Mar 25, 1996, implying a caustic crossing had likely occurred. Based upon the available MACHO data, Bennett & Marshall (1996) were able to successfully predict the second caustic crossing to within 0.15 days. The important features at the time of this prediction were the initial peak in Figure 7.22, due to a cusp approach, and the sparsely sampled $\cup$–shape between caustics. These global constraints on the lightcurve provided enough leverage for an accurate caustic crossing prediction, although this is not necessarily possible with more local constraints, even a well sampled caustic crossing (Albrow et al. 1999a).

Follow–up data taken at the CTIO 1.5m provided the first ever resolution of a binary

caustic crossing, as shown in Figure 7.22. In addition, spectroscopic observations of the object were taken during the crossing (Lennon et al. 1996). As the source crossed out of the caustic region, its brightness peaked at extremely high magnification, $A_{\rm max} \sim 120$. However, the observed magnification of the MACHO object was considerably less, as it is a significant blend ($f \sim 0.2$ for MACHO). Thus, while Lennon et al. (1996) report their spectrum of that of a G0 subgiant, the blend fractions indicate that the source is a G0 dwarf.

Lennon et al. (1996) showed that the source is not a spectroscopic binary, and estimated from their spectra an effective temperature of $T_{\rm eff} = 6100$ K. Their comparison to evolutionary tracks leads to an angular source radius of $\theta_* = 0.94\mu$as. Since these spectra were taken while the source was highly magnified, their $T_{\rm eff}$ should represent the temperature of the lensed source. However, their estimate of the distance to the source, and hence its angular size, depended upon the baseline brightness of the object ($V = 19.2$), instead of the recovered brightness of the lensed source ($V = 20.8$). Our analysis in Chapter 7.3.2, Table 7.7, indicates our estimate of $T_{\rm eff} = 6200$K is in excellent agreement with Lennon et al. (1996), and de–blending the event reasonably leads to a smaller $\theta_* = 0.53\mu$as.

7.2.10 96-BLG-4 (105.21417.101)

96–BLG–4 displays a repeating variability (Figure 7.24), which would generally exclude it as a microlensing candidate. The first peak is well fit by standard microlensing ($\chi^2/dof = 1.2$), and was not a binary candidate until the MACHO Alert System re–triggered on this event ~ 550 days after the first peak. The color of this object ($V = 16.2, V - R = 1.1$) indicates it is unlikely to be a long period variable (LPV), and any periodic variability is ruled out by prior observations. The object does appear to be a bright giant, located close to the tip of the red giant branch.

As is the case with many of our giant sources, we do not detect a significant color shift during the event, and the binary lens fit is consistent with zero blending ($f = 1$). The multiple achromatic peaks suggest lensing of a single giant source by a binary lens, or lensing of a binary system by a single lens. Figure 7.50 indicates that the source appears ~ 1.3 mag brighter than the red clump in this region, so a single lens, binary source event

seems plausible (the probability of a chance superposition of giant stars is extremely small). Stars generally spend only a few percent of their lives on the giant branch (Iben 1967), so it is unlikely for two members of a binary system to reside on the giant branch at the same time. But, given the sample of ~ 350 candidate events that our binary lens sample has been selected from, one binary giant source event is plausible.

Another interpretation of this event is a very widely separated ($a = 7.5R_{\rm E}$) binary lens acting upon a single background giant source. It has been recognized by Di Stefano & Mao (1996) that lensing by widely separated binary systems ($a > 2.5R_{\rm E}$) should occur with $\sim 10\%$ the frequency of close binary events. As shown in Figure 7.25, the caustics for this event are extremely small, which indicates that this event, unlike any of the others presented in this paper, is very much like the superposition of two single lens lightcurves. This makes it difficult to unambiguously discriminate between binary lens and binary source models for this event.

7.2.11 97-BLG-1 (113.18674.756)

97–BLG–1 was initially announced as microlensing on Mar 3, 1997. A substantial deviation from standard microlensing was noticed Mar 11, 1997. This sharp decline, seen in Figure 7.26, signified the source exiting the caustic region, and follow–up efforts were only able to sample the final cusp approach (see Figure 7.27).

This MACHO object appears to be a clump giant, relatively unreddened compared with the other events in our sample. There is little blending in this event, such that the giant is likely the lensed source. The second caustic crossing in this model is resolved with 2 MACHO observations, which leads to an estimate of $t_* = 0.53 \pm 0.03$ days. However, the lack of information prior to the start of the bulge season severely limits our ability to parameterize this event, so we expect that our fit may not be unique. The only strong constraints on this lensing encounter are the magnitude of the final cusp approach and the likelihood of minimal blending for a clump giant source.

7.2.12 97-BLG-24 (101.20650.1216)

The MACHO lightcurve for 97–BLG–24 (Figure 7.28) exhibits a significant deviation from point source microlensing, similar to LMC–1 (Figure 7.7). However, this deviation was noticed in real–time, allowing immediate follow–up observations to be undertaken with the MSO 30" telescope. These data reveal an unusual increase in the object's brightness before observations ended for the evening.

Unfortunately, the lensed source appears $\sim 1.2''$ from the MACHO object, in a region of high crowding. It is difficult to independently photometer the lensed source even in the follow–up photometry, and the data presented here represent the change in brightness of the brightest neighbor to the lensed source – i.e. the event is strongly blended. Nevertheless, we are able to resolve evidence of lens binarity in the deviation near the peak of the lightcurve. This deviation is more heavily sampled than LMC–1, but still suffers from the same model degeneracy. (We note that Figure 7.28 displays the apparent brightening of the MACHO object, not the lensed source, due to the different blend fractions between the two fits presented in Tables 7.5 and 7.6.)

The *solid* and *dashed* line fits in Figure 7.28 display $\widehat{t}$ of 30.7 and 45.5 days, implying overall lens masses of 0.19 and 0.42 $M_\odot$, respectively. The former fit includes a binary system with components of 0.16 and 0.03 $M_\odot$, likely a stellar – brown dwarf system. The latter dashed fit, with a mass ratio of 29 : 1, implies lens masses of 0.41 and 0.014 $M_\odot$, consistent with a stellar lens with a companion of $\sim$ 14 Jupiter masses.

7.2.13 97-BLG-28 (108.18951.593)

After being detected and alerted upon May 29, 1997, this event began to increase in brightness at an unexpected rate on Jun 14, 1997 (day 1990 in Figure 7.31), and both MACHO/GMAN and PLANET issued secondary alerts for a binary lensing event in progress. The PLANET collaboration was able to obtain nearly constant coverage of this event, resulting in parameterization of the limb–darkening coefficients for the source, and an estimate of the lens proper motion of $\mu = 19.4 \pm 2.6\,\mathrm{km\,s^{-1}\,kpc^{-1}}$ (Albrow et al. 1999c).

The results presented here are similar to those of Albrow et al. (1999c). The fit to microlensing suggests a moderate amount of un–lensed blue light in the photometered object,

and the object is likely a lensed clump giant source blended with objects of bluer color. The trajectory of the source plotted in Figure 7.32 indicates the lightcurve deviation was due to a cusp crossing. Resolution of the source face during this crossing allows a measurement of $t_* = 0.760 \pm 0.014$ days. A comparison of event parameters (MACHO:PLANET) with model LD1 of Albrow et al. (1999c) yields $\widehat{t} = (52.8 : 54.4), u_{\rm min} = (0.225 : 0.215), a = (0.71 : 0.69), \epsilon_1 = (0.17 : 0.19), \theta = (1.44 : 1.42), t_* = (0.76 : 0.78)$.

Following the procedure outlined in Chapter 7.3.2 and Table 7.7, we estimate the reddening to be $E(V-R) = 0.67 \pm 0.04$, which yields de–reddened source magnitudes of $V = 15.52 \pm 0.19$ and $R = 14.94 \pm 0.15$. From this we determine $T_{\rm eff} = 4500 \pm 200$K for the source star. Using a bolometric correction of $BC_V = -0.48$, we find an angular source radius of $\theta_* = 6.58 \pm 0.90 \mu$as. For comparison, the PLANET group find a de–reddened $V = 15.27$, $T_{\rm eff} = 4350$K, and $\theta_* = 8.74 \pm 1.17 \mu$as, so our results are in reasonably good agreement.

7.2.14 97-BLG-41 (402.47862.1576)

This event was detected and alerted upon on 18 Jun, 1997. This event exhibited what appeared to be a fairly normal rise and fall for a microlensing event. However, after peak the event did not decline to baseline magnification, but leveled off at A $\sim$ 1.5, and began a slow rise, which itself was fit well by a longer duration microlensing event. The deviation from a normal single lens lightcurve was noted and announced by both the MACHO/GMAN and PLANET collaborations. Near the peak of the event is an apparent caustic or cusp crossing. The MACHO and GMAN data have been plotted in Figure 7.33.

Considerable effort has been made to fit this lightcurve to a binary lens model, but no satisfactory model has been found, even when the possible orbital motion of the lens was included. However, a satisfactory multiple lens fit has been found by Bennett et al. (1999).

7.2.15 98-BLG-12 (179.21577.1740)

98–BLG–12 was detected on Apr 8, 1998, and initially thought to be a rapidly rising, high magnification event. This behavior, evident in Figure 7.34, was a result of the source exiting its first passage through the caustic structure (Figure 7.35). It was not recognized

as a binary lensing event until the source re–entered the caustic structure near May 17.5 UT, 1998 (day 2327.5), and was subsequently observed at high magnification by the survey telescope on May 17.74 UT, 1998 (day 2327.74). The < 3 days spent between caustics allowed little time for follow–up observations to constrain event parameters. Interestingly, in all passbands, this event appears heavily blended ($f \sim 0.2$).

7.2.16 98-BLG-14 (401.48408.649)

This brightening of this apparent clump giant object was detected and alerted on Apr 26, 1998. Initially, it was not clear if the asymmetry in Figure 7.36 was due to the parallax effect (Refsdal 1966; Alcock et al. 1995a), and initial data allowed fits of similar significance for both binary and parallax models. However, the higher precision photometry from CTIO and MSO74 observations clearly favor the binary interpretation over the best fit parallax lightcurve ($\Delta\chi^2 = 115.75$ with 1 less degree of freedom), while the MACHO data also provide $\Delta\chi^2 = 30.32$. Unfortunately, there does remain a degeneracy between binary lens models. Figure 7.37 and Figure 7.38 indicate this is a non–caustic crossing binary event, similar to 95–BLG–12.

The blend fraction for the best fit (*solid* fit in Figure 7.36, and Figure 7.37) is $f \sim 0.5$ for all 4 passbands of coverage, but there is another fit that is almost as good with $f \gtrsim 1$ (*dashed* fit in Figure 7.36, and Figure 7.38). The best fit suggests a blend of clump giant stars, where they are constrained to lie within a seeing disk, or $\sim 1''$. 98–BLG–14 is located closer to the Galactic center than most of our events at $l = 1.96$, $b = -2.29$, where the surface density of giants is quite high. The average separation of clump giants is $5.3''$ in the vicinity of 98–BLG–14, so we expect that $\sim 10\%$ of clump giants will be blended with another clump giant. The de–reddened brightness of the MACHO object would place it at the bright tip of the clump. In the best fit, the lensed source would be somewhat lower than the mean clump brightness. It is thus reasonable for the lensed clump giant source to be blended with an unlensed clump giant. The second–best fit differs from the first by $\Delta\chi^2 = 5$, and from the event timescale of $\widehat{t} = 74$ days and lens mass ratio of $12:1$, we can estimate a lens system comprised of a 1.03 $M_\odot$ primary and 0.088 $M_\odot$ companion.

7.2.17 98-BLG-16 (402.47863.110)

98–BLG–16 was detected and alerted on Apr 28, 1998, and thought to be a high magnification, short timescale event. The initial sharp rise in Figure 7.39 was due to a cusp approach (Figure 7.40). Subsequent lightcurve interpretation was hindered by a significant amount of scatter in the MACHO Red passband, due to a defective amplifier, and a centroid offset of $\sim 1.3''$ between the MACHO object and the lensed source. Follow–up data from the CTIO 0.9m were able to resolve these objects, which allowed them to be independently photometered. Inspection of the CTIO dataset indicates the lensed source has a baseline flux of $\sim 7\%$ of the brightest (constant) neighboring star which serves as the target of MACHO photometry. The binary lens fit determines blend fractions consistent with this, $f_{MACHO} \sim 0.04$ and $f_{CTIO} \sim 1$, indicating there is no significant flux contribution from the lensing objects. The CTIO data from May 4.3 UT, 1998 (day 2314.3) provide a constraint on the lens proper motion for this particular fit, $t_* = 0.163 \pm 0.003$ days.

7.2.18 98-BLG-42 (101.21045.2528)

98–BLG–42 was detected and alerted on Aug 22, 1998 at a magnification of ~ 4.0. The source at this point in time was inside the caustic region depicted in Figure 7.42. The event was immediately followed up by the MPS effort, on the MSO 74" telescope. Over the next 3 nights the source began to rapidly increase in brightness. The PLANET collaboration issued an Anomaly Alert on Aug 26.0 UT, 1998 (day 2428.0) indicating the source underwent a caustic crossing between Aug 25.0 and 25.7 UT, 1998. Our fit presented here indicates a caustic crossing date of Aug 25.77 UT, with a source radius crossing time of $t_* = 0.109 \pm 0.016$ days.

7.2.19 97-BLG-d2 (108.19073.2291)

This event was detected in the 3–year difference image analysis (DIA) of MACHO field 108, originally presented in Alcock et al. (1999b). The event is most closely associated with MACHO object 108.19073.2291, however the DIA technique uniquely identifies the time–varying source. The lightcurve associated with this analysis is purely a lightcurve of residuals around the source's baseline flux, which is not determined. For consistency

with the notation of the other fits in this paper, we have added an arbitrary amount of flux to the residual lightcurve, and fit for the fraction of the combined lightcurve that is lensed. In this way we are able to estimate the baseline brightness of the lensed source. The source trajectory in Figure 7.44 includes 2 cusp approaches, and passage through a caustic structure, which is suggested by 2 MACHO data points at high magnification.

7.2.20 MACHO-108-E (108.19333.1878)

This event was detected in the course of the MACHO bulge 5–year analysis (Alcock et al. 2000f). The deviation occurred with the Alert System in place. However, the Alert System was not triggered since all but 3 of the MACHO Blue data points are removed from the lightcurve due to the object's proximity to the edge of a detector. For this reason we are unable to realistically estimate properties of the lensed source, or set meaningful limits on the lens brightness. The lightcurve (Figure 7.45) is characterized by approaches to 2 of the 3 caustics in the source plane (Figure 7.46).

7.2.21 MACHO-176-A (176.19219.978)

Event 176–A was also detected in the bulge 5–year analysis, and is a good example of a poorly sampled binary lens event. The magnitude of the initial caustic approach is unconstrained, and the fit presented here places the one relevant data point at its peak (Figure 7.47). The $\cup$–shape of the subsequent data suggests a caustic crossing and gradual decline to baseline. The critical and caustic curves are presented in Figure 7.48.

7.3 What Can We Learn?

With our ensemble of 21 binary microlensing candidates, we can begin to consider mapping the properties of the binary events to the lensing population as a whole (Di Stefano 2000; Kerins & Evans 1999). This is most difficult towards the Magellanic Clouds, where we have the additional uncertainty of an unknown or unmodelled lensing population.

7.3.1 Towards the Magellanic Clouds

We have presented 3 candidate LMC binary events out of the 8 events published in Alcock et al. (1997a), and detect no more unambiguous binary lens candidates in the $\sim$ 20 events

(Alcock et al. 2000a) in our 5–year analysis. A color–magnitude diagram, incorporating the de–blended magnitudes of the Magellanic sources from Table 7.4, can be found in Figure 7.49.

LMC–9 is a resolved caustic crossing event, where the measured t_* (assuming a single lensed source) is consistent with the lensing system residing in the LMC (Bennett et al. 1996b), but only if the velocity dispersion and the self–lensing optical depth (Gould 1995) of the LMC are both small. If the LMC self–lensing optical depth is large enough to explain most of the microlensing events seen towards the LMC Sahu (1994), as in the recent models of Aubourg et al. (1999), then the proper motion of LMC–9 is not consistent with an LMC lens, unless the source star is actually a pair of binary stars of similar brightness. However, in this case, we can no longer constrain the proper motion of the lens.

As emphasized by Di Stefano (2000), we should also expect events without obvious caustic crossings, similar to LMC–10. This event is consistent with a binary lens event, but the asymmetry of the lightcurve also resembles what might be expected for some types of stellar variability. A future HST frame of this object could confirm the microlensing prediction for the amount of blending.

Event 98–SMC–1 was recognized to be a caustic crossing event in real time with the GMAN follow–up observations presented here. An unprecedented response by the majority of the microlensing community resulted in dense coverage of the event, including resolution of the second caustic crossing by the PLANET and EROS collaborations. Important constraints on the initial caustic crossing date were provided by the OGLE and MPS collaborations. The lens proper motion derived from each of these datasets is most consistent with a SMC lens. This is the strongest constraint that has yet been placed on the location of the lensing population towards the Magellanic Clouds. However, as Palanque-Delabrouille et al. (1998) point out, the SMC is expected to have a large self–lensing optical depth, so that a large fraction of SMC events are likely to be due to self–lensing, even if most of the LMC events are due to halo lenses.

Kerins & Evans (1999) reach the conclusion that, if the caustic crossing events LMC–9 and 98–SMC–1 are both due to Magellanic lenses, than the bulk of lensing seen so far towards the Magellanic Clouds is most likely due to self–lensing, where the lenses may

reside in Magellanic stellar or dark halos. However, the suggestive evidence that the LMC–9 lens may reside in the LMC only applies for LMC models with a low self–lensing optical depth. Furthermore, as Honma (1999) has pointed out, there is probably a bias in favor of detecting long timescale caustic crossing events. Thus, we may be more likely to detect and characterize caustic crossing features for self–lensing events than for halo lensing events, if the latter tend to have shorter timescales. A potentially more serious bias may be that there may be very few binary lenses in the halo. If most of the LMC events are due to lenses in the Galactic halo, then they comprise a previously unknown population with an unknown binary fraction. So, it is possible that the sample of binary events themselves selects against the halo lensing events. If so, we might expect a smaller fraction of binary lensing events towards the LMC than towards the bulge when the event samples get larger.

7.3.2 Towards the Galactic Bulge

A more representative sample of binary lenses can be found amongst the 17 Galactic bulge candidates. For the duration 1994–1998, the Alert System triggered on 196 Galactic bulge microlensing events. Twelve of the Alert events are presented here as binary lens candidates. Since the Alert System is tuned to detect generic variability, it is reasonable to make the assumption that the 12 binary events out of the 196 Alert events are representative of the detectable binary fraction of the lensing population as a whole. This is consistent with theoretical estimates of a binary lensing rate of order 10% (Mao & Paczyński 1991).

A color–magnitude diagram, incorporating the de–blended magnitudes of the lensed sources from Table 7.4, can be found in Figure 7.50. It is interesting to note that clump giants are over–represented in our sample, implying our binary lens detection efficiency is highest with these bright sources. It is also important to note that for the 6 clump giants lensed, in most cases the blending fraction is quite close to 1 (with the possible exception of 98–BLG–14), indicating there is insignificant contamination from neighboring sources and, most importantly, from the lensing system. This is contrary to the distributions of blending in the majority of binary microlensing events that have been reported in the literature thus far (Di Stefano 2000).

Two of the binary events (97–BLG–24 and 98–BLG–16) are heavily blended in the

MACHO data, but the lensed source star is resolved in the follow–up GMAN data, at separations of 1.2″ and 1.3″, respectively. However, the 97–BLG–24 field is crowded enough that it is difficult to independently photometer the MACHO object and lensed source. For 98–BLG–16, the microlensing fit to CTIO data exhibits no blending, indicating the lens is in fact relatively dark. Candidates 95–BLG–12, 96–BLG–3, and 98–BLG–12 are strongly blended in all passbands ($70 - 80\%$ contamination), and it is possible in these cases that the lens contributes significant flux to the source brightness. High resolution photometry of strongly blended events can disentangle blending due to crowding, and blending due to lens luminosity.

Excluding event 97–BLG–24 for which we have two fits, we find 12 (9) caustic crossing events from our ensemble of 16 (only the 11 Alert) bulge candidates. While not all of the GMAN follow–up data for the interval 1995–1998 have yet been reduced, we so far have found no weakly perturbed systems, at the $\sim 1\%$ level. Di Stefano (2000) indicates that several of these weakly perturbed events should exist for each caustic crossing event (but see Chapter 7.1.1). That we have detected no such events indicates our efficiency at detecting them, or characterizing them as binary microlensing, is currently quite low.

Mass Ratio Distribution

While some of the events here are poorly constrained, and thus can be characterized by multiple combinations of event parameters, we can begin to probe the distribution of mass ratios of the binary lensing population towards the Galactic bulge, given the above fits. Distributions of the binary parameters θ and a are less informative, with θ representing a random orientation between the lens separation axis and motion with respect to the source, and a the projection of the lens separation at a random (unknown) orbital phase. Figure 7.51 contains a histogram of the distribution of mass ratios (q, defined to be ≤ 1) which we find from our bulge events. The 2 fits each for events 97–BLG–24 and 98–BLG–14 are represented by additional shaded areas. The distribution here is free of inclination uncertainties present in studies of spectroscopic binaries (SB), but does likely suffer from non–uniqueness of fits in several cases.

The binary mass ratio distribution function N(q) has been studied by, e.g. Trimble

(1990), who examines SB systems with both giant and relatively bright main sequence primaries. Similar morphologies are found between samples, generally characterized by $N(q) \propto q^{-1}$, with a possible peak near $q \sim 0.3$. However, we expect many of our lenses to be drawn from the lower, more populated portion of the main sequence. Given the apparent dependence of $N(q)$ on spectral type (Abt 1983), it would be more appropriate to compare Figure 7.51 with the study of solar–type SB by Mazeh et al. (1992). They find, with a considerably smaller sample than Trimble (1990), a relatively flat $N(q)$, possibly rising towards larger q. We therefore compare two models, $N(q) \propto q^{-1}$ and $N(q) =$ constant, against the events with $0.1 < q < 1$ using the one–sided Kolmogorov–Smirnov (KS) test. We find probabilities of 0.07 and 0.41, respectively, of finding a KS deviation between data and model as large as that observed. A $N(q) \propto q^{-1}$ is clearly inconsistent with our measured distribution, while a flat $N(q)$ is consistent with our data.

Reddening Estimates

For 10 of our bulge events, the microlensing fits provide a measurement of t_*. However, it is our coverage of events 119–A (Figure 7.14), 96–BLG–3 (Figure 7.22), 97–BLG–28 (Figure 7.31), and 98–BLG–42 (Figure 7.41) which most reliably constrain t_*.

We therefore have 4 events where we believe we have a reliable measurement of the time it takes the lens to transit the source face, $2t_*$. To arrive at an estimate of the proper motion of the lensing system, we must first determine the angular size of the source. This can be done by assuming the source is a blackbody and estimating its effective temperature $T_{\rm eff}$ and apparent bolometric magnitude $m_{\rm bol}$. We first need to determine the extinction, A_V, and reddening, $E(V-R)$, to the source – in the following, we assume $A_V = 3.97E(V-R)$ (Rieke & Lebofsky 1985).

Stanek (1996), in a study of red clump stars in Baade's Window, finds a range of A_V from 1.26 to 2.79, even though this is the clearest and most uniform window through the bulge. This suggests it would be unwise to apply an "average" extinction correction to all of our events. Instead, we estimate the reddening for each source using neighboring RR Lyrae stars, whose intrinsic colors are well known. An intrinsic color–period (P) relationship has

been established for field RR Lyrae by Caputo & De Santis (1992), in the form of

$$(B-V)_0 = 0.658 + 0.097\ [\mathrm{Fe/H}] + 0.710\ \log P. \tag{7.2}$$

We assume [Fe/H] $= -1$, after Walker & Terndrup (1991), and transform to $(V-R)_0$ with the relation (Alcock et al. 1997b)

$$(V-R)_0 = 0.004 + 0.566(B-V)_0. \tag{7.3}$$

We then compute the reddening to all RR Lyrae within $10'$ of the source, excluding significant outliers, and apply the reddening and extinction corrections to our lensed source star. The results of this are listed in the first columns of Table 7.7. We note that two of the events, 119–A and 96–BLG–3, occurred within Baade's Window, but both sources are just outside the extinction grid reported by Stanek (1996).

We next interpolate the ATLAS9 and NMARCS model atmospheres presented in Bessell, Castelli, & Plez (1998) (assuming solar metallicity, $\log g = 2.0$ for giants, and $\log g = 4.5$ otherwise) to determine the source's $T_{\rm eff}$ and bolometric correction in V (BC_V), given its unreddened $(V-R)_0$. It is then straightforward to calculate the angular size of the source θ_* using the bolometric flux method of Gray (1992), and to determine the relative proper motion $\mu = \theta_*/t_*$ between the lens and the source, further described in Chapter 7.3.2.

Lens Proper Motions

The determination of the lens proper motion with respect to the source, μ, yields a $\widehat{v}$ constraint on the parameters of the lensing system. Thus, for the four events with measured μ values, we have a constraint on the total mass of the binary system $M_{\rm tot}$ from Equation 3.13. These solutions are shown in Figure 7.52. We see that $M_{\rm tot}$ grows as function of the lens distance, and passes through the expected lens masses of $0.1 - 2\mathrm{M}_\odot$ at distances of $2 - 7.5\,\mathrm{kpc}$.

In our likelihood analysis (Equation 3.16), we have assumed a distance of $R_0 = 8\,\mathrm{kpc}$ to the Galactic center and $8.5\,\mathrm{kpc}$ to each source star. These results are summarized in Figure 7.52 and Table 7.8. The measured proper motions of $\mu = 1.8 - 3.2\,\mathrm{mas/yr}$ are most consistent with lens systems residing in the bulge, and the best fit primary lens masses are

consistent with main sequence stars fainter than the Sun. The only exception is the heavier lens mass for event 96–BLG–3, which has a best fit mass of $1.2\mathrm{M}_{\odot}$ with an uncertainty of a factor of two.

If the heavier 96–BLG–3 lens is a main sequence star, then we must have $M_2 \leq 1.3\mathrm{M}_{\odot}$ to be consistent with our measurement of the unlensed flux observed at the position of the source star. High resolution imaging of the source might be able to tighten this constraint by resolving some of the unlensed flux into separate stars. Similar constraints apply for the other stars, but are significantly weaker because the implied masses are much lower. However, these constraints do not apply for stellar remnant lenses, which may make up of order 20% of the lens population (Gould 2000).

7.3.3 Conclusions

After a survey of the MACHO database, it is very apparent that microlensing by binary lens systems has been detected, and at a rate that is roughly consistent with theoretical predictions for known stellar populations. However, a rigorous search has not yet been implemented, and we cannot set hard limits on the binary microlensing rate, nor on the characteristics of binary systems in the lensing population. This includes the incidence of planets around lensing stars. However, follow–up efforts such as MPS (Rhie et al. 2000) and PLANET (Albrow et al. 2000a) are undertaking dense lightcurve sampling, and are beginning to set meaningful limits on planetary companions on an event–by–event basis.

It is also apparent that there are difficult degeneracies between binary microlensing fits which cannot be resolved with the sparse sampling ($\sim$ once per night) of the microlensing survey telescopes. This is especially important in short duration and/or low level deviations, such as caustic crossings or planetary 'spikes'. In both cases important information is contained in a small fraction of the lightcurve. It is thus important that microlensing follow–up continues with dense (tens of observations per night), precise ($\sim$ 1%) sampling of event lightcurves. The limitations of undersampled datasets are apparent in the analysis of 97–BLG–24, where we are sure of a binary (possibly even planetary) signal, but are not able to uniquely characterize it.

Three of our bulge events (95–BLG–12, 96–BLG–3 and 98–BLG–12) are strongly blended

in all MACHO and GMAN follow–up passbands, indicating the lensing objects may be luminous at a detectable level. High resolution observations of these sources may eventually reveal the appearance of a "new" source, as the lens proper motion separates it from the lensed source at the rate of $\sim$ milli–arcseconds/yr. This can be accomplished with the HST, or adaptive optics imaging available on systems such as Gemini. On the other hand, our binary events on giant sources tend to show little blending. Event 98–BLG–16, a main–sequence source which is highly blended in the MACHO photometry, is resolved into separate objects in GMAN follow–up data, and fit blend fractions indicate the lensing objects are in fact dark.

We have recovered a distribution of mass ratios for 16 of our Galactic bulge microlensing candidates, and a distribution of lens proper motions for 4 of these events where we have, to some degree, resolved a caustic crossing. The mass ratio distribution is consistent with the relatively flat distribution seen in solar–type spectroscopic binary systems. The lens proper motions, when combined with the likelihood analysis, imply a population of binary lenses residing in the Galactic bulge at a distance of 7 ± 1 kpc. The lens masses generally appear sub–solar.

Finally, we would like to caution against over–interpretation of this binary lens dataset, in particular the Magellanic Cloud subset, which is admittedly incomplete. In fact, there are undoubtedly a number of unquantified biases in our ability to discriminate between the single–lens and binary–lens case, although actual event detection is more a function of the significance of the deviation from baseline than lightcurve morphology. However, observations of on–going binary lensing events towards the Magellanic Clouds, such as 98–SMC–1, may on an event–by–event basis allow us to examine the role the lensing populations play in the larger context of Galactic dark matter.

7.4 Binary Lens Non-Detections

In cases of high–magnification events, it is possible to set stringent limits on the presence of secondary lenses, most importantly planets, around the lensing star (Griest & Safizadeh 1998). This occurs because even a very light secondary lens induces a small caustic structure near the primary lens, and high magnification (small impact parameter) events directly

probe this region. Microlensing in fact offers the only means to currently detect or limit the presence of Earth–mass planets around a normal stellar object (Bennett & Rhie 1996). Part of this dissertation involved constructing a real–time reduction pipeline for the Microlensing Planet Search (MPS) Collaboration. The observing strategy for MPS is optimized for detecting planets around the lensing object. This involved *extremely* high frequency observations during the peak of lensing events. One such heavily studied event is 98–BLG–35 (Rhie et al. 2000).

7.4.1 98-BLG-35

An early alert on this event by the MACHO Alert system allowed the MPS collaboration to begin undertaking observations of this event approximately 1 week before the observed peak. Real–time fitting of the evolving lightcurve indicated a possible high–magnification event, and the intensity of coverage was increased.. The peak of the lightcurve was well sampled by MPS, and additional observations were made by the MOA collaboration. The overall lightcurves of this event are presented in Figure 7.53.

The heavy coverage of the peak of the event allows significant conclusions to be made about any system of planetary companions to the lens. The best fit single and binary lens lightcurves indicate there is a $\Delta\chi^2$ improvement when adding a companion lens, corresponding to a secondary lens 7×10^{-5} the mass of the primary. However, evaluating the significance of this detection is non–trivial, since the detection came when the source was very low on the horizon, and the modeling of photometric error bars is difficult in this situation. This detection formally implies an approximately Neptune–mass planet at 1.35 $R_{\rm E}$ from the lens.

Importantly , concrete limits can be set on the *lack of* more significant deviations in the lightcurve, due to planets in other possible configurations around the lens. By adding planets of various mass ratios to the lensing region, Rhie et al. (2000) are able to derive the extent to which their lightcurve coverage excludes binary companions, seen in Figure 7.54. This exclusion region reaches down below mass ratios of $\epsilon = 10^{-5}$, which is approximately an Earth mass for a typical Galactic disk lens. More than 10% of the lensing region around the lens is excluded at this mass ratio, indicating the very first time limits on such low mass

planets have been established for a normal star.

Subsequent analyses limiting planetary companions have been done by Albrow et al. (2000a), and more recently on an ensemble of events by Albrow et al. (2000b). All lightcurve studies have resulted in null detections. The conclusions of Albrow et al. (2000b), established by a systematic search of 43 microlensing lightcurves, indicate that less than 33% of normal Galactic disk lensing stars ($M_l \sim 0.3\mathrm{M}_\odot$) have Jupiter mass companions between 1.5 and 4 AU. This indicates that microlensing, as a planet–detection method, serves as a powerful and complimentary study to the doppler–shift technique, which is more sensitive to planets at smaller orbital radii (Mayor & Queloz 1995; Vogt et al. 2000).

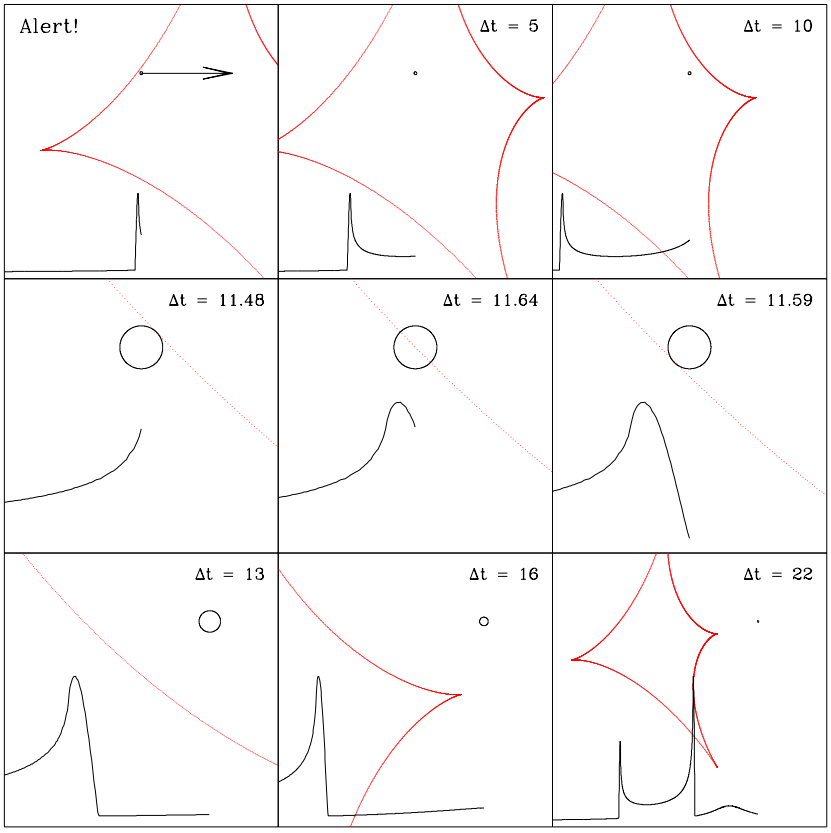

Figure 7.1:
The passage of an extended source through a caustic structure is demonstrated in the 9 panels above. Each illustrates steps in time from $t = 0$ in the upper left hand corner, which signifies the detection of the source entering the caustic structure. The upper region of each panel represents the source plane, where the open circle represents the extended source and the cuspy lines the caustic structure induced by the lens – a local maximum in the isomagnification contours. The lower region shows the only observable information about this event, the lensed source's lightcurve. As the source traverses through the caustic structure, it is possible to predict its time of egress, given proper sampling of the evolving lightcurve. Source resolution is demonstrated in the middle set of highly magnified panels, where the caustic line sweeps across the source face in 0.11 days. The temporal duration of the lightcurve caustic crossing provides, in principle, a means to measure $\widehat{v}$. The bottom set of panels zoom away from the lensing event to show the overall lightcurve as the source moves away from the caustic structure.

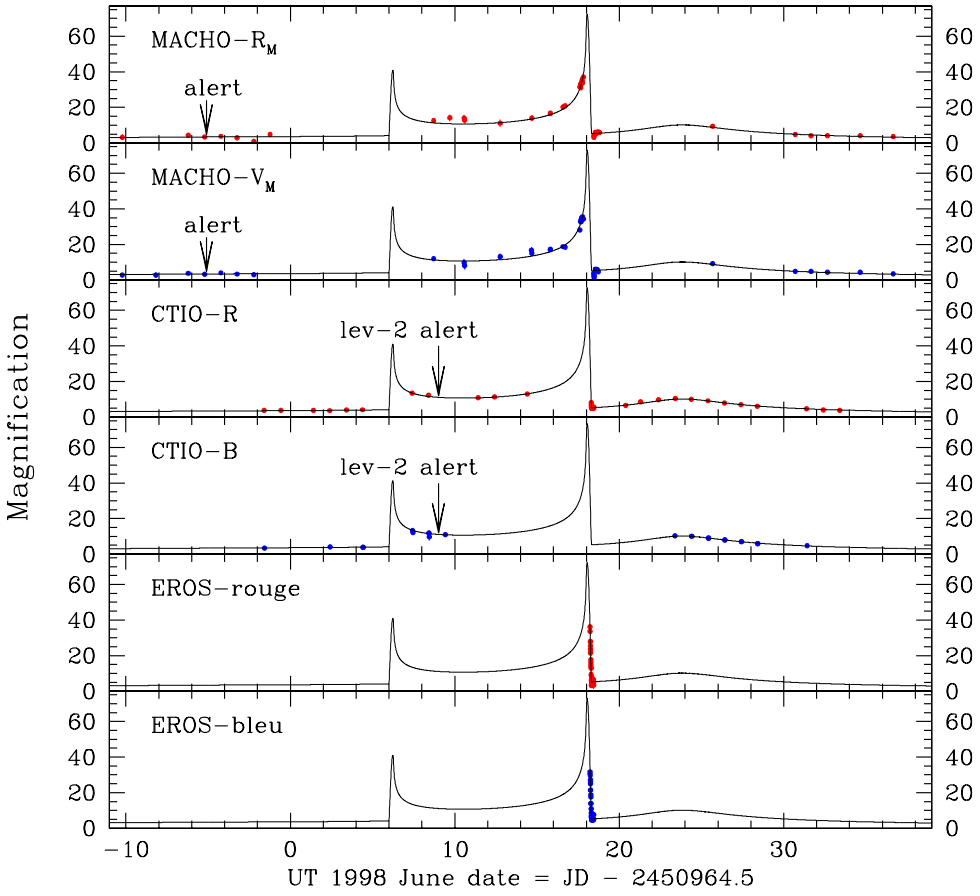

Figure 7.2: The light curve of event 98–SMC–1. The panels show magnification as a function of time, with passbands and sites as indicated. The times of the initial alert and the confirmation of the caustic crossing are shown with arrows. The best fit binary microlensing curve is shown as a solid line.

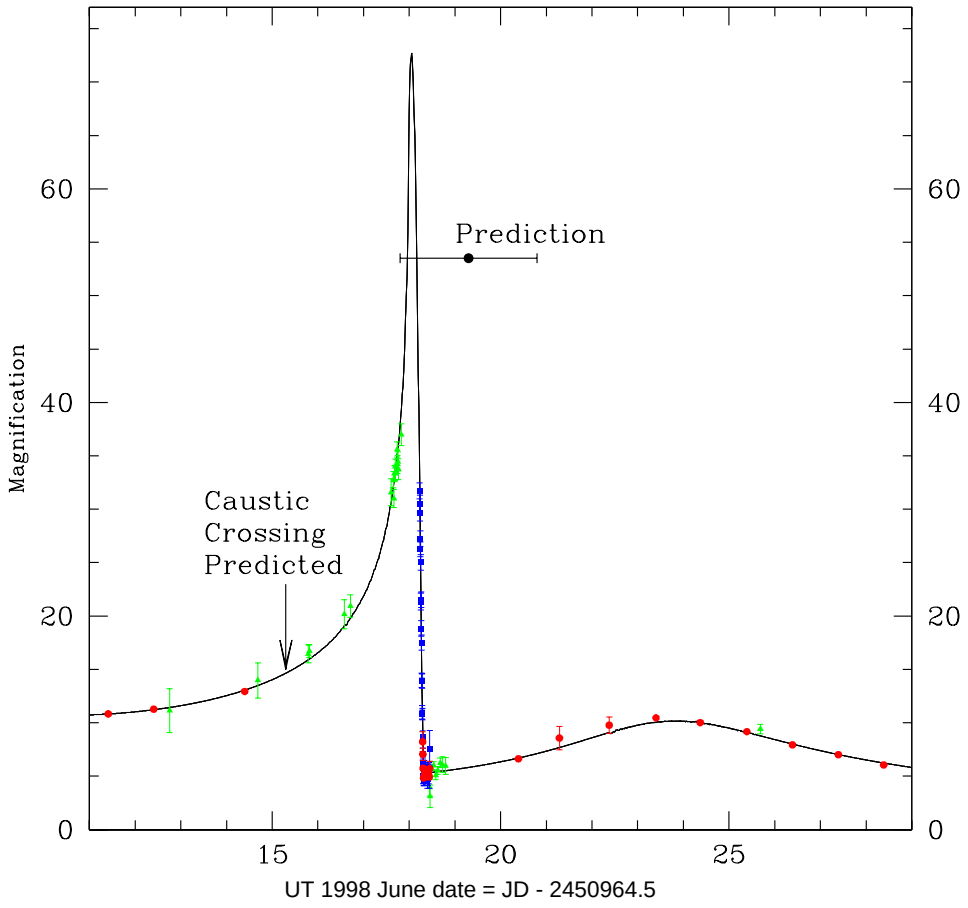

Figure 7.3: A close–up view of the last half of the light curve of event 98–SMC–1. Included are the date of the original second caustic crossing prediction, and the prediction with error bars of 1.5 days. Only the MACHO–R (*triangles*), CTIO–R (*circles*) and EROS–B (*squares*) data are plotted.

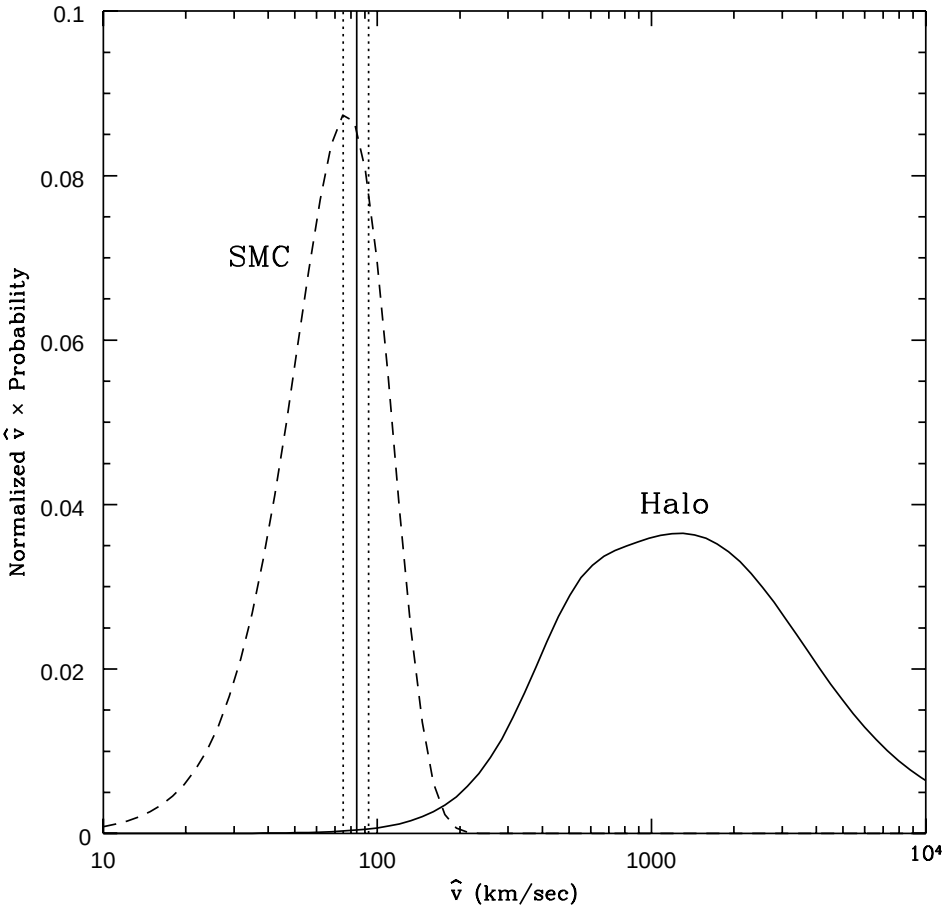

Figure 7.4: Predicted $\hat{v}$ distributions for halo and SMC lenses. The measured value of $\hat{v}$ and error bars for 98–SMC–1 are indicated with vertical lines.

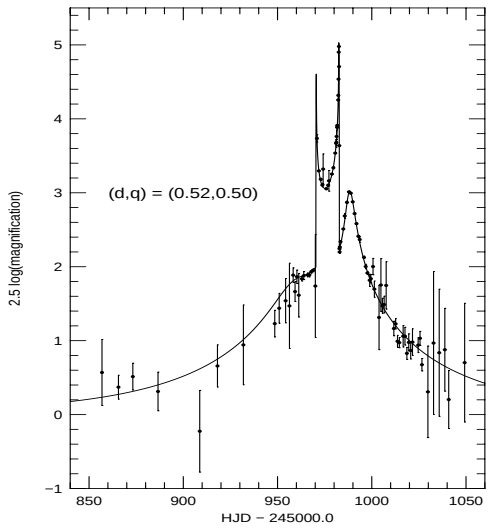

Figure 7.5: The complete lightcurve of event 98–SMC–1, as observed by the EROS (Afonso et al. 1998), OGLE (Udalski et al. 1998), MACHO/GMAN (Alcock et al. 1999a), MPS (Rhie et al. 1999), and PLANET (Albrow et al. 1999b) microlensing collaborations. The is the "close binary" solution presented in Afonso et al. (2000). Figure from Afonso et al. (2000).

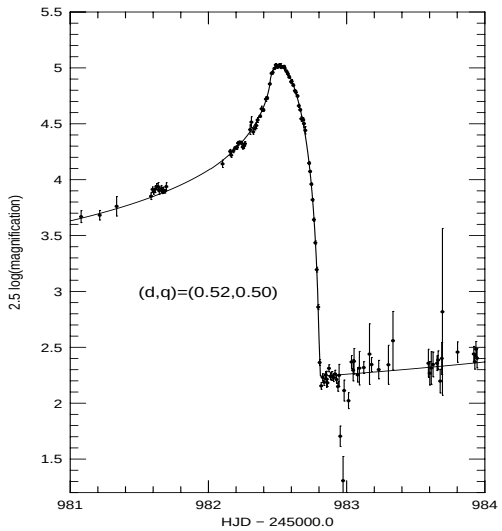

Figure 7.6: Complete coverage of the second caustic crossing of 98–SMC–1, using the same data and fit as in Figure 7.5. Figure from Afonso et al. (2000).

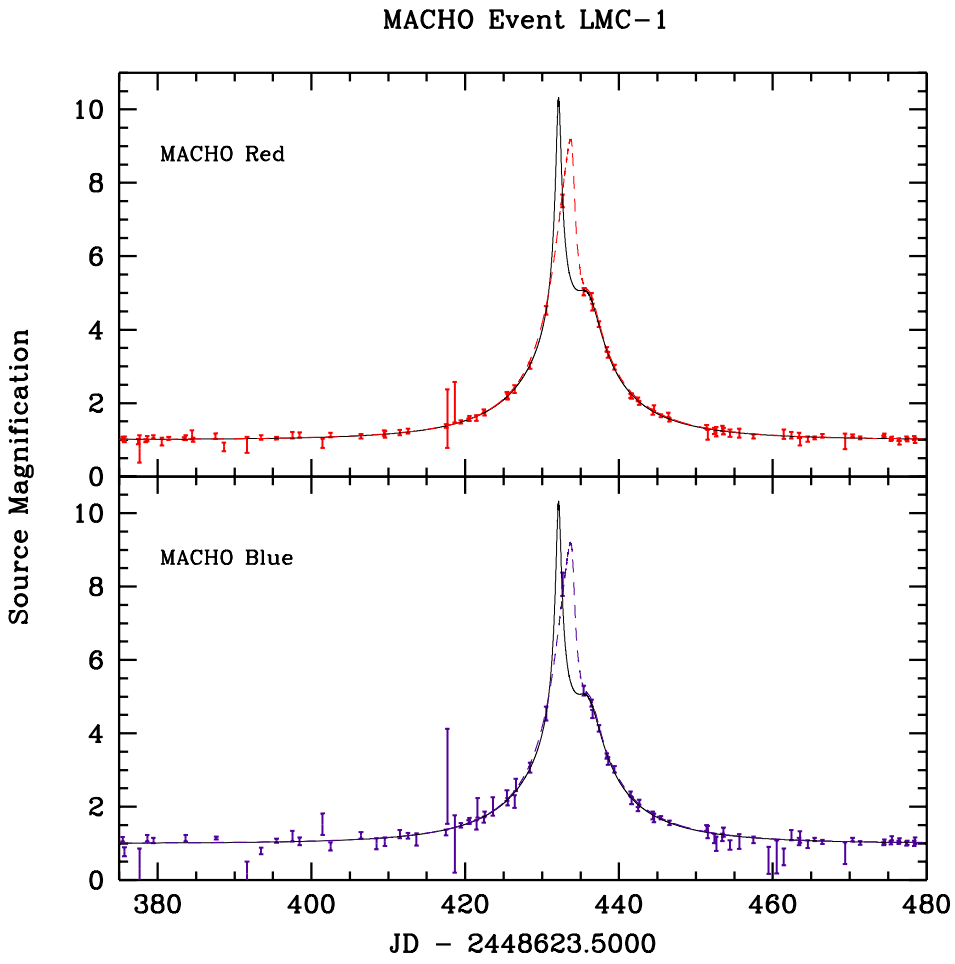

Figure 7.7: Lightcurve of MACHO event LMC-1, including fits indicating a 'planetary' mass secondary lens (*dashed* fit) and a more standard binary system (*solid* fit).

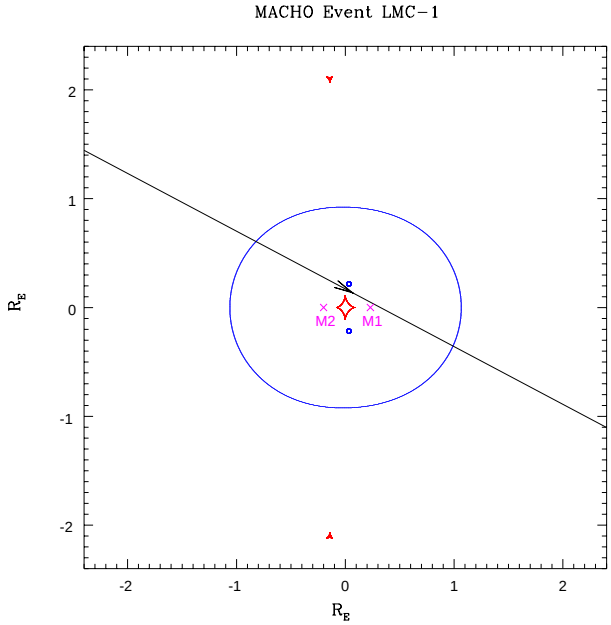

Figure 7.8: Location of the (cuspy) caustic and (smooth) critical curves for the LMC-1 standard binary lens fit (*solid* fit) presented in Figure 7.7. The coordinate system, whose origin is at the center of mass, indicates distance in units of the system's Einstein ring radius $R_{\rm E}$. Also shown are the locations of the lensing objects, and the trajectory of the source through the caustic structure.

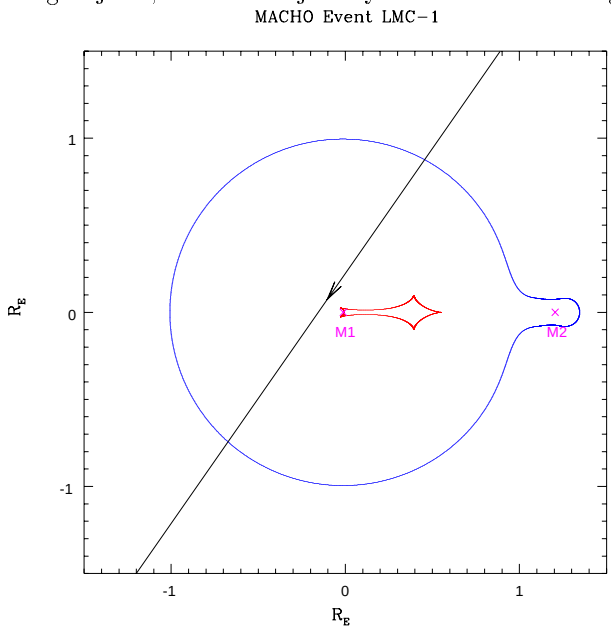

Figure 7.9: Location of the (cuspy) caustic and (smooth) critical curves for the LMC-1 'planetary' binary lens fit (*dashed* fit) presented in Figure 7.7.

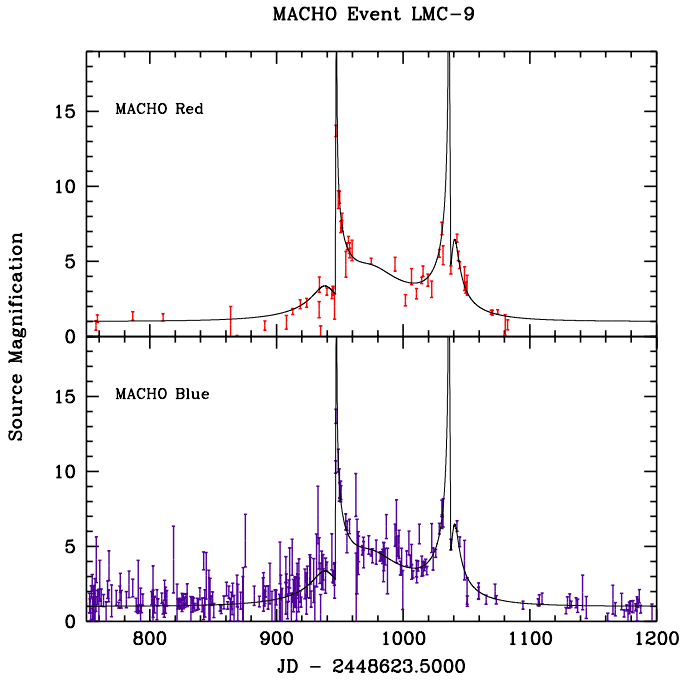

Figure 7.10: Lightcurve of MACHO event LMC-9, including our fit to binary microlensing.

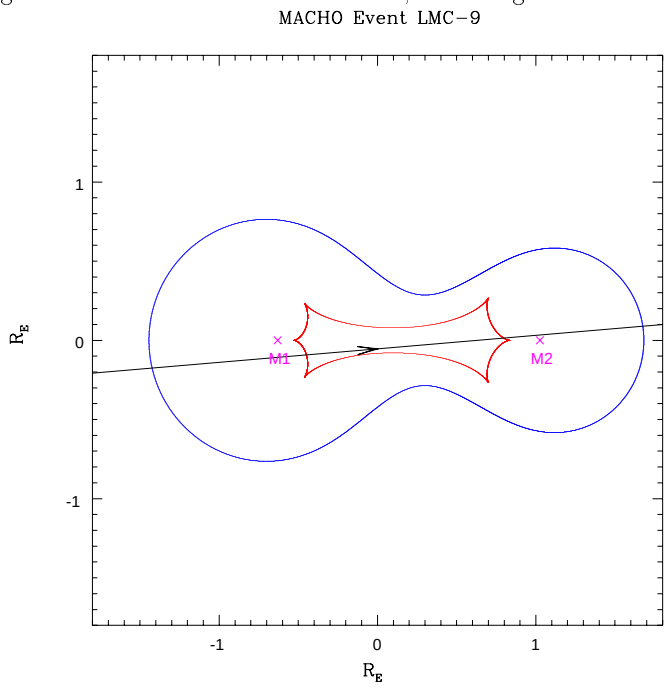

Figure 7.11: Location of the (cuspy) caustic and (smooth) critical curves for the LMC-9 binary lens fit presented in Figure 7.10.

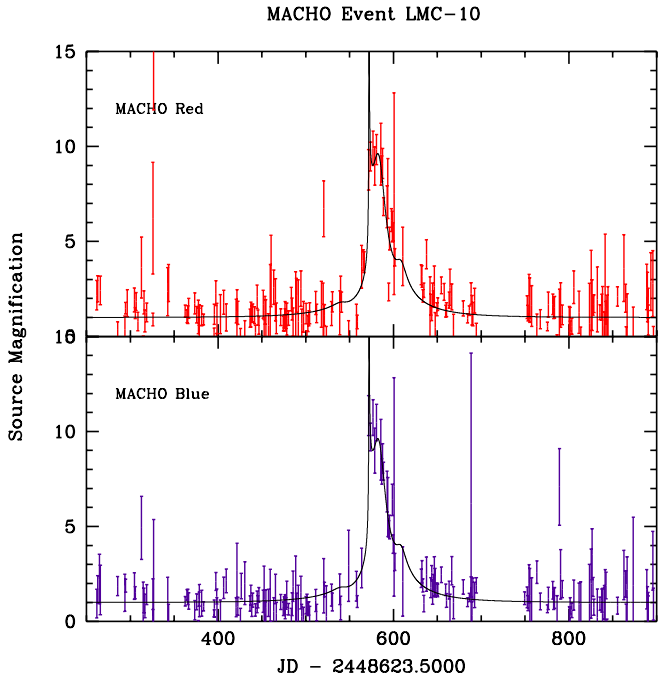

Figure 7.12: Lightcurve of MACHO event LMC-10, including our fit to binary microlensing.

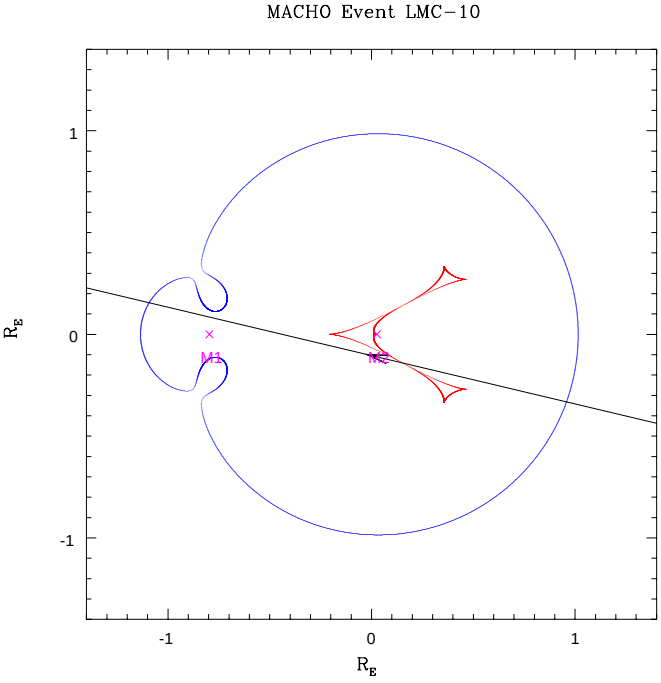

Figure 7.13: Location of the (cuspy) caustic and (smooth) critical curves for the LMC-10 binary lens fit presented in Figure 7.12.

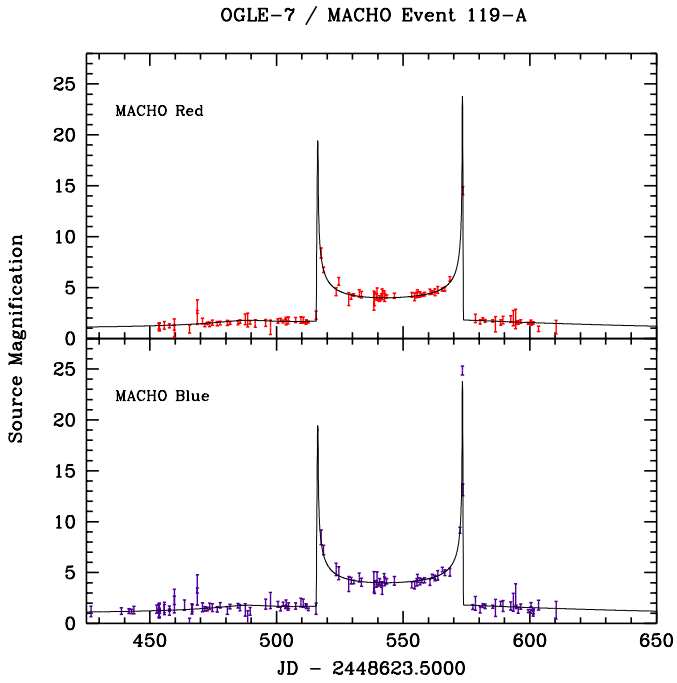

Figure 7.14: Lightcurve of MACHO event 119-A, including our fit to binary microlensing.

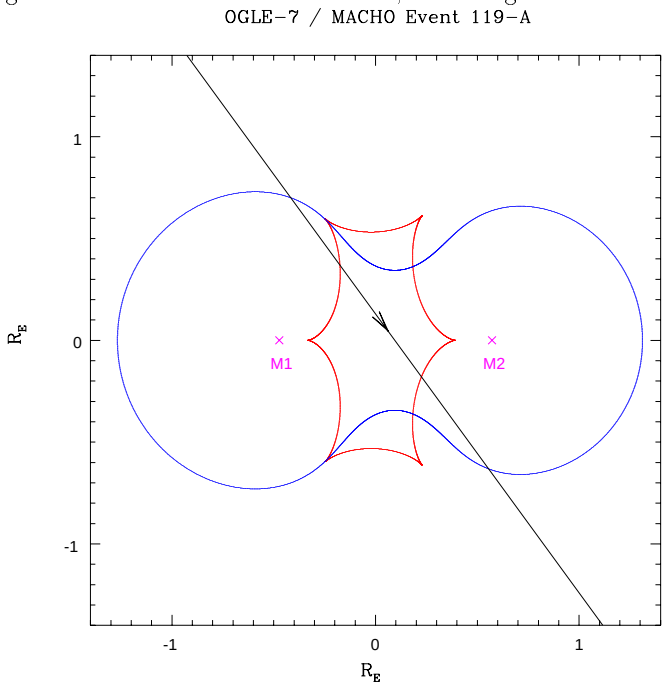

Figure 7.15: Location of the (cuspy) caustic and (smooth) critical curves for the 119-A binary lens fit presented in Figure 7.14.

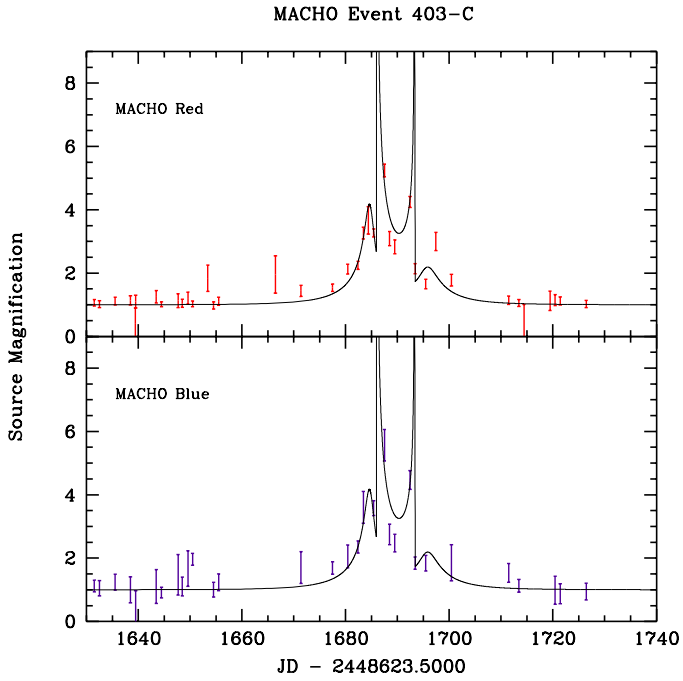

Figure 7.16: Lightcurve of MACHO event 403-C, including our fit to binary microlensing.

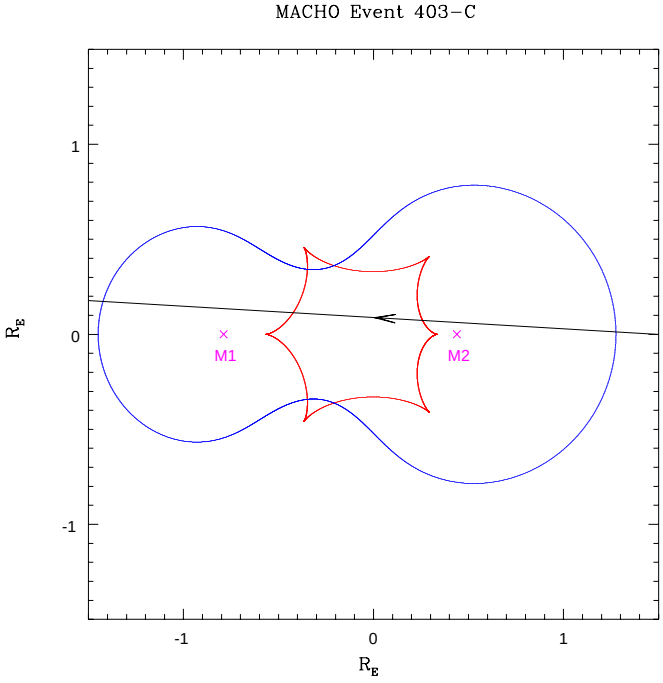

Figure 7.17: Location of the (cuspy) caustic and (smooth) critical curves for the 403-C binary lens fit presented in Figure 7.16.

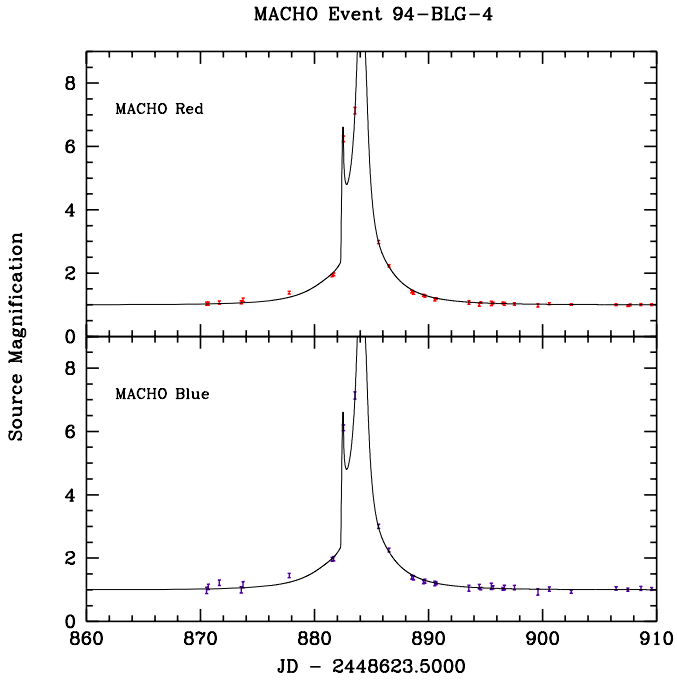

Figure 7.18: Lightcurve of MACHO event 94-BLG-4, including our fit to binary microlensing.

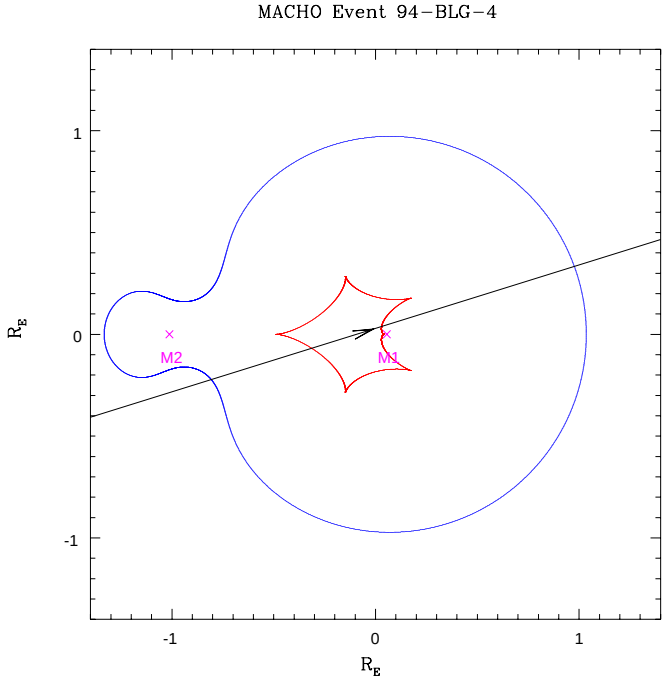

Figure 7.19: Location of the (cuspy) caustic and (smooth) critical curves for the 94-BLG-4 binary lens fit presented in Figure 7.18.

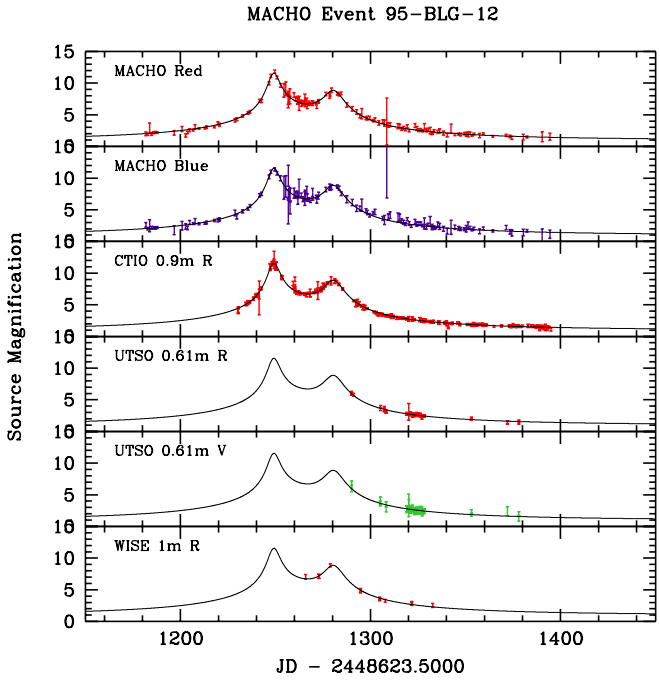

Figure 7.20: Lightcurve of MACHO event 95-BLG-12, including our fit to binary microlensing.

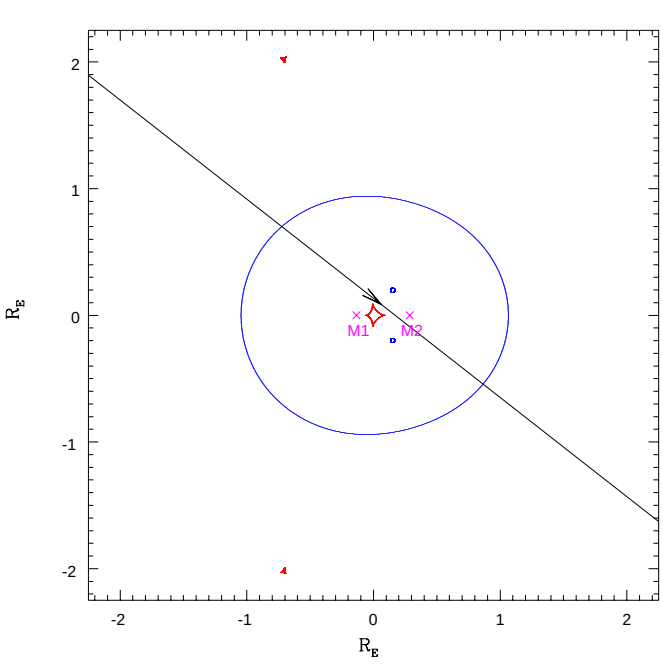

Figure 7.21: Location of the (cuspy) caustic and (smooth) critical curves for the 95-BLG-12 binary lens fit presented in Figure 7.20.

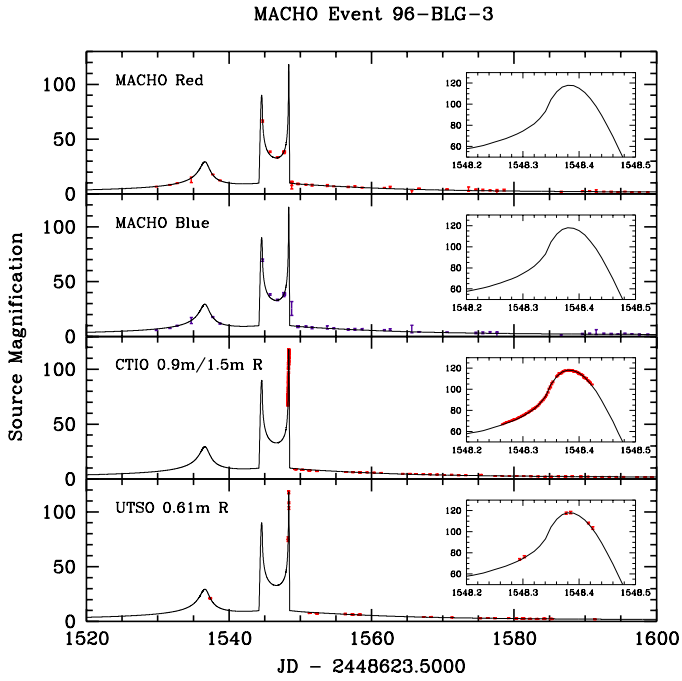

Figure 7.22: Lightcurve of MACHO event 96-BLG-3, including our fit to binary microlensing.

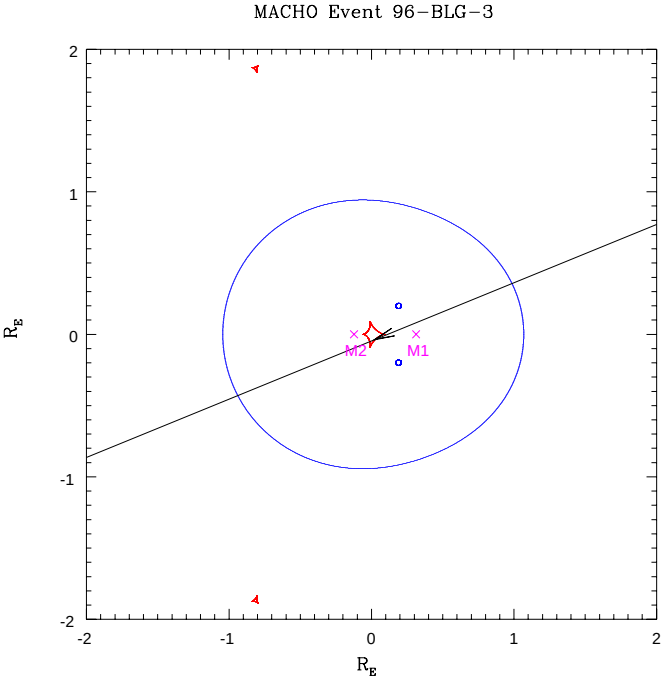

Figure 7.23: Location of the (cuspy) caustic and (smooth) critical curves for the 96-BLG-3 binary lens fit presented in Figure 7.22.

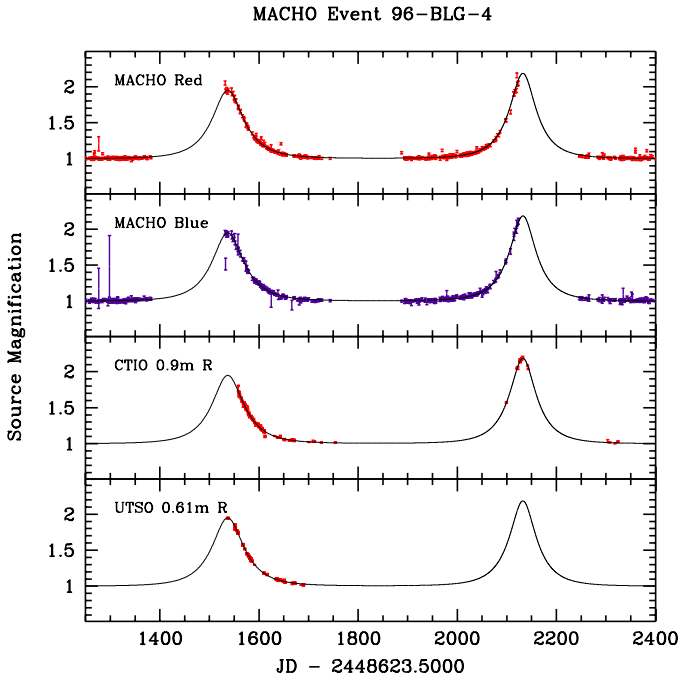

Figure 7.24: Lightcurve of MACHO event 96-BLG-4, including our fit to binary microlensing.

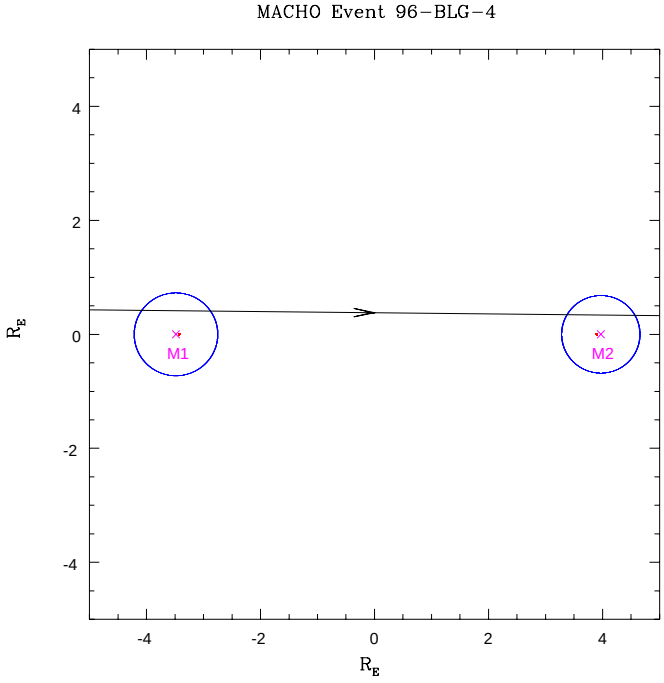

Figure 7.25: Location of the (cuspy) caustic and (smooth) critical curves for the 96-BLG-4 binary lens fit presented in Figure 7.24.

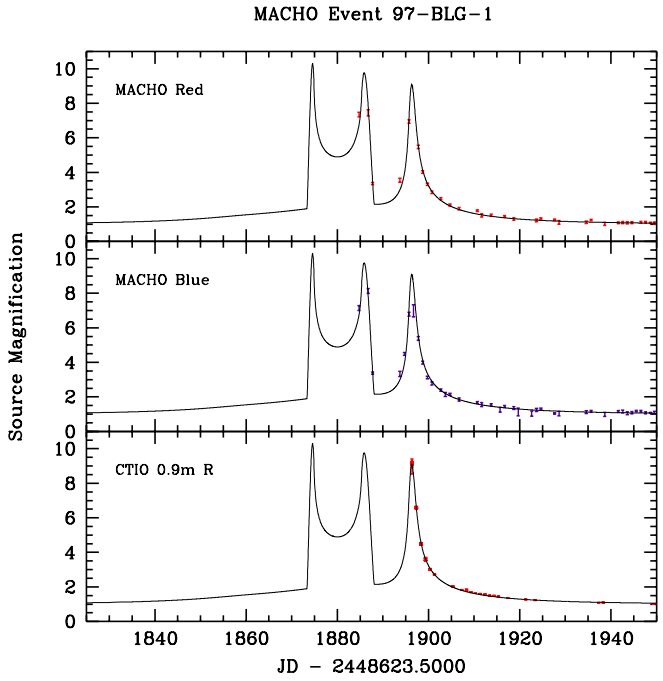

Figure 7.26: Lightcurve of MACHO event 97-BLG-1, including our fit to binary microlensing.

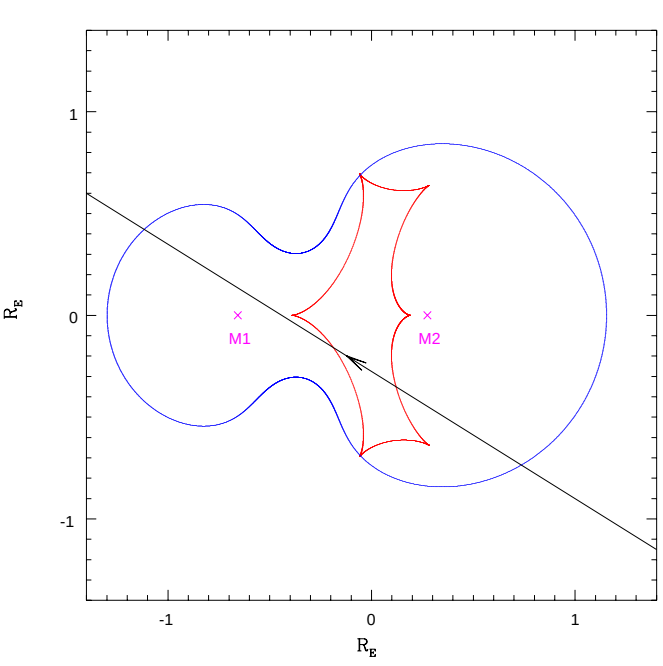

Figure 7.27: Location of the (cuspy) caustic and (smooth) critical curves for the 97-BLG-1 binary lens fit presented in Figure 7.26.

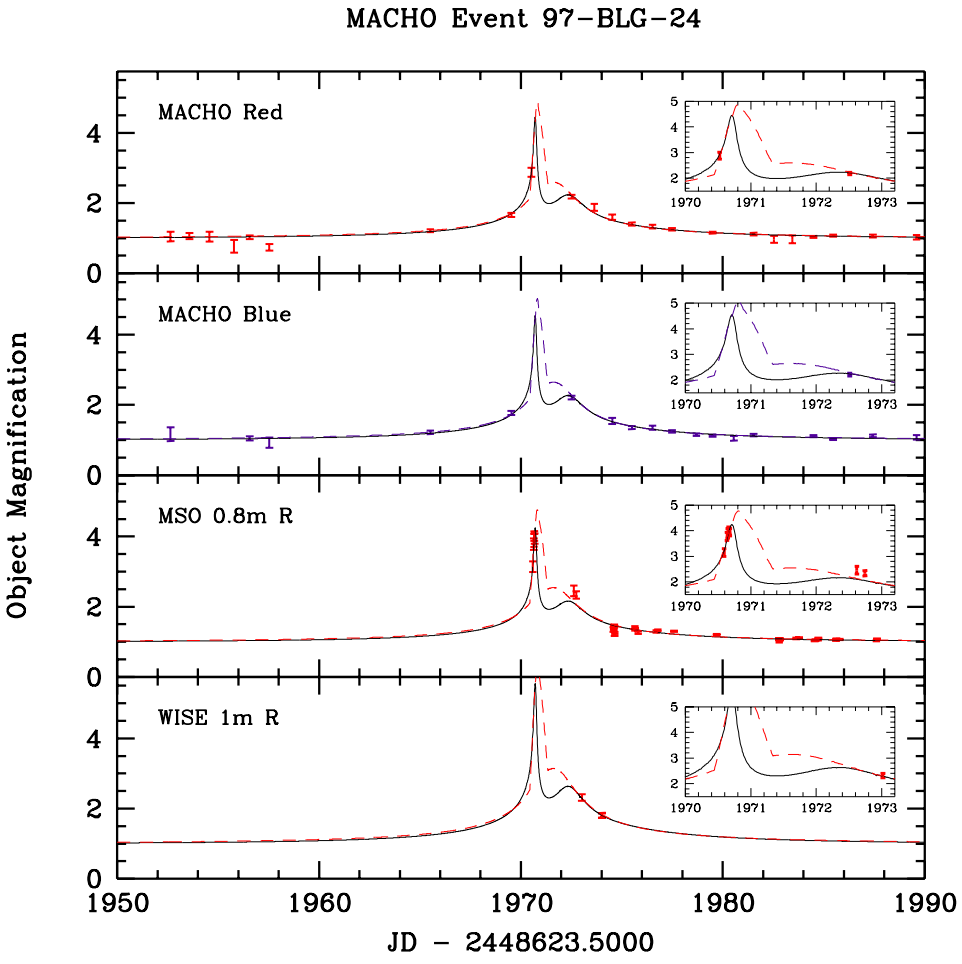

Figure 7.28: Lightcurve of MACHO event 97-BLG-24, including our fits to binary microlensing. Due to the different blending parameters between fits, we plot the observed magnification of the MACHO object, as opposed to the actual lensed source.

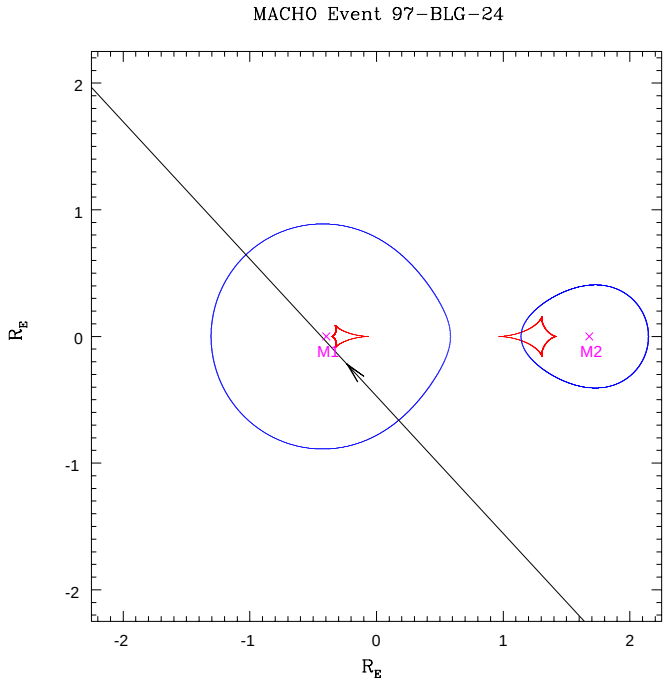

Figure 7.29: Location of the (cuspy) caustic and (smooth) critical curves for the 97-BLG-24 standard binary lens fit (*solid* fit) presented in Figure 7.28.

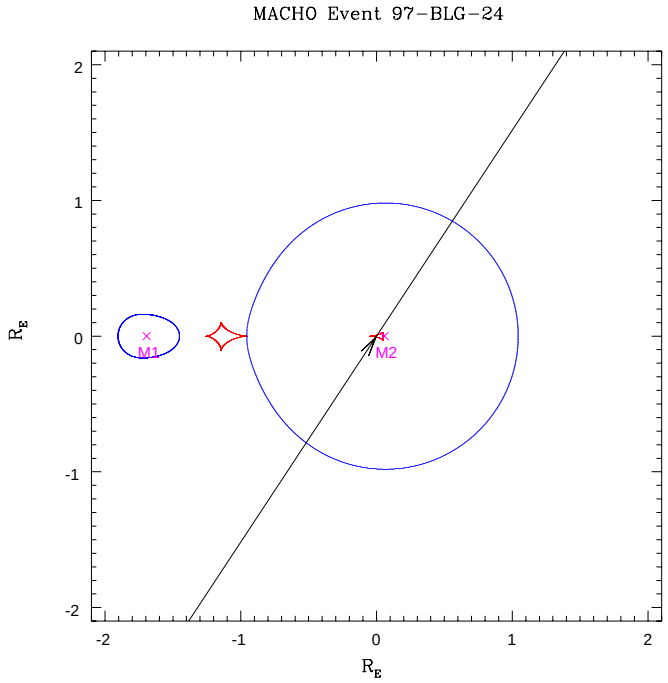

Figure 7.30: Location of the (cuspy) caustic and (smooth) critical curves for the 97-BLG-24 'planetary' binary lens fit (*dashed* fit) presented in Figure 7.28.

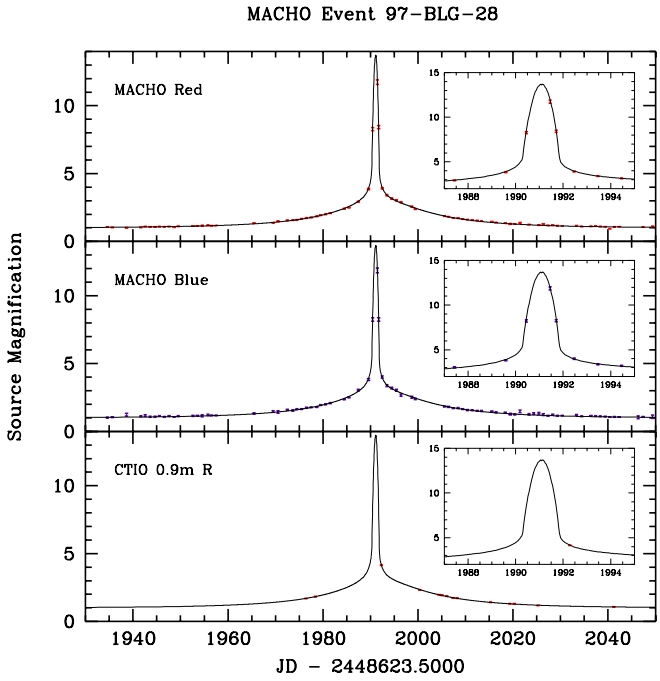

Figure 7.31: Lightcurve of MACHO event 97-BLG-28, including our fit to binary microlensing.

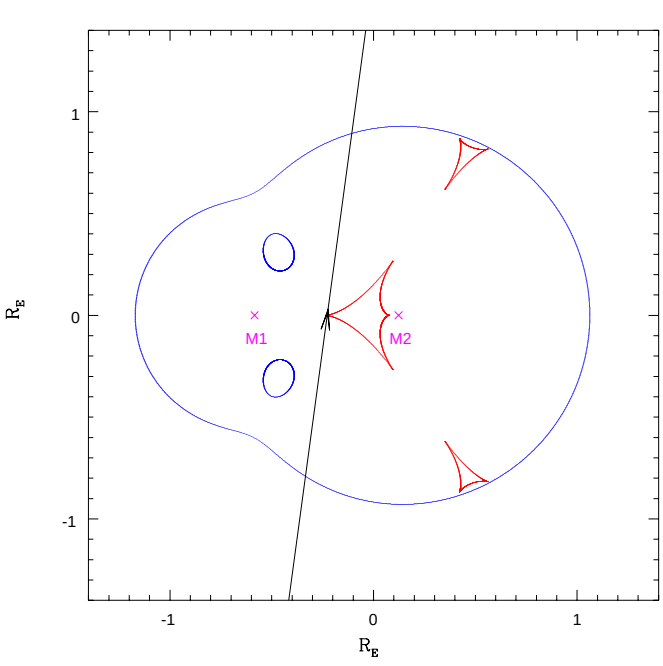

Figure 7.32: Location of the (cuspy) caustic and (smooth) critical curves for the 97-BLG-28 binary lens fit presented in Figure 7.31.

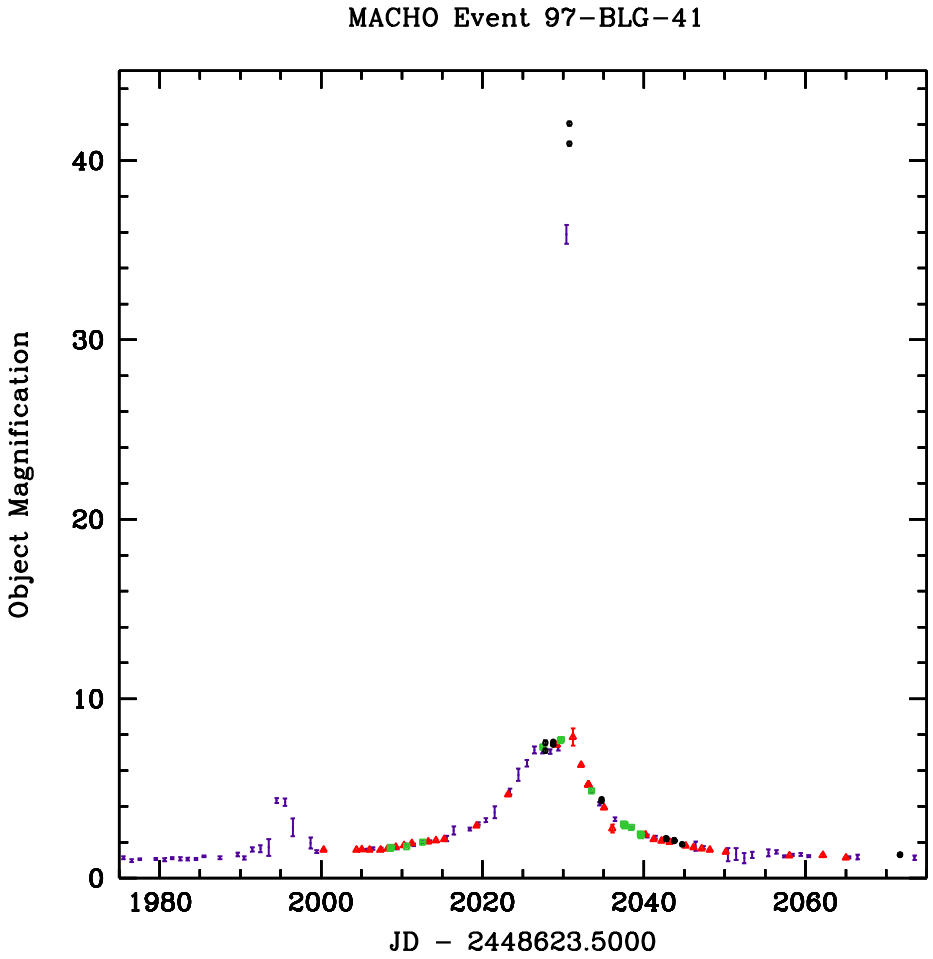

Figure 7.33: Lightcurve of MACHO event 97-BLG-41, with an approximate baseline determined from a fit to the second peak, disregarding the caustic features. Plotted are the MACHO-B (*points*), CTIO-r (*triangles*), MSO30-r (*squares*) and WISE-r (*circles*) data.

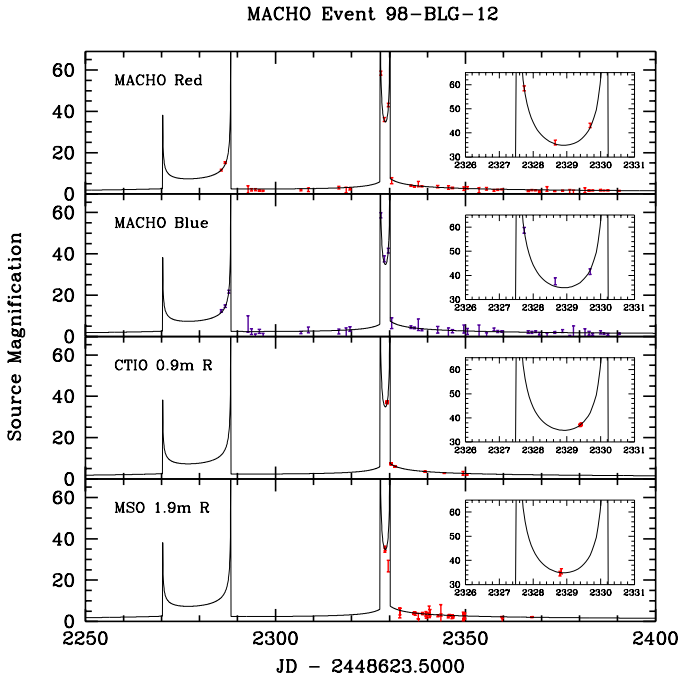

Figure 7.34: Lightcurve of MACHO event 98-BLG-12, including our fit to binary microlensing.

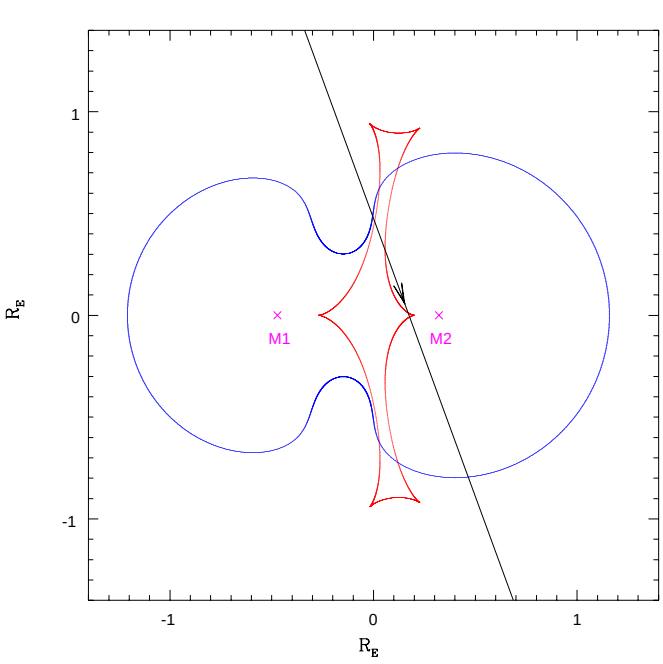

Figure 7.35: Location of the (cuspy) caustic and (smooth) critical curves for the 98-BLG-12 binary lens fit presented in Figure 7.34.

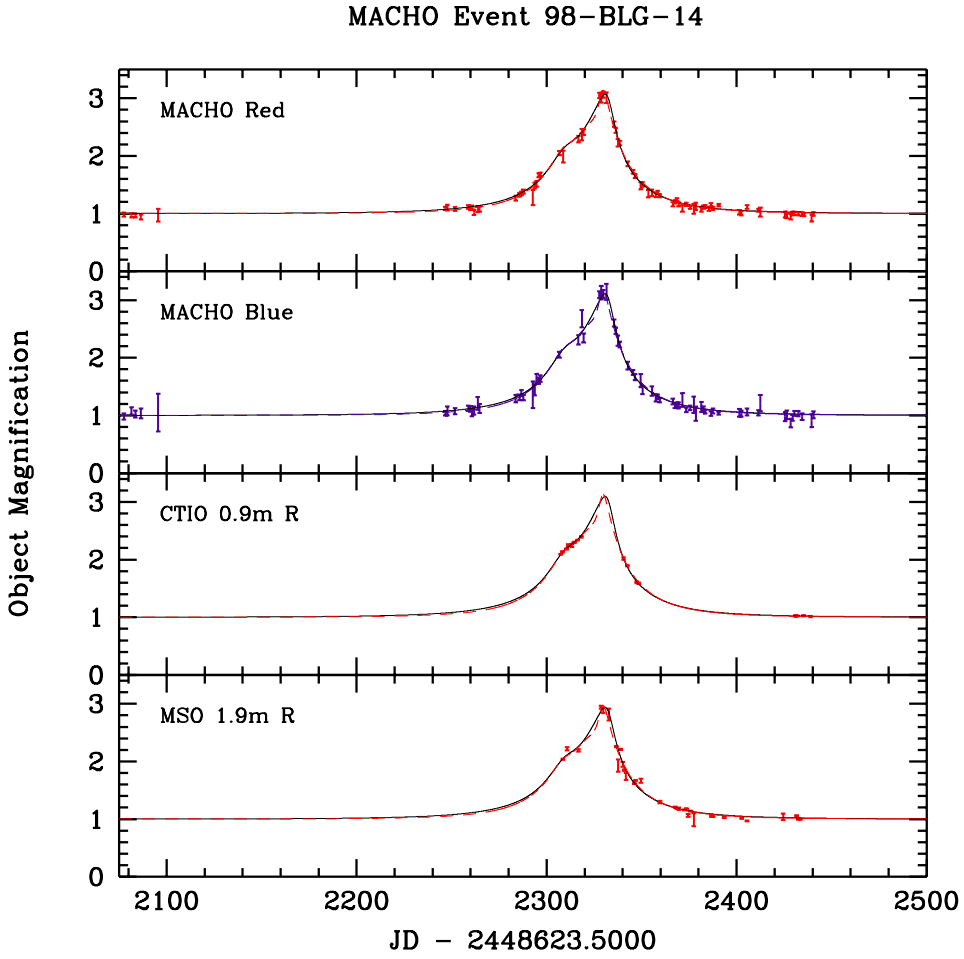

Figure 7.36: Lightcurve of MACHO event 98-BLG-14, including our fits to binary microlensing. Due to the different blending parameters between fits, we plot the observed magnification of the MACHO object, as opposed to the actual lensed source. The MSO74 data have been averaged into 1 day bins.

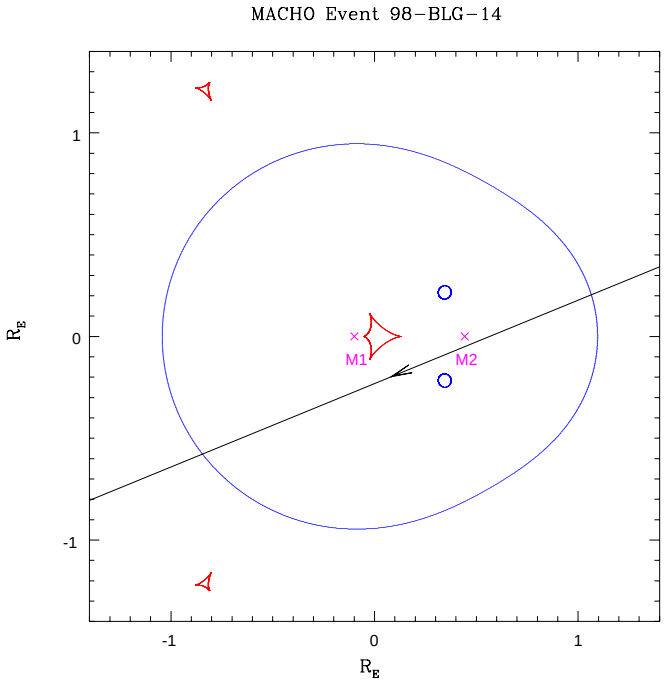

Figure 7.37: Location of the (cuspy) caustic and (smooth) critical curves for the *solid* 98-BLG-14 binary lens fit presented in Figure 7.36.

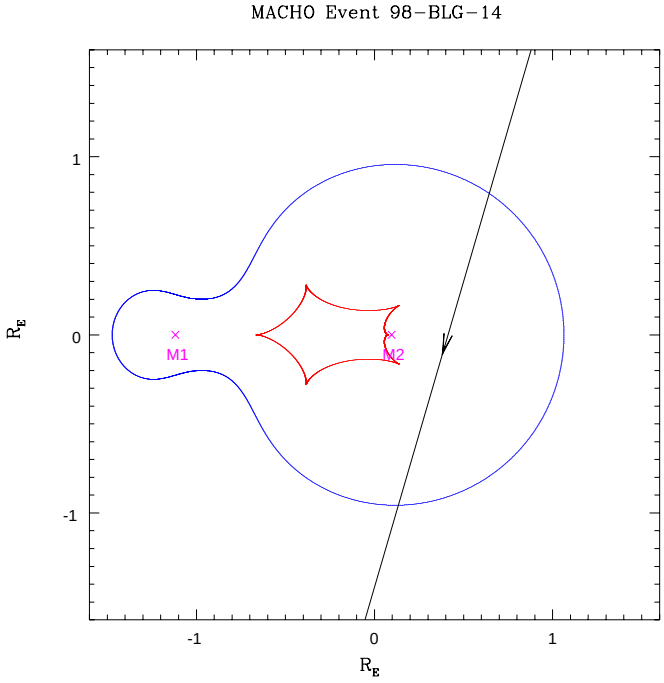

Figure 7.38: Location of the (cuspy) caustic and (smooth) critical curves for the *dashed* (large mass ratio) 98-BLG-14 binary lens fit presented in Figure 7.36.

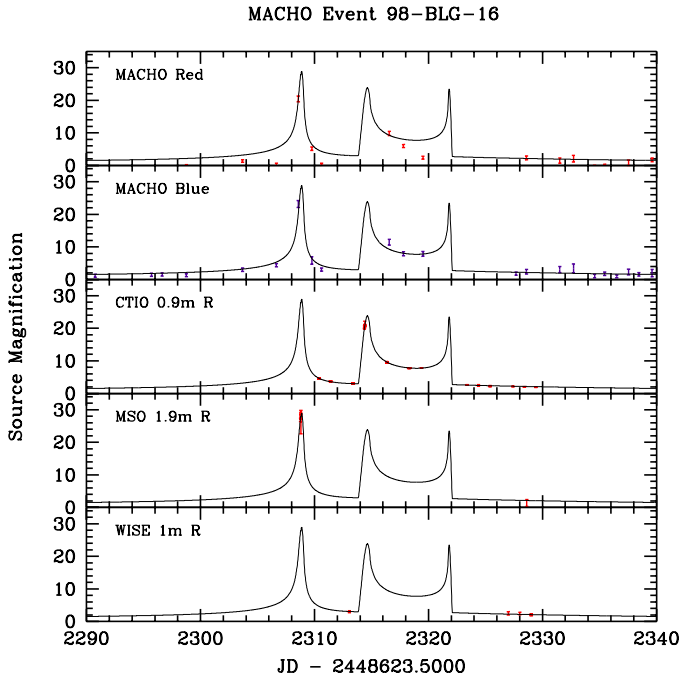

Figure 7.39: Lightcurve of MACHO event 98-BLG-16, including our fit to binary microlensing. The MACHO Red data exhibit excessive scatter due to a defective amplifier.

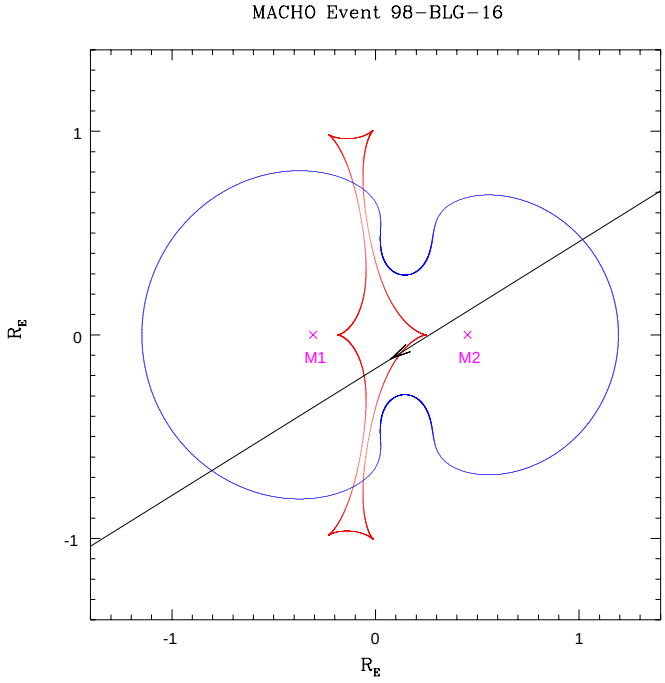

Figure 7.40: Location of the (cuspy) caustic and (smooth) critical curves for the 98-BLG-16 binary lens fit presented in Figure 7.39.

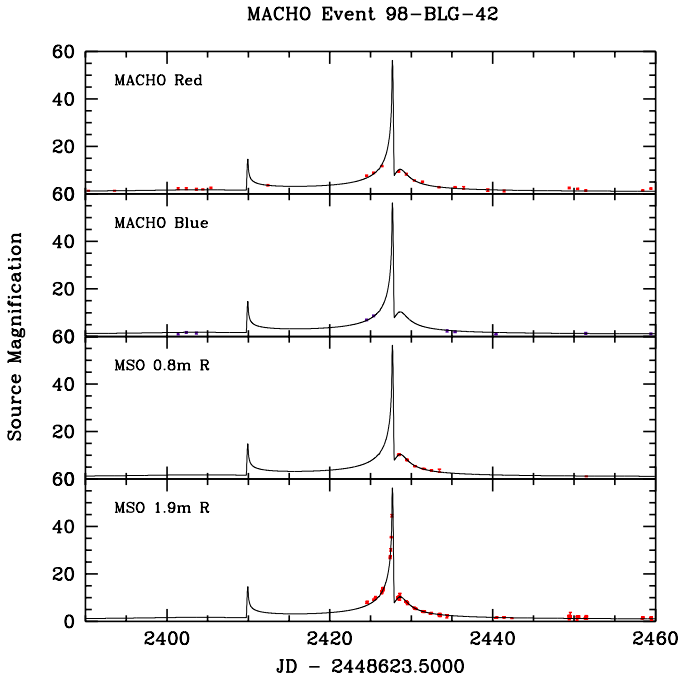

Figure 7.41: Lightcurve of MACHO event 98-BLG-42, including our fit to binary microlensing.

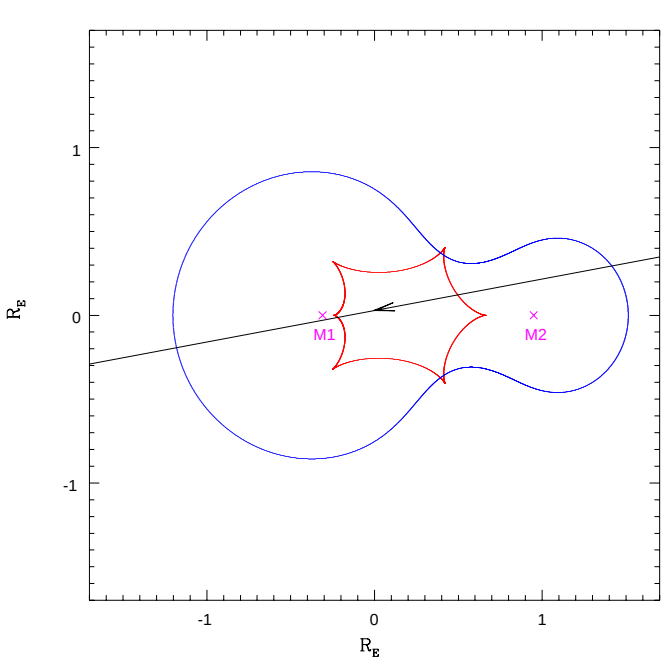

Figure 7.42: Location of the (cuspy) caustic and (smooth) critical curves for the 98-BLG-42 binary lens fit presented in Figure 7.41.

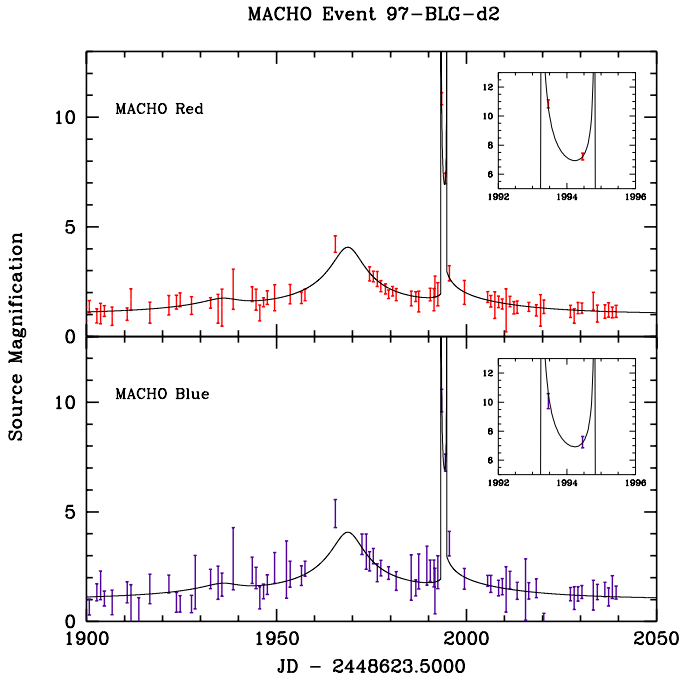

Figure 7.43: Lightcurve of MACHO event 97-BLG-d2, including our fit to binary microlensing.

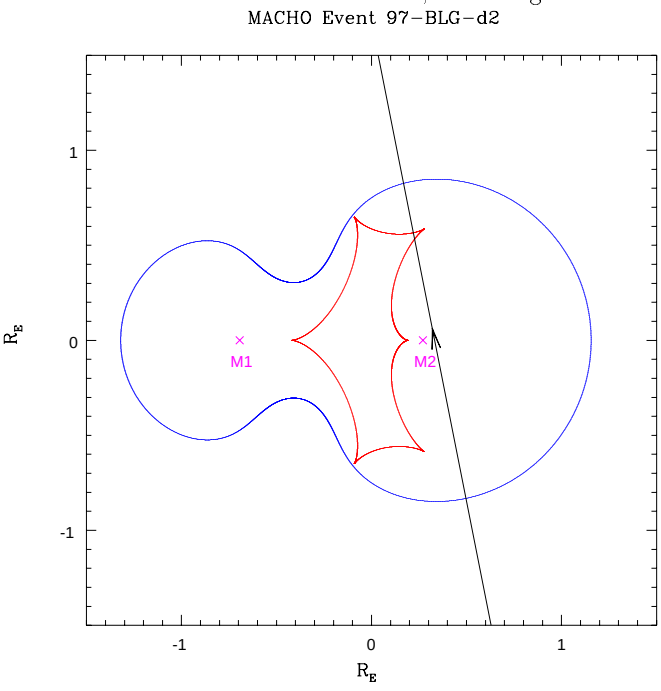

Figure 7.44: Location of the (cuspy) caustic and (smooth) critical curves for the 97-BLG-d2 binary lens fit presented in Figure 7.43.

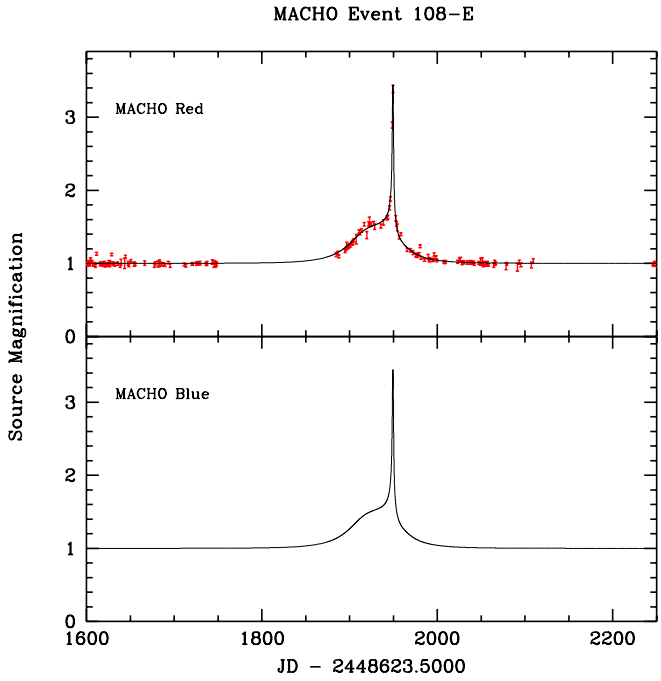

Figure 7.45: Lightcurve of MACHO event 108-E, including our fit to binary microlensing.

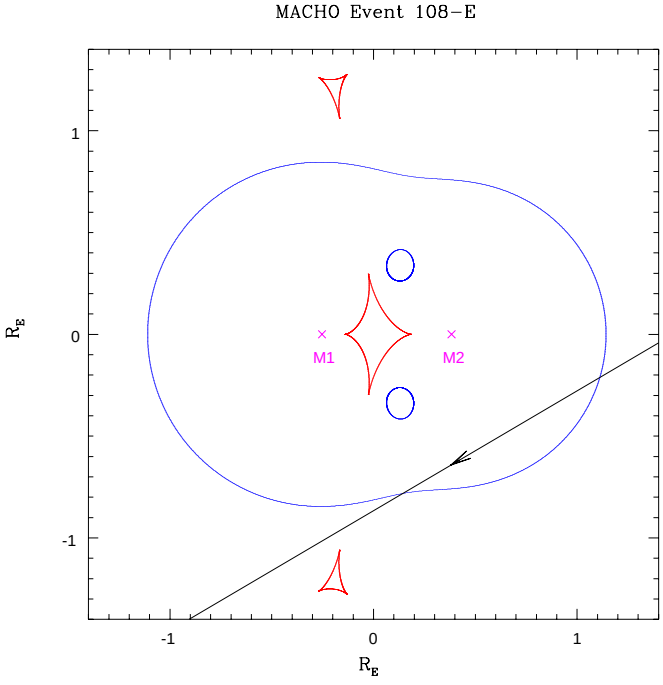

Figure 7.46: Location of the (cuspy) caustic and (smooth) critical curves for the 108-E binary lens fit presented in Figure 7.45.

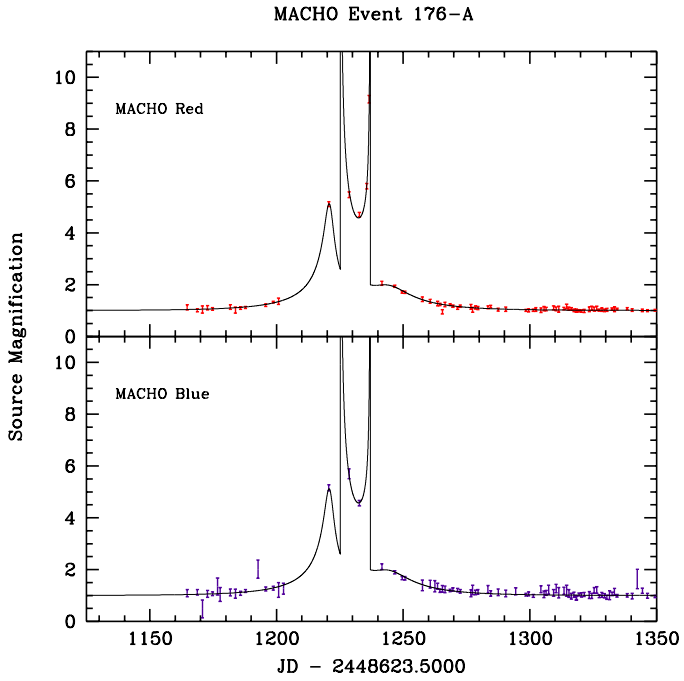

Figure 7.47: Lightcurve of MACHO event 176-A, including our fit to binary microlensing.

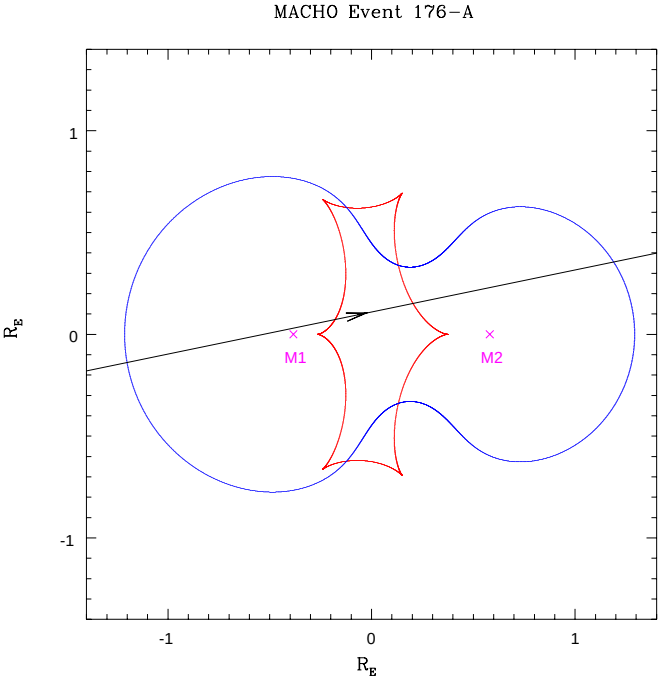

Figure 7.48: Location of the (cuspy) caustic and (smooth) critical curves for the 176-A binary lens fit presented in Figure 7.47.

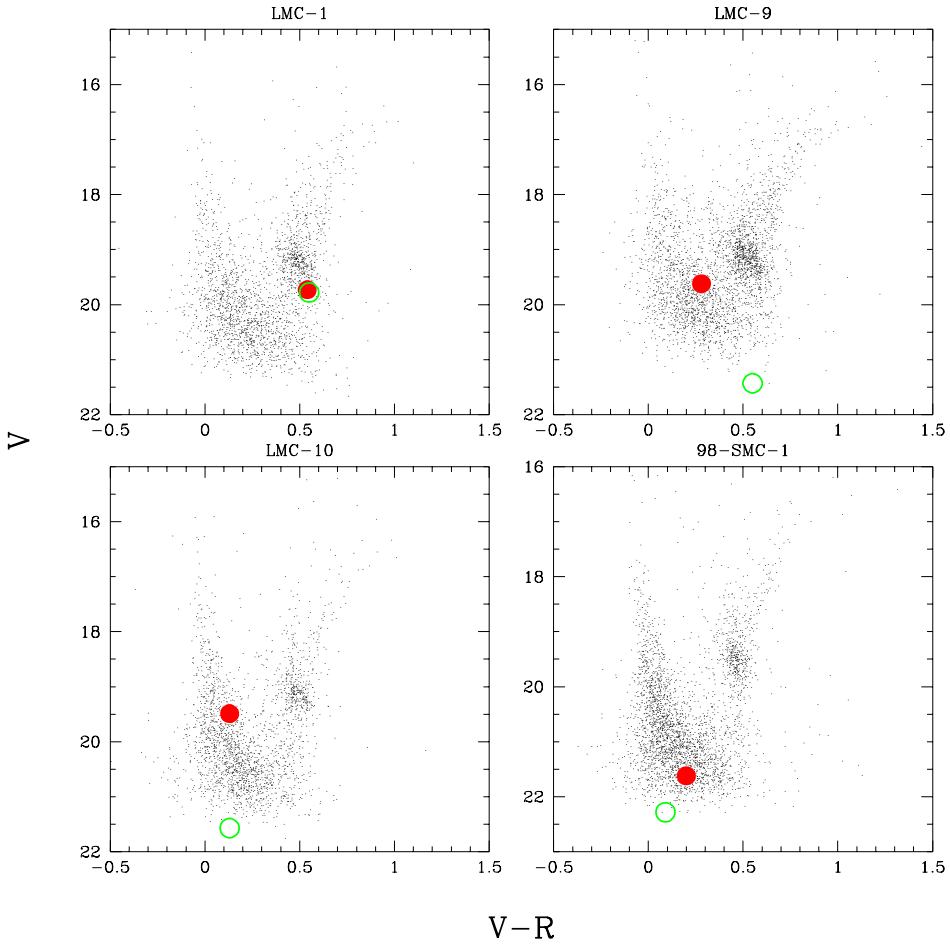

Figure 7.49: Distribution of $V, V-R$ for $\sim 3,000$ stars neighboring the lensed object, indicated with the filled circle, for objects in the Magellanic Clouds. The de-blended source location, determined from blending parameters in the microlensing fit, is indicated with the open circle.

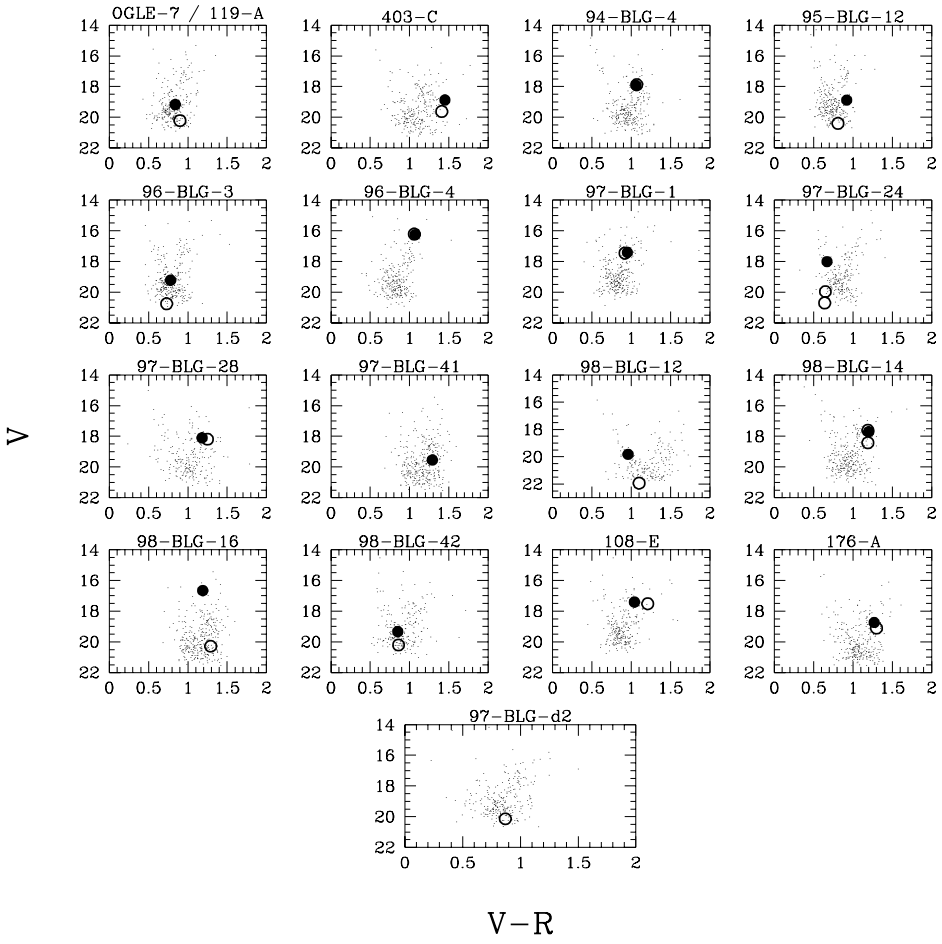

Figure 7.50: Distribution of V, $V-R$ for ~ 300 stars neighboring the lensed object, indicated with the filled circle, for objects in the Galactic bulge. The de-blended source location, determined from blending parameters in the microlensing fit, is indicated with the open circle. Notable cases: 97-BLG-24, where the brighter source is associated with the low mass ratio fit in Figure 7.28; 97-BLG-41, where we have no estimate of the source properties; 98-BLG-14, where the brighter source is associated with the large mass ratio fit in Figure 7.36; 97-BLG-d2, where we only have an estimate of the lensed source properties.

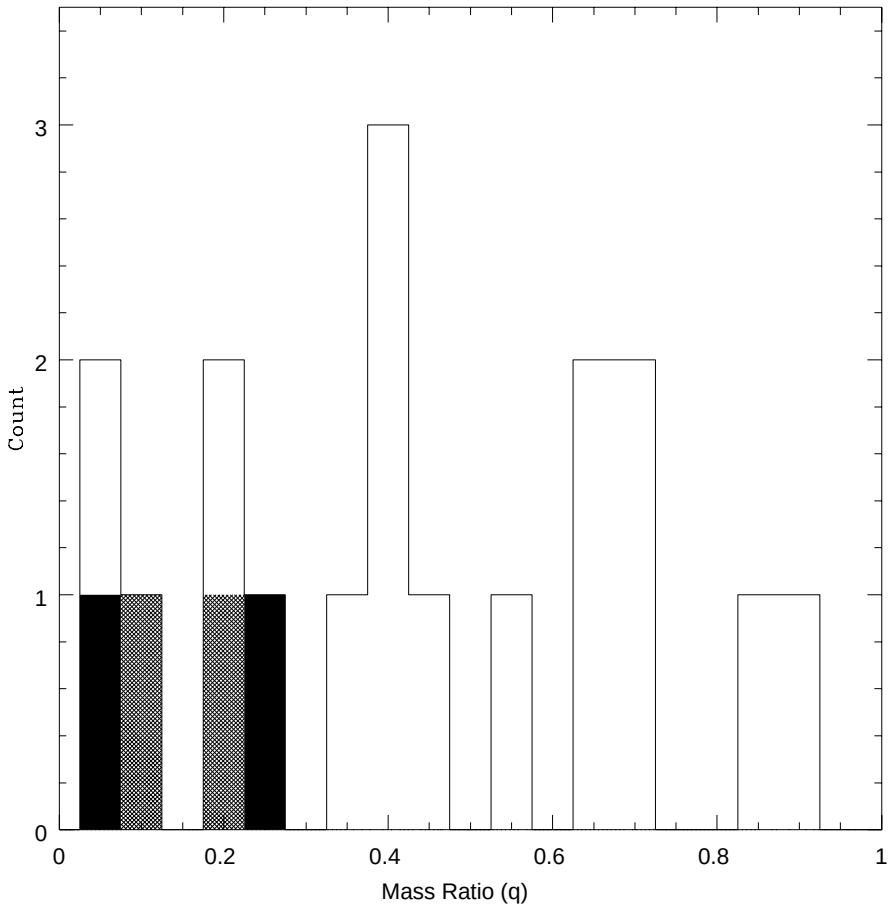

Figure 7.51: The distribution of mass ratios ($q \leq 1$) for our Galactic bulge binary microlensing events. The contribution of our 2 fits each to events 97-BLG-24 and 98-BLG-14 are represented by the dark and light shaded areas, respectively.

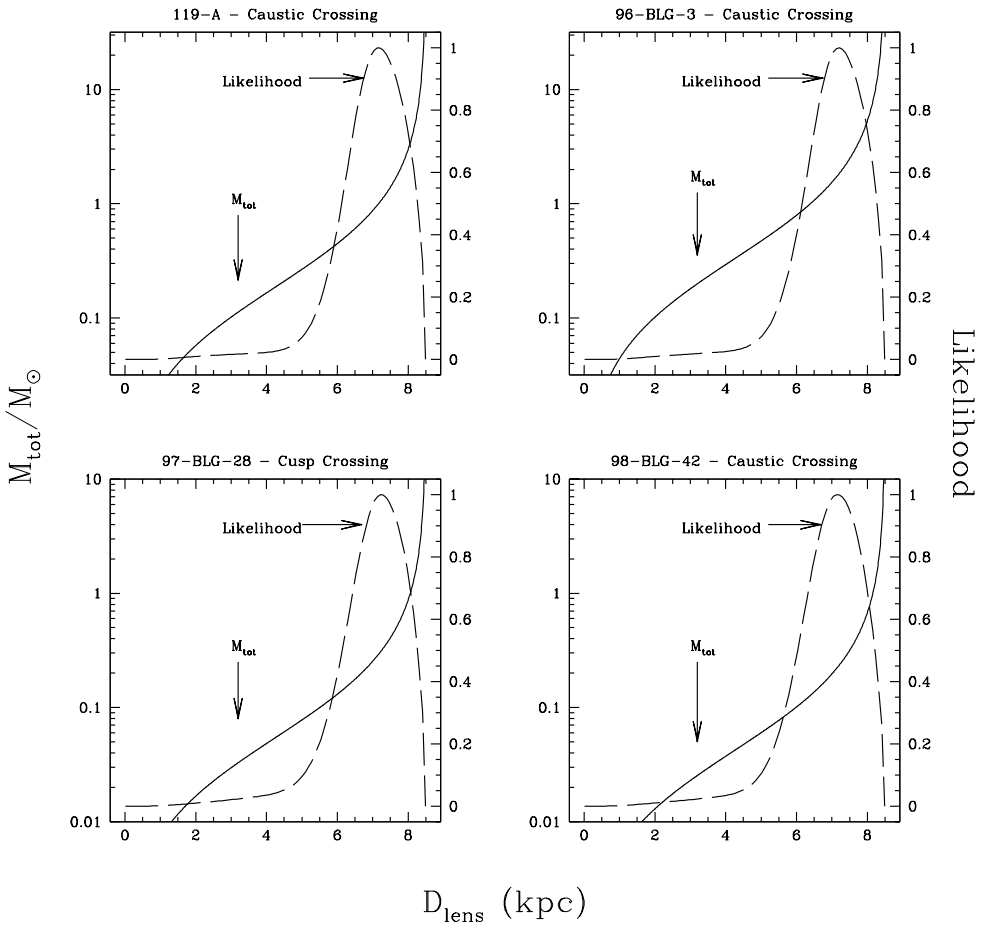

Figure 7.52: The relation between the lens distance, D_l, and the total mass, $M_{\rm tot}$, is shown for the four lensing events with reliable proper motion determinations. Also shown are the results of a likelihood analysis to estimate the lens parameters. The most likely lens distances and masses are given in Table 7.8.

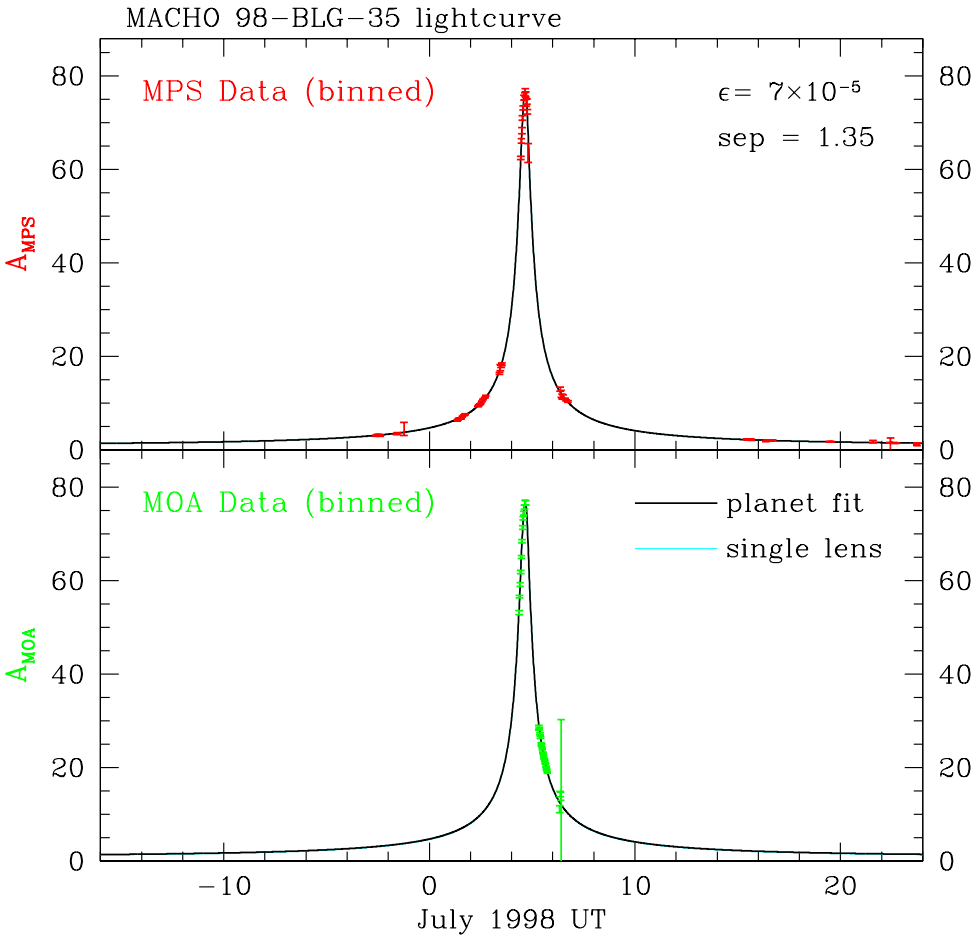

Figure 7.53:
Lightcurve of MACHO event 98-BLG-35, from the MPS and MOA collaborations. Coverage near the peak of this high–magnification event is able to significantly constrain the presence of planets around the lensing object. A marginal planet detection is found with a mass ratio of 7×10^{-5}, corresponding to a Neptune–mass planet, at 1.35 $R_{\rm E}$. Figure from Rhie et al. (2000).

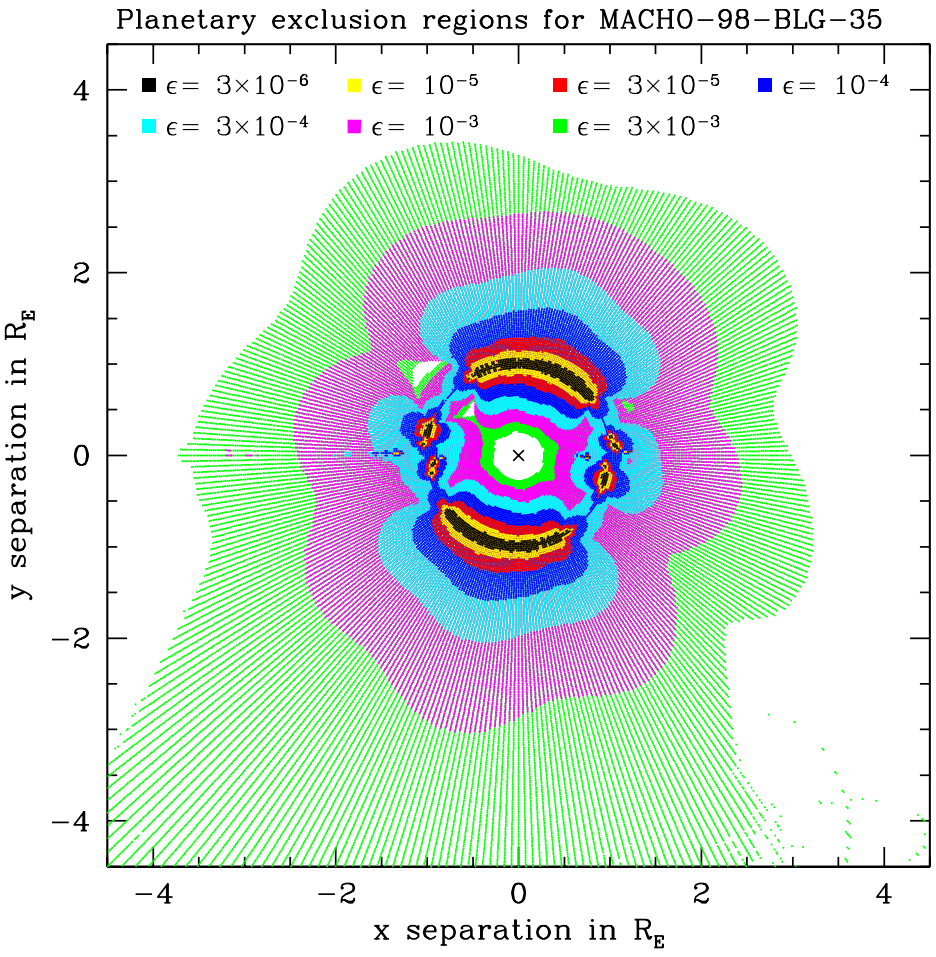

Figure 7.54:
Regions in the lens plane where lightcurve coverage excludes the presence of planets. The second, fourth, and sixth exclusion regions, corresponding to $\epsilon = 10^{-3}, 10^{-4}, 10^{-5}$, exclude the presence of Jupiters, Neptunes, and Earths, respectively. Jupiters are excluded from $\sim 95\%$ of this lensing region, Neptunes $\sim 57\%$, and Earths $\sim 14\%$. This is the very first time constraints on Earth–like planets have been set around (what is likely to be) a normal star. Figure from Rhie et al. (2000).

Table 7.4: Information on the lensed MACHO objects and de-blended source stars. Events LMC-1, 97-BLG-24, and 98-BLG-14 are each presented with 2 fits of similar significance, but different event parameters. We do not present a binary microlensing fit for event 97-BLG-41, and we only include an estimate of the MACHO object's baseline flux. Event 97-BLG-d2 was found through difference image analysis (DIA), which uniquely identifies the lensed source.

[a] Standard magnitudes and color of the MACHO object that received the lensed flux.

[b] Standard magnitudes and color of the actual lensed source star, as determined from the blend fraction in the binary lens fit.

Event	MACHO Id	RA (J2000)	DEC (J2000)	V [a]	$V-R$	V [b]	$V-R$
98-SMC-1	208.15683.4237	00 45 35.2	-72 52 34.1	21.62	0.20	22.28	0.09
LMC-1 (*solid* fit)	79.5628.1547	05 14 44.5	-68 48 00.1	19.73	0.54	19.75	0.55
LMC-1 (*dashed* fit)	...	...	...	19.73	0.54	19.78	0.55
LMC-9	80.6468.2746	05 20 20.2	-69 15 11.8	19.62	0.28	21.43	0.55
LMC-10	18.3324.1765	05 01 16.0	-69 07 33.1	19.49	0.13	21.57	0.13
OGLE-7 / 119-A	119.20226.2119	18 03 35.7	-29 42 01.2	19.16	0.84	20.21	0.90
403-C	403.47793.2961	17 55 57.9	-29 26 12.1	18.87	1.45	19.62	1.41
94-BLG-4	118.18141.731	17 58 36.7	-30 02 19.2	17.92	1.06	17.87	1.07
95-BLG-12	120.21263.1213	18 06 04.7	-29 52 38.1	18.88	0.92	20.39	0.81
96-BLG-3	119.19444.2055	18 01 45.5	-29 49 46.8	20.00	0.78	21.48	0.73
96-BLG-4	105.21417.101	18 06 11.9	-28 16 52.7	16.25	1.07	16.21	1.06
97-BLG-1	113.18674.756	17 59 53.3	-29 09 07.8	17.41	0.95	17.46	0.92
97-BLG-24 (*solid* fit)	101.20650.1216	18 04 20.2	-27 24 45.2	18.01	0.67	19.96	0.65
97-BLG-24 (*dashed* fit)	...	...	...	18.01	0.67	20.7	0.64
97-BLG-28	108.18951.593	18 00 33.7	-28 01 10.4	18.10	1.18	18.19	1.25
97-BLG-41	402.47862.1576	17 56 20.6	-28 47 41.9	19.54	1.29	...	...
98-BLG-12	179.21577.1740	18 06 31.7	-26 16 01.5	18.86	0.96	20.83	1.10
98-BLG-14 (*solid* fit)	401.48408.649	17 59 08.9	-28 24 54.6	17.70	1.20	18.42	1.19
98-BLG-14 (*dashed* fit)	...	...	...	17.70	1.20	17.61	1.19
98-BLG-16	402.47863.110	17 56 18.1	-28 46 04.9	16.66	1.19	20.28	1.29
98-BLG-42	101.21045.2528	18 05 12.6	-27 05 47.1	19.33	0.85	20.20	0.86
97-BLG-d2	108.19073.2291	18 00 39.5	-28 34 43.8	...	...	20.14	0.87
108-E	108.19333.1878	18 01 21.1	-28 32 39.4	17.41	1.04	17.52	1.21
176-A	176.19219.978	18 01 04.4	-27 30 41.3	18.74	1.27	19.11	1.30

Table 7.5: List of binary microlensing event parameters, as described in Chapter 7.1, for each of our candidates. Also included are the binary microlensing fit χ^2, and the degrees of freedom (equal to the number of data points minus 1 for each constraint listed here, and minus 2 for each passband with observations in Table 7.6). Events LMC-1, 97-BLG-24, and 98-BLG-14 are each presented with 2 fits of similar significance, but different event parameters.

[a] (JD − 2448623.50).

Event	$\chi^2/d.o.f.$	$\widehat{t}$	t_0 [a]	$u_{\rm min}$	a	θ (rad)	M_1 / M_2	t_* (days)
98-SMC-1	1771.9/1583	147.58	2354.93	0.046	0.664	-0.180	0.388	0.116
LMC-1 (*solid* fit)	2794.9/2179	35.54	433.58	0.150	-0.430	-0.488	0.861	0.112
LMC-1 (*dashed* fit)	2799.4/2179	34.55	433.58	-0.127	1.217	4.104	108.890	0.122
LMC-9	1476.5/848	143.12	979.59	-0.054	1.657	0.086	1.627	0.651
LMC-10	1672.9/1240	151.05	585.74	0.102	0.823	-3.375	0.034	···
OGLE-7 / 119-A	1997.6/1407	169.04	550.04	0.077	1.045	-0.940	1.212	0.212
403-C	318.7/342	21.37	1688.75	-0.089	1.227	3.082	0.556	···
94-BLG-4	923.5/1418	10.66	884.13	0.028	-1.068	0.302	18.084	0.096
95-BLG-12	1413.4/1466	307.41	1264.07	0.106	0.421	-0.664	2.148	···
96-BLG-3	1934.8/1542	182.45	1545.66	0.043	-0.436	3.530	0.392	0.086
96-BLG-4	1286.0/1605	162.44	1815.29	0.378	7.454	-0.011	1.140	···
97-BLG-1	1237.7/1305	68.52	1884.02	0.234	0.931	2.583	0.418	0.527
97-BLG-24 (*solid* fit)	1230.6/943	30.77	1968.38	0.319	2.077	-3.967	4.236	0.050
97-BLG-24 (*dashed* fit)	1235.0/943	45.49	1970.82	0.0003	1.752	0.988	0.035	0.197
97-BLG-28	2734.9/1404	52.76	1991.87	0.225	0.707	1.437	0.210	0.760
98-BLG-12	440.5/507	239.92	2321.95	0.163	0.793	11.346	0.681	···
98-BLG-14 (*solid* fit)	809.4/714	107.65	2322.32	0.214	0.541	3.531	4.504	···
98-BLG-14 (*dashed* fit)	814.4/714	74.05	2323.56	0.396	1.213	4.429	0.0857	···
98-BLG-16	461.2/616	69.50	2316.57	0.140	0.758	3.699	1.476	0.163
98-BLG-42	890.4/395	49.19	2422.41	-0.028	1.260	3.328	3.065	0.109
97-BLG-d2	314.1/584	92.65	1971.07	-0.326	0.965	1.766	0.390	···
108-E	934.4/597	71.30	1927.66	0.747	0.637	-2.609	1.514	0.557
176-A	684.0/578	60.02	1230.06	0.108	0.965	0.204	1.514	0.068

Table 7.6: List of blending parameters for each of our candidate binary microlensing events. The parameter f represents the fraction of the object's flux which was lensed in each respective passband. Events LMC-1, 97-BLG-24, and 98-BLG-14 are each presented with 2 fits of similar significance, but different event parameters.

Event	f_{MACHO_R}	f_{MACHO_B}	f_{CTIO_R}	f_{CTIO_B}	f_{MSO30_R}	f_{MSO74_R}	f_{UTSO_R}	f_{UTSO_V}	f_{WISE_R}
98-SMC-1	0.47	0.56	0.79	1.07	···	···	···	···	···
LMC-1 (*solid* fit)	0.99	0.98	···	···	···	···	···	···	···
LMC-1 (*dashed* fit)	0.96	0.95	···	···	···	···	···	···	···
LMC-9	0.26	0.17	···	···	···	···	···	···	···
LMC-10	0.15	0.15	···	···	···	···	···	···	···
OGLE-7 / 119-A	0.41	0.37	···	···	···	···	···	···	···
403-C	0.48	0.50	···	···	···	···	···	···	···
94-BLG-4	1.06	1.04	···	···	···	···	···	···	···
95-BLG-12	0.22	0.26	0.26	···	···	···	0.27	0.26	0.31
96-BLG-3	0.23	0.25	0.35	···	···	···	0.33	···	···
96-BLG-4	1.03	1.03	1.05	···	···	···	1.01	···	···
97-BLG-1	0.93	0.97	0.87	···	···	···	···	···	···
97-BLG-24 (*solid* fit)	0.16	0.17	···	···	0.15	···	···	···	0.21
97-BLG-24 (*dashed* fit)	0.08	0.08	···	···	0.08	···	···	···	0.11
97-BLG-28	1.00	0.90	0.97	···	···	···	···	···	···
98-BLG-12	0.17	0.14	0.17	···	···	0.16	···	···	···
98-BLG-14 (*solid* fit)	0.51	0.52	0.52	···	···	0.48	···	···	···
98-BLG-14 (*dashed* fit)	1.08	1.10	1.07	···	···	0.99	···	···	···
98-BLG-16	0.04	0.03	1.10	···	···	1.07	···	···	0.04
98-BLG-42	0.46	0.45	···	···	0.73	0.74	···	···	···
97-BLG-d2	0.30	0.14	···	···	···	···	···	···	···
108-E	1.10	0.86	···	···	···	···	···	···	···
176-A	0.74	0.70	···	···	···	···	···	···	···

Table 7.7: Estimates of the reddening and extinction, as determined from RR Lyrae within $10'$, to each of the 4 sources where we have a well constrained binary lens fit and a reliable measure of t_*. The intrinsic source color $(V-R)_0$ and brightness V_0 are used to determine $T_{\rm eff}$ and $m_{\rm bol}$, and from these we find the source angular radius θ_*.

Event	# RR Lyrae	$< E(V-R) >$	$< A_V >$	$(V-R)_0$	V_0	$T_{\rm eff}$ (K)	$m_{\rm bol}$	θ_* (μas)
119-A	3	0.47 (9)	1.9 (3)	0.43 (9)	18.4 (3)	5350 (500)	18.2 (4)	1.06 (29)
96-BLG-3	6	0.42 (5)	1.7 (2)	0.31 (6)	19.1 (2)	6200 (500)	19.1 (2)	0.53 (11)
97-BLG-28	9	0.67 (4)	2.7 (2)	0.58 (6)	15.5 (2)	4500 (200)	15.0 (2)	6.58 (90)
98-BLG-42	10	0.53 (5)	2.1 (2)	0.33 (7)	18.1 (2)	6050 (500)	18.1 (2)	0.89 (20)

Table 7.8: The lens proper motion measurements, $\mu = \theta_*/t_*$, have been used in the likelihood analysis detailed in Chapter 7.3.2 to produce the most likely lens distance and mass estimates given here. The errors quoted are 1σ. We note that the errors in M_1 and M_2 are completely correlated.

Event	μ (mas/yr)	D_l (kpc)	$M_{\rm tot}/M_\odot$	$M_1/M_\odot$	$M_2/M_\odot$
119-A	1.84 (58)	$7.0^{+0.8}_{-0.9}$	$0.89^{+1.25}_{-0.42}$	$0.49^{+0.69}_{-0.23}$	$0.40^{+0.57}_{-0.19}$
96-BLG-3	2.26 (47)	$7.1^{+0.8}_{-0.9}$	$1.61^{+2.25}_{-0.76}$	$0.45^{+0.63}_{-0.21}$	$1.15^{+1.62}_{-0.55}$
97-BLG-28	3.16 (44)	$7.0^{+0.8}_{-1.0}$	$0.26^{+0.36}_{-0.13}$	$0.05^{+0.06}_{-0.02}$	$0.22^{+0.30}_{-0.11}$
98-BLG-42	2.98 (78)	$7.0^{+0.8}_{-1.0}$	$0.19^{+0.26}_{-0.09}$	$0.14^{+0.20}_{-0.07}$	$0.05^{+0.06}_{-0.02}$

Chapter 8

EXOTIC MICROLENSING: BINARY SOURCE (XALLARAP) EVENTS

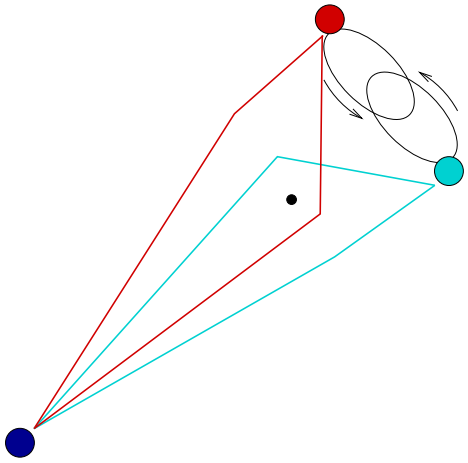

8.1 Xallarap Theory

The study of the lensing of binary sources was first investigated by Griest & Hu (1992). If the binary system is in motion, this effect may be regarded as the inverse of the parallax effect, and may be referred to as the "xallarap" effect, where the orbital motion occurs at the lensed source. Detection of the xallarap modulation in a microlensing lightcurve allows us to fit the semi-major axis of the orbiting system in units of the lens' projected Einstein ring radius. An estimate of the physical semi-major axis of the system then allows a $\widehat{v}$ constraint on the 3 degenerate lens parameters. Han & Gould (1997) describe the use of this effect in discriminating between Galactic halo and LMC lenses.

A useful detection of this type of modulation in a microlensing lightcurve is possible within a certain range of event parameters. First, the binary source should have an orbital period similar to or shorter than the event timescale, such that the sources accelerate appreciably during the time they are microlensed and an orbital period may be determined. Second, the orbital separation of the sources should not be much smaller than the lens'

Einstein ring radius projected to the source, otherwise the system appears to the lens as essentially a single object. This biases the detection of the xallarap effect towards events where the lens is close to the sources, analogous to the parallax effect, which is most easily detected when the lens is relatively close to the Sun-Earth system.

The formalism we use to model a xallarap lightcurve was developed by Dominik (1998b), and includes the following parameters:

- $\tilde{t}_b$, the time of closest approach of the lens to the source system center of mass,
- $t_{\rm E}$, the lens' Einstein radius crossing time,
- $\tilde{b}$, the lens' impact parameter with respect to the source system center of mass, in units of the lens' Einstein radius projected into the source plane,
- $\tilde{\alpha}$, the angle between the lens trajectory and the x source axis,
- $\tilde{f}_1$, the total binary flux fraction of source 1,
- $\tilde{m}_1$, the total binary mass fraction of source 1,
- $\tilde{\rho}$, the orbital semi–major axis in units of the lens' projected Einstein radius,
- $\tilde{\beta}$, the inclination around the x source axis,
- $\tilde{\gamma}$, the inclination around the y source axis,
- $\tilde{T}$, the orbital period in days,
- $\tilde{\xi}_0$, the orbital phase at time $\tilde{t}_b$.

Xallarap fit parameter $\tilde{\rho}$ relates the scale of the lens's projected Einstein radius ($\widehat{R}_{\rm E} \equiv R_{\rm E}/x$) to the binary's physical semi–major axis a. This effectively leads to a measurement of the lens proper motion

$$\mu \equiv \frac{v_\perp}{D_l} = \frac{\widehat{R}_{\rm E}}{t_{\rm E} D_s} = \frac{a}{\tilde{\rho}\ t_{\rm E} D_s} \tag{8.1}$$

8.2 Binary Source Detections

8.2.1 96-LMC-2 (11.8871.2108)

Discovery and Observations

Microlensing Alert MACHO 96–LMC–2 was detected and announced on Oct 3, 1996, with the MACHO object at an observed magnification of $A \sim 1.8$. The source for this event is located at α = 05:34:44.437, $\delta = -70$:25:07.37 (J2000), in the south–east extreme of the LMC bar. This object was constant at $V = 19.42 \pm 0.15, (V - R) = -0.03 \pm 0.10$ in ~ 700 observations over the 4.2 years preceding this brightening, where these magnitude errors are dominated by uncertainty in the calibration of the MACHO database (Alcock et al. 1999c). The MACHO ID number for this star is 11.8871.2108. A $25'' \times 25''$ postage stamp, taken from the MACHO R–band template observation of this field and centered around the lensed object, is presented in Figure 8.1.

Nightly observations were requested on the CTIO 0.9m telescope as part of the Global Microlensing Alert Network (GMAN) microlensing follow–up program. Data were obtained in both B and Kron–Cousins R for the duration of this event. Final sets of baseline observations were made $\sim$ 800 days ($\sim$ 8 times the duration of the event) after the peak. An additional set of observations was made at the UTSO 0.6m telescope. However, closure of the telescope in 1997 prevented baseline measurements from this site.

After the event, cycle–7 HST images were taken with the target star centered in the Planetary Camera of HST instrument WFPC2. These integrations included four 500 second exposures in each of three bands V, R, and I. The images were combined using the IRAF routine imcombine, along with a sigma clipping algorithm to remove cosmic rays. Aperture photometry was performed on all stars using the DaoPhot package (Stetson 1994), with centroids derived from a PSF fit. We use a $0.25''$ aperture, and correct to a $0.5''$ aperture using the brightest stars in the field. We correct for the charge transfer effect and calibrate the magnitudes using the Holtzman et al. (1995) calibrations. A portion of the combined R–

Table 8.1: Standard point source, point lens microlensing fit parameters for event 96–LMC–2. For each passband, f represents the fraction of the objects baseline brightness which was lensed. Reported uncertainties in the final significant digit(s) are the maximum extent of the surface in parameter space which has a χ^2 greater than the best–fit value by 1.

[a] (JD − 2448623.50).

Fit Parameter	
χ^2 / d.o.f.	1872.31 / 2060
t_0 [a]	1767.51 (7)
$\widehat{t}$	98.7 (40)
$u_{\rm min}$	0.301 (17)
f_{MACHO_R}	1.00 (13)
f_{MACHO_B}	1.00 (13)
f_{CTIO_R}	0.99 (12)
f_{CTIO_B}	1.02 (13)
f_{UTSO_R}	0.76 (33)

band image of the WFPC2–imaged field around event 96–LMC–2 is presented in Figure 8.1.

The MACHO/GMAN data for 96–LMC–2 are presented in Figure 8.2. The MACHO data were reduced with MACHO's standard photometry package SoDOPHOT, with minimum errors of 0.014 added in quadrature. The CTIO and UTSO data were simultaneously reduced with the ALLFRAME package (Stetson 1994), and the error estimates are multiplied by a factor of 1.5 to account for global systematics (such as flat–fielding errors and the swapping of CCD detectors) in the time series of data.

Standard Microlensing Fits

Standard microlensing fit parameters, including the effects of unlensed contributions to the source baseline flux, are presented in Table 8.1. We also include 5 additional blending parameters, one f for each passband of observations. In each case, f represents the fraction of the object's baseline flux which was lensed. The $\chi^2/d.o.f$ for this fit is 0.91, formally an acceptable fit. However, there are periodic residuals around this smooth fit, especially in the CTIO data. We have plotted these residuals for the CTIO R and B passbands in Figure 8.3 and Figure 8.4, respectively.

Table 8.2: Xallarap microlensing fit parameters for event 96–LMC–2. The parameters are as defined in Chapter 8.2.1. For each passband, f represents the fraction of the objects baseline brightness which was lensed. Reported uncertainties in the final significant digit(s) are the maximum extent of the surface in parameter space which has a χ^2 greater than the best–fit value by 1.

[a] (JD – 2448623.50).

[b] For fit X1, we are only able to constrain the product of $\tilde{m}_1$ and $\tilde{\rho}$. We assume 0.1 $M_\odot$ and 1.4 $M_\odot$ dark companions to the 2.1 $M_\odot$ primary to determine these parameters for fits X1a and X1b, respectively. The sources for fit X2 are estimated to be 1.9 $M_\odot$. See Chapter 8.2.1 for further details.

Fit Parameter	Fit X1	Fit X1a	Fit X1b	Fit X2
χ^2 / d.o.f.	1799.9 / 2054	···	···	1800.9 / 2053
$\tilde{t}_b$ [a]	1767.600 (79)	···	···	1767.80 (14)
$2 * t_{\rm E}$	101.8 (42)	···	···	108.8 (53)
$\tilde{b}$	0.287 (16)	···	···	0.246 (19)
$\tilde{\alpha}$	-2.15 (37)	···	···	0.236 (77)
$\tilde{f}_1$	0.000 (29)	···	···	0.52 (19)
$\tilde{m}_1$	0.1 [b]	0.045	0.40	0.53 (19)
$\tilde{\rho}$	0.095 (15) [b]	0.208 (33)	0.0237 (39)	0.188 (26)
$\tilde{\beta}$	1.00 (30)	···	···	1.43 (14)
$\tilde{T}$	9.22 (21)	···	···	21.22 (53)
$\tilde{\xi}_0$	-0.23 (37)	···	···	0.40 (12)
f_{MACHO_R}	0.94 (9)	···	···	0.80 (8)
f_{MACHO_B}	0.95 (9)	···	···	0.80 (8)
f_{CTIO_R}	0.93 (9)	···	···	0.79 (8)
f_{CTIO_B}	0.96 (9)	···	···	0.81 (8)
f_{UTSO_R}	0.58 (18)	···	···	0.86 (46)

Binary Source (Xallarap) Microlensing Fits

Fitting this event to an orbiting binary source does provide significant improvement over the standard blended fit. We follow the formalism of Dominik (1998b) for the binary source solution, including a blending parameter f for each passband of observations. Finally, we explicitly assume zero eccentricity circular orbits for the sources, meaning inclination angle $\tilde{\gamma}$ from Dominik (1998b) is redundant, and is set to zero in these fits.

We find 2 minima in this parameter space, separated by $\Delta\chi^2 \sim 1$. Our most significant model is labeled X1, and our second most significant is X2. These fits are a further $\Delta\chi^2 = 72$ from the standard microlensing fit, which we are extremely unlikely to arrive at by chance, even given our additional 8 constraints. Xallarap fit parameters are presented in Table 8.2. Fit X1 indicates a primary which contributes $\sim 100\%$ of the light, a dark secondary, and an orbital period of $T = 9.22 \pm 0.21$ days. The second fit X2 yields a binary source of similar mass and brightness stars, and $T = 21.2 \pm 0.54$ days. These fits and the residuals of these

fits around the standard microlensing fit are plotted along with the data for the CTIO R and B passbands in Figure 8.3 and Figure 8.4, respectively.

We have investigated whether or not the sources contribute significantly different flux fractions in the red and blue, by allowing different $\tilde{f}_1$ fractions for the red and blue passbands. Providing this additional constraint leads to a $\Delta\chi^2 = -0.24(-0.50)$ for fit X1 (X2), indicating this improvement is formally significant at only the 37%(52%) confidence level. For the fit X1 class, the secondary source is dark in both red and blue, to within the reported accuracy of our photometry. For the X2 class, the best fit $\tilde{f}_{1r}/\tilde{f}_{1b}$ is 1.02. In the following we assume $\tilde{f}_{1r} = \tilde{f}_{1b} = \tilde{f}_1$.

The binary source fits for this event are plotted with the data in Figure 8.2. Due to the different blend fractions for these fits, the observed object magnification (as opposed to the lensed source magnification) is plotted as a function of time. It is apparent that without the GMAN follow-up photometry, there would be little support for the binary source interpretation. In fact, 80% of the $\Delta\chi^2$ between the standard fit and fit X1 is contributed by the GMAN data.

Colors of the Lensed Objects

The source object's brightness is well constrained with our V, R, and I HST images. We use the image subtraction method of Tomaney & Crotts (1996b) to locate the lensed source in the MACHO images to within 0.1" (2 PC pixels). Image registration allows us to uniquely determine the centroid of the lensed source in the HST image. This lensed flux aligns with an object with $V = 19.46 \pm 0.02, (V - R) = 0.00 \pm 0.03, (V - I) = 0.12 \pm 0.03$, where the errors represent the quadratic sum of Poisson noise and an adopted error of 2% for our HST magnitudes. Within $1''$ of this source there are at least 2 neighbors, which contribute about 20% of the flux within this region.

Color-magnitude diagrams (CMDs) incorporating ~1800 objects from the Planetary Camera chip of the WFPC2, and a region surrounding the lensed object in the MACHO focal plane, are displayed in Figure 8.5. The lensed object identified in each respective CMD is indicated with the filled circle. We have corrected the CMDs for reddening, using a characteristic LMC reddening in the bar of $E(B - V) = 0.07 \pm 0.01$ (e.g., Olsen 1999

and Holtzman et al. 1999) and the Landolt extinction coefficients of Schlegel, Finkbeiner, & Davis (1998). The intrinsic magnitude and colors of the source star are $V = 19.23 \pm 0.04, (V-R) = -0.04 \pm 0.03, (V-I) = 0.02 \pm 0.03$.

The CMDs in Figure 8.5 indicate the source lies very close to the main sequence in this region of the LMC. There appears to be a slight excess of flux in the I passband, as can be seen in the $(V-R), (R-I)$ and $(V-I), V$ diagrams. There is no apparent excess in the $(V-R), V$ diagram, suggesting this is an infrared excess. Given the direction of the reddening vector in the V, R, and I passbands, this marginal excess cannot be a feature of reddening. This could possibly be due to the lens itself, or in the context of model X1, a signature of the dark companion to the primary. We also indicate in Figure 8.5 the region 0.75 mag *below* the lensed object with an open circle, which would be the location of a single component of this object if it were a blend of equal brightness stars, as model X2 suggests.

Properties of the Binary System

We next attempt to estimate the mass of an object with the colors determined above. Since this object appears on the upper main sequence, it is likely to have higher metallicity than the majority of the field stars in this location. Here we consider Girardi et al. (2000) isochrones for $z = 0.008$. For model class X1, the best fits to the colors and apparent magnitude of the star come from objects with $\log(\text{age[yr]}) = 8.7 - 8.8$, $M = 2.1 \pm 0.1 M_\odot$. In the case of model X2, we require a single object 0.75 mag dimmer than our observed object. Using the same isochrones, we find a wider range in acceptable star age, $\log(\text{age[yr]}) = 8.5 - 8.8$, and a range in mass of $M = 1.9 \pm 0.1 M_\odot$.

The original fits to model X1 yielded $\tilde{m}_1 \sim \tilde{f}_1 \sim 0$. In the case of $\tilde{f}_1 = 0$, we are not able to fit model parameters $\tilde{m}_1$ and $\tilde{\rho}$ individually, but can only constrain their product $\tilde{m}_1 * \tilde{\rho}$. Therefore the fitting process was re–run, setting $\tilde{m}_1 \equiv 0.1$ ($\tilde{m}_1 = 0$ or $\tilde{m}_1 = 1$ imply non–existent secondaries) and fitting for $\tilde{\rho}$. Therefore fit X1 has 1 more degree of freedom than X2. The product $\tilde{m}_1 * \tilde{\rho}$ was similar to that found in the original model. To explore the range of companions to the $2.1 M_\odot$ primary, we consider a "light" dwarf secondary of $0.1 M_\odot$, henceforth fit X1a, and a "heavy" white dwarf or neutron star secondary of $1.4 M_\odot$, fit X1b. Making these assumptions fixes $\tilde{m}_1$ and allows us to extract an associated $\tilde{\rho}$. The

Table 8.3: Characteristics of the lensing object, determined from our xallarap fit parameters and estimates of the individual masses of the lensed binary system. $\widehat{R}_{\rm E}$ represents the lens' Einstein ring radius projected to the source system, and $\widehat{v}$ represents the lens velocity projected to the source system. Lens properties M_l and D_l are estimated using a maximum likelihood technique described in Chapter 8.2.1.

Parameter	Fit X1a	Fit X1b	Fit X2
$\widehat{R}_{\rm E}$ (AU)	0.535 (88)	5.50 (91)	1.24 (18)
μ ($\mathrm{km\,s^{-1}\,kpc^{-1}}$)	0.364 (62)	3.73 (64)	0.79 (12)
$\widehat{v}$ ($\mathrm{km\,s^{-1}}$)	18.3 (31)	188 (32)	39.6 (61)
M_l ($\mathrm{M_\odot}$)	$5.7^{+6.0}_{-3.6} \times 10^{-2}$	$2.4^{+3.8}_{-1.8} \times 10^{-1}$	$2.8^{+3.3}_{-2.0} \times 10^{-1}$
D_l (kpc)	$49.6^{+0.3}_{-1.0}$	$38.5^{+6.5}_{-15.7}$	$49.6^{+0.4}_{-1.6}$

resulting parameters $\tilde{m}_1$ and $\tilde{\rho}$ for fits X1a and X1b are also listed in Table 8.2.

Knowing the total mass of the system and orbital period allows us to solve for the physical Keplerian parameters of the binary source. We find semi-major axes of 0.11, 0.13, and 0.23 AU, and circular velocities of 132, 154, and 120 $\mathrm{km\,s^{-1}}$, for fits X1a, X1b, and X2, respectively.

Constraints on the Lensing Object

The derivation above allows us to express $\widehat{R}_{\rm E}$ in AU, using Equation 8.1, and these results are presented in Table 8.3. To find the velocity of the lens projected to the LMC ($\widehat{v}$), we assume a LMC distance modulus of 18.5, or a distance of 50 kpc. We further assume the source is 1 scale height behind the midplane of the LMC disk (see below), or an additional 260 pc along the line of sight, leading to an assumed source distance of 50.3 kpc. The values of μ and $\widehat{v}$ for each of our fits are presented in Table 8.3. The error bars on these values do not incorporate uncertainty in the distance to the LMC. The $\widehat{v}$ measurement allows a one–parameter family of solutions relating the lens mass and distance from Equation 3.13.

A likelihood analysis is performed using the Galactic and LMC models specified in Chapter 3.4.1, and the likelihood function Equation 3.16.

We find in each analysis that a lens residing in the LMC is preferred to a Galactic halo lens, although only marginally so in fit X1b. In particular, for fit X1a the likelihood of measuring our value of $\widehat{v}_{X1a} = 18.3\,\mathrm{km\,s^{-1}}$ is dominated by the LMC disk model. For this fit, a LMC disk lens is 7 times more likely than a LMC halo lens, and > 950 times more

likely than a Galactic halo lens. We also point out that secondaries less massive than $0.1\mathrm{M}_{\odot}$ become increasingly unlikely, as decreasing the mass of the secondary leads to a lower lens $\widehat{v}$. In this model, $\widehat{v}_{X1a}$ already is drawn from the low velocity tail of the LMC disk probability distribution. As an example, a secondary of approximately Jupiter mass would imply a lens velocity projected to the LMC of $\sim 0.2\,\mathrm{km\,s^{-1}}$, clearly in contradiction to the LMC disk likelihood profile in Figure 8.6. For fit X1b, we find $\widehat{v}_{X1b} = 188\,\mathrm{km\,s^{-1}}$, which is most likely to come from our model of the LMC halo, although it is only 4 times as likely as a Galactic halo lens. In this case, a LMC disk lens is ruled out at high confidence. We note that such a LMC halo population has yet to be detected directly. Given the broad range in secondary mass, and hence the binary's semi-major axis, explored between fits X1a and X1b, we conclude this model favors a lens associated with the LMC. With our model X2, we find $\widehat{v}_{X2} = 39.6 \pm 6.1\,\mathrm{km\,s^{-1}}$, whose likelihood is strongly dominated by the LMC disk. Figure 8.6 shows the probability distributions of $\widehat{v}$ for each component of our Galactic-LMC model. Our measured $\widehat{v}$ for each fit is also displayed with $1-\sigma$ errors. Only in model X1b does a Galactic halo lens appear reasonable.

Our likelihood analysis also yields a probable distance to the lens, and from Equation 3.13, a mass. These parameters are listed in Table 8.3 for each model. Model X1a allows the lightest lens mass, $0.057^{+0.060}_{-0.036}\mathrm{M}_{\odot}$, while models X1b and X2 imply heavier lenses, $0.24^{+0.38}_{-0.18}$ and $0.28^{+0.33}_{-0.20}\mathrm{M}_{\odot}$, respectively. We have referenced the low mass isochrones of Girardi et al. (2000) to determine the expected brightness of a main sequence M-dwarf lens. We use the isochrones for $z = 0.004$, and an assumed lens age of 4 Gyr. We find for objects of $M = 0.3\mathrm{M}_{\odot}$, and also for the upper $1-\sigma$ confidence limit $M = 0.6\mathrm{M}_{\odot}$, absolute V magnitudes of 9.9 and 7.6, respectively. At the distances implied by the likelihood analysis, even the most luminous configuration provides negligible flux from the lens compared to the apparent brightness of the source object. A $0.6\mathrm{M}_{\odot}$ lens at 45 kpc leads to an apparent lens magnitude of $V = 25.9$, or 0.2% of the source brightness. The apparent I–band brightness of this lens is $I = 24.7$, or less than 0.1% of the source brightness in this band. The secondary source is therefore a more likely origin for the possible I–band excess seen in Figure 8.5. The small lens proper motion of $\lesssim 1$ milli-arcsecond year^{-1} implies it will take the next generation of space telescopes to be able to resolve and image the lensing object.

We note that the lens' location (and therefore its mass) can be more accurately determined with direct spectral observations of the source. In particular, the superposition of primary and secondary spectra can provide a discriminant between models X1 and X2, and lead to a better mass estimate for each object. Similarly, the orbital period can be precisely determined with radial velocity measurements. These observations will constrain the Keplerian parameters more directly than our (necessarily) more complicated microlensing analysis has allowed.

Alternate Models

In order to gauge the robustness of these conclusions, we have considered several alternate models, including placing the sources at larger distances behind the LMC, and increasing the amount of reddening to the sources.

Zhao (2000) predicts a strong excess in lensed source reddening for models where the LMC is strongly self–lensing. In these models, the source stars must preferentially lie at the back side of the LMC, and thus will have high interstellar reddenings. On the other hand, if the lenses are Galactic dark matter, the reddenings of the source stars will be statistically the same as surrounding stars along the same lines of sight. Alcock et al. (2000e) use HST colors of 8 microlensed source stars to rule out, at the 85% confidence level, a model where all sources are located $\sim$7 kpc behind the LMC disk. However, it is possible that roughly half of the sources may be in the background. Therefore, we consider a model where the lensed sources are $7 - 9\,\mathrm{kpc}$ behind the LMC. This leads to an increase in source mass of $\sim 0.1\mathrm{M}_{\odot}$, and results in projected velocities of $\widehat{v}_{X1a} = 18\,\mathrm{km\,s^{-1}}, \widehat{v}_{X1b} = 184\,\mathrm{km\,s^{-1}}$, and $\widehat{v}_{X2} = 40\,\mathrm{km\,s^{-1}}$. The $\widehat{v}$ likelihood profiles for this source location differ significantly from those seen in Figure 8.6. Most notably, the LMC disk and LMC halo profiles allow a similar range in $\widehat{v}$, with the LMC halo generally preferred over the LMC disk, and median $\widehat{v} \sim 100\,\mathrm{km\,s^{-1}}$. For the lowest projected velocity (model X1a), the lens is consistent with neither the LMC nor the Galactic likelihood profiles. The LMC halo is the most likely location of the lens in all models, followed by the LMC disk in model X2, and by the Galactic halo in model X1b.

It is also possible the reddening to the sources is larger than our adopted value of

$E(B-V) = 0.07$. For example, the foreground reddening maps of Schwering & Israel (1991) indicate $E(B-V) = 0.12$, while Zaritsky (1999) finds typical LMC source star reddenings of $E(B-V) \sim 0.10$. If we assume a higher reddening to the source object of $E(B-V) = 0.12$, its intrinsic brightness and colors are $V = 19.06, (V-R) = -0.08, (V-I) = -0.05$. For model X1, the primary source would weigh $\sim 2.3 M_\odot$, and for model X2 both sources would weigh $\sim 2.1 M_\odot$. Here we find $\hat{v}_{X1a} = 17\,\mathrm{km\,s^{-1}}, \hat{v}_{X1b} = 181\,\mathrm{km\,s^{-1}}$, and $\hat{v}_{X2} = 41\,\mathrm{km\,s^{-1}}$, whose relative likelihoods can be evaluated using Figure 8.6. This change has more important implications for the source mass than for the projected velocities, and the likelihood results are similar to those from the standard analysis.

Conclusions

We have measured and characterized a periodic modulation in the lightcurve of microlensing event MACHO 96-LMC-2. We model this event using a single object microlensing a rotating binary source, which provides considerable improvement over a single source model. Possible alternate explanations to this modulation include a single source lensed by a rapidly rotating binary lens, or some variant of stellar pulsation. We do not consider such models. MACHO 96-LMC-2 is not the first time that binary source effects have been detected in a microlensing event. EROS-II event GSA2 (Derue et al. 1999) exhibits a similar modulation around the standard microlensing fit. Derue et al. (1999) also find a binary source model degeneracy similar to that between our models X1 (dominant source) and X2 (equal brightness sources).

We are able to constrain the projected Einstein radius of the lens ($\hat{R}_\mathrm{E}$) in the most significant of our fits to be between 0.54 and 5.5 AU, and its velocity projected to the LMC $\hat{v}$ to be between 18.3 and 188 $\mathrm{km\,s^{-1}}$. The weakness of this constraint (an order of magnitude!) is due to our lack of knowledge of the mass of the secondary component of the lensed binary system. In this model we have no means to constrain the secondary's orbit due to its negligible contribution to the system's brightness. We chose example secondaries separated by an order of magnitude in mass ($0.1 M_\odot$ to $1.4 M_\odot$), leading to order of magnitude constraints on $\hat{R}_\mathrm{E}$ and $\hat{v}$. However, in both cases, a LMC lens is preferred to a Galactic halo lens. For the larger velocity lens (model X1b) the object should come from an as yet undetected LMC halo population, and a Galactic halo lens is not strongly ruled out. The

lack of direct evidence for an LMC halo population indicates model X1b is best able to constrain the location of the lens to be out of the LMC disk. Our second most significant model leads to $\widehat{R}_{\rm E} = 1.24 \pm 0.18$ AU, and $\widehat{v} = 39.6 \pm 6.1\,{\rm km\,s^{-1}}$. This model also prefers a lens in the LMC, with the likelihood heavily weighted towards the LMC disk. All 3 of these models suggest a sub-solar mass lens, consistent with an M-dwarf star. Our derived values of $\widehat{R}_{\rm E}$, $\widehat{v}$, M_l, and D_l are in good agreement with the characteristic properties of LMC lenses presented in Table 1 of Han & Gould (1997).

Alternate models for the source system, including one where the sources lie $7 - 9\,{\rm kpc}$ behind the LMC, and one where they are reddened by $E(B-V) = 0.12$, were also considered. By placing the sources far behind the LMC, we are unable to discriminate between the LMC disk and LMC halo population of lenses, and can only state that the lens is most likely associated with the LMC system. However, the qualitative conclusions about the location of the lens are found not to be overly sensitive to the amount of reddening to the sources.

The identification of MACHO 96-LMC-2 with a LMC lens population is consistent with the expected LMC self-lensing signal. This single event microlensing optical depth is $\tau_A = 1.1 \times 10^{-8}, \tau_B = 8.5 \times 10^{-9}$ for criteria "A" and "B" in Alcock et al. (2000a), respectively. This is to be contrasted with an expected self-lensing optical depth of $\tau = 1.6 \times 10^{-8}$ for the LMC disk and $\tau = 1.7 \times 10^{-8}$ for the MACHO component of our model LMC halo (Alcock et al. 2000a). It is also possible that MACHO LMC-9 is due to LMC self-lensing (Alcock et al. 2000d), although we caution this interpretation is based on a caustic crossing resolved with only 2 observations, and other interpretations are possible. LMC-9 is excluded from event set A in Alcock et al. (2000a), and has an optical depth of $\tau_B = 9.3 \times 10^{-9}$. The expected LMC self-lensing signal due to these 2 events is thus likely to lie within the range $1.1 \times 10^{-8} < \tau < 1.8 \times 10^{-8}$. This is approximately half of the expected LMC self-lensing rate. Thus the combined optical depths alone do not not implicate the LMC as the host for the majority of the microlenses, as originally suggested by Sahu (1994).

Kerins & Evans (1999) take the ensemble of events LMC-9 and 98-SMC-1 and argue that the existence of even a few LMC self-lensing events suggests an LMC halo interpretation of all LMC microlensing. In this context, the appearance of another apparent LMC self-lensing event strengthens the case for significant LMC self-lensing. However, because of

the importance of our result for the interpretation of LMC microlensing, we emphasize the bias a study such as this has against revealing a lens residing in our Galactic halo. In particular, a lensed LMC binary source is preferentially more likely to show xallarap modulations if the lens is also in the LMC. To identify Galactic halo lenses, a spectroscopic study of **all** MC microlensing sources should be undertaken to assess whether or not the lensed object is, in fact, a binary system. In the case of a positive detection, we may set limits on xallarap modulation in the microlensing lightcurve, and from this a lower limit on the proper motion of the lensing object. As can be seen from Figure 8.6, Galactic halo lenses start to dominate the likelihood near $\widehat{v} = 230\,\mathrm{km\,s^{-1}}$. A lower limit on $\widehat{v}$ near this value would be highly suggestive of a true halo lens, and thus detection of at least one component of the Galactic dark matter.

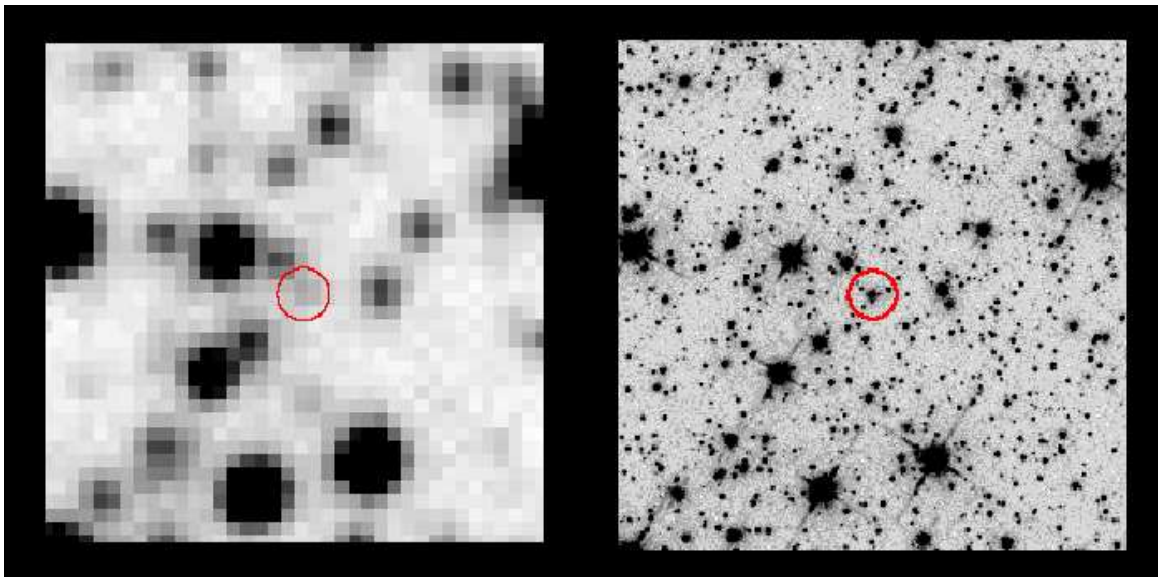

Figure 8.1: Each image represents a $25'' \times 25''$ field centered on the 96–LMC–2 lensed source. The image on the left is from the 300 sec MACHO R–band template observation, and on the right is a 4 x 500 sec combined HST R–band image. The lensed source is in the center of each image, and is indicated by the circle. North is up and east is to the left.

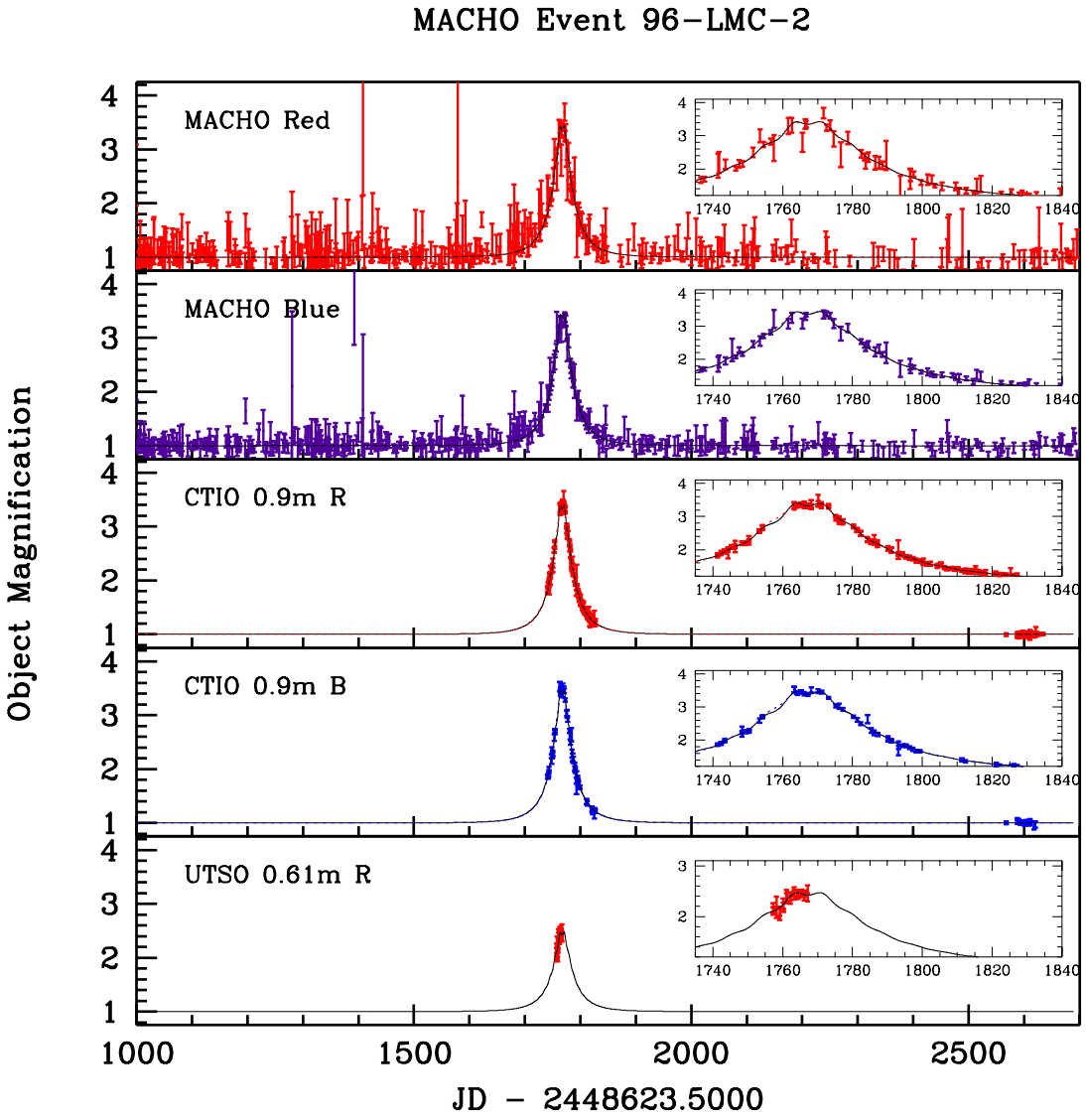

Figure 8.2: The light curve of event 96–LMC–2. The panels show the observed brightening as a function of time, with passbands and sites as indicated. The *solid* line represents the best "xallarap" fit X1, and the *dotted* line fit X2. Insets are provided to better view the region with the strongest binary source signal. The UTSO data are only plotted with the X1 fit curve.

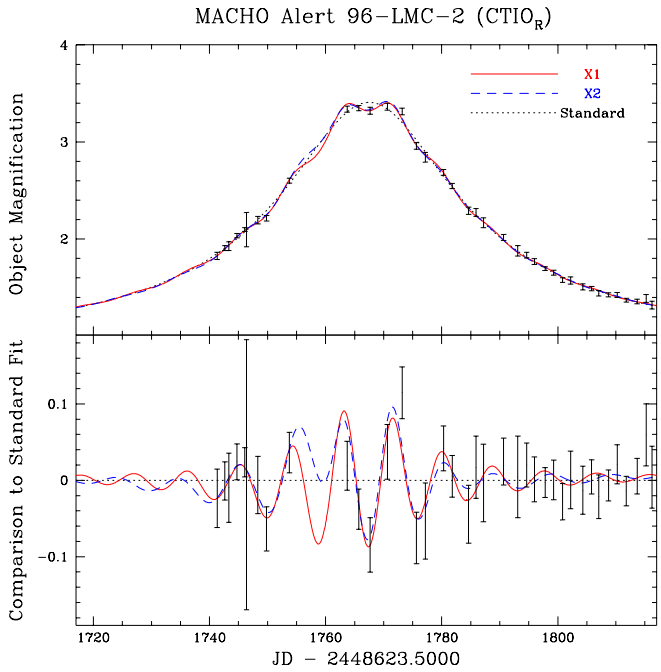

Figure 8.3: The CTIO R–passband light curve of 96–LMC–2. The top panel displays the 3 xallarap fits, along with the CTIO R–band data in 1–day bins. The *dotted* line is the best standard fit, and the *solid* and *dashed* lines the most and second most significant xallarap fits X1 and X2, respectively. The bottom panel indicates the residuals of each fit and the data around the standard fit.

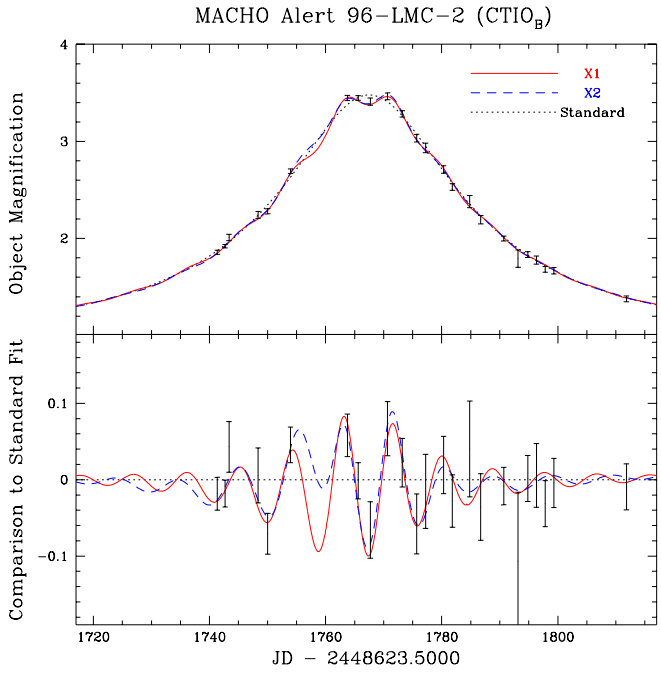

Figure 8.4: Same as Figure 8.3, except with the CTIO B–band light curve.

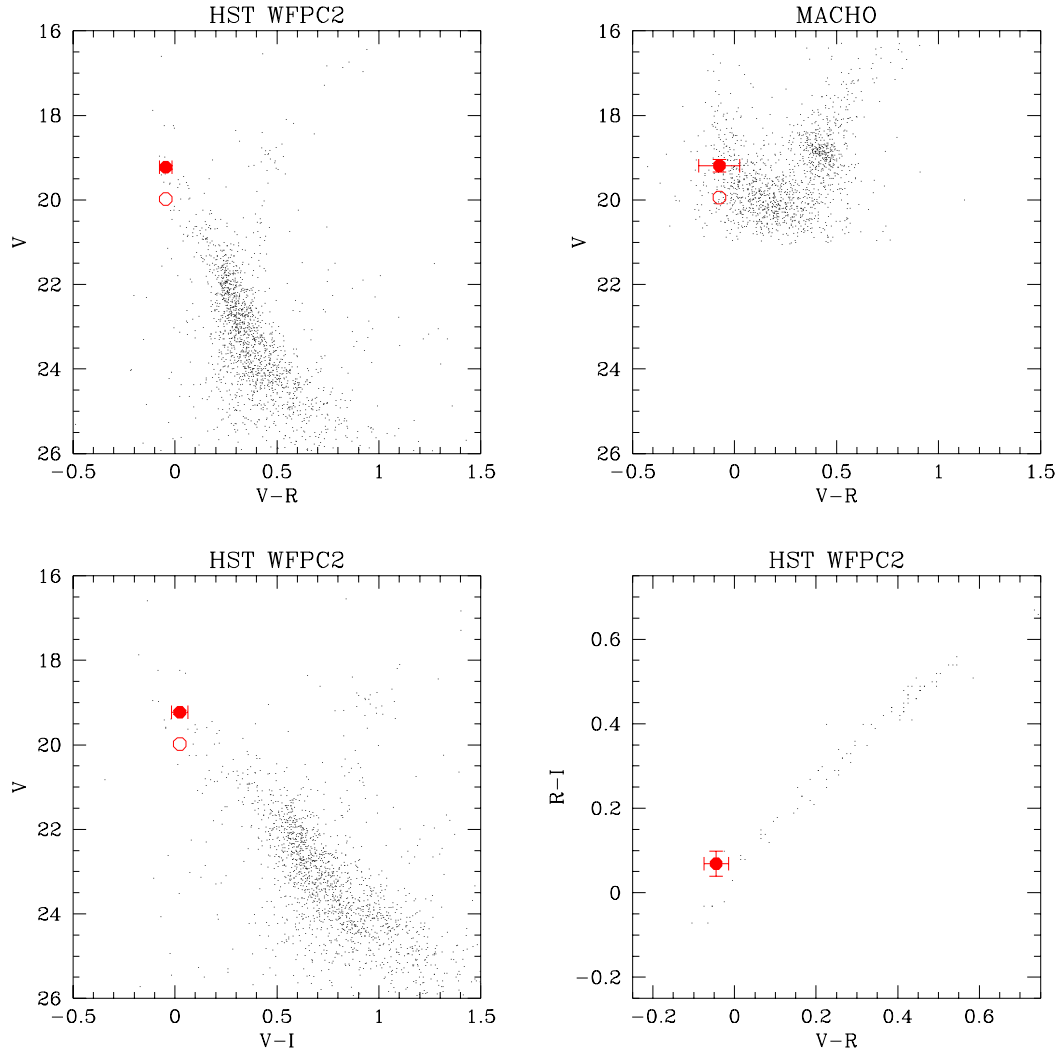

Figure 8.5: Color–magnitude and color–color diagrams of the field surrounding event 96–LMC–2. The lensed object is indicated with a filled circle. The HST CMDs are constructed from cycle–7 observations with the target star centered on the Planetary Camera chip of the WFPC2. The MACHO CMD is taken from a subsection of the template observation of this field. This object resides near the upper main sequence of the LMC field. We indicate with an open circle the region of the CMD where 2 equal brightness stars must be drawn from to create the observed object.

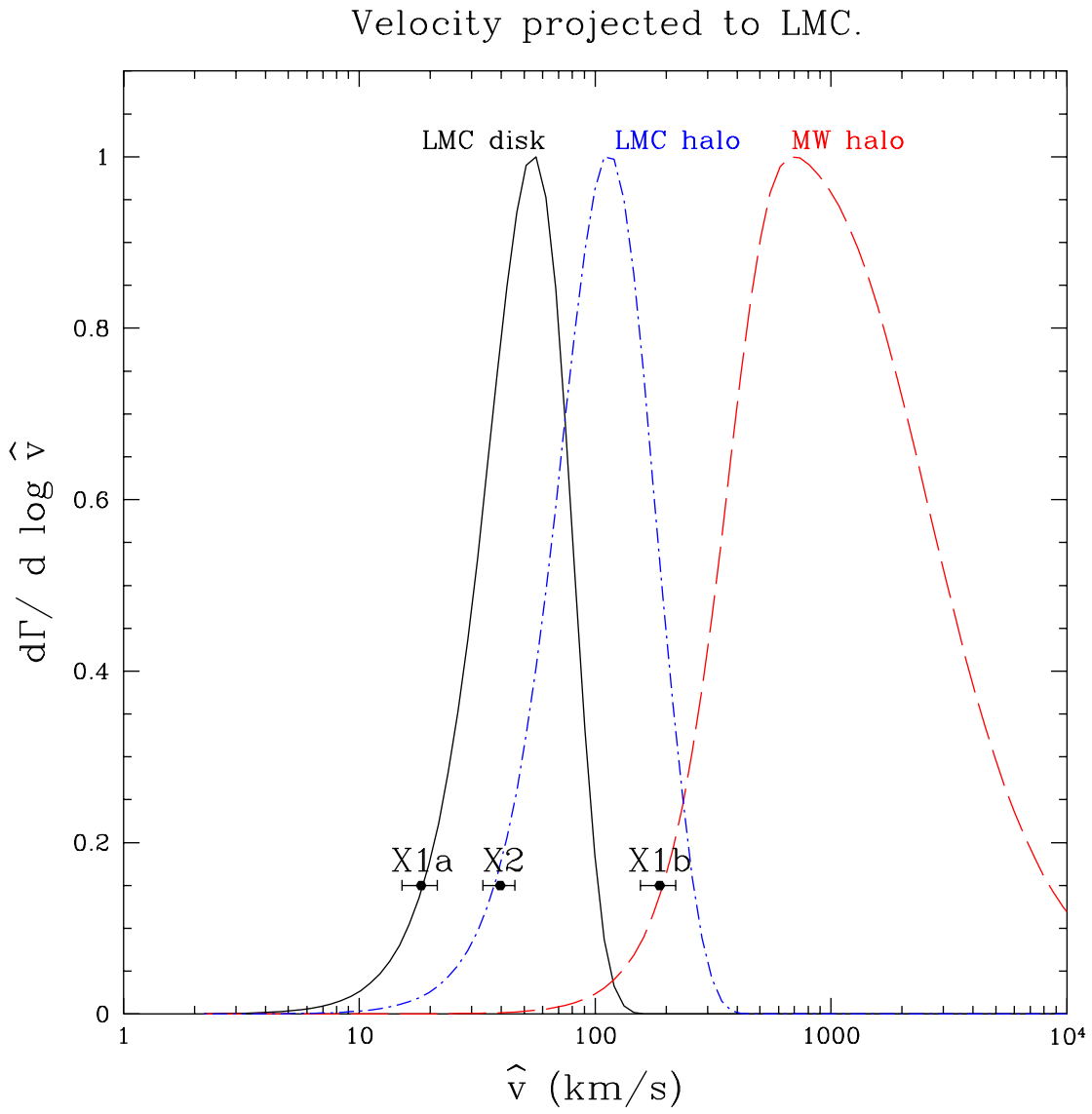

Figure 8.6: 96–LMC–2 probability distributions of $\widehat{v}$ for each component of our Galactic–LMC model, described in Chapter 8.2.1. The measured $\widehat{v}$ for models X1a, X1b, and X2 is also indicated, with respective $1-\sigma$ errors. Note in each case, a LMC lens is preferred over a Galactic halo lens, although this preference is weakest for model X1b.

Chapter 9

THE FINAL CHAPTER

The success of the GMAN project can be measured in the statement that it has resolved all major forms of "exotic" microlensing, in many cases for the first time. These deviations include:

- **Parallax** effects, where the orbital motion of the Earth around the Sun provides significantly different perspectives on a long lensing event. We have likely detected a new population of lenses in massive dark objects heavier than the Sun – a population of stellar remnants including isolated black holes.

- **Extended source** effects, including predicting and characterizing the transit of a lens across the face of a background source star. The lens in this case acted as a sensitive probe of the source's spectral features, leading to the finest known resolution of spectral features in any star other than our own Sun. In several cases, we have also determined broad–band limb–darkening parameters for lensed source stars.

- **Binary lens** events, whose lightcurves can exhibit singular excursions from a standard microlensing brightening profile. Encoded in the temporal width of certain classes of binary lens features is the proper motion of the lensing system. Our ensemble of binary lens events allows a measurement of the mass ratio distribution of the binary lensing population in the Galactic disk. An early alert on a binary lens event seen towards the Small Magellanic Cloud (SMC) allowed the determination of the location of the lens, and limb–darkening features for the source star ~ 85 *nano* arcseconds in radius.

- **Binary source** effects seen in one microlensing event towards the Large Magellanic Cloud (LMC). An orbiting binary system effectively serves as a enormous extended

source. Resolution of effects due to the source's orbital motion allows us to estimate that the lensing object is NOT in fact a component of our Galactic halo dark matter, but is more likely a normal star in the LMC itself.

The ensemble of observed microlensing events allows us to make powerful statements about the mass spectrum of the gravitational lensing population, a class of astronomical objects which would have otherwise remained unconstrained. This tequnique has shown to be sensitive to more than 6 decades in lens mass, from massive black holes (Chapter 5.2.1) to Earth–mass planets (Chapter 7.4.1).

BIBLIOGRAPHY

Abt, H. A. 1983, ARA&A, 21, 343

Afonso, C., et al. 1998, A&A, 337, L17

Afonso, C., et al. 1999, A&A, 344, L63

Afonso, C., et al. 2000, ApJ, 532, 340

Alard, C., Mao, S., & Guibert, J. 1995, A&A, 300, L17

Alard, C. 1996, ApJ, 458, L17

Alard, C., & Guibert, J. 1997, A&A, 326, 1

Alard, C. 2000, A&AS, 144, 363

Albrow, M., et al. 1997, in Variables Stars and the Astrophysical Returns of the Microlensing Surveys, 135

Albrow, M., et al. 1998, ApJ, 509, 687

Albrow, M. D., et al. 1999a, ApJ, 522, 1022

Albrow, M. D., et al. 1999b, ApJ, 512, 672

Albrow, M. D., et al. 2000a, ApJ, 535, 176

Albrow, M. D., et al. 2000b, ApJ, Submitted

Albrow, M. D., et al. 1999c, ApJ, 522, 1011

Alcock, C., et al. 1993, Nature, 365, 621

Alcock, C., et al. 1995a, ApJ, 454, L125

Alcock, C., et al. 1995b, ApJ, 445, 133

Alcock, C., et al. 1997a, ApJ, 486, 697

Alcock, C., et al. 1997b, ApJ, 482, 89

Alcock, C., et al. 1997c, ApJ, 491, L11

Alcock, C., et al. 1997d, ApJ, 479, 119

Alcock, C., et al. 1997e, ApJ, 474, 217

Alcock, C., et al. 1998, ApJ, 499, L9

Alcock, C., et al. 1999a, ApJ, 518, 44

Alcock, C., et al. 1999b, ApJ, 521, 602

Alcock, C., et al. 1999c, PASP, 111, 1539

Alcock, C., et al. 2000a, ApJ, 542, 000

Alcock, C., et al. 2000b, ApJ, Submitted

Alcock, C., et al. 2000c, ApJS, Submitted

Alcock, C., et al. 2000d, ApJ, 541, 270

Alcock, C., et al. 2000e, ApJ, Submitted

Alcock, C., et al. 2000f, In preparation

Alloin, D., & Bica, E. 1989, A&A, 217, 57

Ansari, R., et al. 1997, A&A, 324, 843

Ansari, R., et al. 1999, A&A, 344, L49

Aubourg, É., Palanque-Delabrouille, N., Salati, P., Spiro, M., & Taillet, R. 1999, A&A, 347, 850

Babcock, H. W. 1939, Lick Observatory Bulletin, 19, 41

Bahcall, N. A., & Fan, X. 1998, ApJ, 504, 1

Barbuy, B., Castro, S., Ortolani, S., & Bica, E. 1992, A&A, 259, 607

Becker, A., Rhie, S., & Bennett, D. 1998, IAU Circ., 6935, 1

Begeman, K. G. 1989, A&A, 223, 47

Benetti, S., Pasquini, L., & West, R. M. 1995, A&A, 294, L37

Bennett, C. L., et al. 1996a, ApJ, 464, L1

Bennett, D., & Marshall, S. 1996, IAU Circ., 6361, 1

Bennett, D., & Rhie, S. 1998, IAU Circ., 6939, 2

Bennett, D. P., et al. 1996b, in Nucl. Phys. B (Proc. Suppl.), Vol. 51B, Sources and Detection of Dark Matter in the Universe: Proceedings of the International Symposium on Sources and Detection of Dark Matter in the Universe, ed. D. Cline (Elsevier Science), 131

Bennett, D. P., et al. 1997, in Proceedings of Planets Beyond the Solar System and the Next Generation of Space Missions, ed. D. R. Soderblom (Astronomical Society of the Pacific), 95, astro-ph/9612208, held at STScI, October 16-18, 1996

Bennett, D. P., et al. 1995, in Dark Matter, ed. Holt, S. S. and Bennett, C. L. , AIP Conference Proceedings No. 336, 77

Bennett, D. P., & Rhie, S. H. 1996, ApJ, 472, 660

Bennett, D. P., et al. 1999, Nature, 402, 57

Bertelli, G., Bressan, A., Chiosi, C., Fagotto, F., & Nasi, E. 1994, A&AS, 106, 275

Bessell, M. S., Castelli, F., & Plez, B. 1998, A&A, 333, 231

Bessell, M. S., & Wood, P. R. 1984, PASP, 96, 247

Binney, J., Gerhard, O., & Spergel, D. 1997, MNRAS, 288, 365

Binney, J., & Merrifield, M. 1998, "Galactic astronomy" (Galactic astronomy / James Binney and Michael Merrifield. Princeton, NJ : Princeton University Press, 1998. (Princeton series in astrophysics) QB857 .B522 1998 ($35.00))

Blais-Ouellette, S. ., Carignan, C., Amram, P., & Côté, S. . 1999, AJ, 118, 2123

Blakeslee, J. P., Davis, M., Tonry, J. L., Dressler, A., & Ajhar, E. A. 1999, ApJ, 527, L73

Bolatto, A. D., & Falco, E. E. 1994, ApJ, 436, 112

Bono, G., Caputo, F., Castellani, V., & Marconi, M. 1997, A&AS, 121, 327

Caputo, F., & De Santis, R. 1992, AJ, 104, 253

Cardelli, J. A., Clayton, G. C., & Mathis, J. S. 1989, ApJ, 345, 245

Carlberg, R. G., Yee, H. K. C., Ellingson, E., Abraham, R., Gravel, P., Morris, S., & Pritchet, C. J. 1996, ApJ, 462, 32

Claret, A., Diaz-Cordoves, J., & Gimenez, A. 1995, A&AS, 114, 247

Cline, D., ed. 1996, Nucl. Phys. B (Proc. Suppl.), Vol. 51B, Sources and Detection of Dark Matter in the Universe, ed. D. Cline (Elsevier Science)

Colley, W. N., Tyson, J. A., & Turner, E. L. 1996, ApJ, 461, L83

Corradi, R. L. M., Boulesteix, J., Bosma, A., Amram, P., & Capaccioli, M. 1991, A&A, 244, 27

Cowley, A. P., & Hartwick, F. D. A. 1991, ApJ, 373, 80

Crotts, A. P. S., & Tomaney, A. B. 1996, ApJ, 473, L87

de Bernardis, P., et al. 2000, Nature, 404, 955

Derue, F., et al. 1999, A&A, 351, 87

Di Stefano, R. 2000, ApJ, 539, 000

Di Stefano, R., & Mao, S. 1996, ApJ, 457, 93

Di Stefano, R., & Perna, R. 1997, ApJ, 488, 55

Di Stefano, R., & Scalzo, R. A. 1999a, ApJ, 512, 564

Di Stefano, R., & Scalzo, R. A. 1999b, ApJ, 512, 579

Diaz, A. I., Terlevich, E., & Terlevich, R. 1989, MNRAS, 239, 325

Díaz-Cordovés, J., Claret, A., & Giménez, A. 1995, A&AS, 110, 329

Dominik, M. 1998a, A&A, 330, 963

Dominik, M. 1998b, A&A, 329, 361

Dominik, M. 1999, A&A, 341, 943

Dominik, M., & Hirshfeld, A. C. 1996, A&A, 313, 841

Dyck, H. M., Benson, J. A., van Belle, G. T., & Ridgway, S. T. 1996, AJ, 111, 1705

Einstein, A. 1970, quoted by G. Gamow in "My World Line" (Viking Press, New York)

Eisenstein, D. J., Hu, W., & Tegmark, M. 1999, ApJ, 518, 2

Erdelyi-Mendes, M., & Barbuy, B. 1991, A&A, 241, 176

Ettori, S., & Fabian, A. C. 1999, MNRAS, 305, 834

Feast, M. W. 1996, MNRAS, 278, 11

Ferrarese, L., et al. 2000, ApJ, 529, 745

Freedman, W. L., et al. 1994, ApJ, 427, 628

Frogel, J. A., Persson, S. E., & Cohen, J. G. 1981, ApJ, 246, 842

Frogel, J. A., & Whitford, A. E. 1987, ApJ, 320, 199

Fukugita, M., Hogan, C. J., & Peebles, P. J. E. 1998, ApJ, 503, 518

Gardiner, L. T., & Noguchi, M. 1996, MNRAS, 278, 191

Garnavich, P. M., et al. 1998, ApJ, 509, 74

Gaudi, B. S., Naber, R. M., & Sackett, P. D. 1998, ApJ, 502, L33

Gibson, B. K., et al. 2000, ApJ, 529, 723

Girardi, L., Bressan, A., Bertelli, G., & Chiosi, C. 2000, A&AS, 141, 371

Gould, A. 1992, ApJ, 392, 442

Gould, A. 1994, ApJ, 421, L71

Gould, A. 1995, ApJ, 441, 77

Gould, A. 1996, PASP, 108, 465

Gould, A. 1997, ApJ, 483, 98

Gould, A. 2000, ApJ, 535, 928

Gould, A., & Loeb, A. 1992, ApJ, 396, 104

Gould, A., & Welch, D. L. 1996, ApJ, 464, 212

Graff, D. S., Gould, A. P., Suntzeff, N., Schommer, R. A., & Hardy, E. 2000, ApJ, accpted

Gray, D. F. 1992, The Observation and Analysis of Stellar Photospheres (Second ed.) (Cambridge University Press)

Griest, K. 1991, ApJ, 366, 412

Griest, K., et al. 1991, ApJ, 372, L79

Griest, K., & Hu, W. 1992, ApJ, 397, 362

Griest, K., & Safizadeh, N. 1998, ApJ, 500, 37

Guarnieri, M. D., Renzini, A., & Ortolani, S. 1997, ApJ, 477, L21

Guth, A. H. 1981, Phys. Rev. D, 23, 347

Gyuk, G., Dalal, N., & Griest, K. 2000, ApJ, 535, 90

Han, C., & Gould, A. 1995, ApJ, 447, 53

Han, C., & Gould, A. 1997, ApJ, 480, 196

Hanany, S., et al. 2000, ApJ, submitted

Hart, J., et al. 1996, PASP, 108, 220

Hogan, C. J., Olive, K. A., & Scully, S. T. 1997, ApJ, 489, L119

Holtzman, J. A., et al. 1993, AJ, 106, 1826

Holtzman, J. A., Burrows, C. J., Casertano, S., Hester, J. J., Trauger, J. T., Watson, A. M., & Worthey, G. 1995, PASP, 107, 1065

Holtzman, J. A., et al. 1999, AJ, 118, 2262

Honma, M. 1999, ApJ, 511, L29

Hubble, E. 1929, Proc. Nat. Acad. Sci. U.S., 15, 169

Humphreys, R. M., & Graham, J. A. 1986, AJ, 91, 522

Ibata, R. A., Gilmore, G., & Irwin, M. J. 1994, Nature, 370, 194

Iben, J., I. 1967, ARA&A, 5, 571

Jaffe, A. H., et al. 2000, Phys. Rev. Lett., submitted

James, F. 1994, MINUIT, Function Minimization and Error Analysis, CERN Program Library Long Writeup D506

Jones, J. E., Alloin, D. M., & Jones, B. J. T. 1984, ApJ, 283, 457

Jorgensen, U. G., Carlsson, M., & Johnson, H. R. 1992, A&A, 254, 258

Kelson, D. D., et al. 2000, ApJ, 529, 768

Kerins, E. J., & Evans, N. W. 1999, ApJ, 517, 734

Kiraga, M., & Paczynski, B. 1994, ApJ, 430, L101

Kirkpatrick, J. D., Henry, T. J., & McCarthy, D. W. 1991, ApJS, 77, 417

Lang, K. R. 1992, "Astrophysical Data I. Planets and Stars." (Astrophysical Data I. Planets and Stars, X, 937 pp. 33 figs.. Springer-Verlag Berlin Heidelberg New York)

Lasserre, T., et al. 2000, A&A, 355, L39

Lennon, D. J., Mao, S., Fuhrmann, K., & Gehren, T. 1996, ApJ, 471, L23

Loeb, A., & Sasselov, D. 1995, ApJ, 449, L33

Luppino, G. A., & Kaiser, N. 1997, ApJ, 475, 20

Mao, S. 1999, A&A, 350, L19

Mao, S., & Di Stefano, R. 1995, ApJ, 440, 22

Mao, S., et al. 1994, BAAS, 185, 1705

Mao, S., & Paczyński, B. 1991, ApJ, 374, L37

Maoz, D., & Gould, A. 1994, ApJ, 425, L67

Marshall, S., et al. 1994, in IAU Symposium #161: Astronomy From Wide Field Imaging, ed. H. T. MacGillivray et al., 67

Mayor, M., & Queloz, D. 1995, Nature, 378, 355

Mazeh, T., Goldberg, D., Duquennoy, A., & Mayor, M. 1992, ApJ, 401, 265

Mihalas, D., & Binney, J. 1981, Galactic Astronomy (2 ed.) (W. H. Freeman and Company)

Minniti, D. 1996, ApJ, 459, 579

Minniti, D., Liebert, J., Olszewski, E. W., & White, S. D. M. 1996, AJ, 112, 590

Moore, B., & Silk, J. 1995, ApJ, 442, 5

Mould, J. R., et al. 2000, ApJ, 529, 786

Nemiroff, R. J., & Wickramasinghe, W. A. D. T. 1994, ApJ, 424, L21

Nevalainen, J., Markevitch, M., & Forman, W. 2000, ApJ, 536, 73

Ng, Y. K., Bertelli, G., Chiosi, C., & Bressan, A. 1997, A&A, 324, 65

Olive, K. A., Steigman, G., & Walker, T. P. 2000, Physics Reports, 333-334, 389

Olsen, K. A. G. 1999, AJ, 117, 2244

Ortolani, S., Barbuy, B., & Bica, E. 1990, A&A, 236, 362

Paczyński, B. 1986, ApJ, 304, 1

Paczyński, B. 1991, ApJ, 371, L63

Paczynski, B. 1996, ARA&A, 34, 419

Palanque-Delabrouille, N. 1997, Ph.D. thesis, Université de Paris 7

Palanque-Delabrouille, N., et al. 1998, A&A, 332, 1

Peale, S. J. 1997, Icarus, 127, 269

Peebles, P. J. E. 1993, "Principles of physical cosmology" (Princeton Series in Physics, Princeton, NJ: Princeton University Press, —c1993)

Peng, E. W. 1997, ApJ, 475, 43

Perlmutter, S., et al. 1999, ApJ, 517, 565

Persic, M., Salucci, P., & Stel, F. 1996, MNRAS, 281, 27

Phillips, M. M., Lira, P., Suntzeff, N. B., Schommer, R. A., Hamuy, M., & Maza, J. . 1999, AJ, 118, 1766

Pratt, M., et al. 1996, in Astrophysical Applications of Gravitational Lensing: Proceedings of the 173rd Symposium of the International Astronomical Union, ed. C. S. Kochanek & J. N. Hewitt, International Astronomical Union Symposium Series No. 173 (Kluwer Academic Publishers), 221

Press, W. H., Teukolsky, S. A., Vetterling, W. T., & Flannery, B. P. 1992, "Numerical recipes in C. The art of scientific computing" (Cambridge: University Press, —c1992, 2nd ed.)

Refsdal, S. 1964, MNRAS, 128, 295

Refsdal, S. 1966, MNRAS, 134, 315

Renault, C., et al. 1997, A&A, 324, L69

Rhie, S. H., Becker, A. C., Bennett, D. P., Fragile, P. C., Johnson, B. R., King, L. J., Peterson, B. A., & Quinn, J. 1999, ApJ, 522, 1037

Rhie, S. H., & Bennett, D. P. 1996, in Nucl. Phys. B (Proc. Suppl.), Vol. 51B, Sources and Detection of Dark Matter in the Universe: Proceedings of the International Symposium on Sources and Detection of Dark Matter in the Universe, ed. D. Cline (Elsevier Science), 86

Rhie, S. H., et al. 2000, ApJ, 533, 378

Rieke, G. H., & Lebofsky, M. J. 1985, ApJ, 288, 618

Roberts, M. S., & Whitehurst, R. N. 1975, ApJ, 201, 327

Roulet, E., & Mollerach, S. 1997, Phys. Rep., 279, 67

Ryan, S. G., Beers, T. C., Olive, K. A., Fields, B. D., & Norris, J. E. 2000, ApJ, 530, L57

Sahu, K. C. 1994, Nature, 370, 275

Sakai, S., et al. 2000, ApJ, 529, 698

Sasselov, D. 1997, in Variables Stars and the Astrophysical Returns of the Microlensing Surveys, 141

Schechter, P. L., Mateo, M., & Saha, A. 1993, PASP, 105, 1342

Schlegel, D. J., Finkbeiner, D. P., & Davis, M. 1998, ApJ, 500, 525

Schneider, P., Ehlers, J., & Falco, E. 1992, Gravitational Lenses (Springer-Verlag)

Schneider, P., & Weiss, A. 1986, A&A, 164, 237

Schwering, P. B. W., & Israel, F. P. 1991, A&A, 246, 231

Small, T. A., Ma, C., Sargent, W. L. W., & Hamilton, D. 1998, ApJ, 492, 45

Smith, S. 1936, ApJ, 83, 23

Stanek, K. Z. 1996, ApJ, 460, L37

Stetson, P. B. 1994, PASP, 106, 250

Stetson, P. B. 1994, User's Manual for DAOPHOT II, Dominion Astrophysical Observatory

Stubbs, C., et al. 1993, BAAS, 183, 7205

Stubbs, C. W. 1999, in ASP Conf. Ser. 165: The Third Stromlo Symposium: The Galactic Halo, 503

Tomaney, A. B., & Crotts, A. P. S. 1996a, AJ, 112, 2872

Tomaney, A. B., & Crotts, A. P. S. 1996b, AJ, 112, 2872

Tonry, J. L., Blakeslee, J. P., Ajhar, E. A., & Dressler, A. 2000, ApJ, 530, 625

Trimble, V. 1990, MNRAS, 242, 79

Turnshek, D. E. 1985, "An Atlas of digital spectra of cool stars" (Tucson, Ariz. : Western Research Co., 1985.), 85...

Tyson, J. A., Kochanski, G. P., & dell'Antonio, I. P. 1998, ApJ, 498, L107

Udalski, A., Kubiak, M., Szymanski, M., Pietrzynski, G., Wozniak, P., & Zebrun, K. 1998, Acta Astronomica, 48, 431

Udalski, A., Szymański, M., Kaluzny, J., Kubiak, M., Krzeminski, W., Mateo, M., Preston, G. W., & Paczyński, B. 1994, Acta Astronomica, 44, 165

Udalski, A., Szymanski, M., Mao, S., di Stefano, R., Kaluzny, J., Kubiak, M., Mateo, M., & Krzeminski, W. 1994, ApJ, 436, L103

Udalski, A., Zebrun, K., Szymanski, M., Kubiak, M., Pietrzynski, G., Soszynski, I., & Wozniak, P. 2000, Acta Astronomica, 50, 1

Valls-Gabaud, D. 1995, in Large scale structure in the universe, Proceedings of an international workshop, Potsdam, Germany, edited by J.P. Muecket, S. Gottloeber and V. Mueller 1995 (World Scientific Co.), p. 326, 326

van Albada, T. S., Bahcall, J. N., Begeman, K., & Sancisi, R. 1985, ApJ, 295, 305

Van Waerbeke, L., et al. 2000, A&A, 358, 30

Vogt, S. S., Marcy, G. W., Butler, R. P., & Apps, K. 2000, ApJ, 536, 902

Walker, A. R., & Terndrup, D. M. 1991, ApJ, 378, 119

Witt, H. J., & Mao, S. 1994, ApJ, 430, 505

Wittman, D. M., Tyson, J. A., Kirkman, D., Dell'Antonio, I., & Bernstein, G. 2000, Nature, 405, 143

Yock, P., et al. 2000, in 9th Marcel Grossmann meeting (astro–ph/0007317

Zaritsky, D., Shectman, S. A., Thompson, I., Harris, J., & Lin, D. N. C. 1999, AJ, 117, 2268

Zaritsky, D. 1999, AJ, 118, 2824

Zhao, H., Rich, R. M., & Spergel, D. N. 1996, MNRAS, 282, 175

Zhao, H. S. 2000, ApJ, 530, 299

Zwicky, F. 1933, Helvetica Physica Acta, 6, 110

The Dark Matter is Coming!

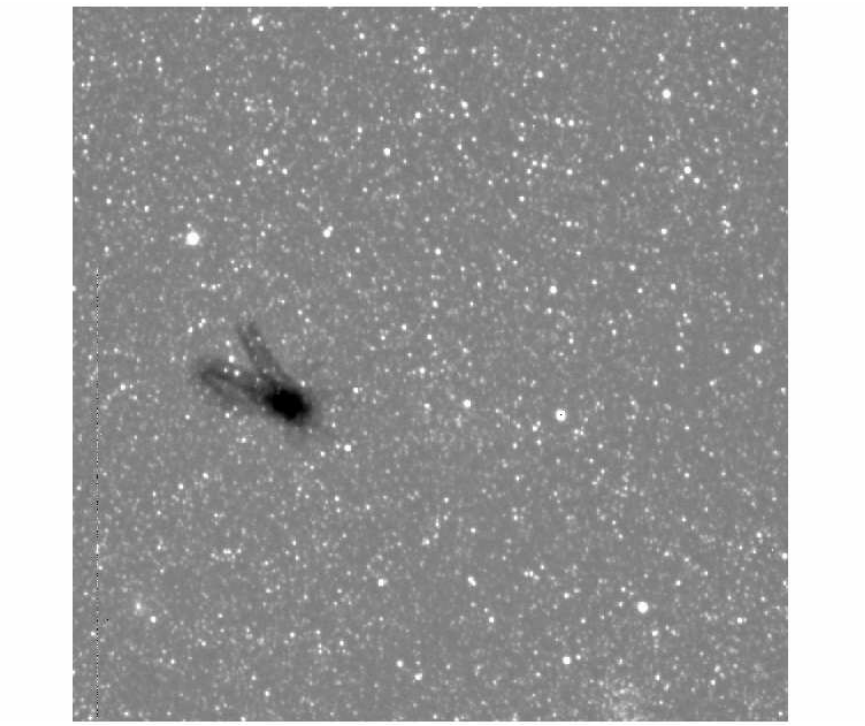

VITA

Andrew Cameron Becker was born on Friday, April 13, 1973 in Madison, Wisconsin to Philip Cameron Becker and Joan Dale Becker. When he was a child he wanted to chase tornadoes, even though the only one he has actually seen sent him scurrying into the basement. He still fancies such a thing, actually, and finds himself thinking he would like to take his children out tornado chasing some future summer.

Early in life, "zoom kid" as he was known to his parents developed a strong interest in music, and by the age of 8 he had begun to play percussion. This was his first foray into the world of music, which would eventually provide him with some of the most enjoyable and passionate moments in his existence. He was supported throughout by his parents, who sent him to Drum Corps, watched him win first chair in State Orchestra, and cringed as he grew his hair out (and out and out) while playing in a heavy metal band. They repeatedly endured deafening volumes of music, for reasons Andy did not fully understand until his recent Ph.D. defense, where their rationale was revealed : "at least we knew where he was."

An off–the–cuff remark he made at a High School science fair (Q: And what do you want to do, son? A: I want to become an astrophysicist. Read: Now buzz off buddy!) soon became a challenge for him, and he decided to pursue this field which he perceived contained the most difficult subject matter available. Primarily for this reason, he enrolled in Physics at Purdue University (his father's Alma Matter) and with a mohawk to boot, receiving his B.Sc. in 1995 at the top of his class and with Highest Honors. The motivational promise his parents had made deep in his youth ("lets say we'll give you a Ferrari if you make Highest Honors") has yet to be fulfilled except in jest.

He made his choice for graduate school by visiting several west coast departments, weighting heavily the quality of education *and life* he expected to attain at each. His goal was to understand the fundamental workings of the Universe, from a scientific and factual perspective. He accepted the University of Washington's Department of Astronomy over

the University of California, Berkeley's Department of Physics. He feels no regrets for this whatsoever, and has fallen in love with the local environment of Seattle. He received his M.Sc. in Astronomy in 1996, and feels the true individuals he has met in this program have strengthened his belief in humankind. They are motivated neither by money nor by power, but by the pursuit of the real truth behind the machinations of the Universe. He can think of no better people to have as friends.

A job offer at the prestigious Bell Labs (now Lucent Technologies), to weigh the Universe of all things, was enough to scuttle his ambiguous plans to stay in Seattle, and so he moves to the East Coast a week after composing this very paragraph. He has not forgotten his first passion, music, and plans on frequenting the sweaty bars of New York City on his path to getting this goddamn world's attention through the power of **Rock and Roll**!